COMPOSITIONAL SIMULATION OF CARBON DIOXIDE OIL RECOVERY EXPERIMENTS

by

Kiyoshi Ogino, B. S., M. S. in Mineral Engineering

THESIS

Presented to the Faculty of the Graduate School of
The University of Texas at Austin
in Partial Fulfillment
of the Requirements
for the Degree of

MASTER OF SCIENCE IN ENGINEERING

THE UNIVERSITY OF TEXAS AT AUSTIN
May, 1988

This thesis is dedicated to

my loving wife Masako

and

my children Sotaro, Reina, and Ryo.

ACKNOWLEDGEMENTS

I gratefully acknowledge the persistent encouragement and helpful recommendations by my supervising professors, Drs. Gary A. Pope and Kamy Sepehrnoori. In particular, I thank Dr. Pope for his numerous valuable comments through this study.

I also would like to thank our "CO_2 group," Dr. Mojdeh Delshad, Doug Perschke and Yih-Bor Chang, for the many comments and suggestions. In particular, I thank Yih-Bor Chang for the many comments and discussions which contributed to this thesis.

Finally, I would like to thank Japan Petroleum Exploration CO., Ltd (JAPEX) and Japan National Oil Corporation (JNOC) for their financial support during this research.

Kiyoshi Ogino
The University of Texas at Austin
Austin, Texas

May, 1988

Table of Contents

Table of Contents, Continued

CHAPTER 6

CHAPTER 7

CHAPTER 8

Table of Contents, Continued

LIST OF TABLES

LIST OF FIGURES

Chapter 1 Introduction

In the design of CO_2-flood field applications several steps are necessary to evaluate technical feasibility and to optimize CO_2 injection scheme.

Laboratory experiments including phase behavior measurements, slim tube and core displacements provide fundamental data to characterize CO_2-oil mixtures and to determine possible displacement mechanisms. Experimental data are also used for fine-tuning of phase behavior packages in compositional simulation models.

Phase behavior plays a dominant role in the vaporization or extraction process by which miscibility is achieved. Slim tube tests are useful to determine the pressure for generation of multiple contact miscibility. Core displacement tests are particularly important to evaluate the effect of rock properties on the displacement efficiency.

Phase behavior and displacement mechanisms are complex and cannot be fully explained by experiments only. A combination of experimental investigation and simulation model studies provides insight into these mechanisms. Numerical simulation is considered a reliable means to analyze design and operation criteria for CO_2-flood applications.

The objective of this thesis is to evaluate the CO_2-flood displacement performance by using the equation-of-state based compositional simulation model. A multicomponent, multiphase equation-of-state (EOS) compositional simulator, UTCOMP version 1.0[C3], was employed for these simulation studies.

The procedure shown in Fig. 1.1 and discussed below was used to compare calculated and experimental results.

1.0 Input Data Preparation for Hydrocarbon Components

Physical properties of each hydrocarbon component or pseudo component are necessary for the phase behavior calculation. Because a large number of components exists in all crude oils, the concept of pseudo components is necessary. The procedure for determining these pseudo components and their properties is illustrated in Fig. 1.2 and described in detail in Chapters 5, 6 and 7. Critical properties, acentric factors and binary interaction coefficients of each pseudo components are determined from the correlations indicated on Figs. 1 and 2.

2.0 Phase Behavior Calculation

The phase behavior was calculated using the Peng Robinson equation-of-state (PREOS) using the EOS parameters from step 1.0 above. Calculated ternary diagrams and pressure-composition diagrams were compared with experimental phase behavior data and adjustment of these EOS parameters used to achieve a better match.

3.0 Simulation of Slim Tube Displacement

First the computed densities and viscosities of the original oil were compared with experimental values and adjustments made if needed. Then the simulation of the slim tube displacement was conducted using the compositional simulator (UTCOMP) in which the same phase behavior package used in step 2.0 was implemented. The oil recovery, producing GOR, and in some cases the concentration histories (produced concentrations) were calculated and compared with experimental data and further adjustment of EOS parameters made as needed to improve agreement with the experiment.

4.0 Simulation of Coreflood Displacement

Reservoir data (core properties, configuration, etc) was first prepared and the same input data as used for the slim tube in 4.0 above initially used for these coreflood simulations. Then the effect of dispersion and other input were determined in a sensitivity study. Chapter 4 gives the results of a case which used three pure hydrocarbons. Chapters 5, 6 and 7 give the results for these crude oils.

Fig. 1.1 Flow chart for procedure of study.

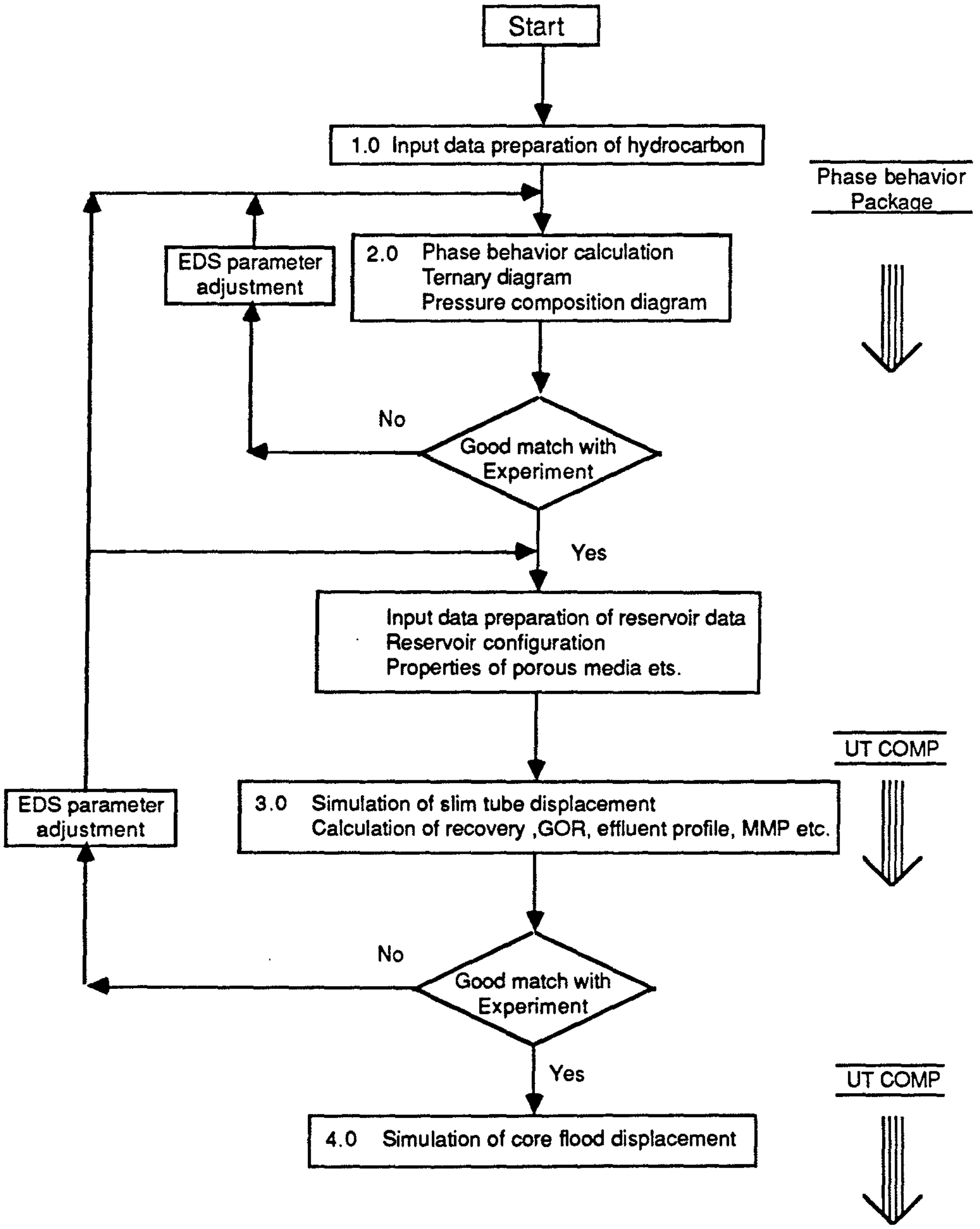

Fig 1.2 Flow chart of input data preparation of hydrocarbon

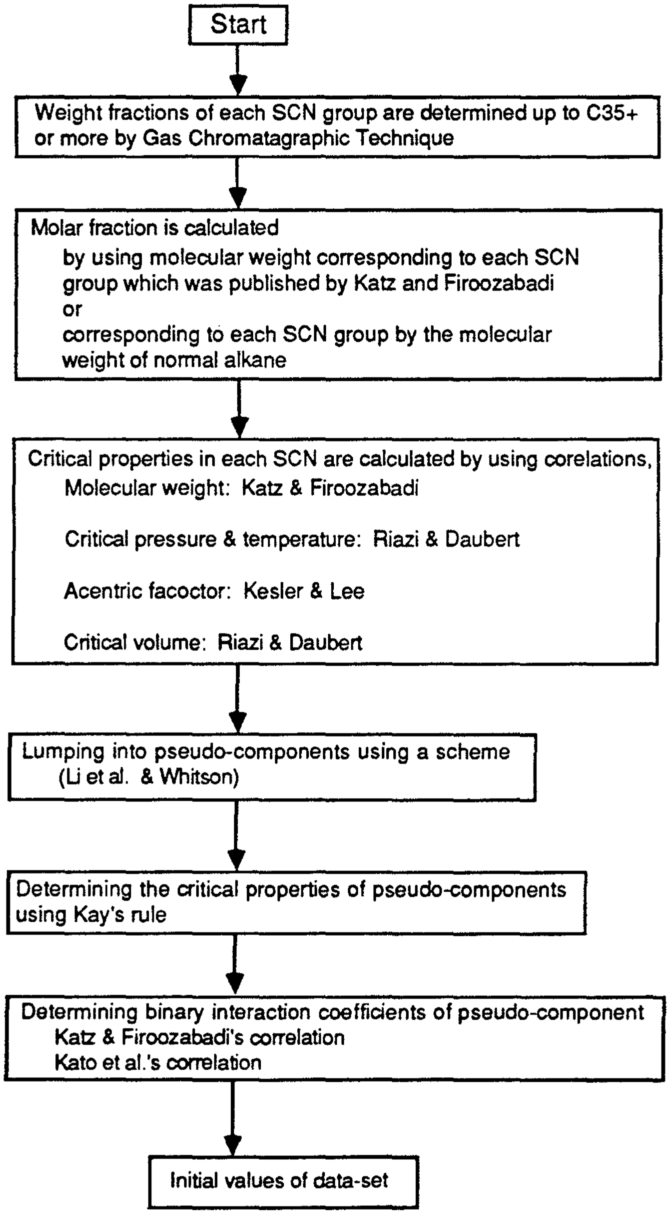

Chapter 2 Literature Review

For maximum displacement efficiency, CO_2 flooding should be conducted at displacement pressures greater than the minimum miscibility pressure (MMP). Effects of parameters such as temperature, oil composition and injection gas composition on the MMP have been the topic of several research efforts. The MMP tends to increase steadily with increasing temperature, and an oil of higher density and molecular weight requires a larger MMP.

Previous investigators [A1, H1, H2, J1, O3, S1, Y1] have presented correlations for the prediction and determination of the MMP. Yelling and Metcalfe [Y1] showed a correlation that gave the MMP as a function of temperature. They defined miscibile displacements as those in which recovery at 1.2 PV was very near the maximum recovery obtained in a series of displacements of increasing pressure.

Holm and Josendal [H1, H2] correlated the MMP against the temperature and oil C_5^+ molecular weight. The correlations proposed by Johnson and Pollin [J1], Alston et al. [A1] and Sebastian et al. [S1] take into account the effects of injection gas composition. As for the effects of oil composition on the MMP, only a few correlations have been proposed. Holm and Josendal [H3] argued that the C_5 through C_{30} hydrocarbons are extracted by CO_2 more efficiently than the heavier ones and that the MMP is related inversely to the amount of extractable C_5 through C_{30} hydrocarbons present in the oil. They also observed that the MMP is relatively lower for oil containing a larger C_5 through C_{12} fraction in the C_5 through C_{30} group. Orr et al. [O3] also reported a similar correlation. Some recent reports [H3, M1] have proposed that the molecular type of the C_5 through C_{30} fraction, i.e. paraffinic or aromatic, should have some effects on the MMP. Effects of oil composition on phase behavior of CO_2-oil mixtures and the interaction between phase behavior and displacement performance have been subjects of research in recent years [G1, H3, M2, O3].

Because of the complexity of the phase behavior and displacement mechanisms, and the high cost of laboratory experiments, a combination of experimental investigation and model studies is usually desirable.

A definition of MMP that would produce repeatable measurements from one laboratory to another should be included. In addition to breakthrough and final oil recovery amounts, a specification of the tube length and diameter, packing material and particle size and displacement rates should be made. Slim tube displacements come closest to the ideal displacements, since 1) porous medium is nearly uniform, 2) the diameter of the tube is small, and 3) assumption that fluids are well mixed is reasonable. Because viscous-finger growth is inhibited by the walls of the tube and by the development of a transition zone, the flow is nearly one dimensional. Therefore the slim tube experiment is a useful one that provides a simple test of the effect of pressure on displacement efficiency. It provides direct evidence concerning the minimum pressure for efficient displacement of the oil. The results of slim-tube displacements provide the simplest test available of the accuracy of a numerical simulation.

Simple cubic equations of state (EOS) have proven to be an adequate means to predict the phase behavior of CO_2-oil mixtures. One significant problem with using an EOS is the difficulty in characterizing heavy oil components. The use of pseudo-components is required in dealing with actual crude oils. The regrouping scheme and EOS parameters for each component must be determined. Several regrouping schemes were presented by Li [L1] and Whitson [W1] and several critical property correlations were also presented by Whitson [W2] if these properties are not given. Whitson [W1] proposed simple regrouping scheme and showed that the choice of critical property correlation has a significant influence on equation of state predictions. It is often possible to match experimental phase behavior data if the EOS parameters are adjusted (tuning). Simulation model studies with EOS simulators have been conducted to examine the performance of CO_2 displacements. The EOS can be incorporated directly in a compositional model [C1, L2, N1, N2, S2, Y3], or can be used first for ternary representations which are incorporated into a compositional model [G1, O4]. Sigmund et al. [S2] used a one-dimensional model and obtained reasonable agreement between the predictions and experimental slim tube displacement. They used the Peng-Robinson EOS with interaction coefficients adjusted to match measured phase behavior. Leach and Yellig [L2] successfully simulated displacements of a synthetic oil by CO_2 with an EOS compositional simulator, in which the Redlich-Kwong EOS was used. Their procedure for prediction was:

1. The equation of state was tuned to predict single contact (PVT) phase equilibrium for mixtures of CO_2 and synthetic model oil.
2. A simulator using this equation of state was used to predict the multiple-contact phase equilibria during a CO_2 displacement test.
3. The criteria for achieving a match of laboratory performance include:
    a. Compositions of predicted and experimentally determined oil recovery

b. And effluent compositional profiles for each component as functions of hydrocarbon pore volumes [HCPV] of CO_2 injected.

Nghiem and Li [N2] described the incorporation of three-phase flash calculations in a compositional model and confirmed the consistent results of slim tube simulation with experimental observations. They also showed that two-phase flash calculations can be performed in the three-phase region if the three-phase region is very narrow.

On the other hand, CO_2 core displacements are more difficult to interpret than slim tube experiments, because even in linear cores displacement efficiency can be affected by viscous fingering, gravity segregation, channeling or bypassing of oil due to core heterogenities, and trapping or shielding oil from contact with CO_2 by high mobile-water saturations, as well as by the complexities of CO_2/crude-oil phase behavior.

Gardner and Ypma [G2] have postulated that not only density, viscosity, permeability and dip angle determine the stabilized flood rate above which viscous fingers appear, but that dispersion of solvent into the oil phase must be accounted for. Tiffin and Yelling [T1] have reviewed the effect or noneffect of mobile water on oil recovery.

However, even with their drawbacks, Orr et al. [O2] feel core floods do seem appropriate for answering at least three questions directly:

1. Can CO_2 mobilize tertiary oil under conditions that are closer to field displacement conditions than those occurring in slim tube displacement?
2. What is the residual oil saturation in the swept zone of a CO_2 displacement?

3. Does CO_2 injection alter core permeability?

Core-flood results that answer the first question build confidence that CO_2 can displace oil under conditions that are more realistic than in slim tubes. Even so, the recovery efficiency obtained in core displacements is significantly higher than can be expected in a field displacement, because vertical conformance and areal sweep will be less favorable in the field. Craig et al. [C2] measured vertical sweepout at breakthrough in homogeneous and isotropic cross-sectional laboratory models. Maximum sweep is obtained when the displacement front proceeds through the reservoir as a plane perpendicular to the bedding plane. Any forces that act to distort this plane will reduce vertical sweep. Unfavorable mobility ratios act to accelerate the growth of the gravity tongue and to reduce breakthrough sweepout, while larger viscous forces result in improved sweepout at breakthrough.

Core floods may be important for testing numerical simulation models. Oil recovery, pressure drop, and produced-fluid compositions all can be compared with simulator predictions. Leach and Yelling [L2], as described before, simulated successfully displacements of a synthetic oil by CO_2 from an 8 foot Berea core. They used a fully compositional simulator and a version of the Redlich-Kwong EOS. Following their study, Kremesec et al. [K1] successfully simulated oil recovery and effluent compositional profiles of different reservoir oils. They showed predictions of oil recovery are more sensitive to the number of grid blocks than to adjustments in the fluid property descriptions. In their study, the viscous instabilities can be simulated as numerical dispersion.

Chapter 3 General Description of Models Used

Two simulators were used in this simulation study. The basic version of the UTCOMP was used in the most part of this study, and a modified Young and Stephensen (YS) method [T3] was adapted in the study for physical dispersion.

3.1 Brief Description of UTCOMP

A multicomponent, multiphase equation-of-state compositional simulator UTCOMP has been developed by Chang [C3].

UTCOMP models flow in one, two or three dimension and flow of up to four phases: water, oil, gas and a second hydrocarbon liquid phase, however, the basic version of UTCOMP which models three phases was used in this study.

The UTCOMP simulator is based on the formulation proposed by Acs et al. [A-2]. It is an IMPES-type procedure in which the pressure equation includes the compositional effects. The solution technique is the same as that of the implicit pressure, explicit saturation method: pressure is treated implicitly but instead of the phase saturation the component material balances (concentrations) are treated explicitly.

3.1.1 The Pressure Equation

The starting point for the compositional formulation is the saturation constraint equation for a grid block.

$$\sum_{j=1}^{np} S_j = 1 \tag{3.1.1}$$

Multiplying by the grid block pore volume, V_p, Eq (3.1.1) becomes

$$\sum_{j=1}^{np} [V_p S_j] = V_p \tag{3.1.2}$$

The left hand side of Eq (3.1.2) can be interpreted as the sum of fluid volume of all phases, i.e., the total fluid volume. Eq (3.1.2) can then be rewritten as

$$V_t^{n+1} = V_p^{n+1} \tag{3.1.3}$$

Where V_t is the total fluid volume and the superscript n+1 is added to indicate at the (n+1)th time level.

Based on a thermodynamic argument, Acs, et al. suggested that (n_c+1) partial differential equations were needed to describe the isothermal flow of n_c components. The pressure equation was formed by expressing the volumetric constraint, Eq. (3.1.3), in terms of these parameters, and combining with the conservation equations. Treating a grid block volume as a function of pressure only, the right hand side of Eq (3.1.3) can be linearized as

$$V_p^{n+1} \cong V_p^o[1+c_f(P^{n+1}-P^o)] = V_p^n + c_f V_p^o (P^{n+1}-P^n) \tag{3.1.4}$$

where
$$V_p^n = \phi^n V_b \tag{3.1.5}$$

$$V_p^o = \phi^o V_b \tag{3.1.6}$$

and
$$\phi^n = \phi^o[\,1+c_f(P^n-P^o)\,] \tag{3.1.7}$$

The volume of fluid in the grid block at the end of the (n+1)th time step, V_t^{n+1}, is linearized in terms of P, N_i ($i=1,..n_c, n_c+1$), where N_i is the number of moles of component i.

$$V_t^{n+1} \cong V_t^n + \left[\frac{\partial V_t^n}{\partial P}\right]_{NI} (P^{n+1}-P^n)$$

$$+ \sum_{i=1}^{nc+1} \left[\frac{\partial V_t^n}{\partial N_i}\right]_{P;Nr:\,r\neq 1} (N_i^{n+1}-N_i^n) \tag{3.1.8}$$

where the letter I indicates the list of component indices i, $i=1,...n_c, n_c+1$.

Defining the partial molar volume as

$$V_{ti} = \left[\frac{\partial V_t}{\partial N_i} \right]_{P;Nr:\, r\neq i} \tag{3.1.9}$$

Eq (3.1.8) can be written as

$$V_t^{n+1} \cong V_t^n + \left[\frac{\partial V_t^n}{\partial P} \right]_{NI} (P^{n+1} - P^n) + \sum_{i=1}^{nc+1} \overline{V}_{ti}^n (N_i^{n+1} - N_i^n) \tag{3.1.10}$$

The molar balance of component i can be expressed as

$$\frac{\partial N_i}{\partial t} \equiv \frac{N_i^{n+1} - N_i^n}{\Delta t} = V_b \sum_{j=1}^{np} [\, K \lambda_{rj} \xi_j \; x_{ij}]^n \nabla \; \Phi_j \; + q \tag{3.1.11}$$

where ξ_j is the phase molar density.

Substituting Eq (3.1.11) into Eq (3.1.8)

$$V_t^{n+1} \cong V_t^n + \left[\frac{\partial V_t^n}{\partial P} \right]_{NI} (P^{n+1} - P^n)$$

$$+ \sum_{i=1}^{nc+1} \overline{V}_{ti}^n \, \Delta t \, \{ \, V_b \sum_{j=1}^{np} \nabla \, [K \, \lambda_{rj} \, \xi_j \, x_{ij}]^n \nabla \; \Phi_j \; + q \, \} \tag{3.1.12}$$

Substituting Eqs (3.1.4) and (3.1.12) into (3.1.3) gives

$$\{c_f V_p^o - [\frac{\partial V_t^n}{\partial P}]_{NI}\} (P^{n+1} - P^n)$$

$$= [V_t^n - V_p^n] + \Delta t \sum_{i=1}^{nc+1} \bar{V}_{ti}^n \{V_b \sum_{j=1}^{np} \nabla [K \lambda_{rj} \xi_j x_{ij}]^n \nabla \Phi_j + q\} \qquad (3.1.13)$$

Eq (3.1.13) has two kinds of partial derivative terms, and these terms can be calculated directly from an equation-of-state. The Peng-Robinson equation-of-state (PR-EOS) is implemented in UTCOMP. Details of the procedure used to derive these terms for the PR-EOS and the details of the transformation to finite difference form are described in the 1988 CEOGRR Annual Report [P3].

3.1.2 Computation Procedure in UTCOMP

The computational procedure in UTCOMP is similar to that of the conventional IMPES black oil simulator. The computation algorithm consists of seven steps:

(1) Construct an implicit pressure equation and solve it for pressure, p^{n+1}, at the new time level.

(2) Update porosity, ϕ^{n+1}, at P^{n+1}.

(3) Compute the volumetric flux of each phase at each block boundary. using P^{n+1} and the saturations at the nth time level using Darcy's Law.

(4) Compute component material balances in moles, N_i^{n+1}.

(5) Do a flash calculation using N_i^{n+1} and P^{n+1}

(6) Compute the phase densities ξ_j^{n+1}

(7) Compute the saturations, S_j^{n+1}, relative permeabilities and capillary pressures, and go to step (1) for next time-step.

3.1.3 Phase Equilibrium and Related Equations

The conditions for thermodynamic equilibrium at constant temperature and pressure leads to the requirement that

$$f_{i2} = \text{- - - - -} = f_{in_p} \qquad (i = 1, 2, \ldots n_c) \qquad (3.2.1)$$

when f_{ij} is the fugacity of component i in phase j. This holds for all phases in a n_p-phase system.

Fugacities are often replaced with dimensionless values called fugacity coefficients which are defined as:

$$\phi_{ij} \equiv \frac{f_{ij}}{P\,x_{ij}} \qquad (j = 2,3,\ldots\ldots,n_p) \qquad (3.2.2)$$

The utility of fugacities lie in the ability to obtain them from an equation of state. The equation implemented in this study is the Peng-Robinson equation of state:

$$P = \frac{RT}{v-b_i} - \frac{a_i(T)}{v(v+b_i) + b_i(v-b_i)} \tag{3.2.3}$$

$$b_i = \Omega_b \frac{RT_{ci}}{P_{ci}} \tag{3.2.4}$$

$$a_i = \Omega_a \frac{R^2 T_{ci}^2}{P_{ci}^2} \alpha_i(T) \tag{3.2.5}$$

$$\alpha_i(T) = [1 + m_i (1 - \sqrt{\frac{T}{T_{ci}}})]^2 \tag{3.2.6}$$

$$m_i = k_0 + k_1 \omega i + k_2 \omega i^2 \tag{3.2.7}$$

$\Omega_a = 0.45724$, $\Omega_b = 0.07782$ and $k_0 = 0.37464$, $k_1 = 1.54226$, $k_2 = -0.26992$ for PR-EOS, where P_{ci} is the critical pressure, T_{ci} is the critical temperature, and ω_i is the acentric factor of component i.

The Ω_a and the Ω_b appearing in the above equations are "theoretically" universal constants which are determined by forcing the EOS to satisfy the Van der Waals conditions:

$$\left(\frac{dP}{dv}\right)_T = 0 , \quad \text{and} \quad \left(\frac{d^2P}{dv^2}\right)T = 0$$

at critical point.

In practical, however, the Ω_a and the Ω_b are generally treated as component-dependent functions [C4]. Several recent publications [C4, W2] have suggested that EOS constants Ω_a and Ω_b can be adjusted to match experimental PVT data. It can be seen that the method is essentially the same as the earlier practice of adjusting individual component critical properties. In Chapter 7, the adjustment of EOS parameter is performed based on Whitson's suggestion [W2] (more details will be discussed in Chapter 7).

It is convenient to introduce the compressibility factors

$$Z = \frac{P\ v}{R\ T} \tag{3.2.8}$$

into the equation of state. Doing so gives a cubic equation in Z:

$$Z^3 - (1 - B)\ Z^2 + (A - 3\ B^2 - 2\ B)\ Z - (AB - B^2 - B^3) = 0 \tag{3.2.9}$$

$$\text{where: } A = \frac{a\ P}{R^2\ T^2} \tag{3.2.10}$$

$$B = \frac{b\ P}{R\ T} \tag{3.2.11}$$

For mixtures, the following mixing rules are often used.

$$a = \sum_{i=1}^{nc} \sum_{j=1}^{nc} x_i \ y_j \ a_{ij} \tag{3.2.12}$$

$$b = \sum_{i=1}^{nc} x_i \ b_i \tag{3.2.13}$$

$$\text{where} \quad a_{ij} = (1 - \delta_{ij})\, a_i^{1/2} \ a_j^{1/2} \tag{3.2.14}$$

for $i = 1,2,.........,n_c$

$j = 1,2,.........,n_c$

with δ_{ij} being a binary interaction coefficient. The values a_i and b_i are given by Eqs. (3.2.4) and (3.2.5) for each component in the mixture.

Phase compressibility and fugacity coefficients are related by the following thermodynamic relationship:

$$\ln \phi_i = \lim_{p_o \to o} \int_{P_o}^{P} (Z_i - 1) \frac{dP}{P} \tag{3.2.15}$$

$$\text{where} \quad Z_i = Z + \frac{\partial Z}{\partial \xi_\iota} - \sum_{\varphi=1}^{\nu\chi} \xi_\varphi \frac{\partial Z}{\partial x_j} \tag{3.2.16}$$

Substituting Eq (3.2.9) into these expressions gives the fugacity coefficient of a component in a mixture;

$$\ln \phi_i = \frac{b_i}{b}(Z-1) - \ln(Z-B)$$

$$- \frac{A}{2\sqrt{2}B}\left(\frac{2\sum_{k=1}^{n_c} x_k a_{ik}}{a} - \frac{b_1}{b}\right) \ln \frac{Z+2.414B}{Z-0.414B}$$

for the Peng-Robinson equation of state.

3.1.4 Correlation and Miscellaneous Remarks

As mentioned before, the Peng-Robinson EOS was used in the UTCOMP simulator to calculate fugacities and hydrocarbon phase densities. The partial derivative terms in the pressure equation are calculated based on these quantities. The flash routines are performed by an accelerated successive substitution based on the algorithms by Nghiem and Aziz [N1], and Mehra et al. [M3]. Details are given by Perschke [P1] and in the 1987 CEOGRR Annual Report [P2].

The molar density of water is computed as below:

$$\xi_1 = \xi_r^1 [1 + C_1 (P - P_r^1)]$$

where superscript r represents a convenient reference state.

The viscosity of water is constant and is specified as an input parameter in the simulator. The hydrocarbon phase viscosities are computed using published correlation [J2, H4, S3] based on the procedure developed by Lohrenz et al. [L3, P2] . The relative permeabilities for sands presented by Naar et al. [N3] are mainly used, and those have a simple function of saturation exponential form. Capillary pressure and interfacial tension are neglected in this study except for the final case in Chapter 7.

The following well constrains are implemented in UTCOMP [C3]:

(a) Constant molar flow rate

(b) Constant bottomhole pressure

In this study, constant molar flow rate injection and constant bottomhole production constraints were used.

The following notations are used in expressing well terms. q_t is the total (water and hydrocarbon) molar flow rate, $f_{w,inj}$ is the molar fraction of water in q_t, $Z_{hc,inj}$ is the overall hydrocarbon composition injected.

For constant molar flow rate injectors, q_t, $f_{w,inj}$, and $Z_{hc,inj}$ are specified as input. The water flow rate and the hydrocarbon component flow rates are computed as:

$$q_{n_c+1} = f_{w,inj}\ q_t$$

$$\text{and} \qquad q_i = z_{hc,inj}\ (q_t - q_{n_c+1}) \qquad (i = 1,\ldots\ldots,n_c)$$

The component flow rates into layer m are:

$$(q_i)_m = q_i \frac{\left[Wf\left(\sum_{j=1}^{n_p} \lambda_{rj} \xi_j\right)\right]_m}{\sum_{\text{layers}} \left[Wf\left(\sum_{j=1}^{n_p} \lambda_{rj} \xi_j\right)\right]} \qquad (i=1,\ldots\ldots\ldots,n_c+1)$$

For constant bottomhole pressure producers, the flowing bottomhole pressure of the most upper layer is specified and the flowing bottomhole pressure of other layers are computed using:

$$P_{wf;m+1} \cong P_{wf;m} + (P_{m+1} - P_m)$$

The component flow rates for layer m are

$$(q_i)_m = [Wf \, (\sum_{j=2}^{n_p} \lambda_{rj} \, \xi_j \, x_{ij}) \, (P_{wf} - P)]_m$$

and

$$(q_{n_c+1})_m = [Wf \, (\lambda_{r1} \, \xi_1) \, (P_{wf} - P)]_m$$

where the well factor Wf is defined as:

$$Wf = \frac{\sqrt{K_X \, K_Y} \, \Delta z \, \Delta x}{158.03644 \, \frac{\Delta y}{2}} \qquad \text{for 1- D flow in y-direction}$$

and

$$Wf = \frac{\sqrt{K_X \, K_Y} \, \Delta z}{25.14872 \, \ln \frac{r_o}{r_w}} \qquad \text{for 2 or 3-D flow}$$

where r_0 is the equivalent radius and field units have been used in above equations, i.e., flow rate is cuft/day, permeability in md, viscosity in centipoise (cp) and length in ft.

Negligible capillary pressure is assumed in the well blocks and the fluid properties and rock properties are assumed to be constant at the grid block pressure.

3.2 Brief description of the modified Y-S method

The modified Y-S method which includes dispersion was developed by Takeda [T3] based on the original Y-S formulation described by Young and Stephensen [Y3] and by Thele [T2].

The basic equations to be solved in the Y-S formulation (without dispersion term) are listed below (all symbols are defined in the nomenclature).

(1) Hydrocarbon component material balances

$$\frac{\partial}{\partial t}\{\phi \sum_{j=2}^{np} (x_{ij}\,\xi_j\, S_j))\} + \nabla\, \{\sum_{j=2}^{np} (x_{ij}\,\xi_j\, u_j\,\} - \frac{q_i}{V_b} = 0 \qquad (3.3.1)$$

(2) Water material balances

$$\frac{\partial}{\partial t}\{\phi\, \xi_1\, S_1\} + \nabla\, \{\xi_1\, u_1\} - \frac{q_1}{V_b} = 0 \qquad (3.3.2)$$

(3) Thermodynamic phase equilibrium

$$f_{2i} - f_{3i} = 0 \tag{3.3.3}$$

(4) Saturation constraint

$$\sum_{j=1}^{np} S_j = 1 \tag{3.3.4}$$

(5) Composition constraint

$$1 - \sum_{i=1}^{nc} x_{i2} = 0$$
$$1 - \sum_{i=1}^{nc} x_{i3} = 0 \tag{3.3.5}$$

These equations in conjunction with the correlation of other physical properties (described in 3.1.4) must be solved for every grid block at each time step. Young and Stephensen used the Newton-Raphson scheme to solve these strongly non-linear equations. They treated the saturation - and concentration - dependent terms explicitly, while pressure was evaluated implicitly. The Jacobian is sparse and nearly upper triangular and the unknowns can be solved efficiently. The modified Y-S method contains the dispersion flux term in the conservation equation.

For component i, the flux term of the species conservation equation may be written as:

$$\nabla \, N_i = \nabla \sum_{j=1}^{np} (\rho_j \, \omega_{ij} \, u_j - \phi \, \rho_j \, S_j \, \overset{\Rrightarrow}{K}_{ij} \, \nabla \, \omega_{ij}) \qquad (3.3.6)$$

where r_j is the mass density

ω_{ij} is the mass fraction of component i in phase j

and $\overset{\Rrightarrow}{K}_{ij}$ is a dispersion coefficient tensor.

As the Y-S formulation is solved on mole balance basis, the mass fraction of component i in phase j may be expressed as follows:

$\omega_{ij} = (M_{wi} \, x_j \;\; x_{ij}) / r_j$ hence , cancelling M_{wi} ,

$$\nabla \sum_{j=2}^{np} \{ \phi \rho_j \;\; S_j \;\; \overset{\Rrightarrow}{K}_{ij} \, [\, \nabla \, (\xi_j \;\; x_{ij} \,)/r_j \,] \, \}$$

$$= \nabla \sum_{j=2}^{np} \{ \phi \rho_j \, S_j \, \overset{\Rrightarrow}{K}_{ij} \, [(1/\rho_j \,) \nabla (\xi_j \;\; x_{ij} \,) - (\xi_j \;\; x_{ij} \, / \rho_j^2 \,) \nabla \rho_j \,] \}$$

$$\cong \nabla \sum_{j=2}^{np} [\, \phi \, S_j \;\; \overset{\Rrightarrow}{K}_{ij} \, (\, \nabla \, \xi_j \;\; x_{ij} \,) \,] \qquad (3.3.7)$$

where x_{ji} is a mole fraction of the ith component in phase j. Here, in the final expression, $-(\xi_j x_{ji}/\rho_j)\nabla\rho_j$ was neglected [T3]. The physical dispersion coefficient in a two-dimensional tensor form is

$$\vec{\vec{K}}_{ij} = \begin{vmatrix} K_{XXij} & K_{XYij} \\ & \\ K_{YXij} & K_{YYij} \end{vmatrix} \qquad (3.3.8)$$

where the expression of individual component is given by Bear [B-2] as:

$$K_{XXij} = D_{ij}/\tau + [\alpha_{lj}/(\phi\, S_j)]\,(u_{Xj}^2/\,|\vec{u}_j|)$$

$$+\ [\alpha_{tj}/(\phi\, S_j)]\,(u_{Yj}^2/\,|\vec{u}_j|) \qquad (3.3.9.a)$$

$$K_{XYij} = K_{YXij} = [(\alpha_{lj} - \alpha_{tj})/(\phi\, S_j)]\,(u_{Xj}u_{Yj})/\,|\vec{u}_j| \qquad (3.3.9.b)$$

$$K_{YYij} = D_{ij}/\tau + [\alpha_{lj}/(\phi\, S_j)]\,(u_{Yj}^2/\,\vec{u}\,j$$

$$+\ [\alpha_{tj}/(\phi\, S_j)]\,(u_{Xj}^2/\,|\vec{u}_j|) \quad (3.3.9.c)$$

$$|\vec{u}_j| = \sqrt{u_{xj}^2 + u_{yj}^2} \qquad (3.3.10)$$

where u_{xj}, u_{yj} are superficial velocities of each direction.

If molecular diffusion coefficients are negligible, the dispersion coefficients are proportional to interstitial phase velocity $\frac{u_j}{\phi S_j}$. This implies the concentration profiles depends on length but not on velocity. In the modified Y-S method, these dispersion terms are treated explicitly, which means evaluated at the previous time step and added to the residual vector. In chapter 7, the modified Y-S method is used to check the effect of physical dispersion on core flood displacements in both 1-D and 2-D cross-sectional cases.

The following methods are adopted in those cases.

1. Composition 2-Point upstream weighting of concentrations [N1] was used.
2. Molecular diffusion coefficients are set to zero.
3. Constant grid block sizes are always used.
4. Injection conditions specified by molar rate and the bottomhole pressure constraints are used for production wells (as described in 3.1.3).
5. The same dispersivities are used in both oleic and gas phases.
6. 35% connate water saturation exists in the displacement.

Chapter 4 Simulation of a Slim Tube Displacement With Three Pure Components

4.1 Input Data Review

The UPCOMP simulator was used to perform a history match of a slim-tube displacement experiment conducted by Kossack and Hagen [K1]. Although slim-tube experiments are generally done using crude oils, the phase behavior of these complex mixtures becomes difficult to model and a test of the ability of a simulator to adequately describe the recovery process becomes mixed in the problems of a poor phase behavior definition. Therefore, Kossack and Hagen's experiments are ideal for simulation analysis because of the small number of components used and the component's well-defined phase behavior properties. The displacement was done at an injection rate of 0.03457 mole/day in a stainless steel tube 17m (55.8 feet) long with an internal diameter of 0.597 cm. The block area used in the simulator was 0.0003ft^2. The tube was packed with glass beads, 50-100 mesh, giving a porosity of 39% and an absolute permeability of 73.3 darcies. A mixture of 85 mole % methane and 15 mole % propane displaced n-decane at a pressure of 2530psia and a temperature of 100 ^oF. There was no initial water saturation. Component critical data and acentric factor are given in Table 4-1. Table 4-2 gives the binary interaction parameters used by Kossack and Hagen in their simulator study and ours.

Experimental relative permeability data given by Kossack and Hagen were presented as the ratio of effective permeabilities (k_g/k_o) as a function of oil saturation.

The separate k_g and k_o curves can not be uniquely estimated since the pressure drop was not measured in their experiment. However, Kossack and Hagen showed a set of relative permeability curves which are from their gas oil ratio (GOR) curve history match study with the constraint that the ratio of the gas/oil relative permeabilities are consistent with those of the experimental ratio values.

4.2 Sensitivity Study

4.2.1 Relative Permeability

Several approximations to the relative permeability curves were used in this simulation study as described below.

The gas/oil relative permeability calculated from these functions are compared with those measured by Kossack and Hagen in Fig 4.1. All of these curves deviate from the experimental data by about the same degree.

A best fit curve was adjusted to match the calculated relative permeability curves provided by Kossack and Hagen.

The equations for these curves are given by:

$$k_{r2} \left[\begin{array}{ll} 0.95\left(\frac{S_2}{0.50}\right)^{2.98} & S_2 \leq 0.50 \\ 1.0 & S_2 > 0.50 \end{array} \right. \tag{4.1}$$

$$k_{r3} = \left[\begin{array}{ll} 0.98(\frac{S_3}{0.65})^{2.22} & S_3 \leq 0.65 \\ 1.0 & S_3 > 0.65 \end{array} \right. \tag{4.2}$$

Solvent was injected for two pore volumes and the computed recovery using Eqs (4.1) and (4.2) differed substantially from the experimental data after about 0.8 pore volume injections.

To examine the effect relative permeability had on the recovery, several simple models were used in this simulation study. These models are given below:

Case 1:

$$k_{r2} = \left[\begin{array}{ll} 8.0\ S_2{}^3 & S_2 \leq 0.50 \\ 1.0 & S_2 > \supseteq 0.50 \end{array} \right. \tag{4.3}$$

$$k_{r3} = \left[\begin{array}{ll} 8.0\ S_3{}^3 & S_2 \leq 0.65 \\ 1.0 & S_2 > 0.65 \end{array} \right. \tag{4.4}$$

Case 2:

$$\begin{array}{c} k_{r2} = S_2^2 \\ \\ kr_3 = S_3^2 \end{array} \tag{4.5}$$

Case 3:

$$k_{r2} = S_2^{1.5}$$

$$k_{r3} = S_3^{1.5} \tag{4.6}$$

These curves are plotted in Figs. 4.2 and 4.3 and the associated recovery curves are shown in Fig. 4.4. Also shown on these plots are Kossack and Hagen's curves from their history match and the curves given by Eqs. (4.1) and (4.2). Note that Eqs. (4.1) and (4.2) are called Case 4 in these figures.

All the computed recovery curves are quite close to each other but still fall far from the experimental curve. The computed values are not affected substantially by the choice among these simplified relative permeability models, but Case 4 provided the closest match to the experimental recovery curve. Recall that Case 4 did not agree with the experimental ratio data any better than the other cases. This uncertainty can only be reduced by measuring pressure drop so that both k_o and k_g can be independently estimated.

4.2.2. Grid Refinement

Ten grid blocks were used for each of the simulation runs shown above. Additional runs were made using more grid blocks and the results are shown in Fig. 4.5. The relative permeability model used for these runs is given by Eqs. (4.1) and (4.2). As the number of grid blocks increases, the experimental data is more closely matched. However, substantial differences are still present after 0.8 pore volumes have been injected; for example at 1.6 pore volumes injected, experimental recovery is about eight percent higher than the computed recovery using 160 grid blocks. Note that , as shown in Fig. 4.6, after 40 grid blocks, the recovery is not changed significantly by increasing grid size. The recoveries shown in Fig. 4.6 are those computed at about 1.8 pore volumes of fluid injection.

4.2.3 Binary Interaction Coefficient

Using the relative permeability model of Eqs. (4.1) and (4.2) for eighty grid blocks, several simulation runs were made after changing the binary interaction coefficients. These parameters have some effect on the recovery since the size of the two-phase region changes with these coefficients.

A run was made with the coefficient for each binary pair set, in turn, to zero. The associated recoveries are given in Fig. 4.7. Table 4-3 lists the runs by case name. Case 5 is the base case in which all binary interaction coefficients are nonzero and are the same as the values used by Kossack and Hagen.

As can be seen in Fig 4.7, the recovery curves of Cases 6 and 8 more closely match the experimental curve than do Cases 5 and 7. These differences can be explained by close examination of the phase behavior computed with each set of binary interaction coefficients.

Fig. 4.8 shows the composition route at 0.915 pore volumes injected for the base case, Case 5. The injected composition is indicated at J and the initial composition is at I. At 2530 psia, it appears that an injection composition of about 0.75 C_1/0.25 C_3 would be required for developed miscibility.

Fig. 4.9 shows the composition route for Case 6. In this run, the interaction parameter between methane and decane is set to zero. Comparing Figs. 4.8 and 4.9, the two-phase region has been greatly reduced in size. However, the slopes of tie-lines are nearly unchanged. The injection composition required for developed miscibility to occur is closer to the actual injected fluid than that in Case 5, and improved recovery results from this and a smaller two-phase region.

Fig. 4.10 shows the composition route for Case 7 in which the methane-propane binary interaction coefficient is zero. Comparison with Fig. 4.8 shows only small differences in phase behavior, but these differences occur in the near-critical region. Although the two-phase region is reduced slightly in size, the slopes of the tie-lines in the critical region are not as steep for Case 7, and an injection fluid much richer in propane would be required for developed miscibility. However, only small differences occur in recovery for the two cases.

The composition route for the final case, Case 8, is shown in Fig. 4.11. Here the propane-decane interaction coefficient is set to zero. The two-phase region is actually larger than that computed for Case 5. The two recovery curves are almost identical until about 1.2 pore volumes when the Case 8 recovery increases much more than Case 5. The improvement can be explained by the steeper tie-lines of Case 8 than Case 5 in the critical region. Case 8 is closer to developed miscibility than Case 5.

4.3 History matching of slim tube displacement

Recovery is clearly affected by two aspects of the phase behavior: size of two-phase region and slope of tie-line (which means equivalently the location of critical point and the limiting tie-line). Each of these can be changed by the values of the binary interaction coefficients. Thus, it becomes a question of finding the optimum set of values. Figures 4.12 and 4.13 show a comparison of the phase envelope computed with an approximation of experimental phase compositions for Case 5, Fig. 4.12, and Case 6, Fig. 4.13. These comparisons are made at 3000 psia rather than the slim-tube pressure of 2530 psia because the phase behavior data was not reported at 2530 psia. Fig 4.12 shows a closer overall match in phase boundary than Fig. 4.13, yet the recovery curve of Case 6 more closely compares to the experimental recovery data than does Case 5.

On the other hand, comparisons among Cases 5, 6, 7 and 8 should take into account the tie-line slopes. For Case 8, the tie-line slope, especially the limiting tie-line slope, is steeper than the others. This suggests that decreasing binary interaction coefficient between propane and decane ($\delta_{2,3}$) increases this slope.

Figures 4.14 and 4.15 show a comparison between the computed phase envelope and tie-lines and an approximation of experimental phase composition for Case 9 at 2000 psia (Fig. 4.14) and the same case at 3000 psia (Fig. 4.15). Critical properties and acentric factor of Case 9 are the same as those of Case 8 except the binary interaction coefficient between propane and octane ($\delta_{2,3}$), which is set to 0.4. At both pressures, tie-line slopes and the location of critical point of computed results are very close to experimental results, however the phase envelope is still different, especially at the higher pressure (3000 psia). Simulations of slim-tube displacement at 2530 psia and 3118 psia using parameters of Case 9 were performed with 80 grid blocks.

Figures 4.16 and 4.17 show the recovery histories of those two cases. Closer results to the experimental data than before were obtained.

These results can be summarized as follows:

1. Binary interaction coefficients affect the phase behavior of this ternary mixture in a strong and important way:
    (a) An increase of $\delta_{1,3}$ increases the tie-line slope, and also expands the envelope slightly (compare Cases 5 and 7).
    (b) A decrease of $\delta_{3,10}$ increases the tie-line slope, and slightly expands the envelope (compare Cases 5 and 8).
    (c) An increase of $\delta_{1,10}$ expands the envelope in the direction of C_1 to C_{10}, but does not affect the tie-line slopes (compare Cases 5 and 6).
2. Even for this simple three component case, the slim tube displacement and phase behavior could not simultaneously be matched within experimental error by changing only the binary interaction coefficients, although the overall quality of these matches is good.

Table 4-1 Component Critical Data for Slim-Tube Simulation

Component	P_c (psia)	T_c (°R)	Acentric Factor (ω)
CH_4	667.8	343.4	0.0104
C_3H_8	616.4	666.0	0.1524
n-$C_{10}H_{22}$	303.8	1112.1	0.4885

Table 4-1 Component Critical Data for Slim-Tube Simulation

Component	P_c (psia)	T_c (°R)	Acentric Factor (ω)
CH_4	667.8	343.4	0.0104
C_3H_8	616.4	666.0	0.1524
n-$C_{10}H_{22}$	303.8	1112.1	0.4885

Table 4-2 Binary Interaction Parameters for Slim-tube Simulation

	C_3H_8	n-$C_{10}H_{22}$
CH_4	0.076	0.037
C_3H_8	-----	0.087

Table 4-3 Binary Interaction Parameters by Case

Case	$\delta_{1,3}$	$\delta_{1,10}$	$\delta_{3,10}$
5	0.076	0.037	0.087
6	0.076	0.000	0.087
7	0.000	0.037	0.087
8	0.076	0.037	0.000
9	0.076	0.037	0.040

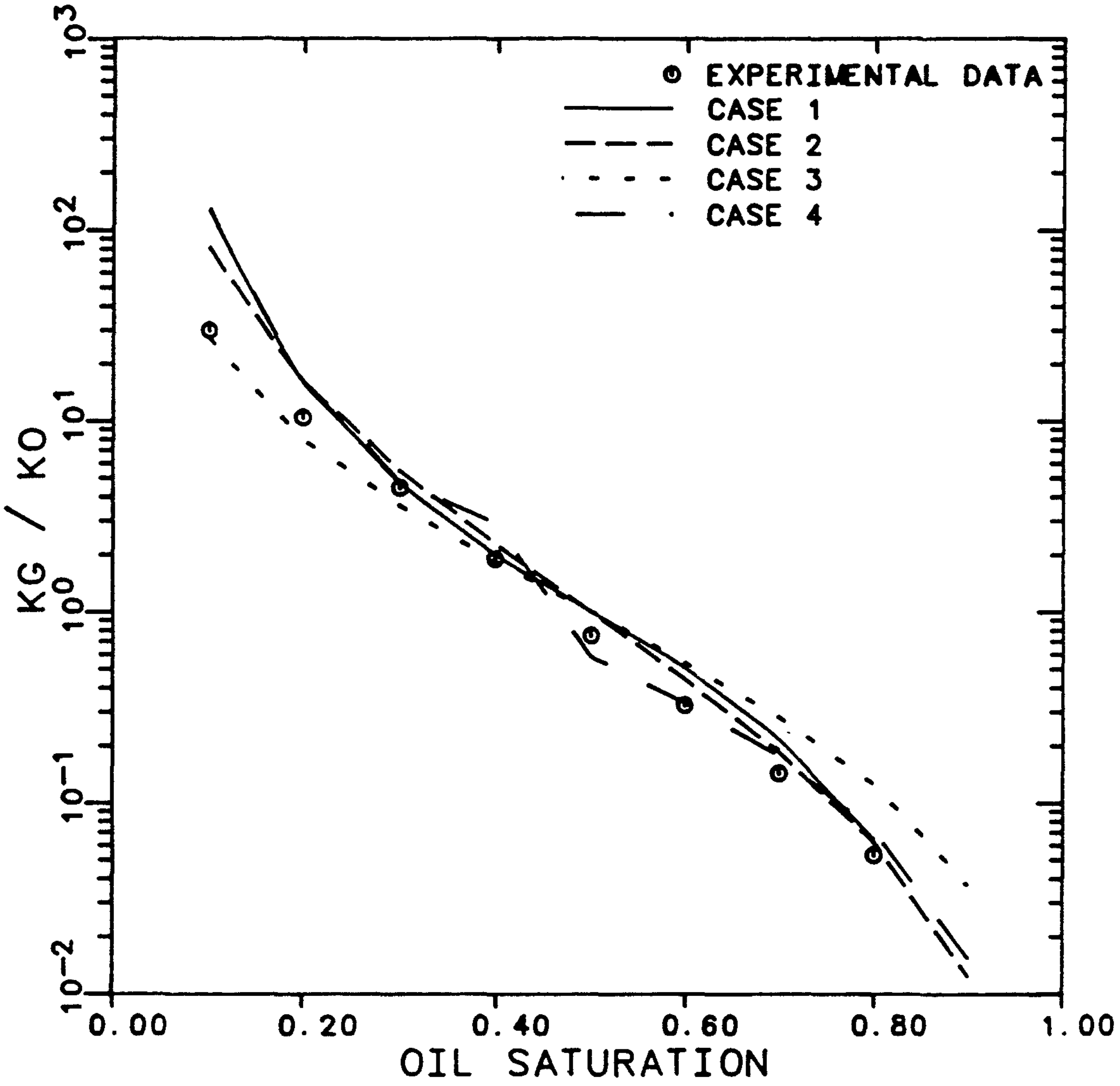

Figure 4.1 Comparison of Computed and Experimental Gas / Oil Relative Permeability Ratio as a Function of Oil Saturation

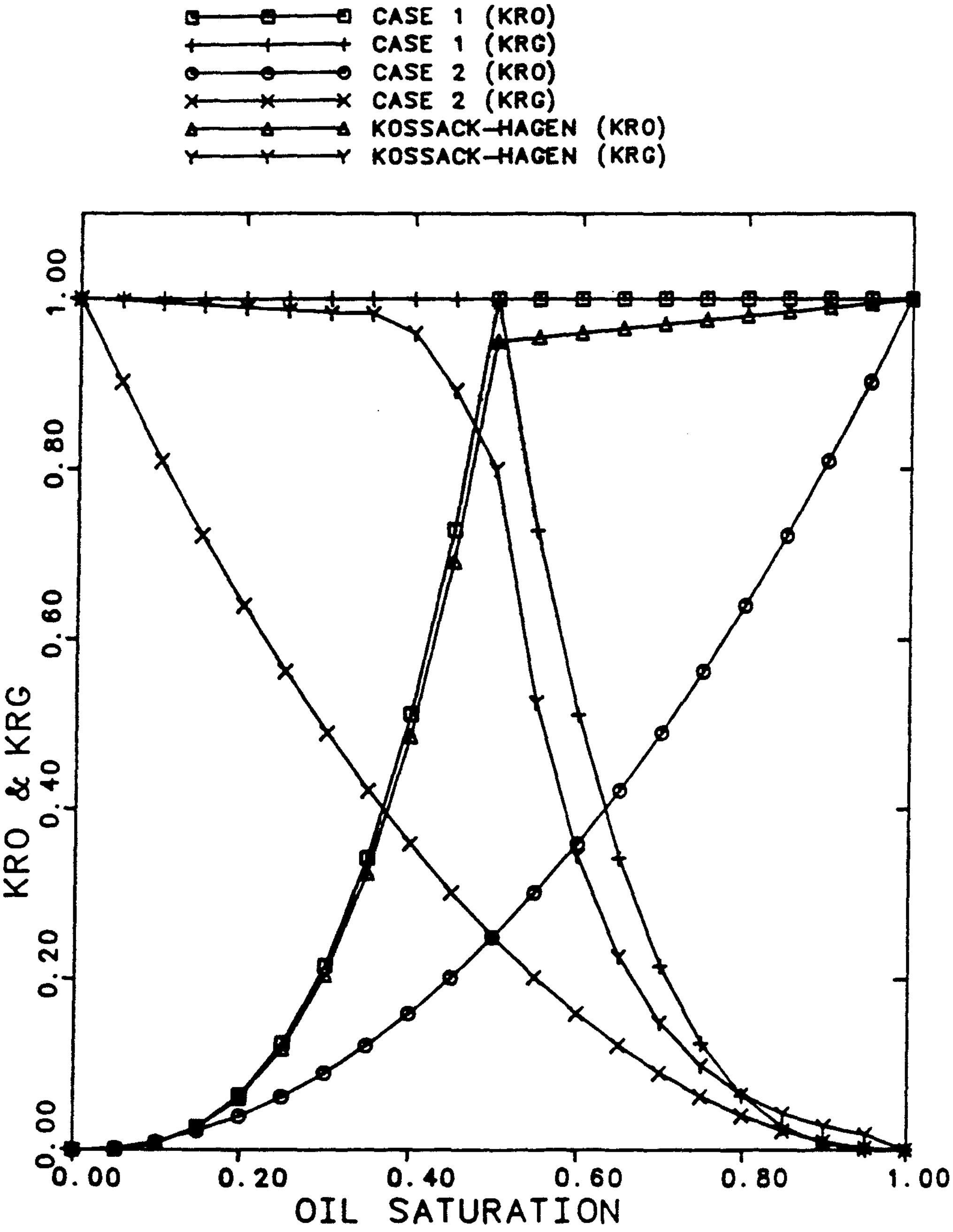

Figure 4.2 Comparison of Computed Relative Permeabilities of Cases 1 and 2 with those Calculated by Kossack and Hagen (Ref. [K1])

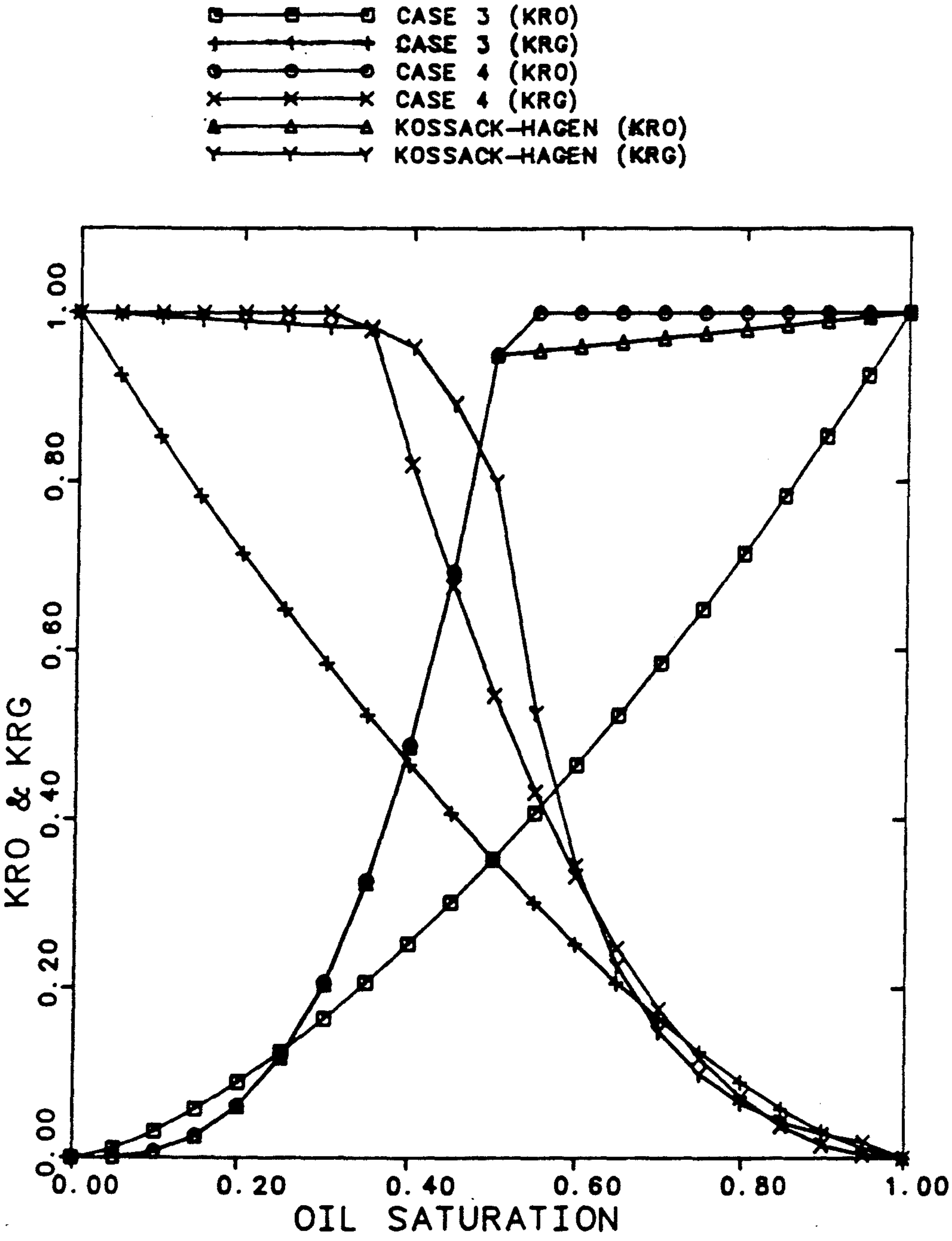

Figure 4.3 Comparison of Computed Relative Permeabilities of Cases 3 and 4 with those Calculated by Kossack and Hagen (Ref. [K1])

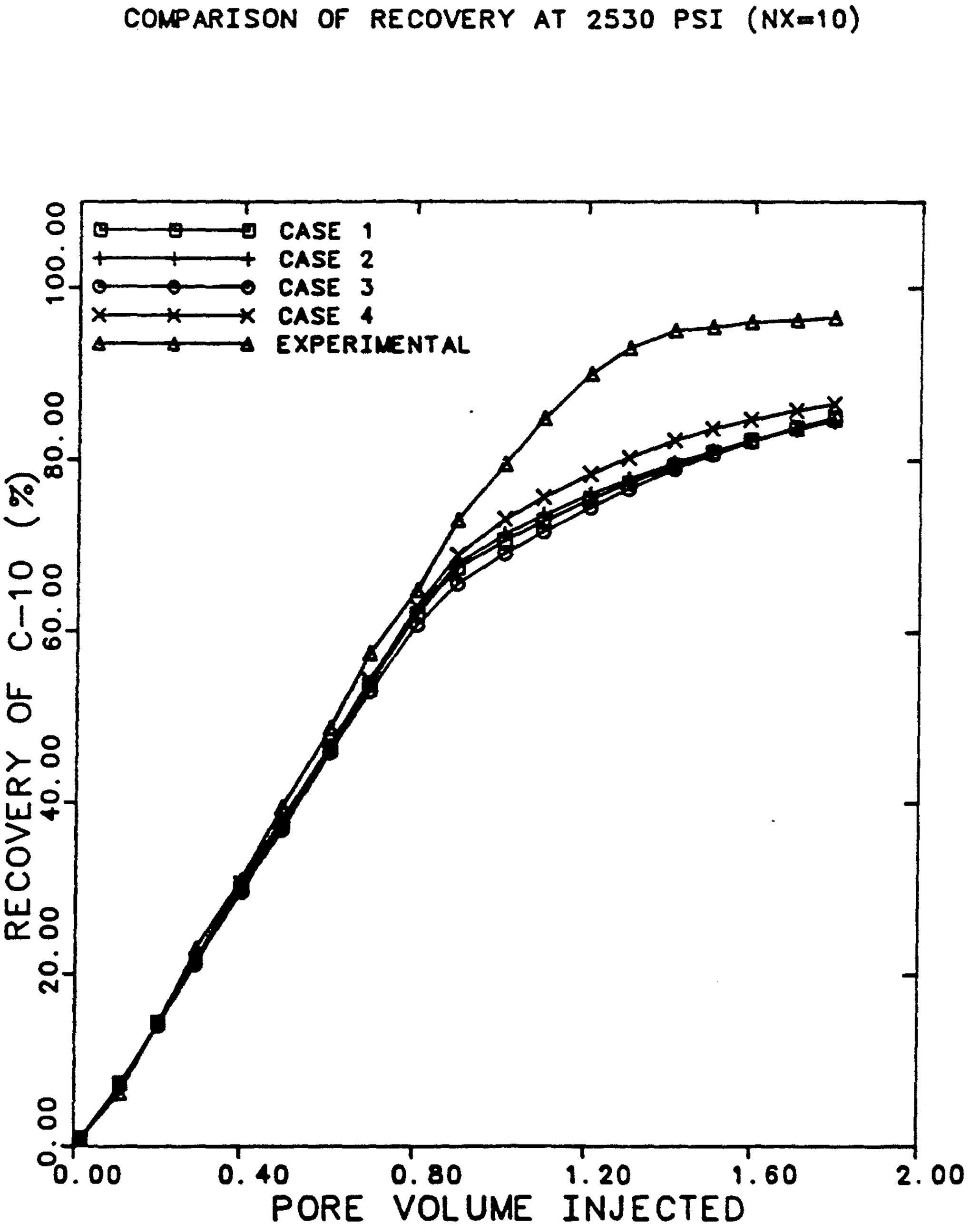

COMPARISON OF RECOVERY AT 2530 PSI (NX=10)

Figure 4.4 Comparison of Oil Recovery for Different Relative Permeability Functions with the Experimental Data of Kossack and Hagen (Ref.[K1])

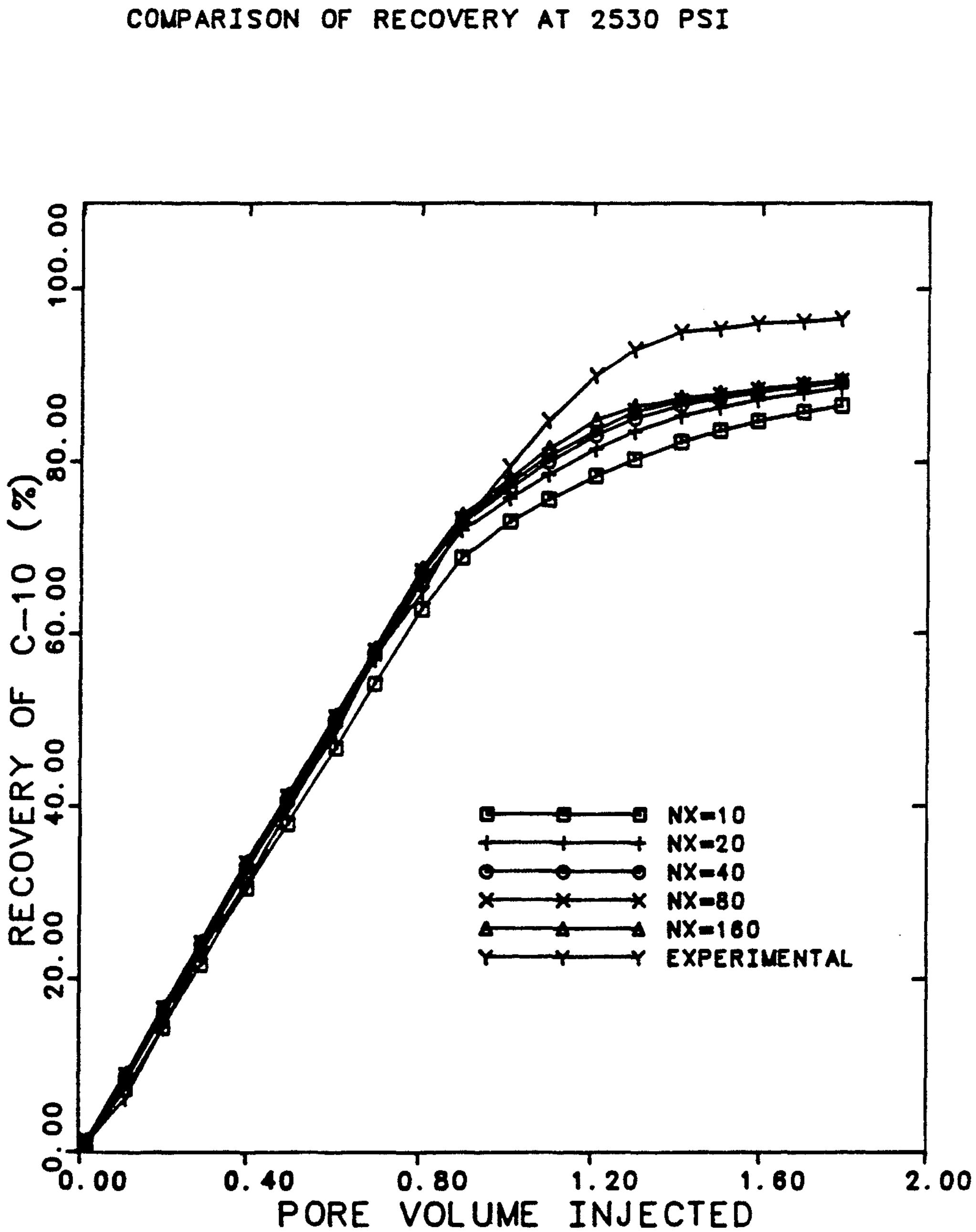

Figure 4.5 Comparison of Oil Recovery at Different Number of Blocks with the Experimental Data of Kossack and Hagen (Ref. [K1])

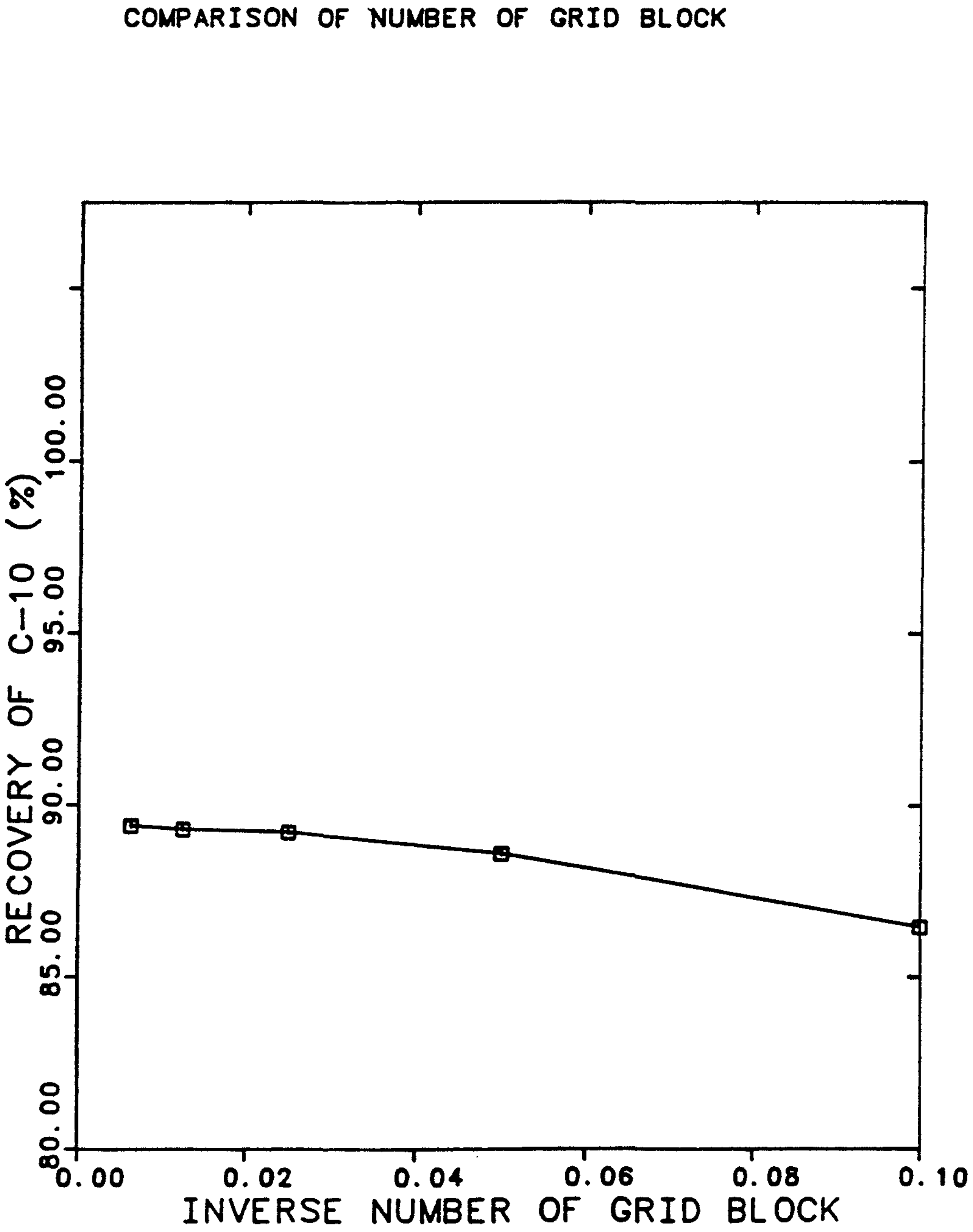

Figure 4.6 Effect of Number of Grid Blocks on Oil Recovery

COMPARISON OF RECOVERY AT 2530 PSI

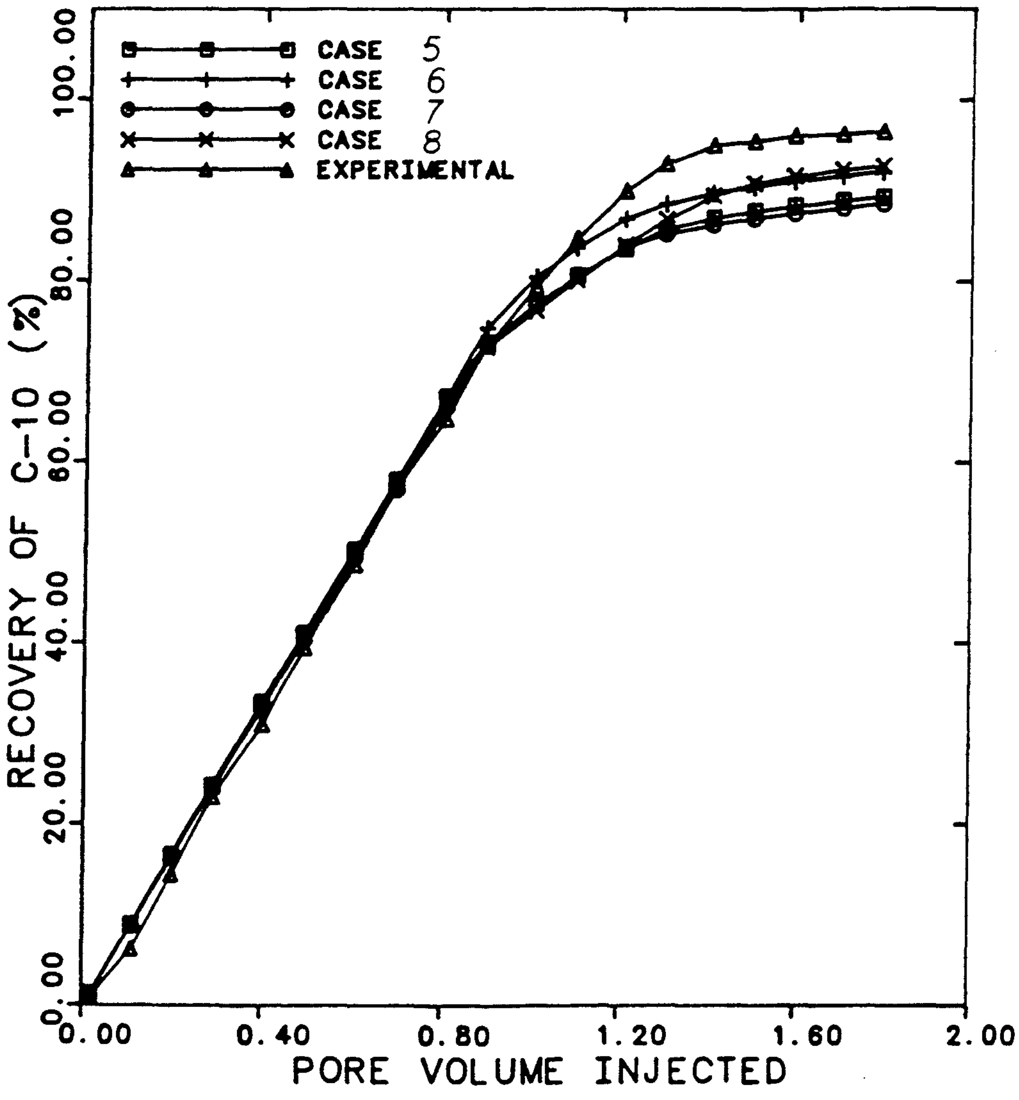

Figure 4.7 Recovery Curves using Various Sets of Binary Interaction Coefficients for Slim-tube Displacement Simulation

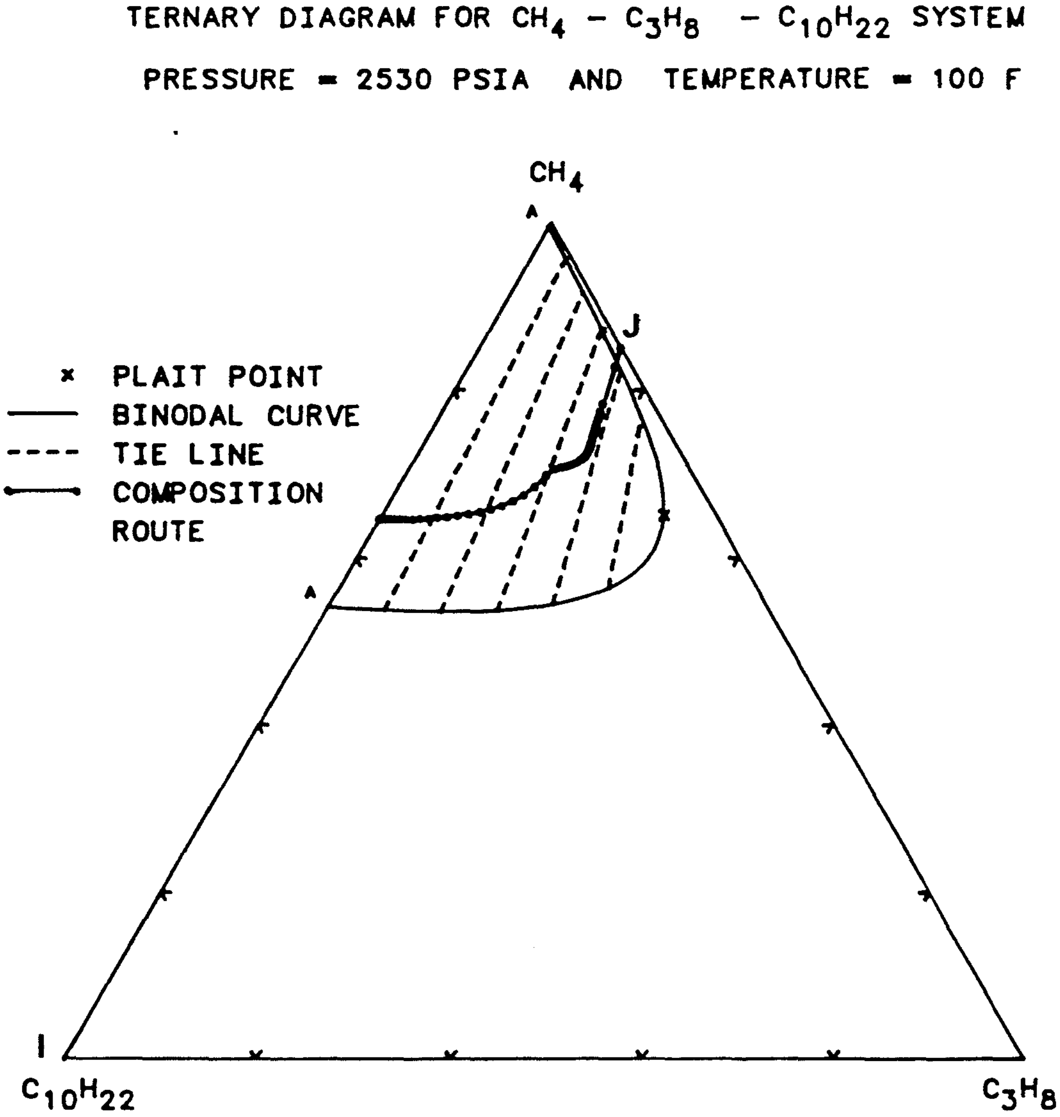

Figure 4.8 Compositiom Route for Case 5 (base case) Set of Binary Interaction Coefficients

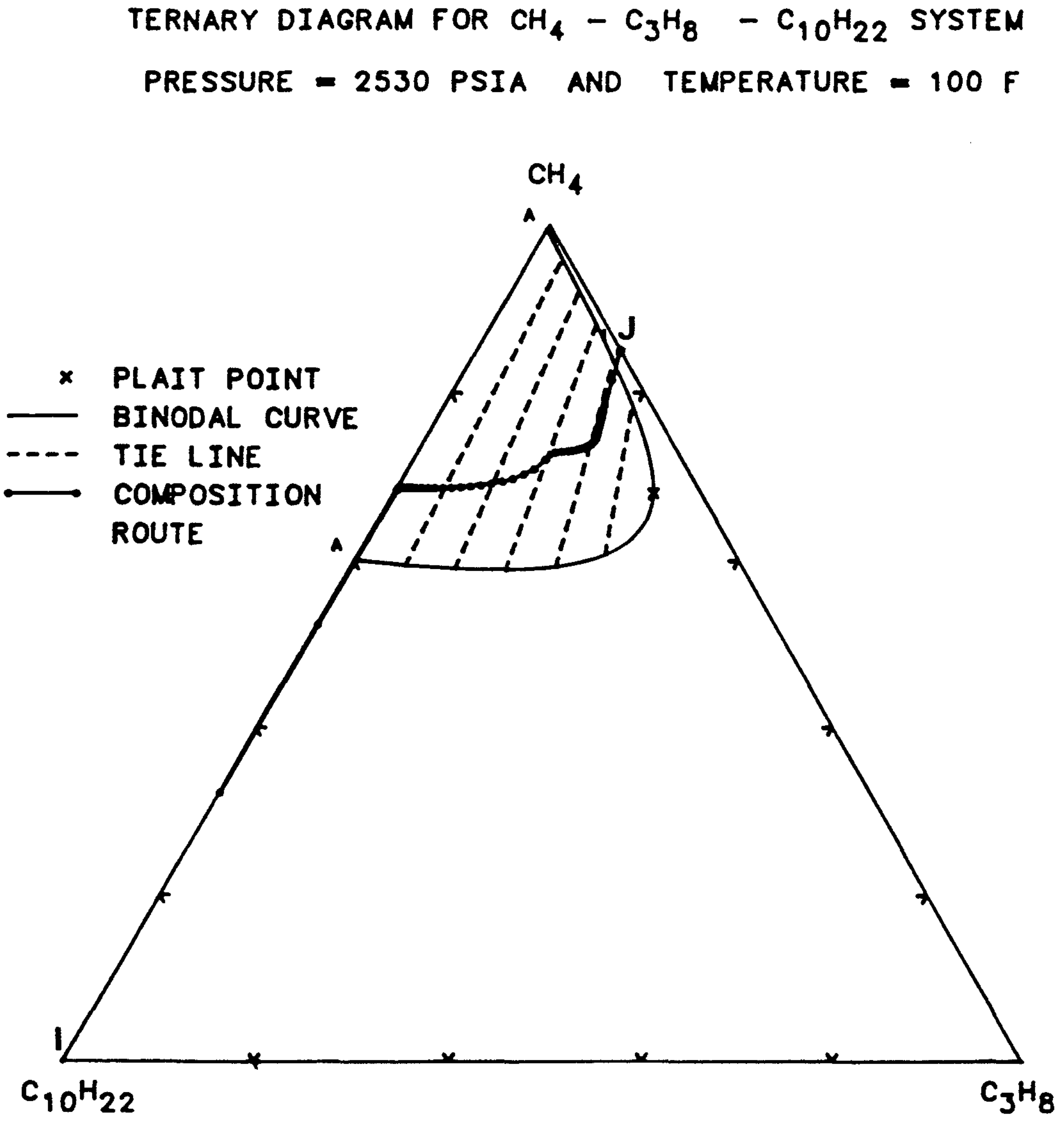

Figure 4.9 Composition Route for Binary Interaction Coefficients of Case 6 ($\delta_{1,10}$= 0)

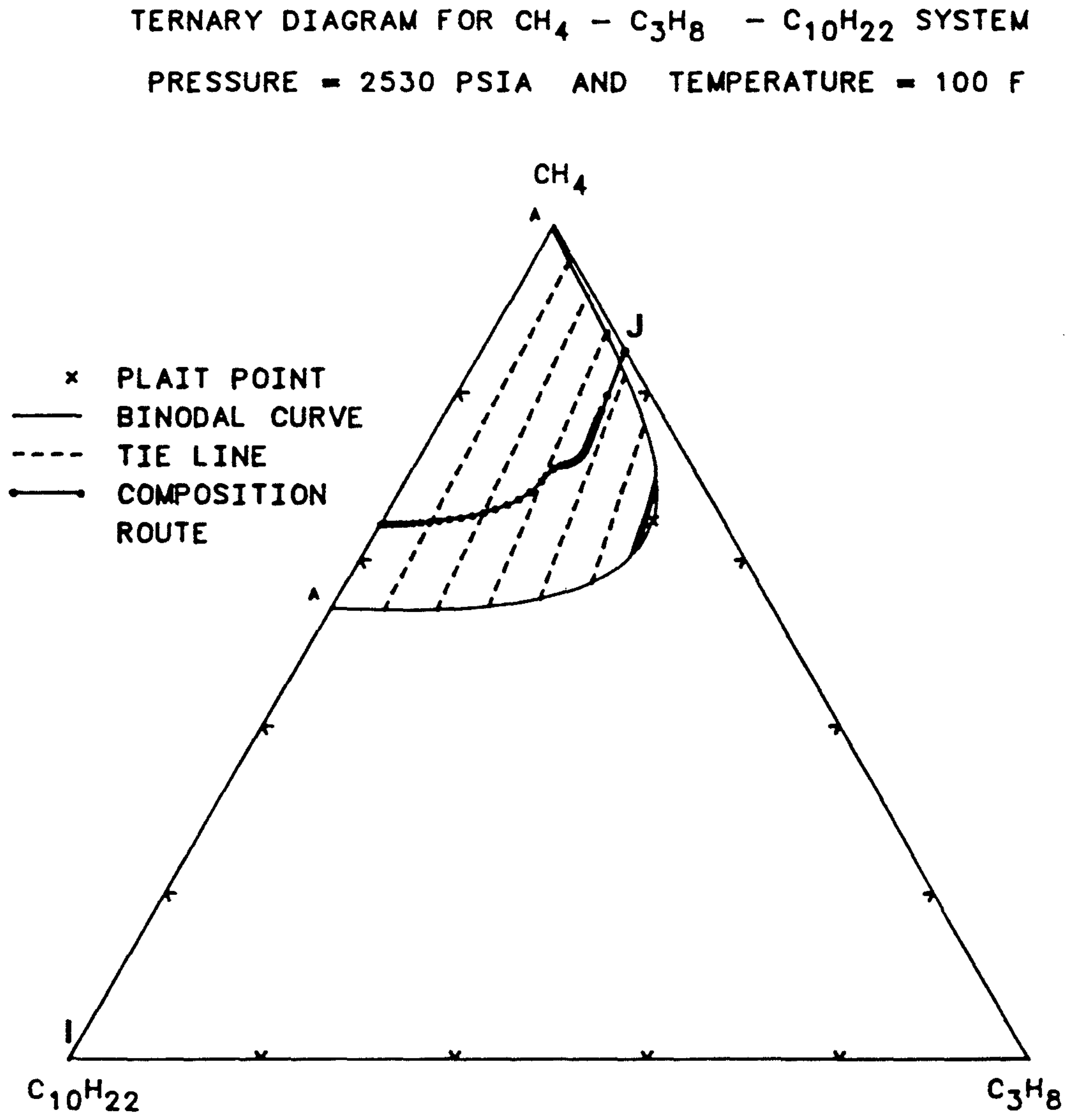

Figure 4.10 Composition Route for Binary Interaction Coefficients of Case 7 ($\delta_{1,3}$= 0)

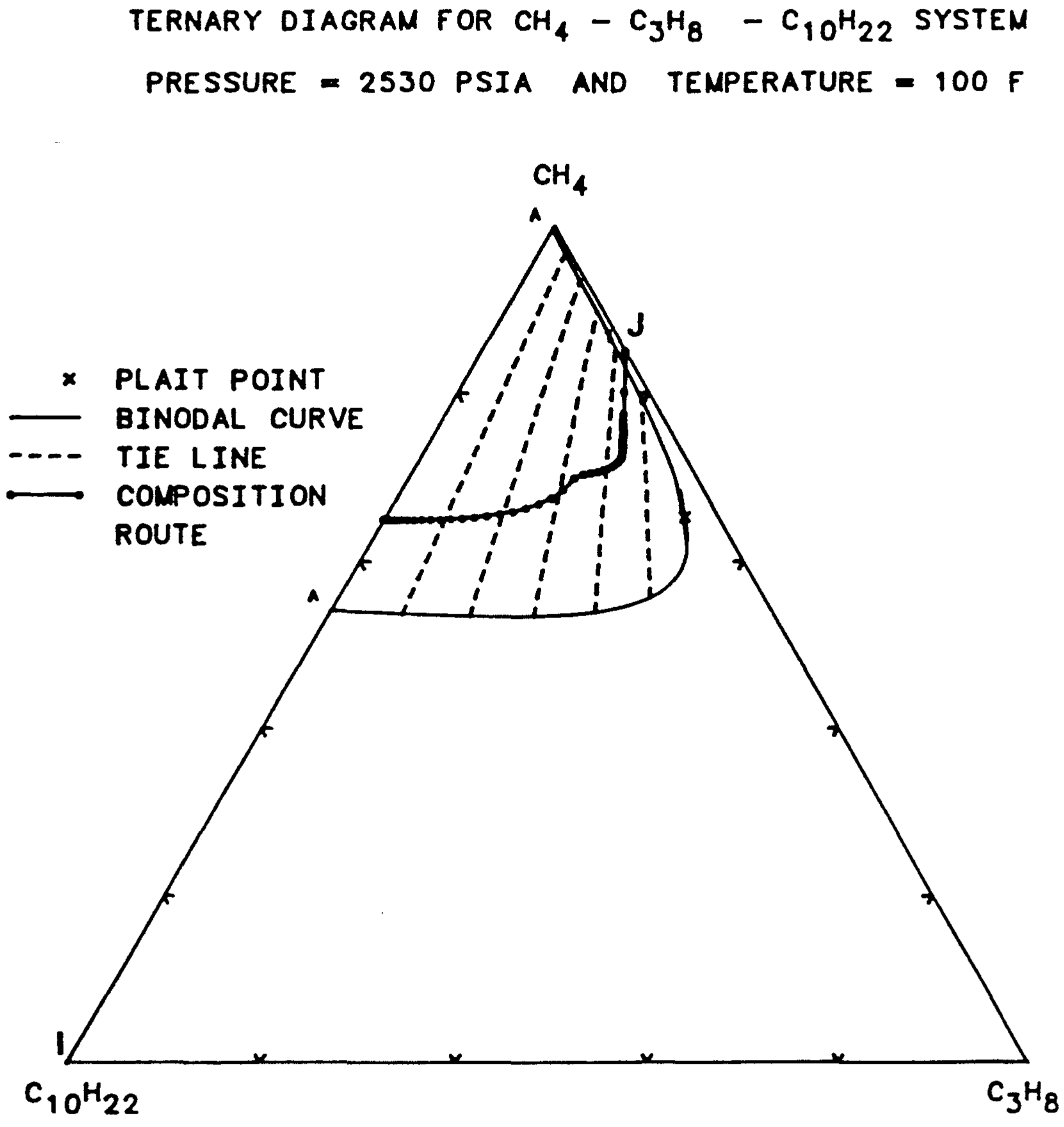

TERNARY DIAGRAM FOR CH_4 – C_3H_8 – $C_{10}H_{22}$ SYSTEM

PRESSURE = 2530 PSIA AND TEMPERATURE = 100 F

Figure 4.11 Composition Route for Binary Interaction Coefficients of Case 8 ($\delta_{3,10}$= 0)

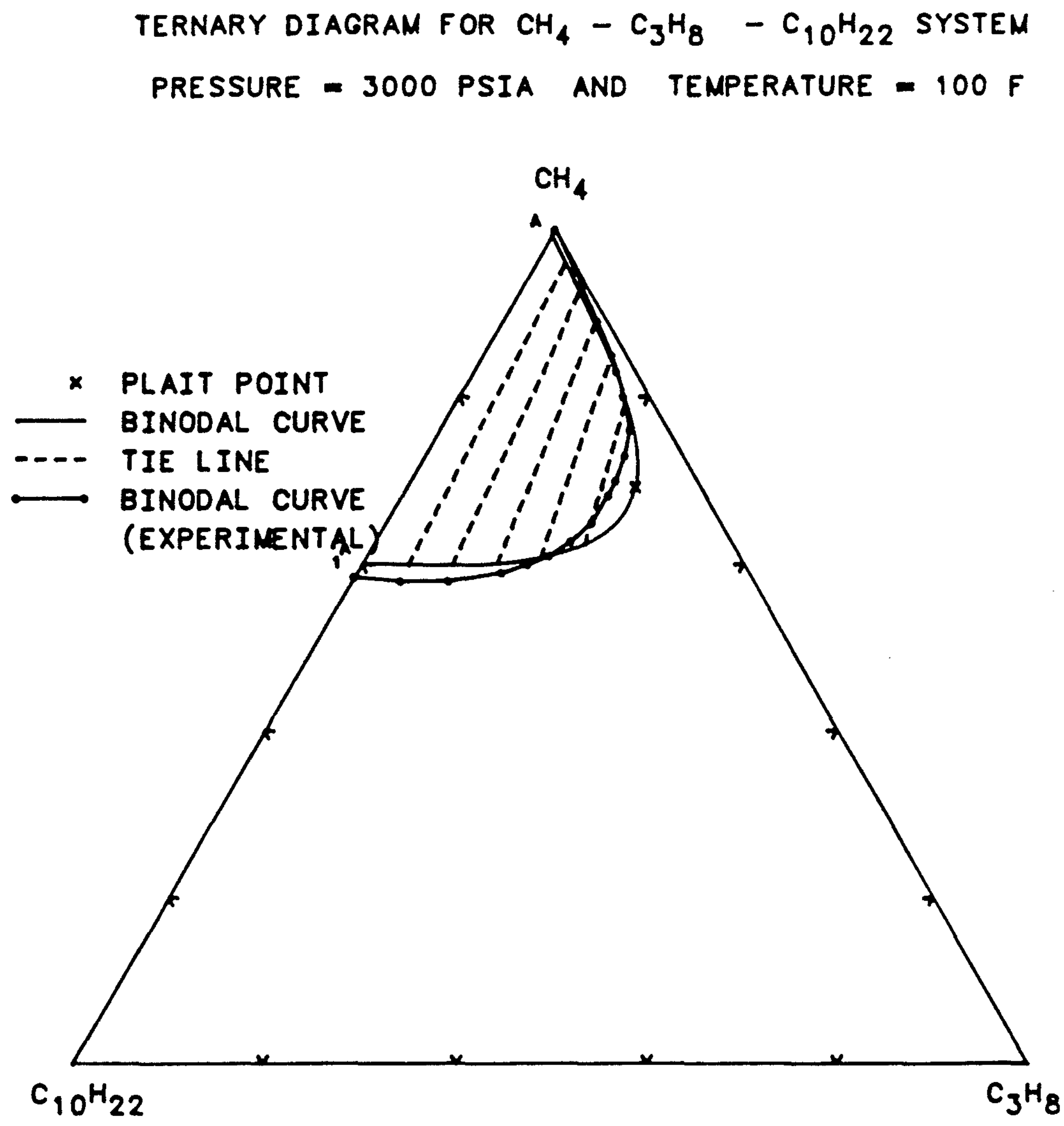

Figure 4.12 Computed Phase Envelope at 3000 psia using Binary Interaction Coefficients of Case 5

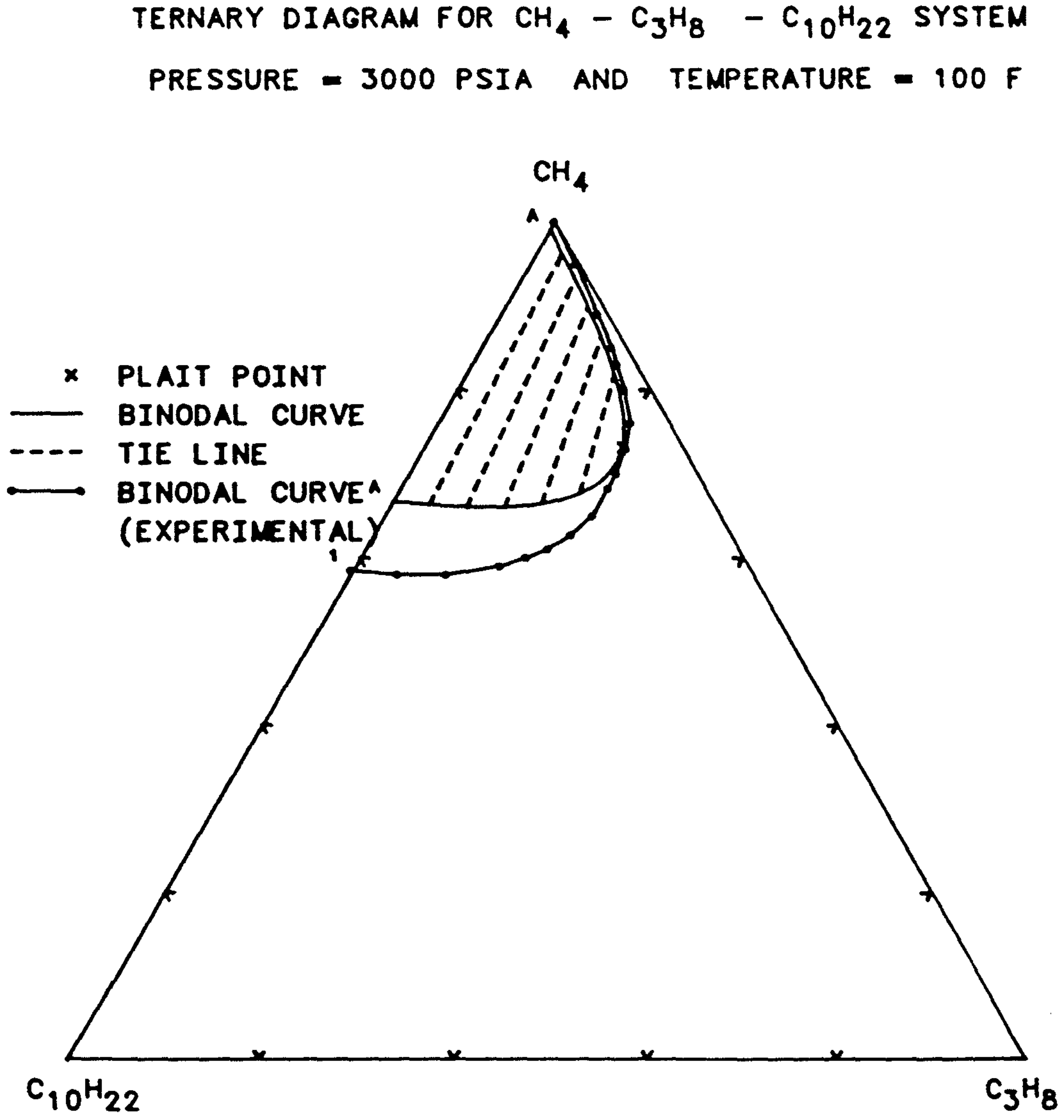

Figure 4.13 Computed Phase Envelope at 3000 psia using Binary Interaction Coefficients of Case 6

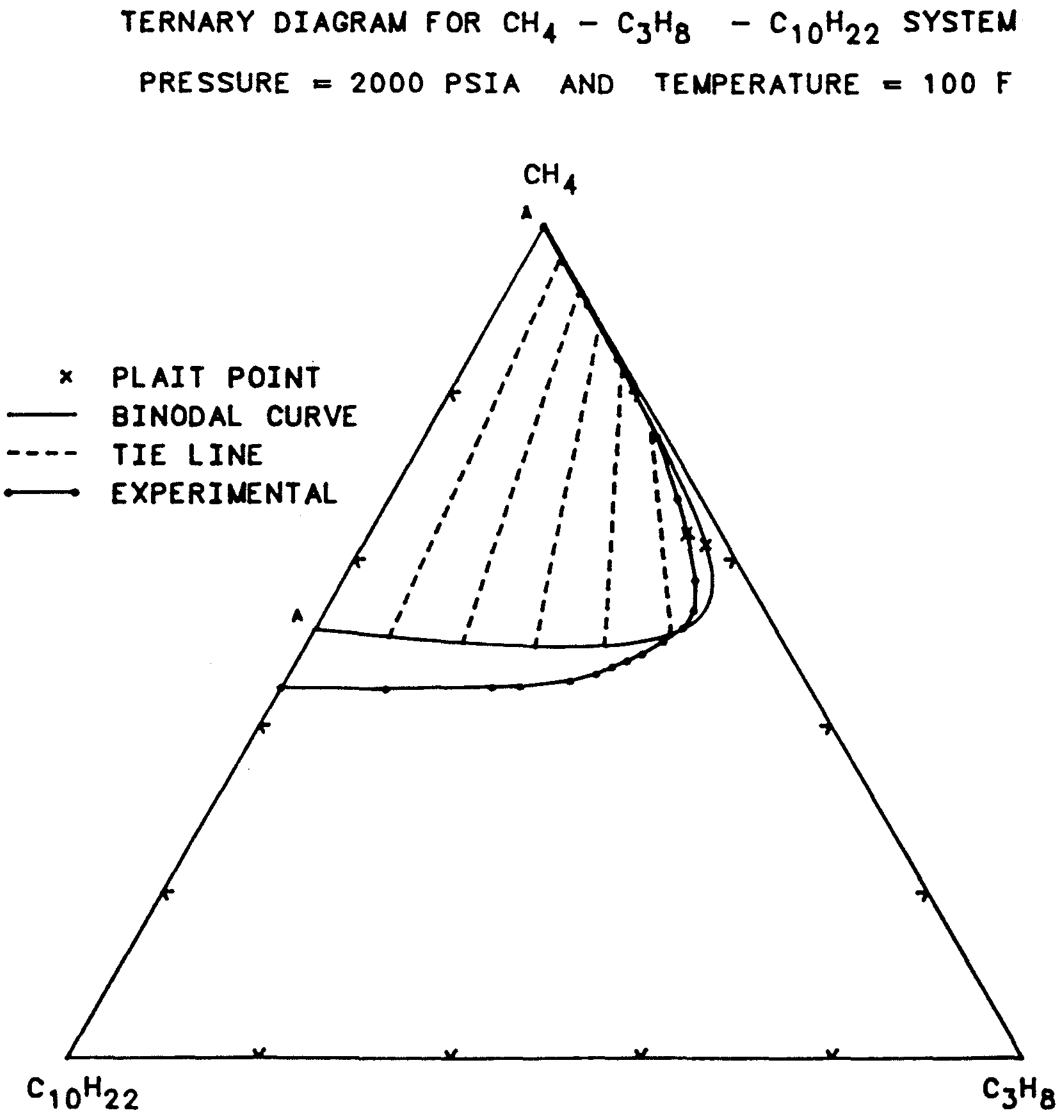

Figure 4.14 Computed Phase Envelope at 2000 psia using Binary Interaction Coefficients of Case 9 ($\delta_{3,10}$= 0.04)

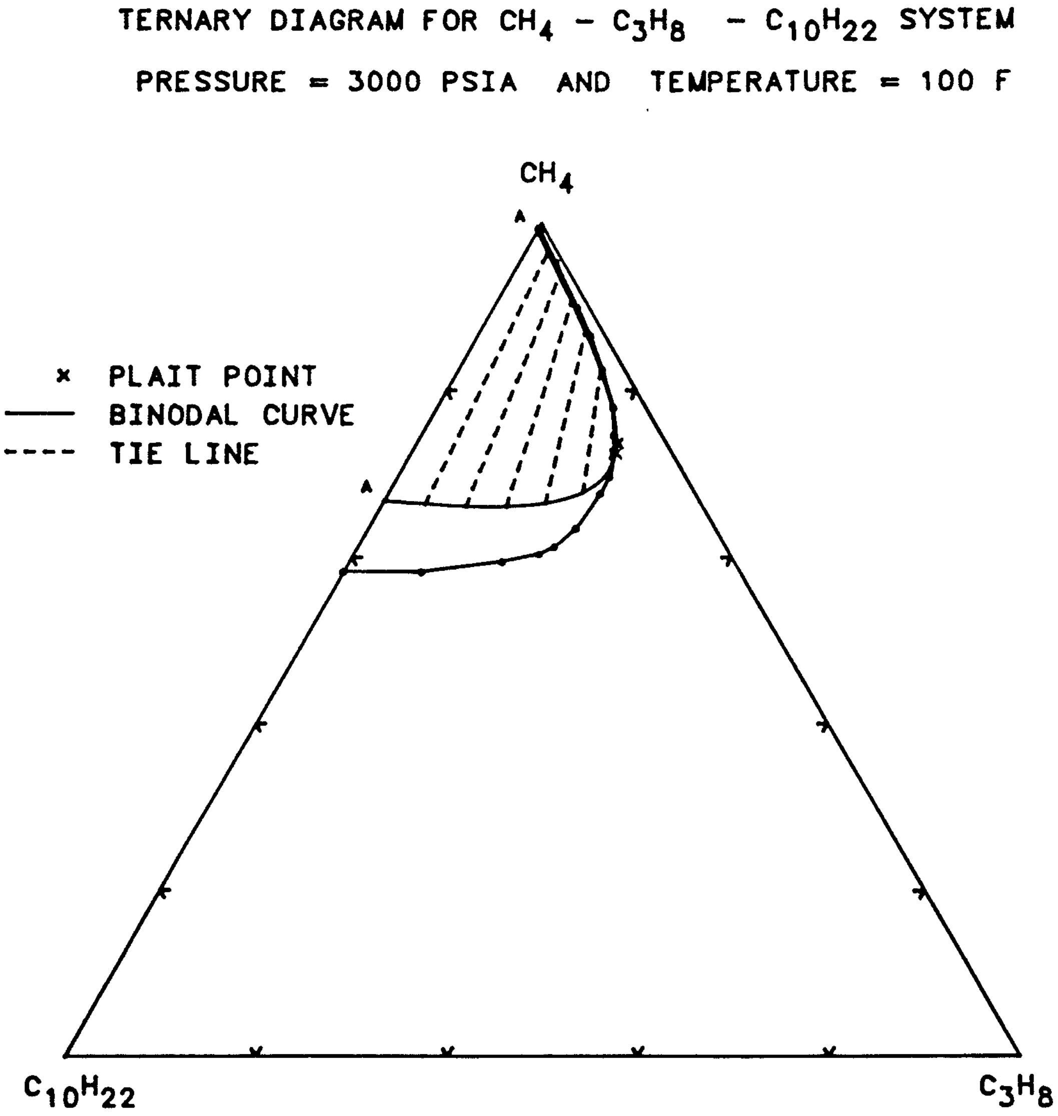

Figure 4.15 Computed Phase Envelope at 3000 psia using Binary Interaction Coefficients of Case 9 ($\delta_{3,10}$= 0.04)

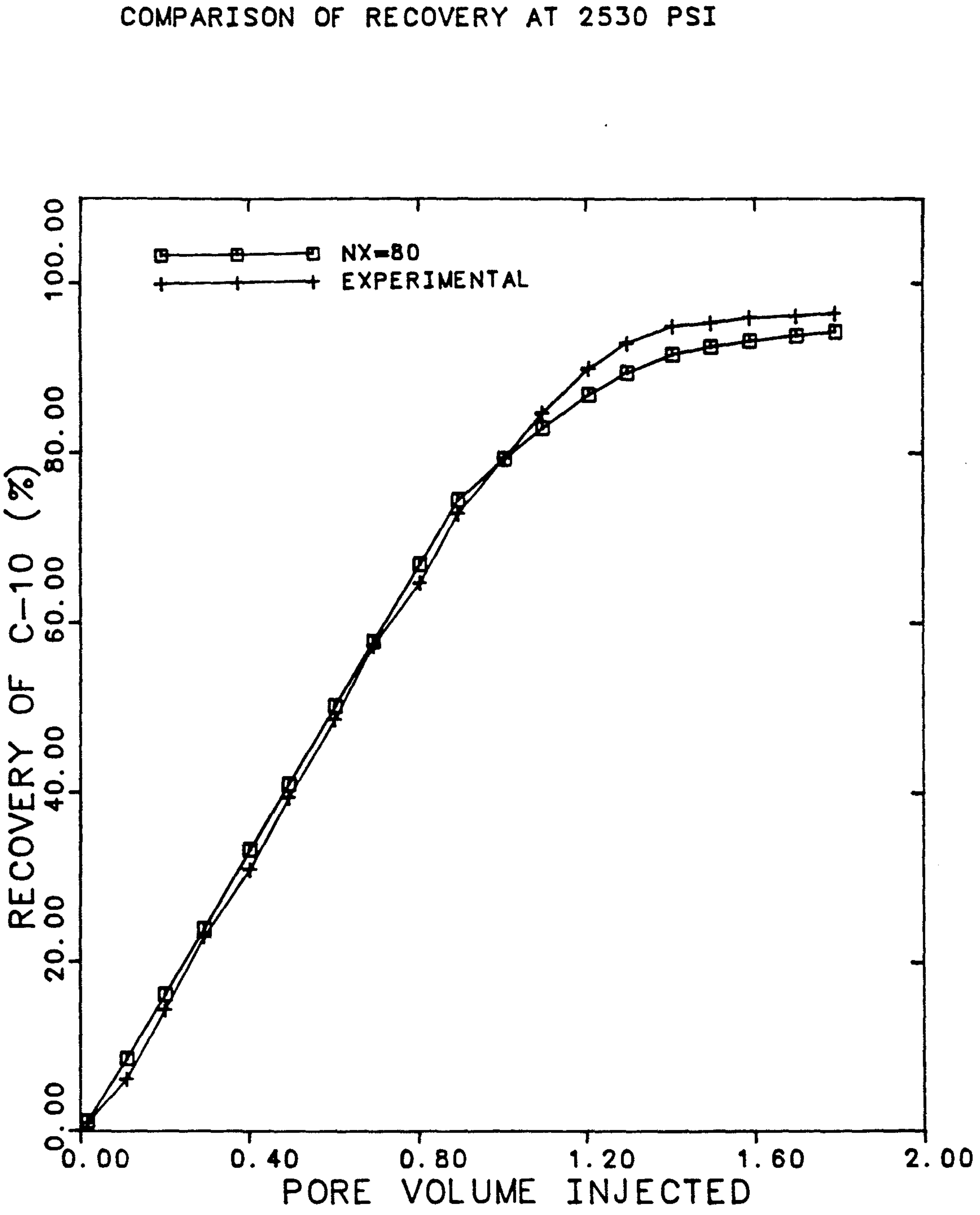

Figure 4.16 Recovery Curves at 2530 psia using Binary Interaction Coefficients of Case 9

COMPARISON OF RECOVERY AT 3118 PSI

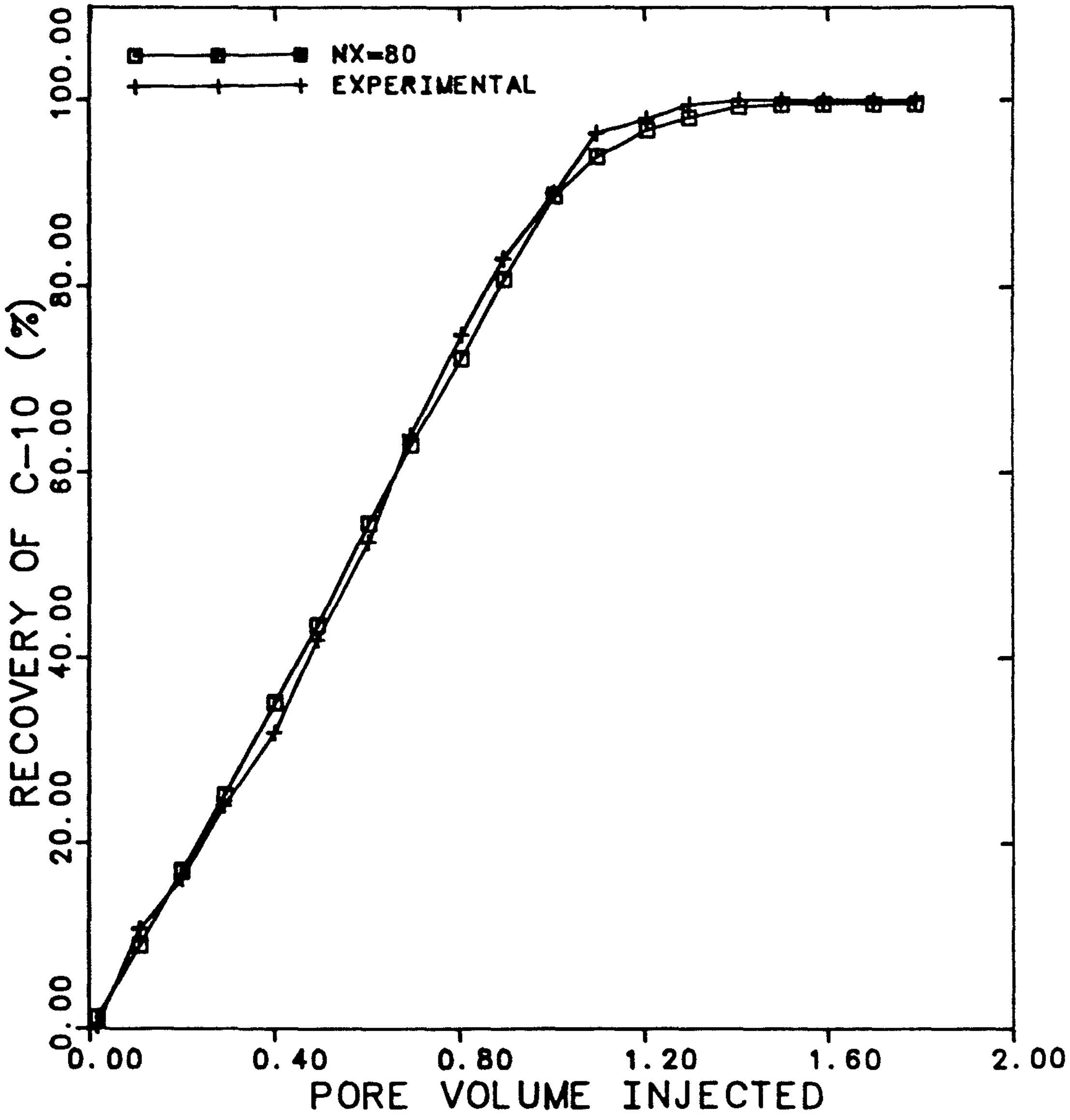

Figure 4.17 Recovery Curves at 3118 psia using Binary Interaction Coefficients of Case 9

Chapter 5 Simulation of Maljamer Separator Oil Displacement in a Slim Tube.

5.1 Input Data Review

In this chapter, an actual crude oil displacement is studied. A ternary diagram representation is used to describe the phase behavior. The composition route on this diagram is used to help understand the displacement mechanism.

Since a crude oil has a very large number of components, it is difficult to characterize it using only a few hydrocarbon components, and these must be selected based upon the concept of pseudo components.

Orr et al. [O5] conducted an excellent series of laboratory experiments and simulations to evaluate a field prospect for CO_2 flooding. In their studies, separator oil from the Maljamar field (Lea County, New Mexico) was used. Their characterization of this oil is summarized below. Some properties of the Maljamar separator oil are given in Table 5-1. Hydrocarbon analysis of this oil is given in Table 5-2. Gas chromatographic techniques were used for this hydrocarbon analysis in the range of C_5 to C_{36}. Gas chromatographic techniques provide the weight fractions of each component. The molecular weight of the normal alkane corresponding to each carbon number (CN) was used to convert to the mole fraction basis shown in Table 5-2.

Results of a single contact phase behavior study for mixtures of CO_2 and Maljamar separator oil are summarized in Fig 5.1. In their experimental procedure, appearance or disappearance of phases was determined visually and from measurements of the overall compressibility of the cell contents. Bubble point pressures were easily detected since there is a large change in system compressibility when a gas phase appears or disappears. Liquid-liquid saturation pressures and dew point pressures were determined visually since the appearance or disappearance of a liquid phase in the presence of a gas or another liquid phase has only a small effect on the overall compressibility of the system. Phase volumes were determined from cathetometer measurements of the positions of interfaces between phases.

Mixtures of CO_2 and Maljamar separator oil containing less than about 75 mol% CO_2 formed vapor-liquid mixtures at low pressures and single phase mixtures at pressures about the bubble point pressure. That is, all the CO_2 present dissolved in the oil at pressures above that given by the curve labeled 100% L_1 in Fig. 5.1. Mixtures containing more than about 75 mol% formed two liquid phases at high pressures, while at low pressures, liquid and vapor phases were observed. There was a small range of pressures over which three phases, two liquids and a vapor, coexisted ($L_1 + L_2 + V$).

Fig. 5.2 shows a pseudo-ternary plot for the CO_2-Maljamar separator oil at 1200 psia. These results were produced by multiple contact experiments. The mole fractions shown in Fig. 5.2 were calculated from the weight fraction data obtained by chromatography and assigning the molecular weight of the appropriate normal alkane to each carbon number (CN) cut. The molecular weight of the C_{37} + fraction was assumed to be that of C_{40}.

Slim tube displacement results from Orr et. al. [O5] are shown in Fig. 5.3. The displacements were preformed at 90°F and four pressures: 800 psia, 1000 psia, 1200 psia, 1400 psia. In each displacement, the slim tube was filled with oil at the displacement pressure. CO_2 was injected continuously until the test was terminated. Details of the slim tube displacement are described in section 5.4 below.

The approach used in this study is now summarized. First, the phase behavior was matched using both composition data from the pseudo ternary diagram and the pressure-composition diagram. The Peng-Robinson equation-of-state was used in all cases. Pseudo component properties were estimated by two methods based upon mixing rules and correlations from the literature. The pressure-composition was matched based upon Whitson's pseudoization procedure [W1]. Then the same parameters obtained from these matches were used in simulations of the slim tube displacements. Displacements at pressures both below and near the MMP were simulated. The development of miscibility was analyzed by examining composition, saturation and density profile from these simulations.

5.2 Phase behavior matching using three pseudo-components

5.2.1 Determination of critical properties

Using pseudo ternary diagram (Fig. 5.2) representation of CO_2 and Maljamar separator oil, phase behavior matching was performed. From Orr et al.'s data, the oil composition was described as shown on the following table.

No.	Component	Molecular Weight	Composition (mole%)
1	CO_2	44	0.0
2	C_{5-12}	119	66.4
3	C_{13+}	323	33.6

In order to determine the critical values of each pseudo component, the following two methods were applied.

Method #1: Assuming each hydrocarbon CN was a normal alkane, and using the hydrocarbon analysis of this oil (Table 5-2), the critical values and acentric factor of each pseudo component were calculated with a molar average mixing rule (Kay's rule). Data from references [D2, S4] were used for the basic physical properties of hydrocarbons.

Method #2: By using the Katz and Firoozabadi's [K4] correlation, the specific gravity and boiling point were determined with each carbon number and then critical values and acentric factors were calculated using the correlations.
Figures 5.4 (a), (b) and Table 5-3 give the correlation of average boiling points, liquid densities, and molecular weight based on reservoir condensates and crude oils. Fig. 5.4 (a) of density vs. boiling point correlation shows large discrepancy between the hydrocarbon groups (based on condensates and crude oils) and normal paraflias, and the difference increases with boiling point.

There are many correlations presented to determine the critical values [W2], and there is not one correlation or characterization scheme which is better than all others. In method #2, the following general correlations which were suggested by Whitson [W2] were adopted.

1.0 For molecular weight correlation

Katz-Firoozabadi's correlation [K4, W2] was used;

$$Mw = 72.5257 + 1.1380E\text{-}2\ t + 5.5708E\text{-}4\ t^2 - 1.1995E\text{-}7\ t^3$$

where $t = 1.8\ T_b - 459.67$

T_b: boiling point (°K)

2.0 For critical pressure correlation

Riazi-Daubert (Whitson extension) correlations [R1, W2] were used;

when T_b (°K) ≤ 475

$$P_c = 3.112281E{+}9\ (1.8T_b)^{-2.31250}\ \gamma^{2.3201}$$

when T_b (°K) > 475

$$P_c = 2.41490E{+}14\ (1.8T_b)^{-3.86618}\ \gamma^{4.2448}$$

where P_c : critical pressure (psia)

γ : specific gravity at 15.5 °C

3.0 For critical temperature correlation

Riazi-Daubert correlation [R1] was used;

$$T_c = 24.2787\ (1.8T_b)^{0.58848}\ \gamma^{0.3596}$$

where T_c : critical temperature (°R)

4.0 For acentric factor correlation

Kesler-Lee [K3] correlations were used;

when $\theta \le 0.8$

$$\omega = \frac{-\ln(P_c/101.325)-5.92714+6.09648/\theta+1.28862(\ln\theta)-0.169337\theta^6}{15.2518-15.6875/\theta-13.4721(\ln\theta)+0.43577\theta^6}$$

when $\theta > 0.8$

$$\omega = -7.904 + 0.1352Kw - 0.007465K_w^2 + 8.359\theta$$

$$+ (1.408 - 0.01063Kw)\theta^{-1}$$

where θ : reduced normal boiling point ($= T_b/Tc$)

Kw: Watson characterization factor ($= (1.8T_b)^{1/3}/\gamma$)

5.0 For critical volume correlation

Riazi-Daubert correlation [R-1] was used;

$$V_c = 7.5214E\text{-}3\ (1.8T_b)^{0.2896}\ \gamma^{-0.7666}\ Mw$$

where V_c: critical volume [$ft^3/lb \cdot mole$]

Mw: molecular weight

Calculated critical values using the above two methods are given in Tables 5-4 and

5-5. The computed pseudo-ternary diagrams for these two cases are shown in Figs. 5.5 (a), (b) for 1200 psia and Figs. 5.6 (a), (b) for 800 psia. No large differences is observed between these two methods at 800 psia. The two-phase boundary of the ternary diagram using Method #1 is slightly larger than that using Method #2. The two-phase boundary can be extended with increasing critical temperature, but this effect is small. In the following, Method #1 is used as the base case.

5.2.2 Adjustment of binary interaction coefficients

The example given in Chapter 4 illustrated the adjustment of binary interaction coefficients as one method to match phase behavior. In this example, the binary interaction coefficients between CO_2 and the two pseudo components C_{5-12} and $C_{13}+$ are adjusted. The binary interaction coefficient between these two hydrocarbon pseudo components was assumed to be zero.

Orr et al.'s experimental slim tube results show that multiple contact miscibility (MCM) is developed at about 1200 psia. When the critical tie line on Fig. 5.5 (a) is extended, it is found to lie to the right of the critical point I (66.4 mole percent C_{5-12} and 33.6 mole percent $C_{13}+$). Therefore the binary interaction coefficients $\delta_{1,2}$ and $\delta_{1,3}$ were adjusted until the point I was on the critical tie line as shown in Figure 5.7 (a). This ensures that a miscible displacement will occur according to first order theory [D1]. The values for the binary interaction coefficients corresponding to Figure 5.7 (a) are $\delta_{1,2} = 0.09$ and $\delta_{1,3} = 0.14$. The first component (CO_2) is denoted by the first subscript and the second and third components ($C_{5\text{-}12}$ and C_{13}+) by subscripts 2 and 3 in these δij. This combination of binary interaction coefficients was adopted for later slim tube simulations.

5.3 Phase behavior matching using seven pseudo-components

5.3.1 Regrouping (Pseudoization)

The cost required for simulating phase and volumetric behavior increases considerably with the number of components used to described the fluid. Some authors [F1, H5, K4, K6, L1, W2] have suggested that as few as 2 or as many as 50 components may be required to predict reservoir fluid behavior.

In general, one might expect that the accuracy of EOS predictions would increase with the number of components used to describe the reservoir fluid at least up to a certain number.

Li et al. [L1] proposed a technique for grouping the components of a reservoir fluid into pseudo components by using the K-values of all components at a typical operating pressure and temperature. They suggested that it is necessary to group the heavy fraction (e.g. C_6 + fractions) because of the large number of components, and furthermore, that it is also advantageous to lump the light fractions in order to minimize simulation costs.

Whitson [W1] developed a simple scheme for regrouping. A method is proposed for estimating the number of Multiple-Carbon-Number (MCN; e.g. pseudo component) groups needed for adequate plus-fraction description, as well as which Single-Carbon-Number (SCN) groups belong to the MCN group. Whitson's regrouping scheme was adopted in this study as well as his suggestions of which physical property correlations to use.

The following equations are developed by Whitson,

$$N_g = \mathrm{Int}\,[\,1 + 3.3\,\log_{10}(\,N - n\,)\,]$$

$$M_I = M_n\,\{\,\exp\,[(\,1/N_g\,)\ln\,(M_N/M_n)\,]\,\}^I$$

where

N_g: number of MCN groups

N: last SCN (or MCN) in a Cn^+ fraction

n: first SCN in a Cn^t fraction

M_N: molecular weight of last SCN (or MCN) in a Cn^+ fraction

M_n: molecular weight of first SCN in a Cn^+ fraction

I: multiple carbon number index (= 1, 2, 3 . . . . .N_g)

Using the above scheme, Maljamar separator oil is described as shown in Tables 5-6 and 5-7. The same two methods for estimating these properties were used as before in section 5.2.1. Whitson's scheme results in the approximation of this oil into six pseudo components as shown in these tables.

The pressure-composition diagram (Fig. 5.1) is now used for phase behavior matching instead of the pseudo ternary diagram. Results calculated using the Peng Robinson EOS with methods #1 and #2 are given in Fig. 5.8 (a) and Fig. 5.8 (b), respectively. There is not much difference between the results of these two methods.

5.3.2 Adjustment of binary interaction coefficients

Katz and Firoozabadi [K4] focused on methane interaction coefficients for use with the Peng Robinson EOS. For various methane binaries, the interaction coefficient δ_{ij} was determined by minimizing the error of calculated bubble points. These δ_{ij} were plotted against the jth component density (at 15.5 °c) and a best fit correlation was made.

Kato et al. [K5] optimized the carbon dioxide binary interaction coefficients, also for use with the PR EOS. Kato et. al. proposed the following correlation with acentric factor and temperature.

$$\delta_{CO2-i} = a' (T - b')^2 + c'$$

where

$$a' = -0.70421\ 10^{-5} \log_{10} \omega i - 0.13210^{-7}$$

$$b' = 301.58\ \omega i + 226.57$$

$$c' = -0.0470356 (\log_{10} \omega i + 1.08884)^2 + 0.13040$$

Lawal [L4] presented a correlation which predicts binary interaction coefficients for hydrocarbon/hydrocarbon and non hydrocarbon/hydrocarbon binary mixtures based on the correlation from Tsonopoulos.

$$\delta_{ij} = \frac{\theta_p}{T_{bi}} \{ \ln M_{wj} - M_{wi} + 1 \}^{n_f}$$

where

T_{bi} = boiling point of component i (°R)

M_{wi}, M_{wj}: Molecular weight of component i, j

θ_p: constant for family of binaries

paraflin/paraflin = 1.688574E-3

CO_2/paraflin = 1.378162

n_f: constant exponent for family of binaries

paraflin/paraflin = 5.382733

CO_2/paraflin = 2.155123

θp and n_f are parameters which depend on the type of binary mixture, and these were obtained by a least - square regression analysis. For mixed-type binaries, e.g. hydrocarbon/nonhydrocarbon, the nonhydrocarbon is taken as the i^{th} component. Otherwise, the lighter molecule is taken as the i^{th} component.

In this study, Kato et al.'s equation and Lawal's equation are used for determination of the initial trial values of the binary interaction coefficients. Calculation results using these methods are given Table 5-8. All the binary interaction coefficients form the Kato et al. correlation are equal except the lightest one, while those from Lawal's correlation increase with increasing carbon number of the hydrocarbon. Pressure-composition diagrams calculated using PR EOS for each case are given in Fig. 5.9. Recall that all binary interaction coefficients between hydrocarbon and hydrocarbon were set to zero in these calculations.

The calculated phase behavior using Kato et al.'s correlation is closer to the experimental data than that using Lawal's correlation. Therefore, the constant value of 0.11 was used for all coefficients as a starting place and for simplicity of adjustment. Values of 0.115 and 0.12 were also tried and 0.115 found to be the best. When differing values similar to Lawal's correlation were used to give the best fit, the values in Table 5-9 were obtained and the calculated pressure-composition diagram is shown in Fig. 5.10.

Sensitivity study for EOS parameter of slim tube displacement was not performed in the simulation of Maljamar separator oil, because a good agreement with experimental data was obtained as described in section 5.4.3. Sensitivity study for EOS parameter was conducted in Chapters 6 and 7.

The equal value of 0.115 was used in subsequent calculations when the slim tube displacements were simulated as described below.

5.4 Simulation of slim tube displacement

5.4.1 Input data for simulation of slim tube test

According to Orr et al.'s report [O5], slim tube displacements were performed using a 12.2, (40 ft), 0.635 cm (1/4 in.) ID stainless steel tube packed with 170-200 mesh glass beads. The slim tube had a pore volume of 147.3cm^3, a porosity of 38.1%, and a permeability of 5800 md. The packed tube was rolled and installed in a temperature controlled (constant temperature set at 90°F) water bath. CO_2 was injected at 12 cm^3/hr and 1200 psia, and at 24 cm^3/hr and 800 psia. Gas-oil relative permeability data given by Naar et al. [N3] for unconsolidated sand were used without adjustment. K_{ro} vs. S_o and K_{rg} vs. S_o are given in Fig. 5.11.

5.4.2 Simulation using three pseudo components

First the slim tube displacement using the three pseudo component description was simulated. Simulations using 80 and 160 grid blocks at 1200 psia were made (Fig. 5.12). The simulated breakthrough time as indicated by the break in the recovery curves is too early in both cases compared to experiment and the slope of these curves after breakthrough is steeper than that of experiment. Recovery increases with increasing number of grid blocks, but the difference between these cases is not so large.

The simulated composition route on the ternary diagrams using 160 grid blocks at 800 psia, 1200 psia, and 1600 psia are shown in Figures 5.13 (a), (b) and (c), consecutively. From the comparison of these diagrams, the following observation can be seen. The compositional path at 800 psia enters in the multiphase region earlier than that of higher pressure displacements, because the phase behavior of this pressure has larger multiphase region than those of higher pressures. When the multiphase region is entered, the amount of residual oil left behind is larger than in the higher pressure displacement. Figures 5.13 (b) and (c) show that the displacement is close to being multiple contact miscible, because the composition routes pass near the critical point and closely follows the binodal curve (phase boundary). Discrepancy between composition route and binodal curve decreases with increasing pressure, but still a small discrepancy exists even if at 1600 psia.

5.4.3 Simulation using seven pseudo components

Next the seven pseudo component description (sections 5.3.1 and 5.3.2) was used for input data for the simulation of the slim tube. Fig. 5.14 shows the oil recovery curve at 1200 psia in which a grid refinement was done. Oil recovery increased as the number of grid blocks increased. The difference in recovery between NX = 120 and NX = 80 is very small, so 80 grid blocks seem to be enough for this case. Agreement between the simulated and experimental results for this case is excellent. (Fig. 5.15). Comparison of Figs. 5.12 and 5.15 shows that the agreement between experimental and simulated recoveries is better using seven pseudo components. This is consistent with a better agreement between calculated and experimental pressure-composition diagrams as shown in Fig. 5.16. The larger single phase region of the seven pseudo component case evidently results in a slightly higher recovery. Simulation of slim tube displacements at three different pressures (1400 psia, 1200 psia, and 800 psia) were performed using seven hydrocarbon pseudo components. Fig. 5.17 shows the oil recovery at 1.1 pore volumes CO_2 injected for these pressures. The break in the curve occurs at about 1100 psia and by this criterion the MMP could be only 1100 psia rather than 1200 psia as before.

The production gas-oil-ratio (GOR) is very sensitive to the EOS parameter, but did not calculate in the Maljamar separator oil case, because no experimental production GOR is available in the Orr et al.'s report.

5.5 Discussion of displacement mechanism

One of the important uses of simulation studies is to provide insight into the displacement mechanism. A detailed analysis is necessary to explain the displacement mechanism. The process of multi-contact miscibility is illustrated in this section using compositional simulator.

Figs. 5.18 through 5.21 are UTCOMP calculated profiles of the Maljamar 1200 psia slim-tube displacement at 0.514 pore volumes CO_2 injected using three pseudo components. The figures demonstrate saturation, density, overall composition and oleic phase concentration profiles. Fig. 5.22 is a composite diagram of these profiles. The profiles are divided into several zones for ease of understanding and discussion. A stripping zone, miscible zone, enrichment zone and oil zone are defined as shown in Fig. 5.22.

5.5.1 Density profile in Multi Contact Miscibility

In the stripping zone, the concentration of heavy hydrocarbon increases in the vapor phase and therefore, the vapor density is increasing. Near the miscible zone, the ratio of heavy hydrocarbon component and light hydrocarbon component in gas phase is increasing, and the vapor density is also increasing. The oil density decreases slightly in the stripping zone, because the concentration of the heavy component (C_{13}+) decreases in the oleic phase.

In the miscible zone, the oil and gas densities are getting closer to each other. The difference between the physical properties of these phases is getting small, and finally it is difficult to discriminate between them.

In the enrichment zone, the gas density decreases abruptly, but the oil density changes a little. The oil density in the oil zone approaches the original oil density. Overall, there is not a significant change in the oil density, while the gas density changes in each zone.

5.5.2 Composition profile in MCM

The density changes discussed above were the result of compositional changes only, because the temperature was constant and the pressures almost constant. From the oil zone to the miscible zone, CO_2 in the oleic phase is rapidly increasing, while the other two components are decreasing. In the stripping zone, the CO_2 concentration in the oleic phase first decreases and then approaches a constant. The concentration of the intermediate hydrocarbon component (C_{5-12}) in the oleic phase decreases gradually from the oil zone to the stripping zone and finally disappears into the middle of the stripping zone. The concentration of the heavy hydrocarbon component (C_{5-12}) in the oleic phase decreases gradually from the oil zone to the stripping zone and finally disappears in the middle of the stripping zone. The concentration of the heavy hydrocarbon component (C_{13}+) in the oleic phase decreases from the oil zone to the enrichment zone, and the minimum value is obtained at the miscible zone, and after that the concentration increases again in the stripping zone. The increase of heavy hydrocarbon in the stripping zone corresponds to a decrease in the intermediate hydrocarbon until only CO_2 and heavy hydrocarbon remain.

The example shows that the change in oil composition is important and thus suggests that a larger number of hydrocarbon components might be needed to give a good description of the process.

Figs. 5.23 through 5.27 are simulated profiles of saturation, oleic phase concentration, gas phase concentration, overall composition and density at 0.8081 PV CO_2 injected at 1200 psia using a seven pseudo components description of the oil. The oleic phase concentration profile (Fig. 5.24) shows a gradual stripping from the light hydrocarbon components to the heaviest components.

Fig. 5.28 shows the density profiles at different times (0.17, 0.34, 0.51, 0.68, 0.85 pore volume CO_2 injected). The densities of the oleic phase and the gas phase approach each other with increasing time in a remarkable way. This process can be considered equivalent to the development of miscibility. This agrees with the conclusion that some distance is necessary to attain miscibility. However, the role of dispersion in this process is important and must be investigated before a complete understanding is possible.

5.5.3 Profile in Immiscible Flood

Simulation of this same slim-tube test at 800 psia for Maljamar separator oil is given in Figs. 5.29 through 5.31. Fig. 5.29 shows the oil recovery history. Fig. 5.30 shows the oil saturation profiles at different times, and Fig. 5.31 shows density profiles. The density profile shows no miscible zone exists where densities approach each other, but rather large differences between densities exist. This means that two phases exist everywhere and miscibility does not develop.

One more remarkable observation comes from a comparison of the two oil saturation profiles of Fig. 5.30 (for immiscible case at 800 psia) and Fig. 5.32 (MCM case at 1200 psia) . The oil saturations in Fig. 5.30 are always above 35%, while those in Fig. 5.31 are less than 20%. The rate of advance of the oil zone for the immiscible case is slower than that for the 1200 psia case. These differences resulted entirely from the pressure difference.

Table 5-1 Properties of Maljamar Separator Oil at Atomospheric pressure (Ref. [05])

Density (15.6 °C)	0.8294 g/cm^3
Viscosity (34.4 °C)	2.8 mPa s
Molecular Weight	183.7
Molecular Weight of C_{7+}*	199.3
Density of C_{7+} (15.6 °C)*	0.8441 g/cm^3

* Calculated from measured values of molecular weight and density and oil composition

Table 5-2 Composition of Maljamar Separator Oil (Ref. [05])

Carbon Number	Separator Oil (mole %)
5	3.90
6	9.37
7	10.27
8	13.54
9	11.97
10	7.50
11	5.59
12	4.32
13	3.93
14	3.29
15	2.73
16	2.26
17	2.23
18	1.34
19	1.07
20	1.36
21	1.10
22	0.77
23	0.96
24	0.88
25	0.68
26	0.38
27	0.59
28	0.38
29	0.40
30	0.40
31	0.40
32	0.40
33	0.13
34	0.14
35	0.14
36	0.13
37+**	7.51

** Assumed Molecular weight of 563.0

Table 5-3 Generalized Properties of Petroleum Hexane Plus Groups (Ref. [K1])

Hydrocarbon Group	Boiling Range (°C)	Boiling Range (°F)	Average Boiling Point (°C)	Average Boiling Point (°F)	Density (g/ml)	Molecular Weight
C_6	36.5 to 69.2	97.9 to 156.7	63.9	147	0.685	84
C_7	69.2 to 98.9	156.7 to 210.1	91.9	197.5	0.722	96
C_8	98.9 to 126.1	210.1 to 259.1	116.7	242	0.745	107
C_9	126.1 to 151.3	259.1 to 304.4	142.2	288	0.764	121
C_{10}	151.3 to 174.6	304.4 to 346.4	165.8	330.5	0.778	134
C_{11}	174.6 to 196.4	346.4 to 385.5	187.2	369	0.789	147
C_{12}	196.4 to 216.8	385.5 to 422.2	208.3	407	0.800	161
C_{13}	216.8 to 235.9	422.2 to 456.7	227.2	441	0.811	175
C_{14}	235.9 to 253.9	456.7 to 489.2	246.4	475.5	0.822	190
C_{15}	253.9 to 271.1	489.2 to 520.0	266.0	511	0.832	206
C_{16}	271.1 to 287.3	522.0 to 547.0	283.0	542	0.839	222
C_{17}	287.0 to 303.0	547.0 to 577.0	300.0	572	0.847	237
C_{18}	303.0 to 317.0	577.0 to 603.0	313.0	595	0.852	251
C_{19}	317.0 to 331.0	603.0 to 628.0	325.0	617	0.857	263
C_{20}	331.0 to 344.0	628.0 to 652.0	338.0	640.5	0.862	275
C_{21}	344.0 to 357.0	652.0 to 675.0	351.0	664	0.867	291
C_{22}	357.0 to 369.0	675.0 to 696.0	363.0	686	0.872	305
C_{23}	369.0 to 381.0	696.0 to 717.0	375.0	707	0.877	318
C_{24}	381.0 to 392.0	717.0 to 737.0	386.0	727	0.881	331
C_{25}	392.0 to 402.0	737.0 to 756.0	397.0	747	0.885	345
C_{26}	402.0 to 413.0	756.0 to 775.0	408.0	766	0.889	359
C_{27}	413.0 to 423.0	775.0 to 793.0	419.0	784	0.893	374
C_{28}	423.0 to 432.0	793.0 to 810.0	429.0	802	0.896	388
C_{29}	432.0 to 441.0	810.0 to 826.0	438.0	817	0.899	402
C_{30}	441.0 to 450.0	826.0 to 842.0	446.0	834	0.902	416
C_{31}	450.0 to 459.0	842.0 to 857.0	456.0	850	0.906	430
C_{32}	459.0 to 468.0	857.0 to 874.0	463.0	866	0.909	444
C_{33}	468.0 to 476.0	874.0 to 888.0	471.0	881	0.912	458
C_{34}	476.0 to 483.0	888.0 to 901.0	478.0	895	0.914	472
C_{35}	483.0 to 491.0	901.0 to 915.0	486.0	908	0.917	486
C_{36}			493.0	922	0.919	500
C_{37}			500.0	934	0.922	514
C_{38}			508.0	947	0.924	528
C_{39}			515.0	959	0.926	542
C_{40}			522.0	972	0.928	556
C_{41}			528.0	982	0.930	570
C_{42}			534.0	993	0.931	584
C_{43}			540.0	1004	0.933	598
C_{44}			547.0	1017	0.935	612
C_{45}			553.0	1027	0.937	626

Table 5-4 Computed Properties by Method #1 for 3 Components

Carbon Number	Molar Fraction (%)	Molecular Weight	Critical Temp (°R)	Critical Press. (psia)	Critical Volume (ft^3/lbmole)	Acentric Factor
CO_2	0.0	44.00	548.0	1071.0	1.200	0.2230
C_{5-12}	66.40	118.50	1031.9	366.7	6.850	0.3435
C_{13+}	33.60	331.10	1423.5	189.4	20.843	0.8684

Table 5-5 Computed Properties by Method #2 for 3 Components

Carbon Number	Molar Fraction (%)	Molecular Weight	Critical Temp (°R)	Critical Press. (psia)	Critical Volume (ft^3/lbmole)	Acentric Factor
CO_2	0.0	44.00	548.0	1071.0	1.200	0.2230
C_{5-12}	66.40	112.12	1061.4	395.6	7.377	0.3375
C_{13+}	33.60	310.80	1515.0	178.59	23.063	0.8935

Table 5-6 Pseudo Component Properties by Method #1 for 7 Components

Comp No.	Carbon Number	Molar Fraction (%)	Molecular Weight	Critical Temp (°R)	Critical Press. (psia)	Critical Volume (ft ^{3}/lbmole)	Acentric Factor
1	CO_2	0.0	44.00	548.0	1071.00	1.200	0.2230
2	C_{5-7}	23.54	89.79	930.0	432.81	6.142	0.2651
3	C_{8-10}	32.95	125.43	1062.2	344.53	8.671	0.3644
4	C_{11-14}	17.13	174.02	1203.5	269.98	12.374	0.4987
5	C_{15-20}	10.99	240.34	1342.5	214.85	17.507	0.6606
6	C_{21-28}	5.74	336.39	1462.8	173.58	25.137	0.8771
7	C_{29+}	9.65	536.64	1646.7	123.80	43.203	1.2789

Table 5-7 Pseudo Component Properties by Method #2 for 7 Components

Comp No.	Carbon Number	Molar Fraction (%)	Molecular Weight	Critical Temp (°R)	Critical Press. (psia)	Critical Volume (ft ^{3}/lbmole)	Acentric Factor
1	CO_2	0.0	44.00	548.0	1071.00	1.200	0.2230
2	C_{5-7}	23.54	89.79	937.9	471.35	5.732	0.2533
3	C_{8-10}	32.95	124.92	1074.2	389.83	7.824	0.3387
4	C_{11-14}	17.13	174.51	1211.2	366.32	11.002	0.5709
5	C_{15-20}	10.99	242.75	1354.3	277.42	15.418	0.7356
6	C_{21-28}	5.74	329.59	1492.6	189.77	21.156	0.8685
7	C_{29+}	9.65	477.42	1682.1	118.53	31.075	1.1575

Table 5-8 Binary Interaction Coefficients

Binary Interaction Coefficient	Kato et al. Correlation	Lawal Correlation
CO_2- Pseudo Comp.#1	0.120	0.070
CO_2- Pseudo Comp.#2	0.110	0.100
CO_2- Pseudo Comp.#3	0.110	0.120
CO_2- Pseudo Comp.#4	0.110	0.140
CO_2- Pseudo Comp.#5	0.110	0.170
CO_2- Pseudo Comp.#6	0.110	0.200

Note : See Table 5-7 for definitions of each pseudo component

Table 5-9 Best Fit Parameter for Binary Interaction Coefficients

Binary Interaction Coefficient	Kato et al. Correlation	Lawal Correlation
CO_2- Pseudo Comp.#1	0.115	0.050
CO_2- Pseudo Comp.#2	0.115	0.100
CO_2- Pseudo Comp.#3	0.115	0.100
CO_2- Pseudo Comp.#4	0.115	0.120
CO_2- Pseudo Comp.#5	0.115	0.140
CO_2- Pseudo Comp.#6	0.115	0.080

Note : See Table 5-7 for definitions of each pseudo component

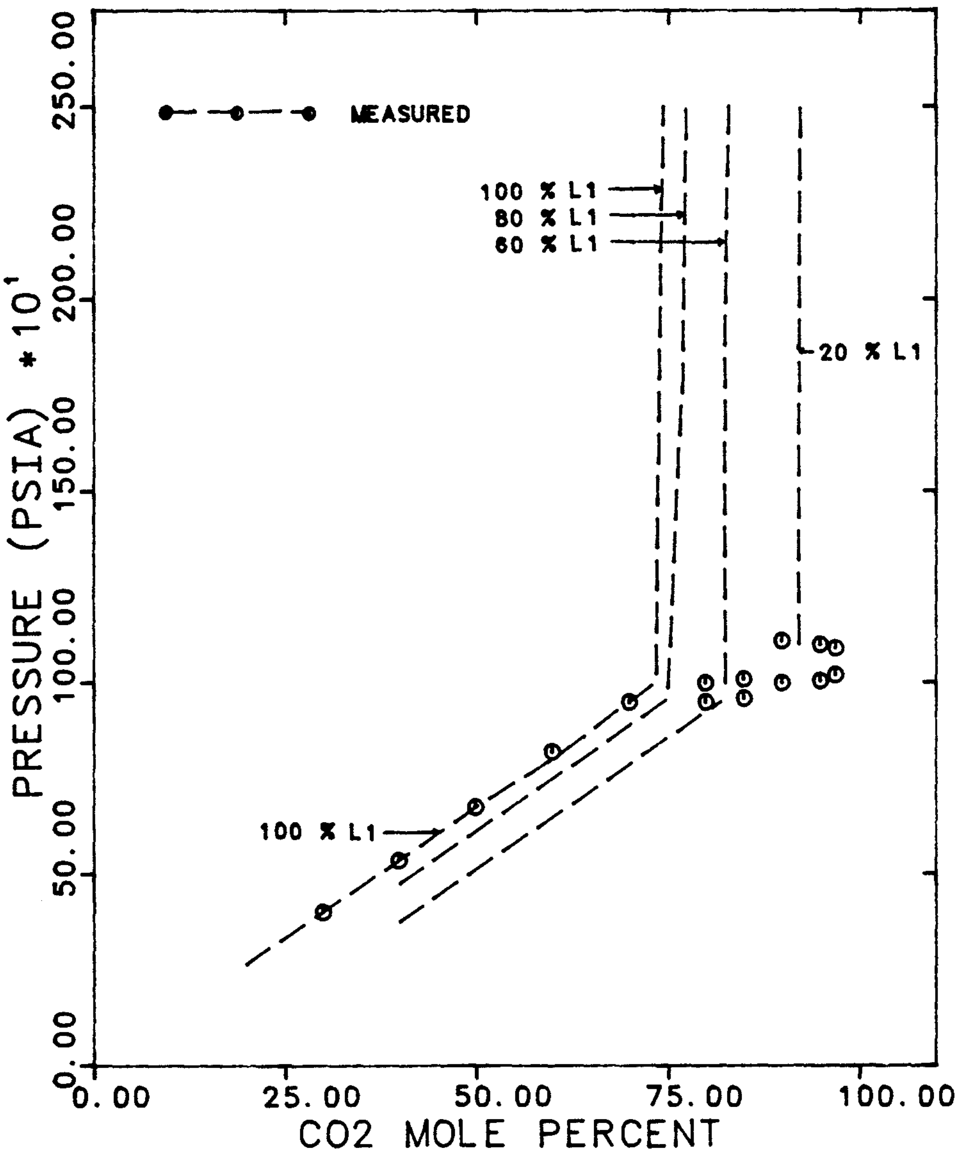

Figure 5.1 Phase Behavior of Binary Mixtures of CO2 with Maljamar Separator Oil at 32 °C (90 °F)

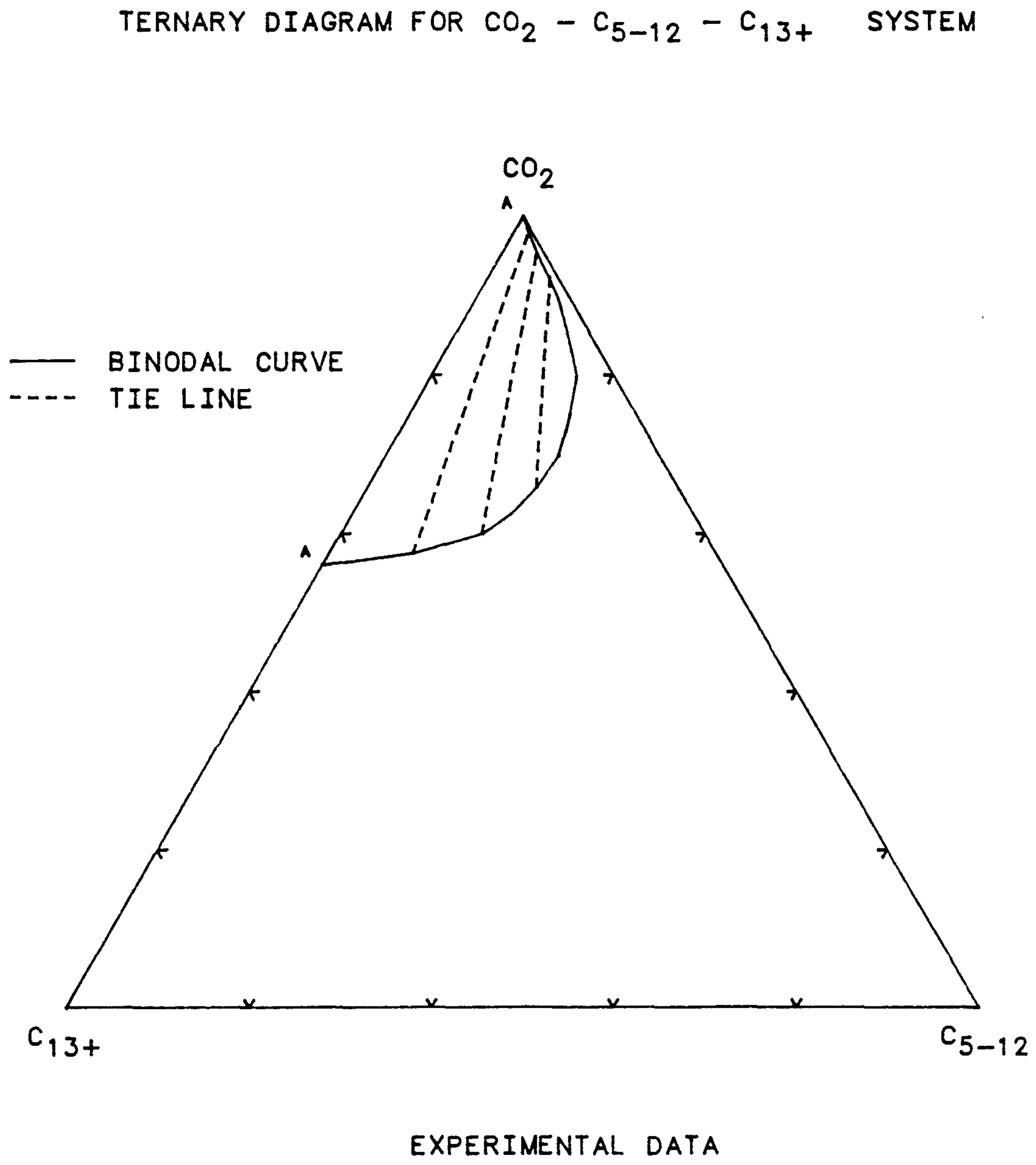

Figure 5.2 Pseudo-Ternary Phase Diagram for Maljamar Separator Oil at 1200 psia & 32 °C (90 °F)

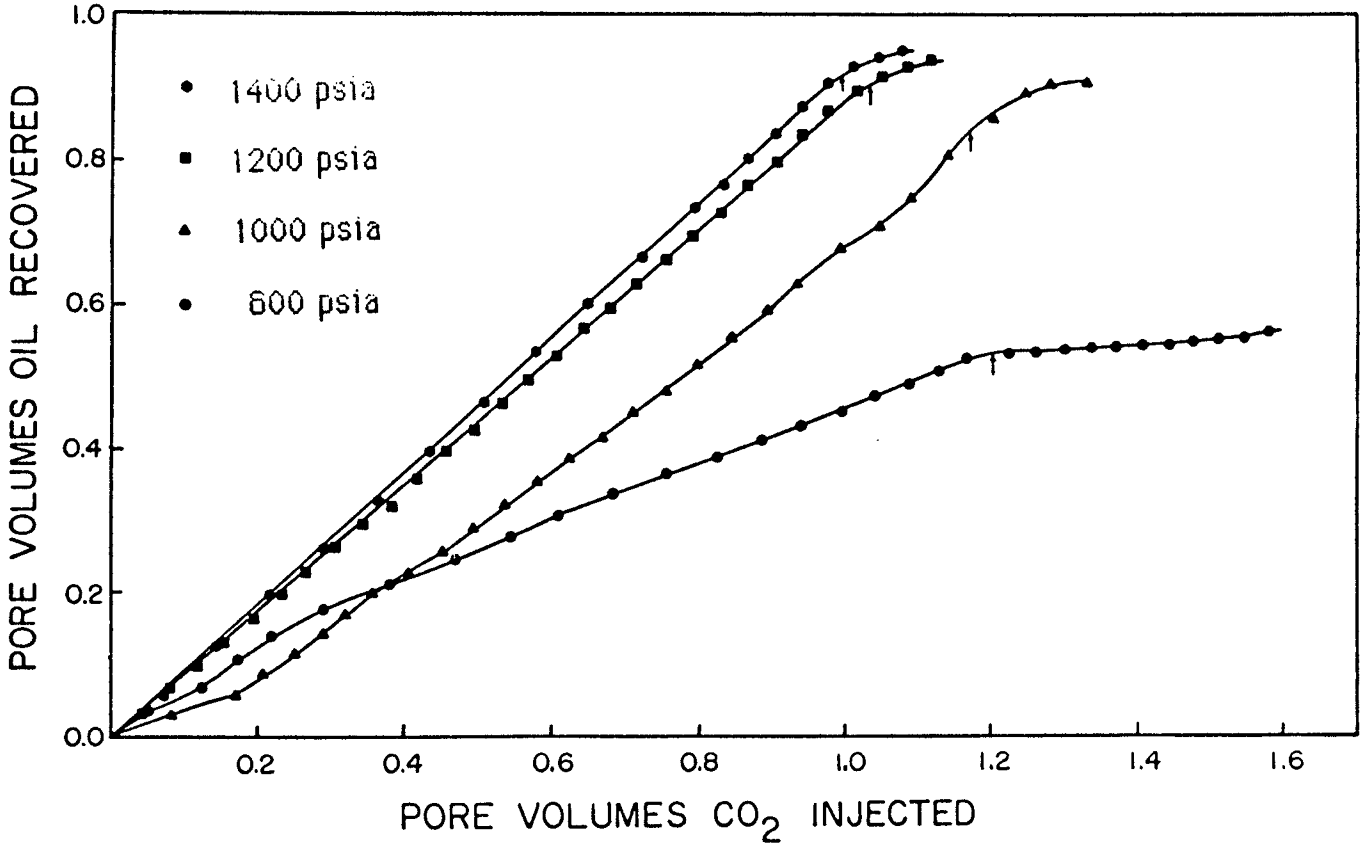

Figure 5.3 Recovery of Maljamar Separator Oil from Slim-tubes by Continuous Displacement with CO2 at 32 °C (90 °F)

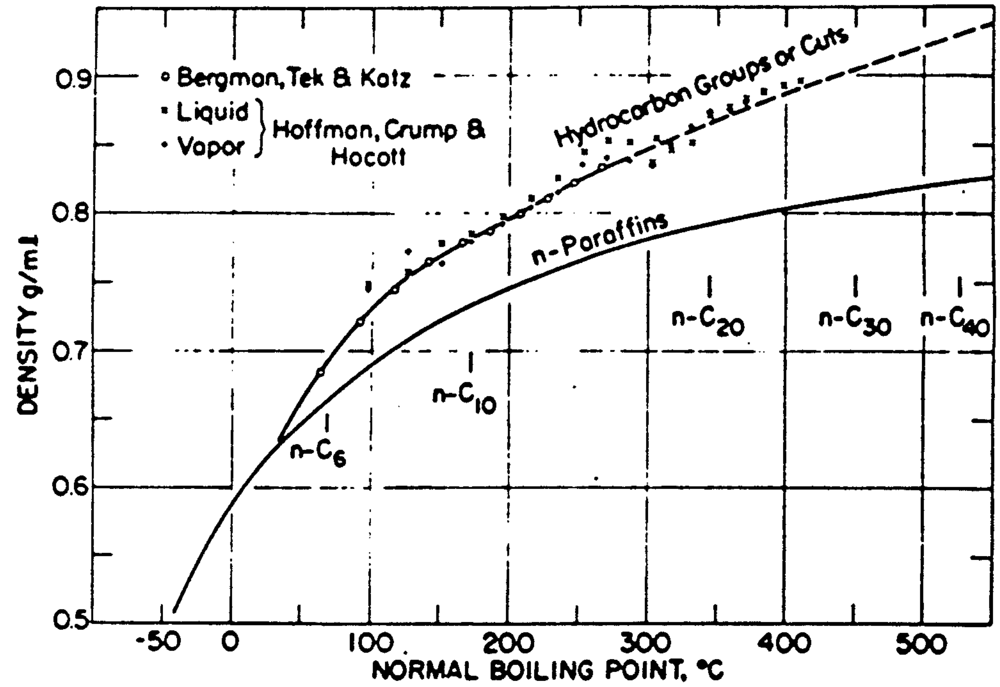

Fig. 5.4(a) Molecular vs boiling points of hydrocarbon groups in crude oil and condensate systems. (Ref. [K4])

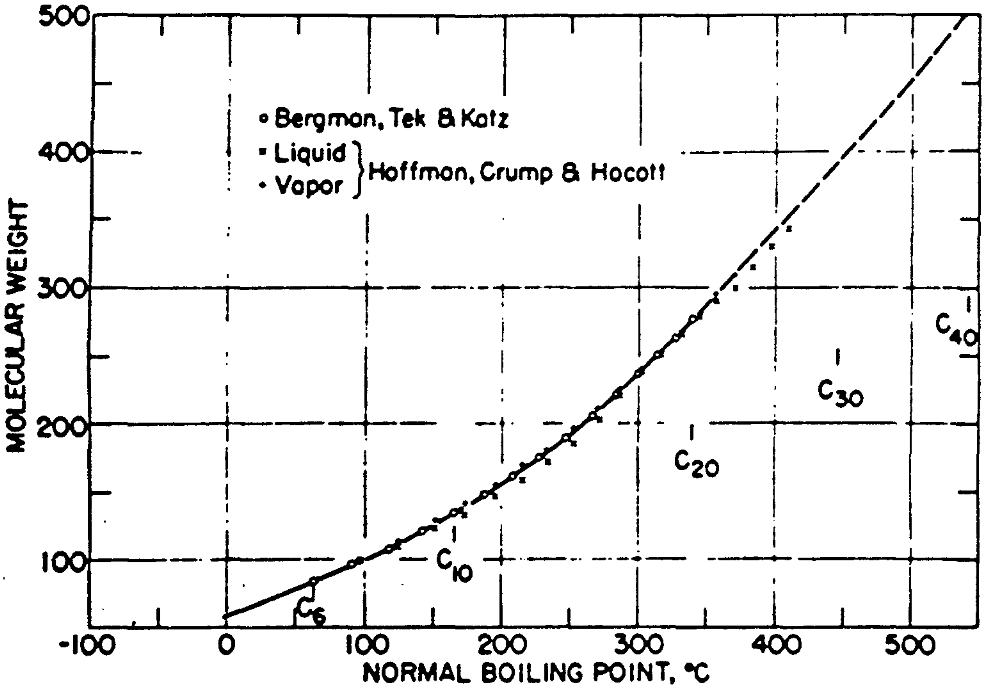

Fig. 5.4(b) Density vs boiling points of hydrocarbon groups in crude oil and condensate systems. (Ref. [K4])

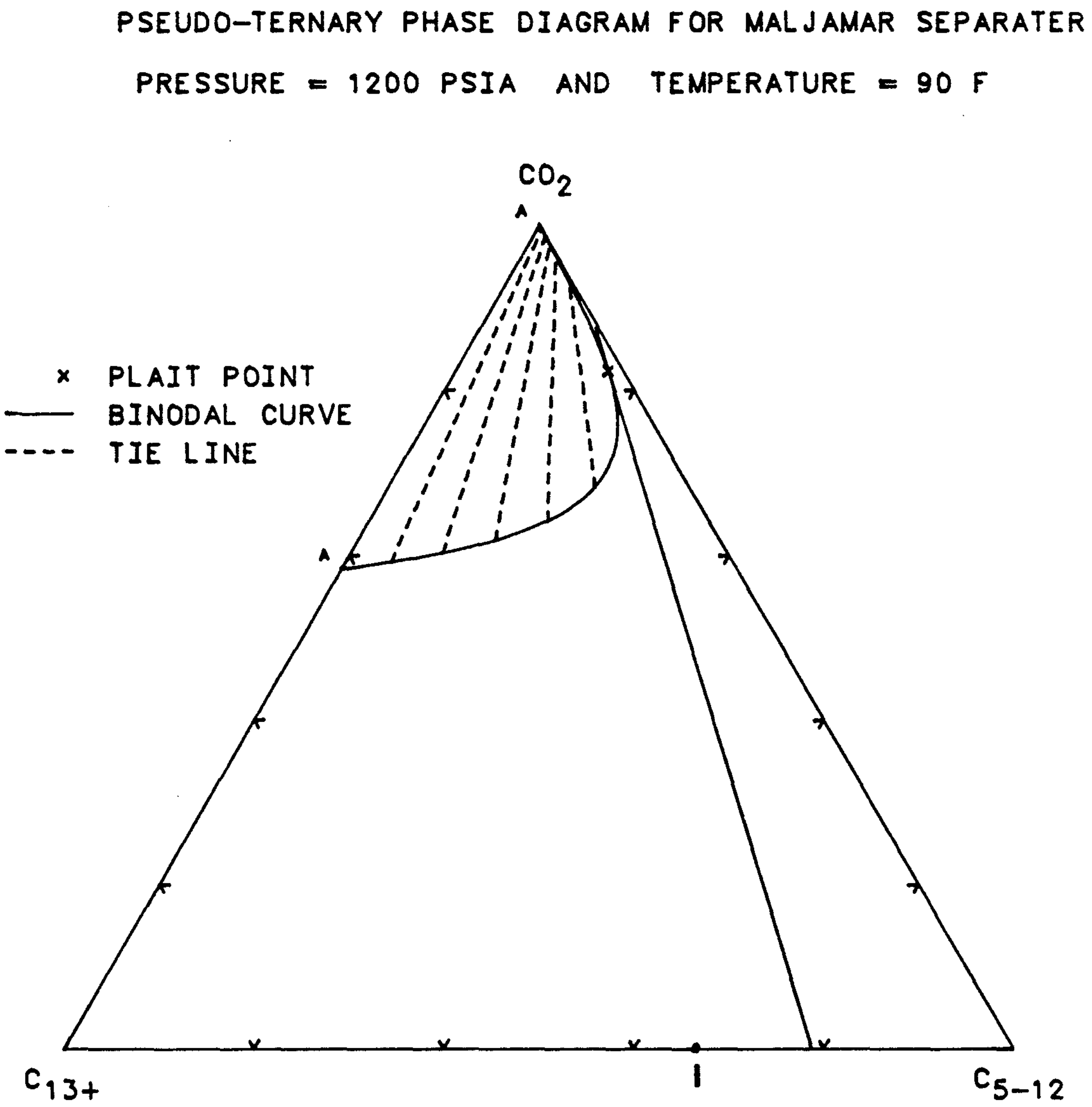

Figure 5.5(a) Pseudo-Ternary Phase Diagram for Maljamar Separator Oil at 1200 psia & 32 °C (90 °F) (Critical values by method #1)

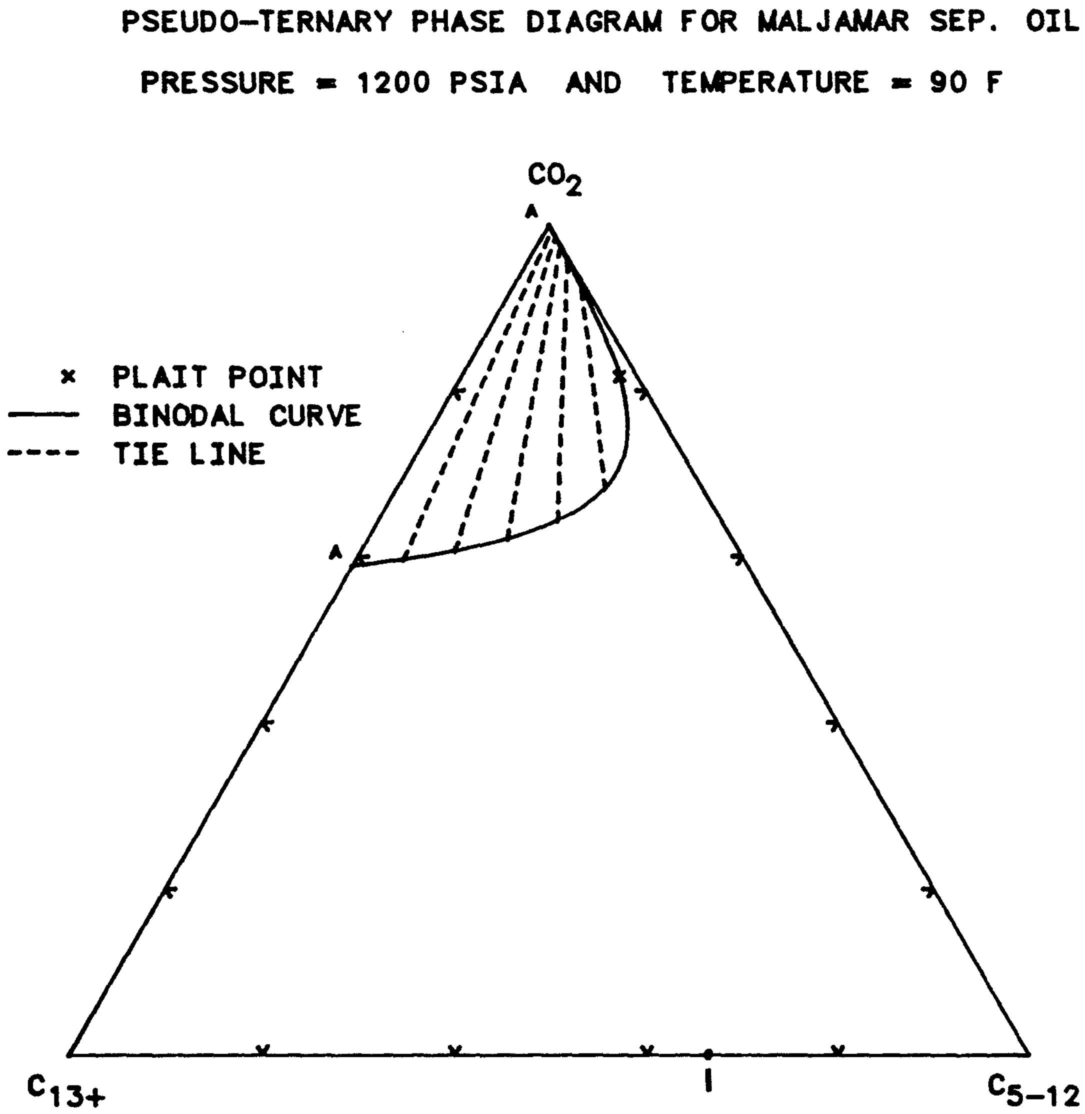

Figure 5.5(b) Pseudo-Ternary Phase Diagram for Maljamar Separator Oil at 1200 psia & 32 °C (90 °F) (Critical values by method #2)

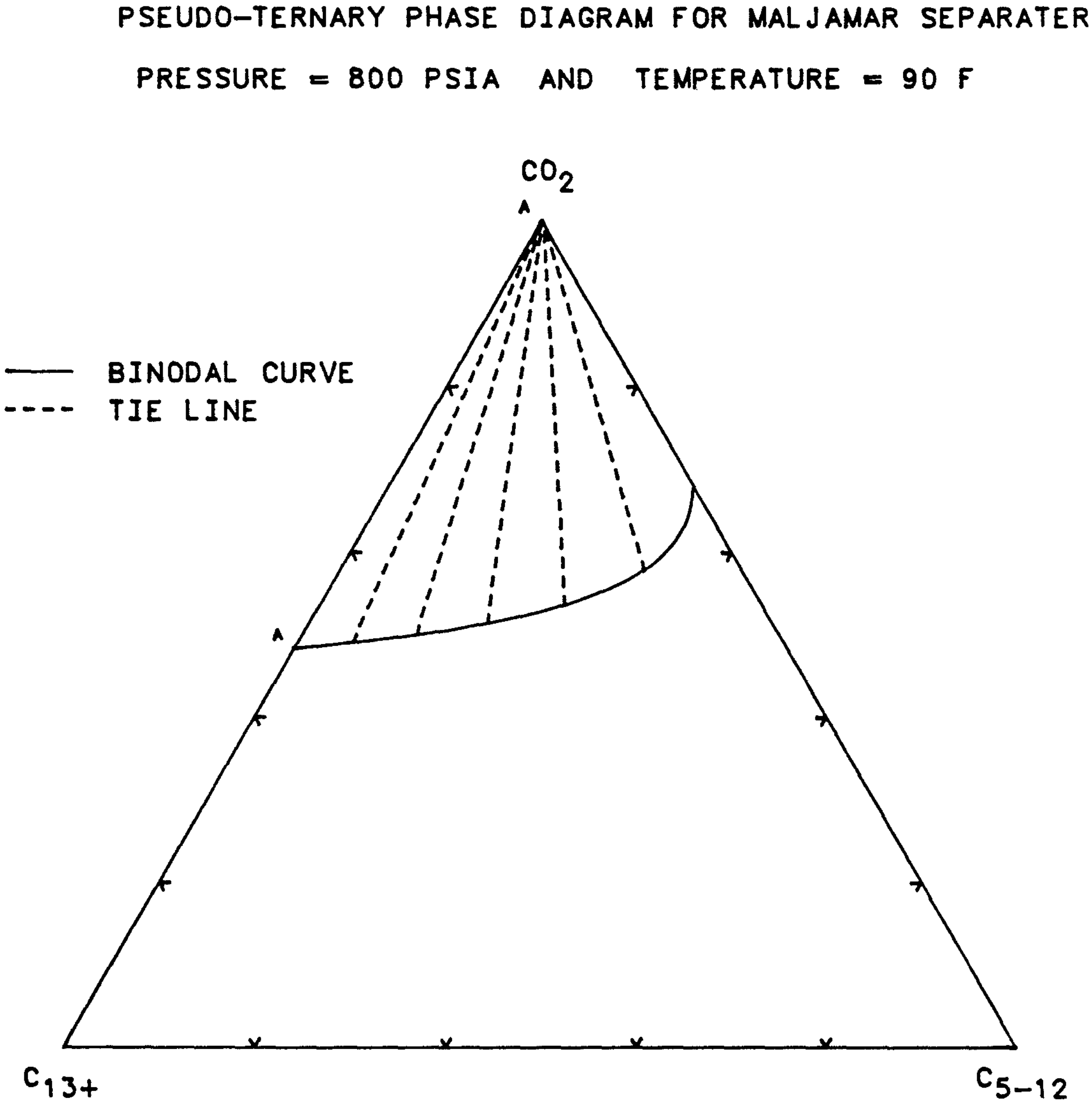

Figure 5.6(a) Pseudo-Ternary Phase Diagram for Maljamar Separator Oil at 800 psia & 32 °C (90 °F) (Critical values by method #1)

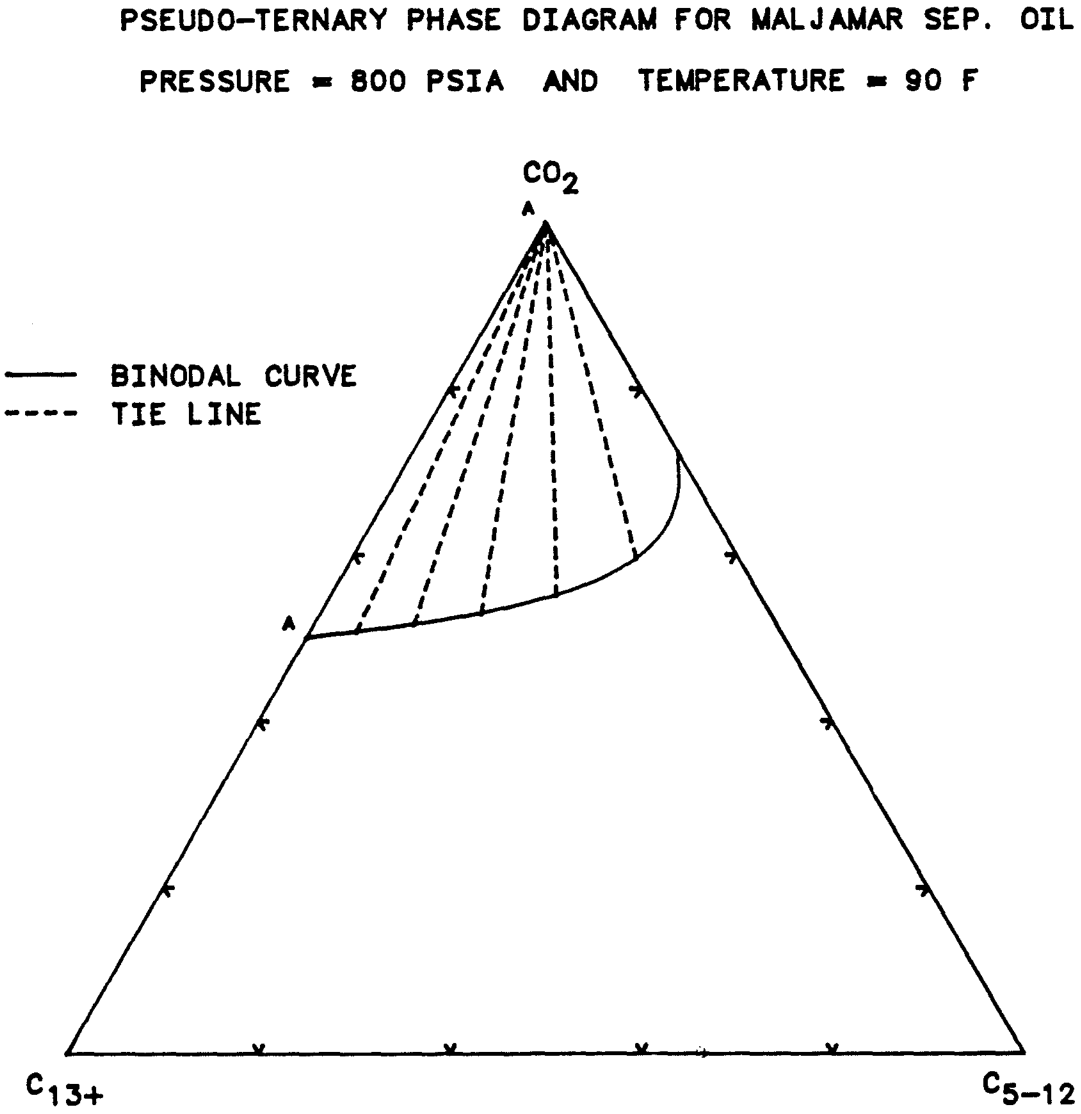

Figure 5.6(b) Pseudo-Ternary Phase Diagram for Maljamar Separator Oil at 800 psia & 32 °C (90 °F) (Critical values by method #2)

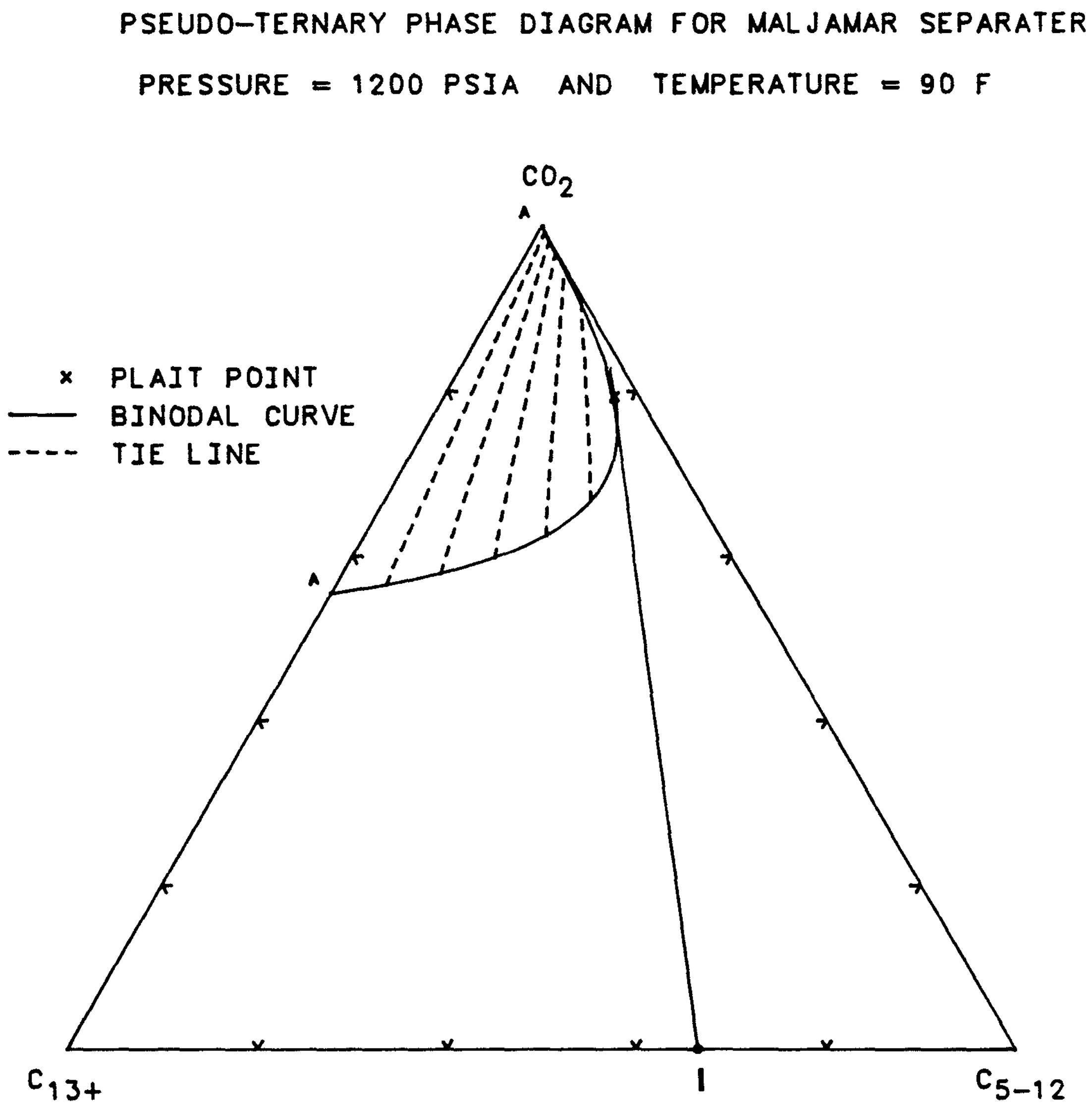

Figure 5.7(a) Pseudo-Ternary Phase Diagram for Maljamar Separator Oil at 1200 psia & 32 °C (90 °F)

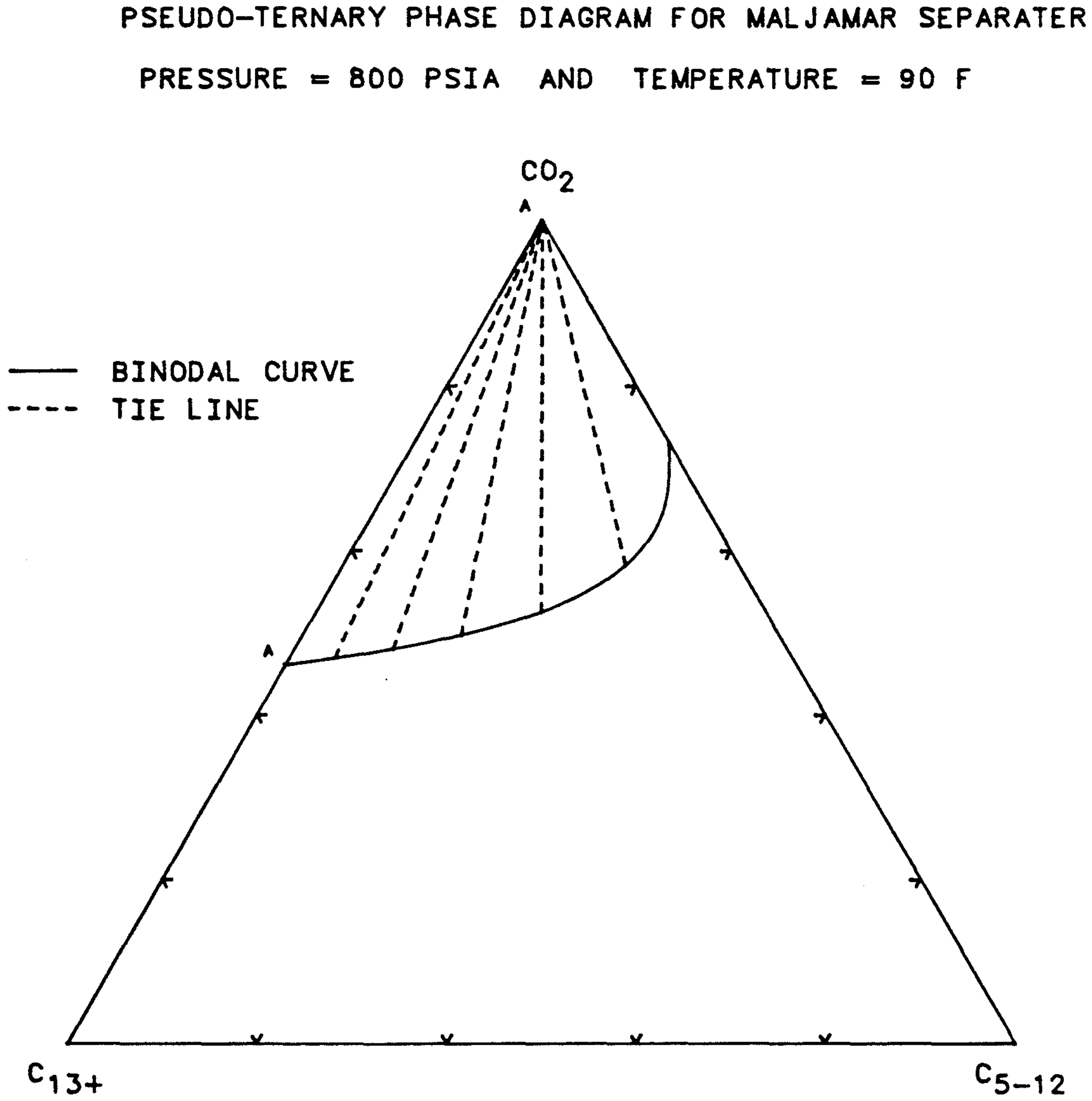

Figure 5.7(b) Pseudo-Ternary Phase Diagram for Maljamar Separator Oil at 800 psia & 32 °C (90 °F)

Figure 5.8(a) Comparison of Calculated and Experimental Phase Behavior Using Three Pseudo-Components and Method #1 for Property Estimation

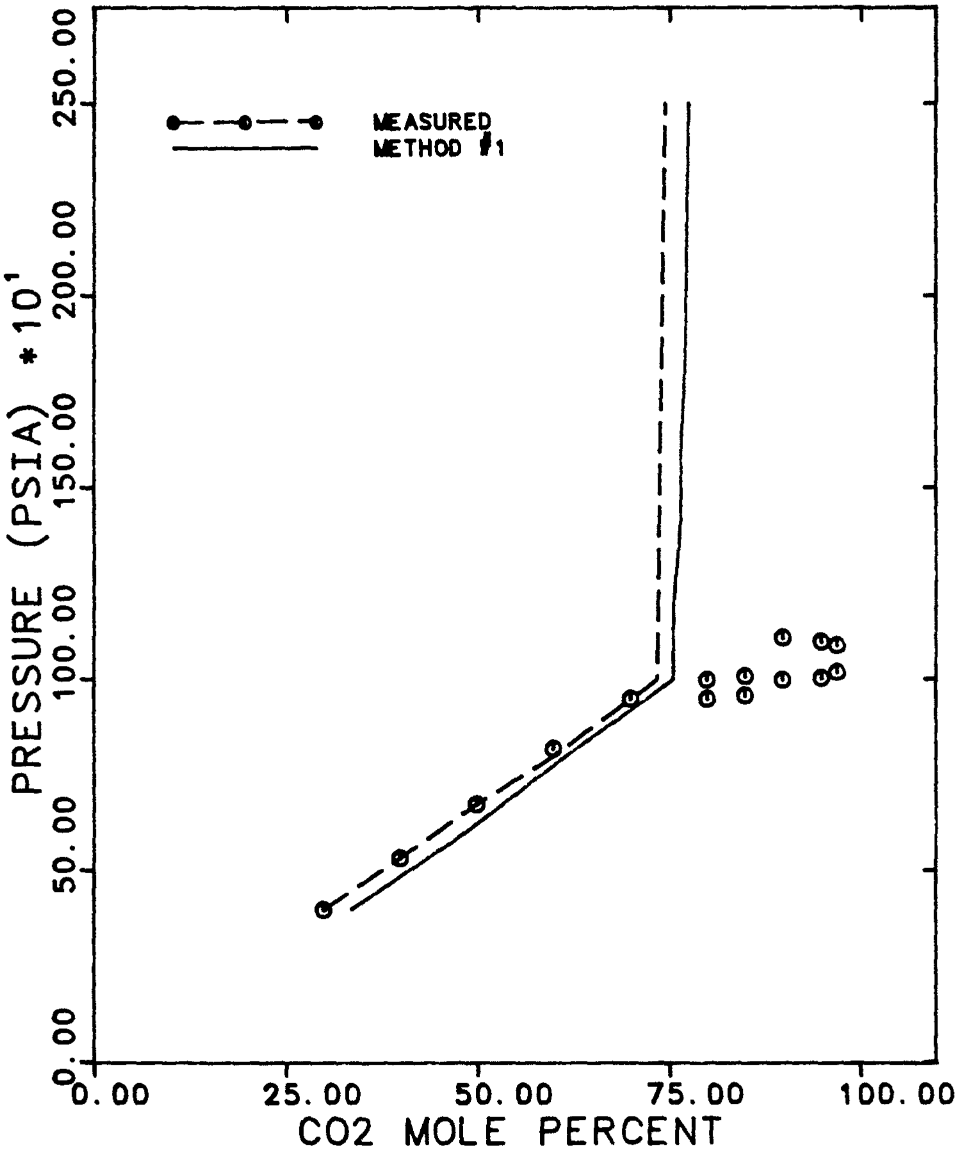

Figure 5.8(b) Comparison of Calculated and Experimental Phase Behavior Using Three Pseudo-Components and Method #2 for Property Estimation

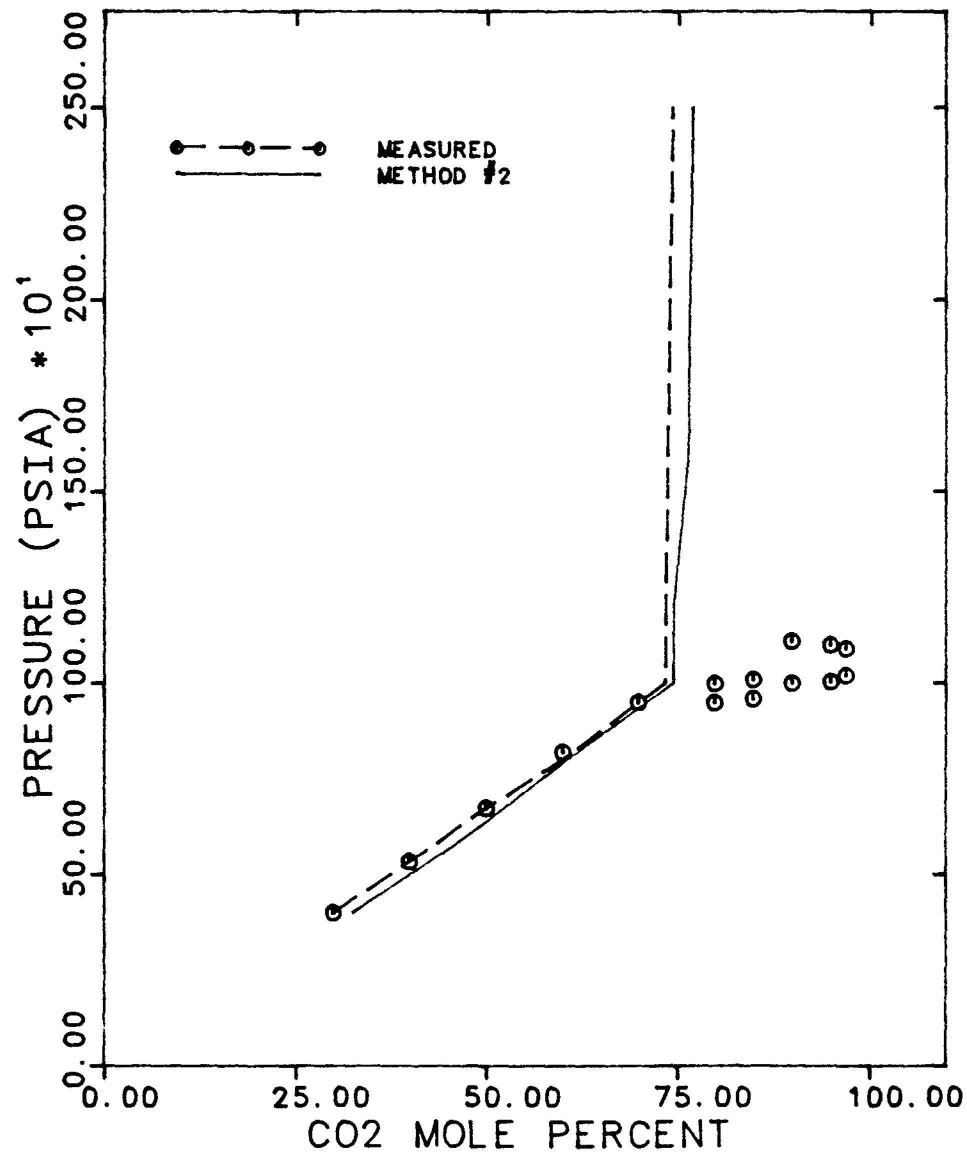

Figure 5.9 Comparison of Calculated and Experimental Phase Behavior Using Three Pseudo-Components and Kato's or Lawal's Correlations for Binary Interaction Coefficients (Initial Values)

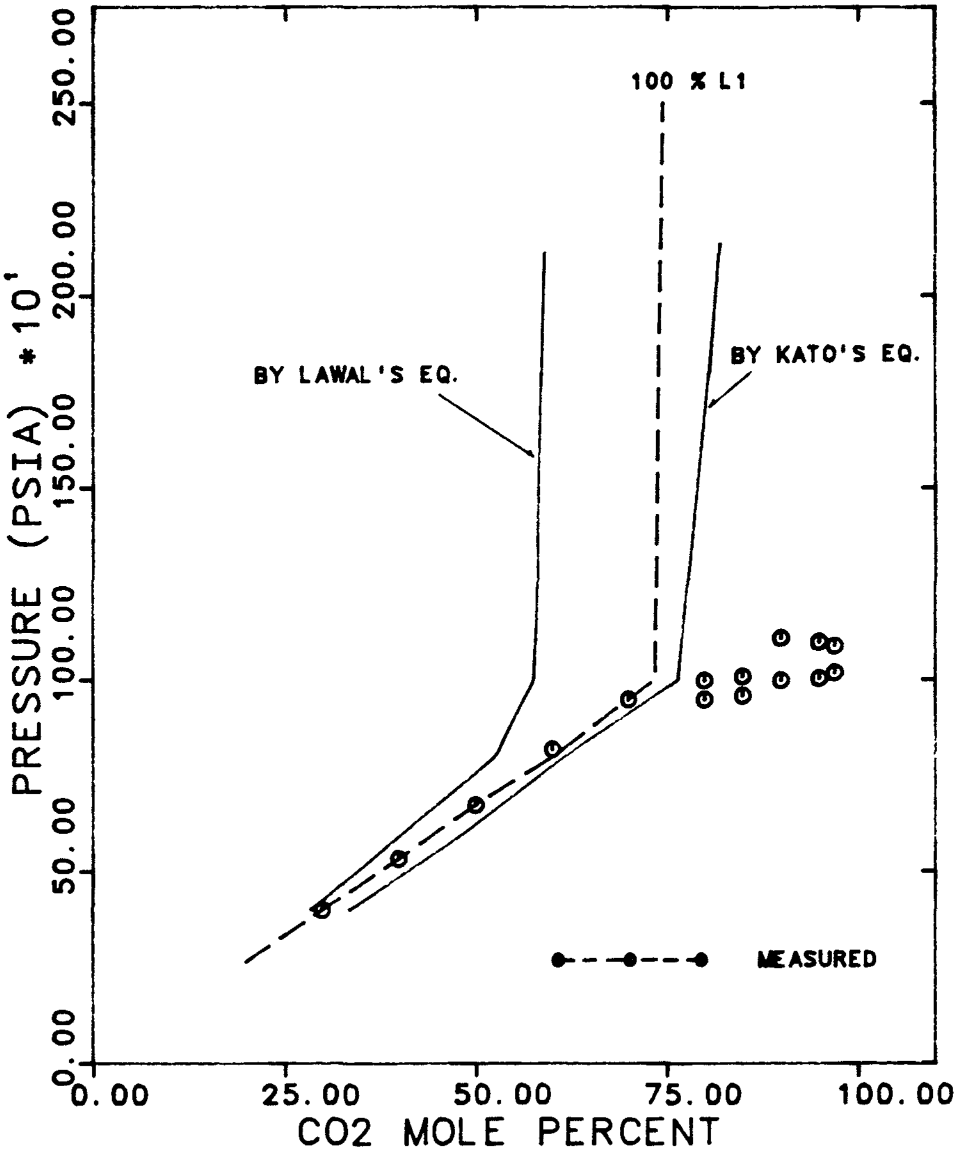

Figure 5.10 Comparison of Calculated and Experimental Phase Behavior Using Three Pseudo-Components and Kato's or Lawal's Correlations for Binary Interaction Coefficients (Matched Values)

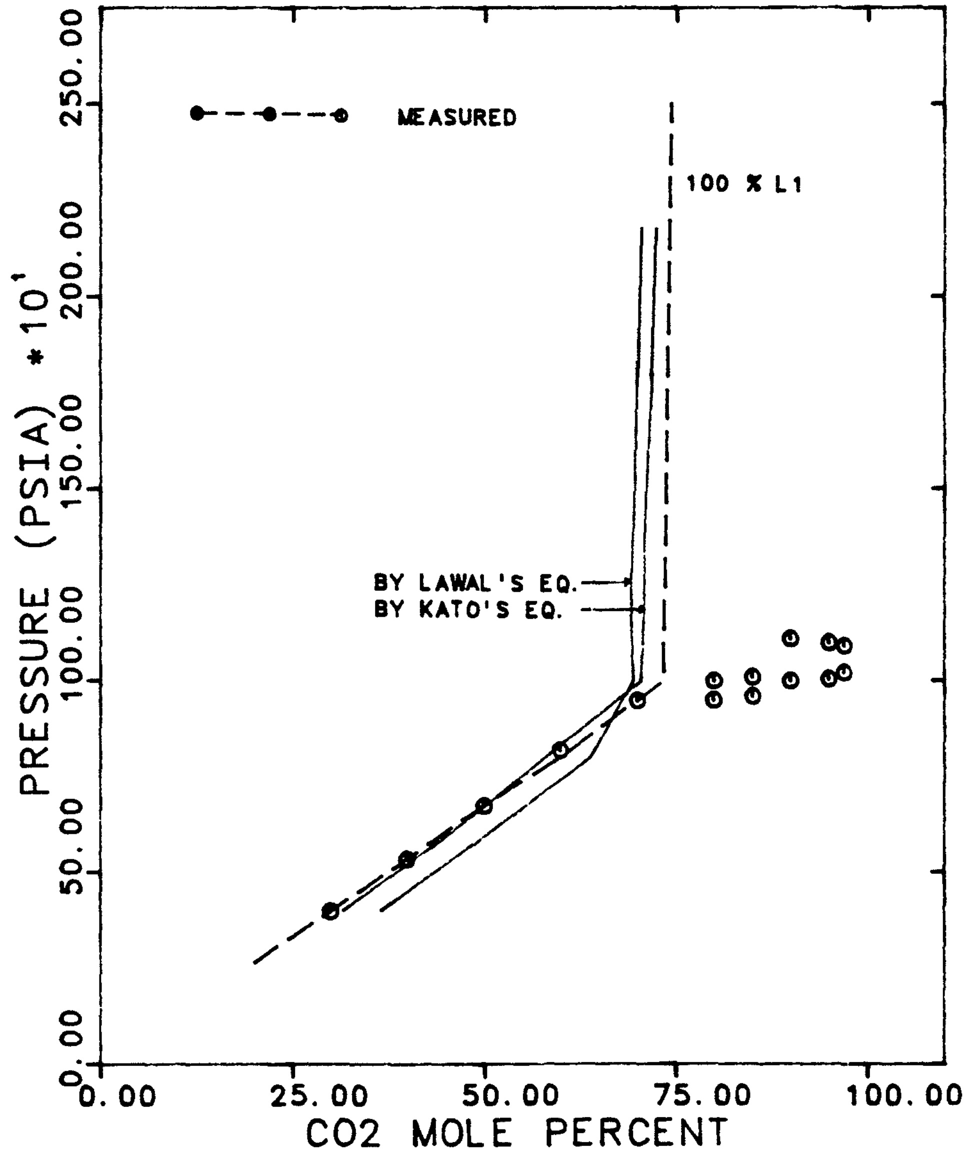

Figure 5.11 Comparison of Computed and Experimental Relative Permeability as a Function of Oil Saturation

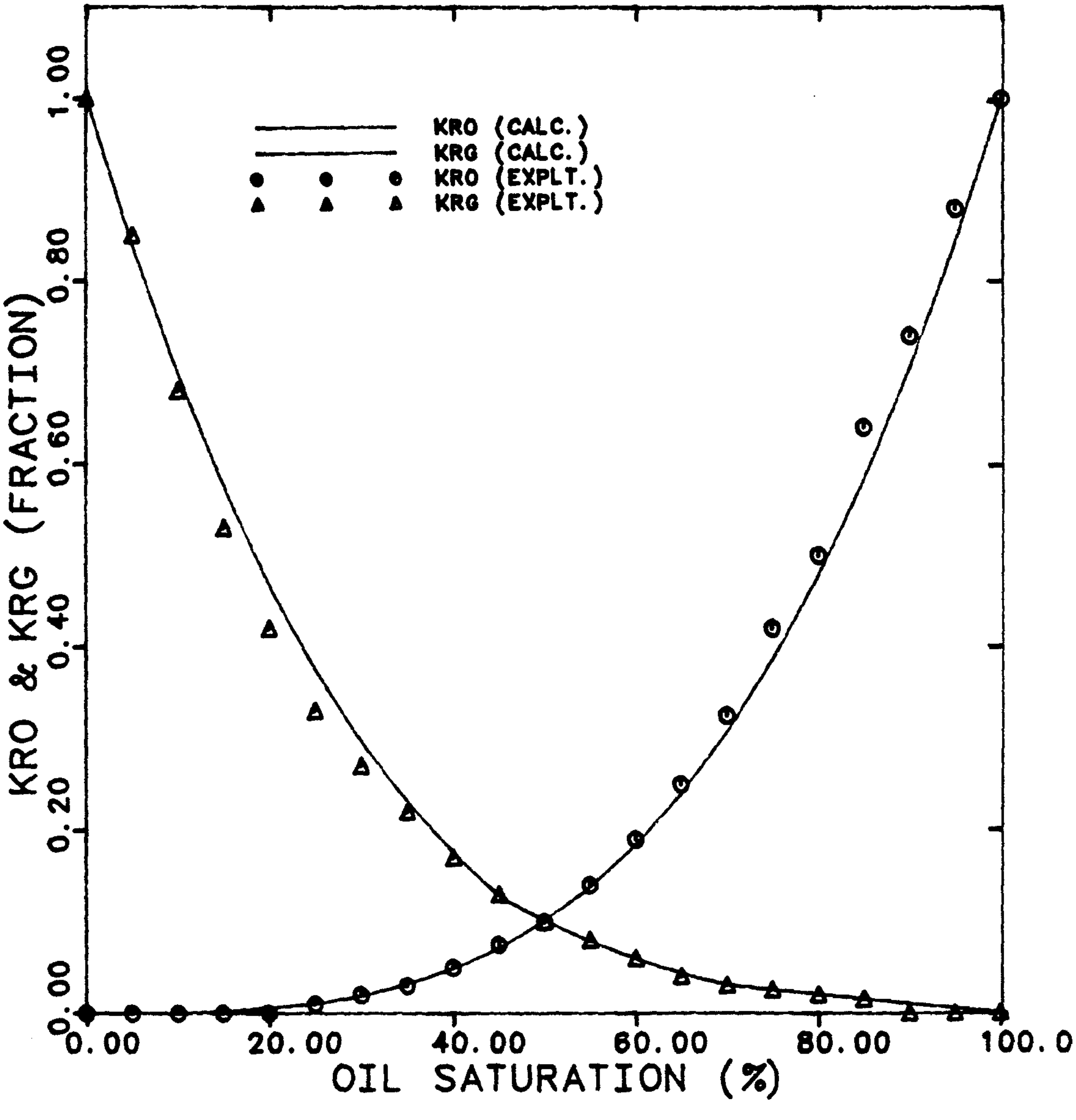

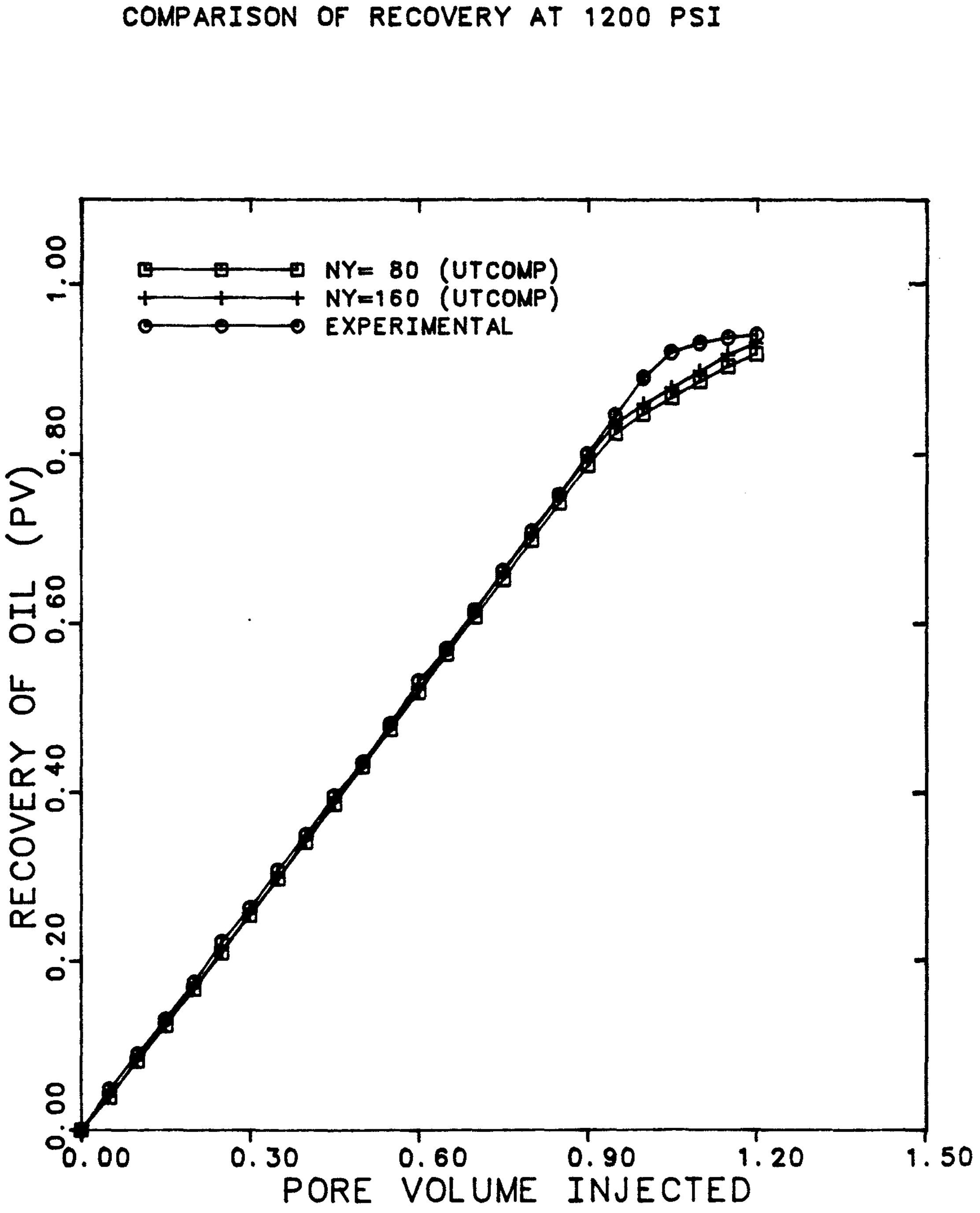

Figure 5.12 Recovery Curve Comparison for Maljamar Separator Oil at 1200 psia (3 components)

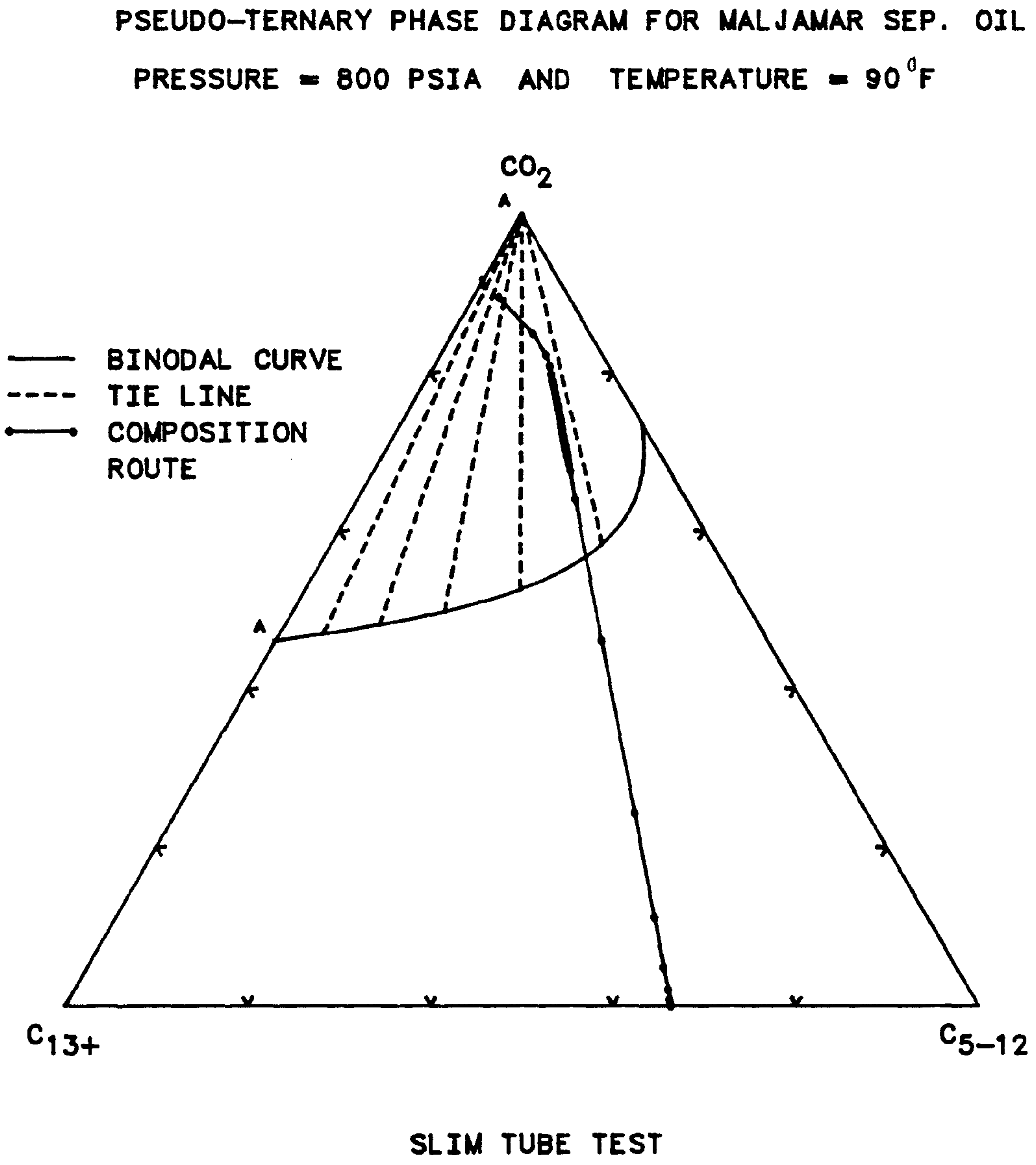

PSEUDO-TERNARY PHASE DIAGRAM FOR MALJAMAR SEP. OIL

PRESSURE = 800 PSIA AND TEMPERATURE = 90 °F

SLIM TUBE TEST

Figure 5.13(a) Pseudo-Ternary Phase Diagram and Simulated Compositional Pass for Maljamar Separator Oil Slim - tube Displacement at 800 psia & 90 °F

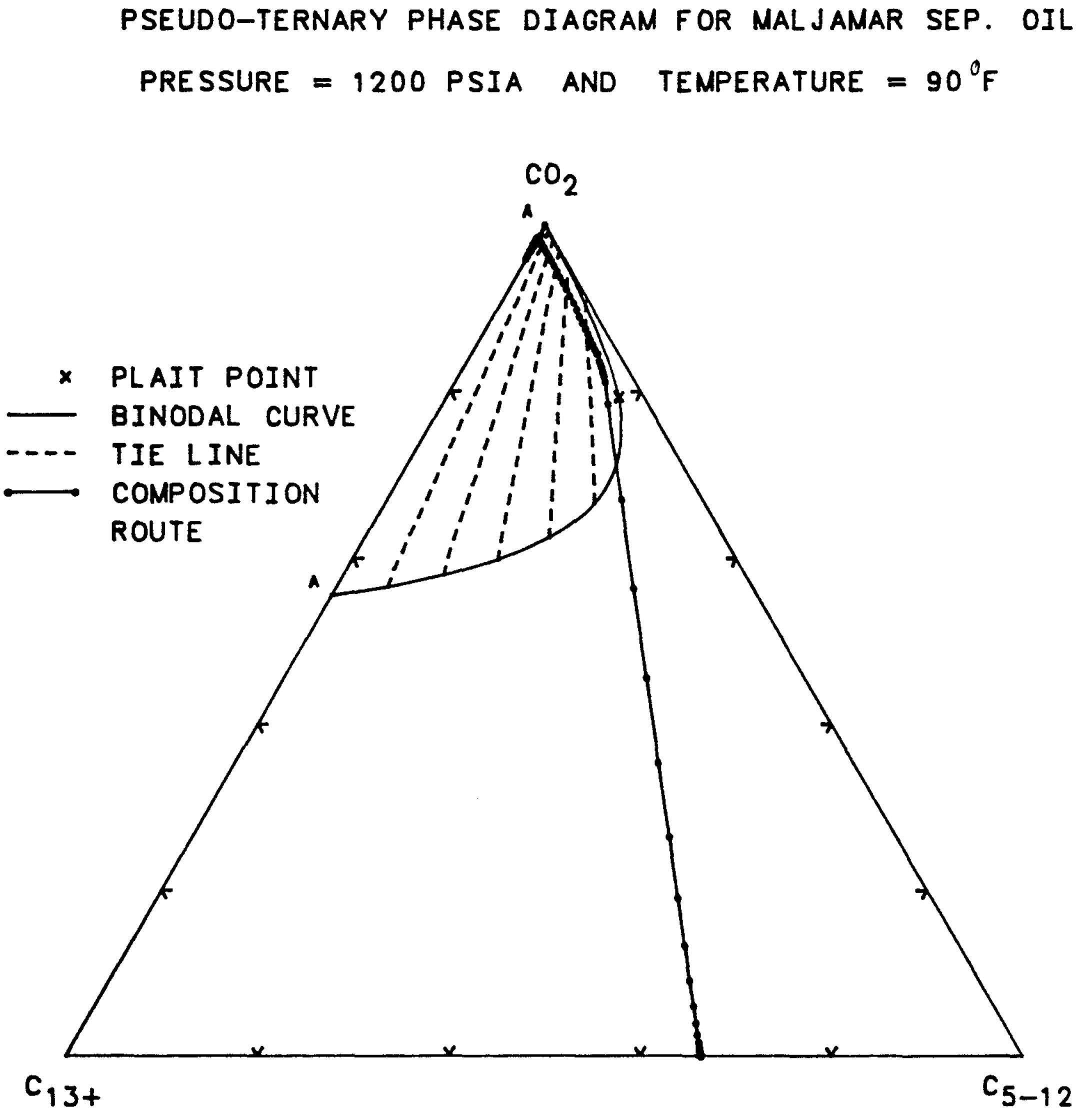

Figure 5.13(b) Pseudo-Ternary Phase Diagram and Simulated Compositional Pass for Maljamar Separator Oil Slim - tube Displacement at 1200 psia & 90 °F

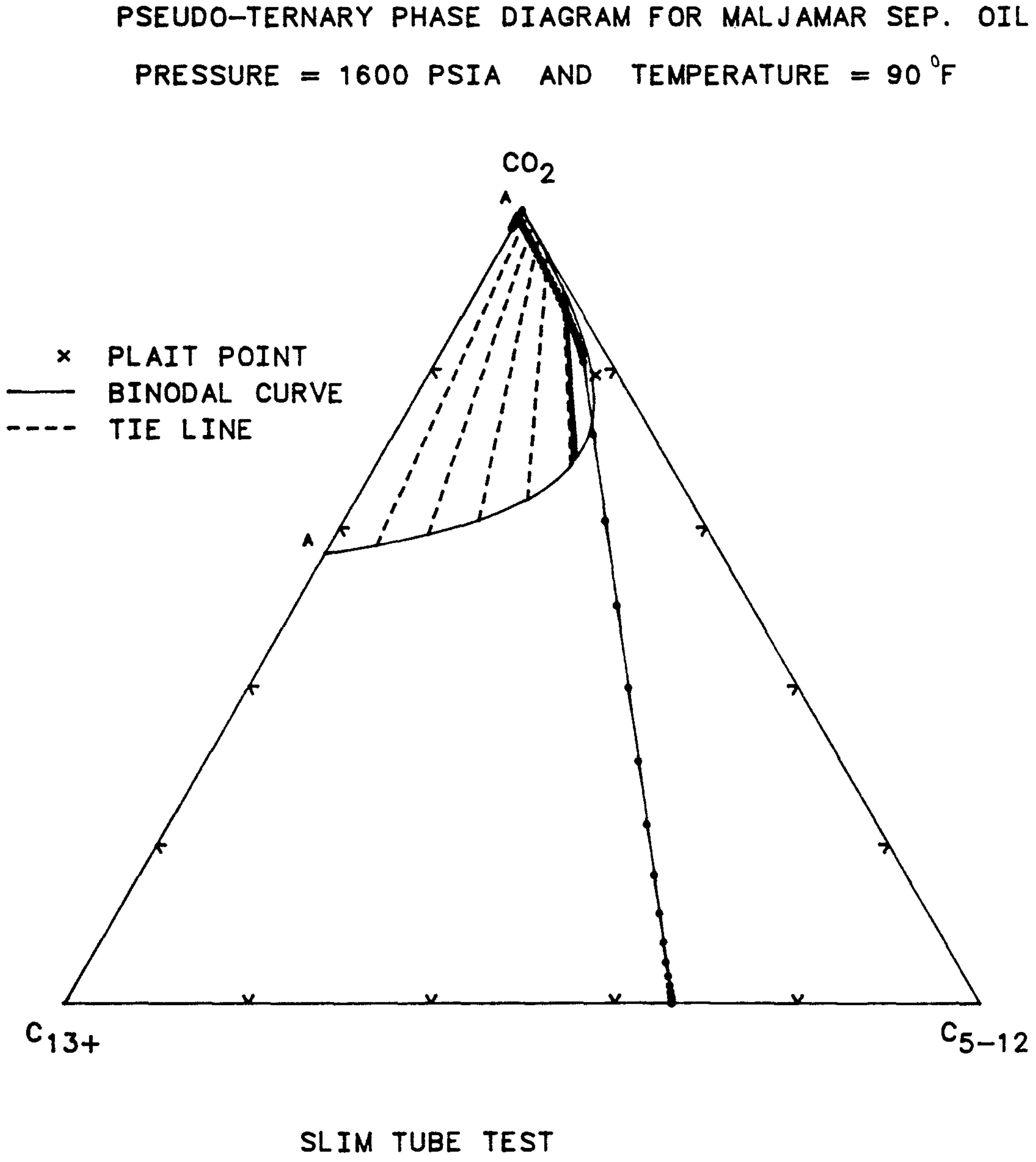

Figure 5.13(c) Pseudo-Ternary Phase Diagram and Simulated Compositional Pass for Maljamar Separator Oil Slim - tube Displacement at 1600 psia & 90 °F

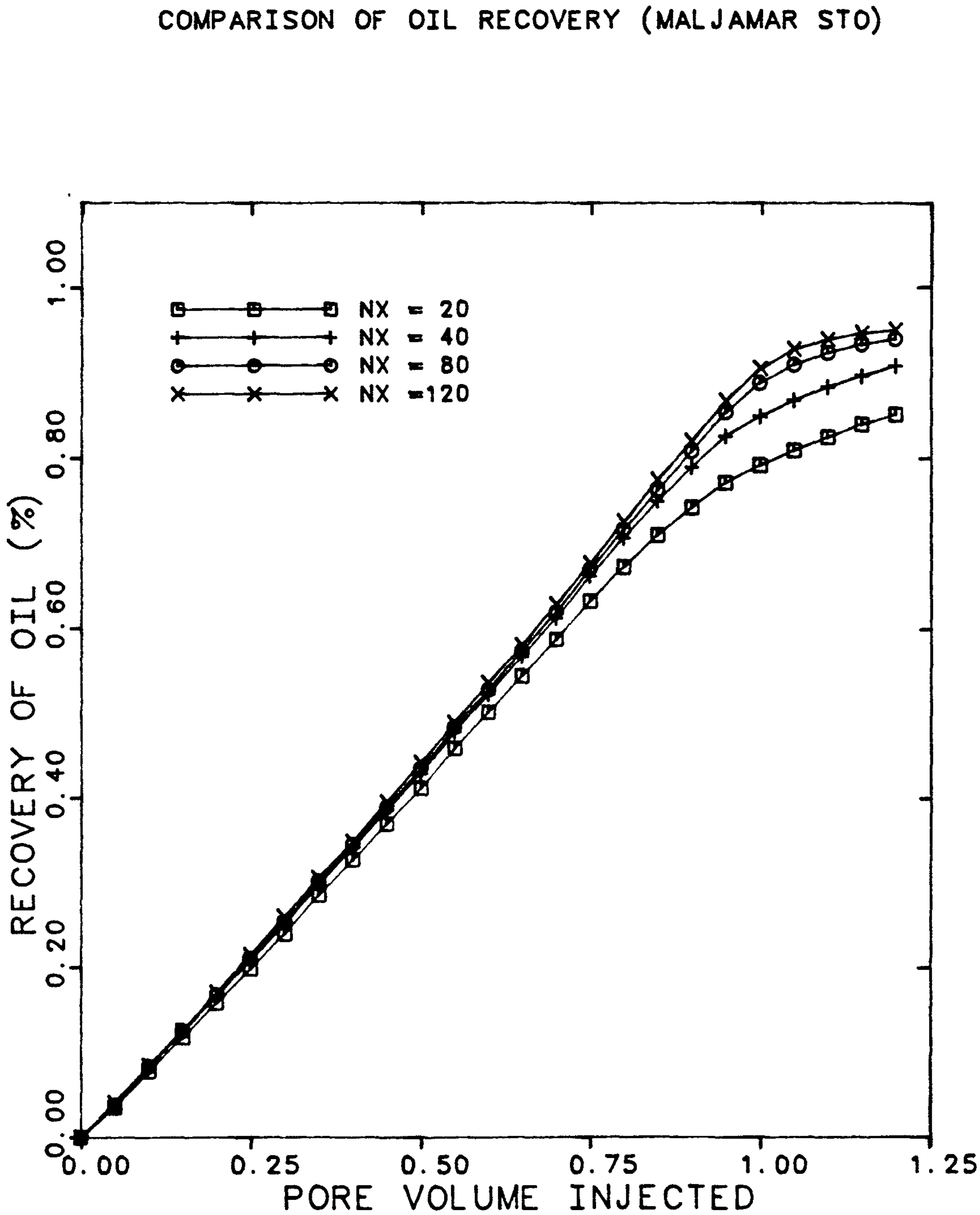

Figure 5.14 Recovery Curve Comparison for Maljamar Separator Oil at 1200 psia (7 components)

COMPARISON OF RECOVERY AT 1200 PSI

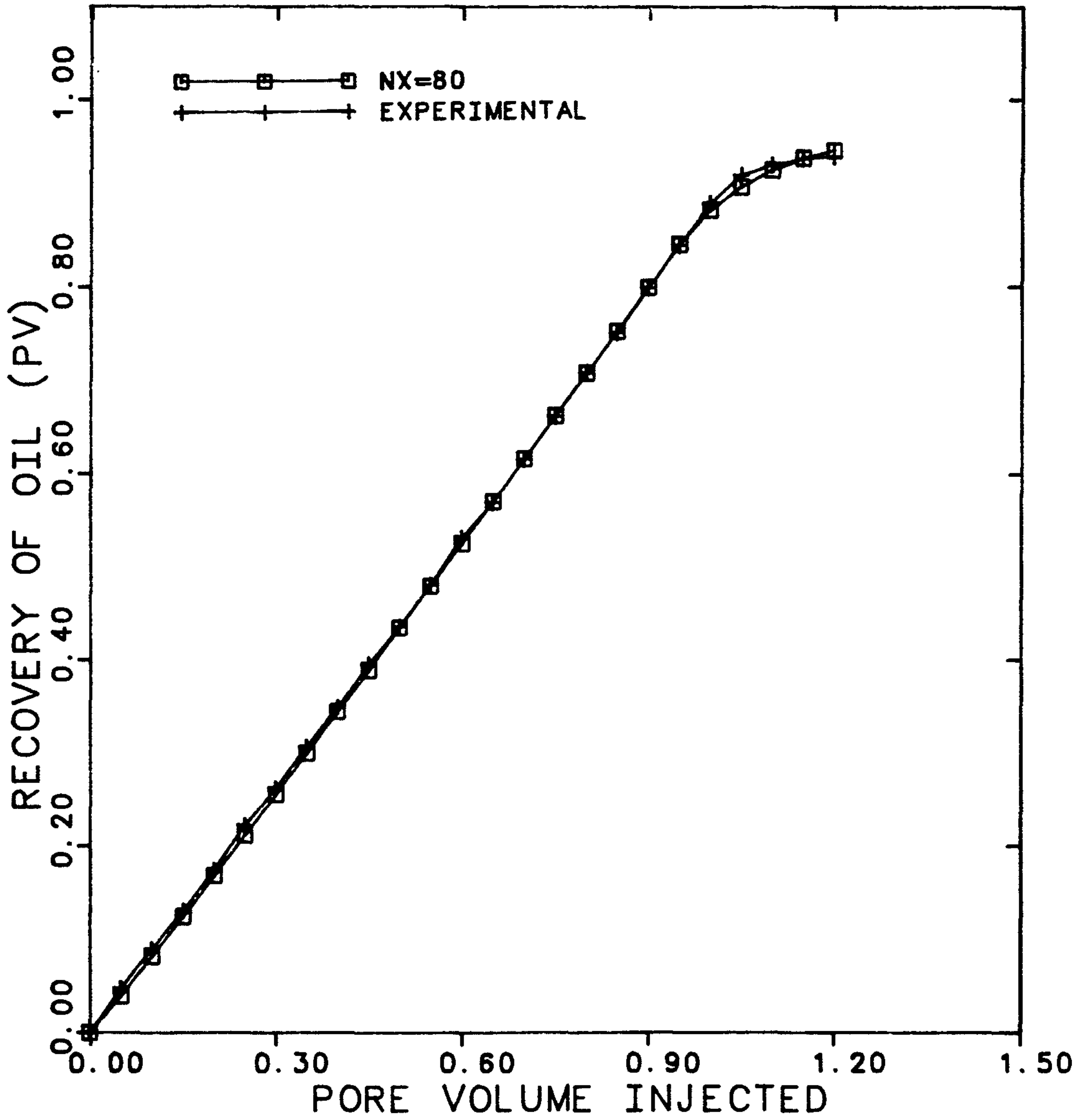

Figure 5.15 Recovery Curve Comparison for Maljamar Separator Oil at 1200 psia (7 components)

Figure 5.16 Comparison of Computed and Experimental Phase Behavior Using 7 components and 3 components

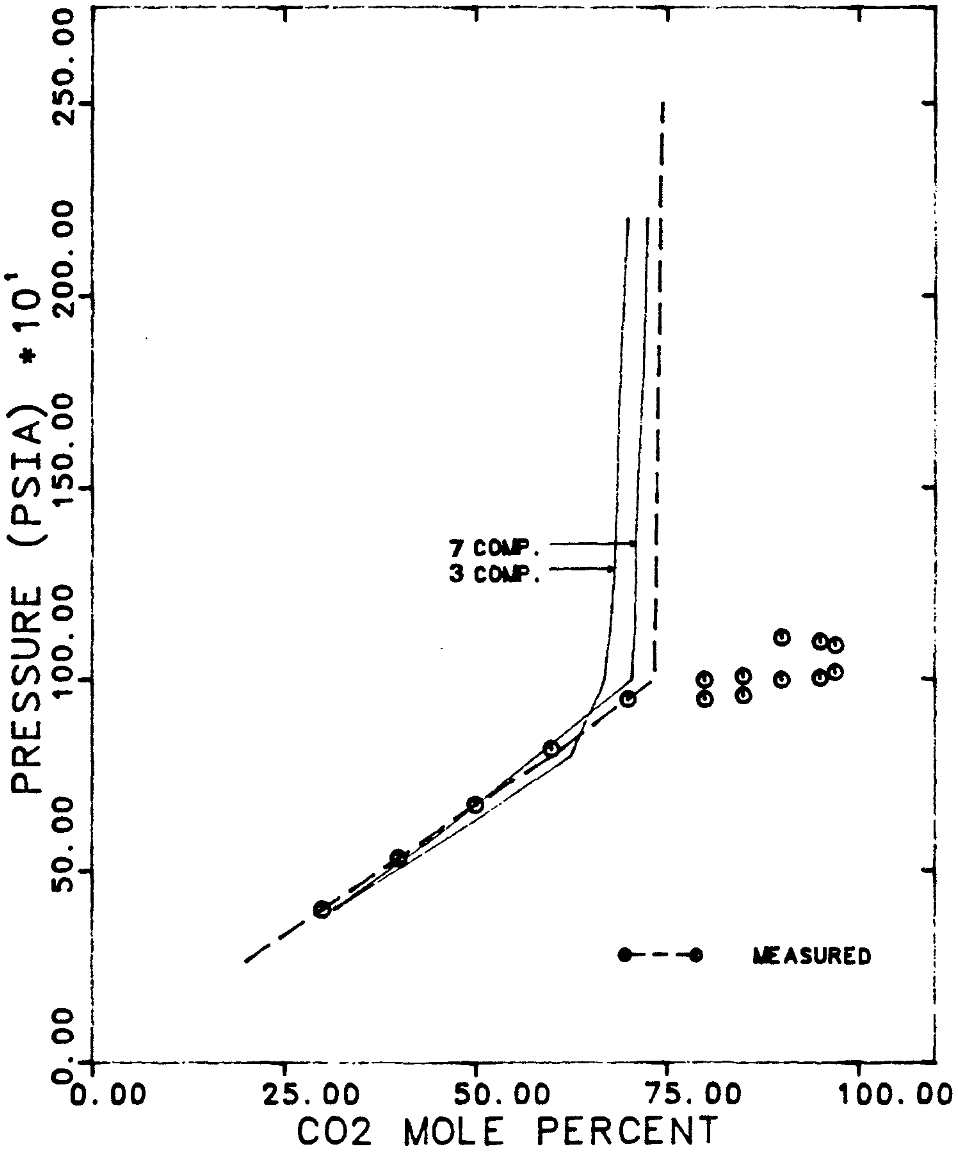

Figure 5.17 Comparison of Computed and Experimental Pressure - Recovery Diagram for Maljamar Separator Oil Slim-tibe Test

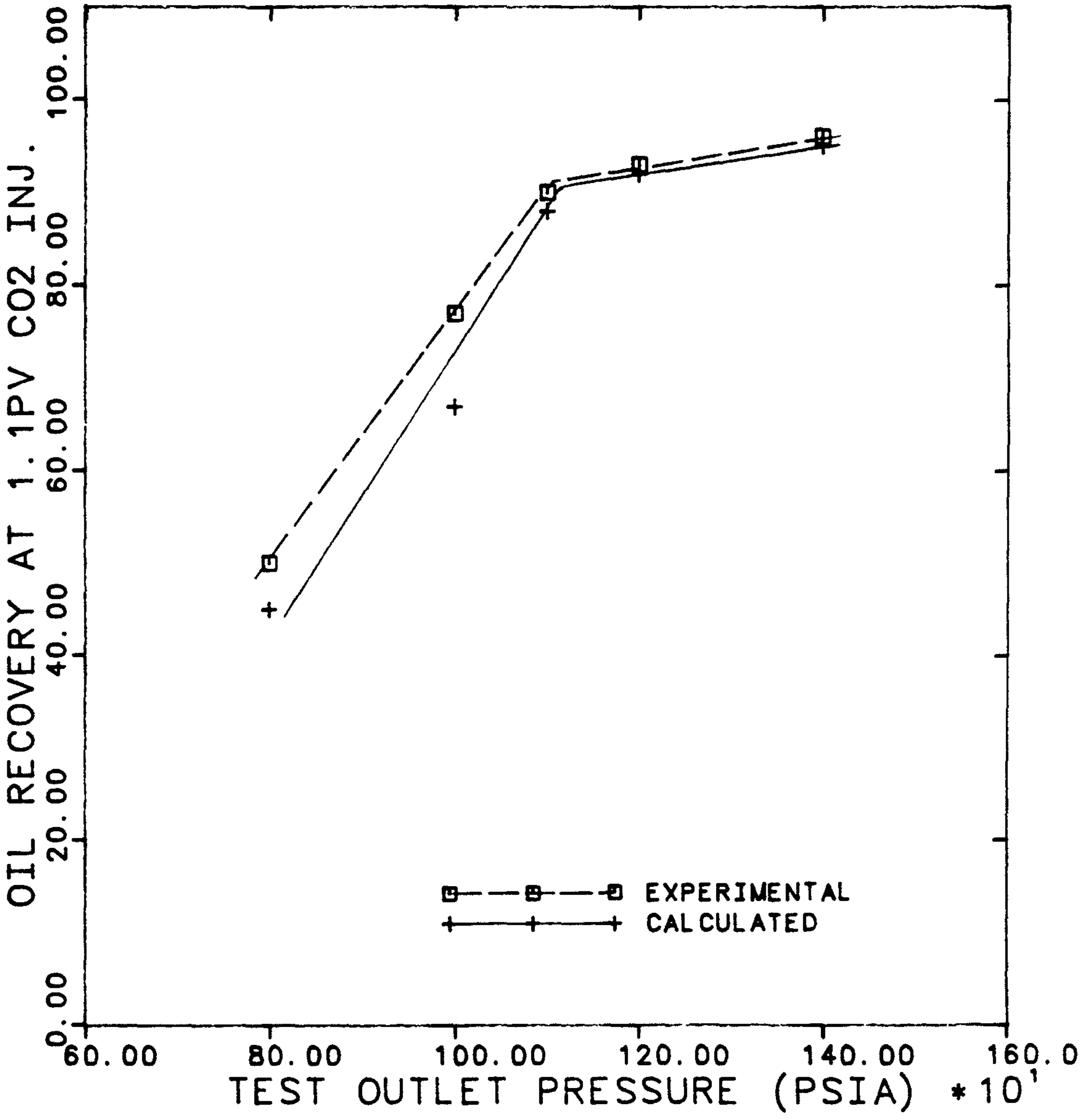

Figure 5.18 Saturation Profile for Maljamar Separator Oil at 0.514 Pore Volumes CO2 Injected (3 components)

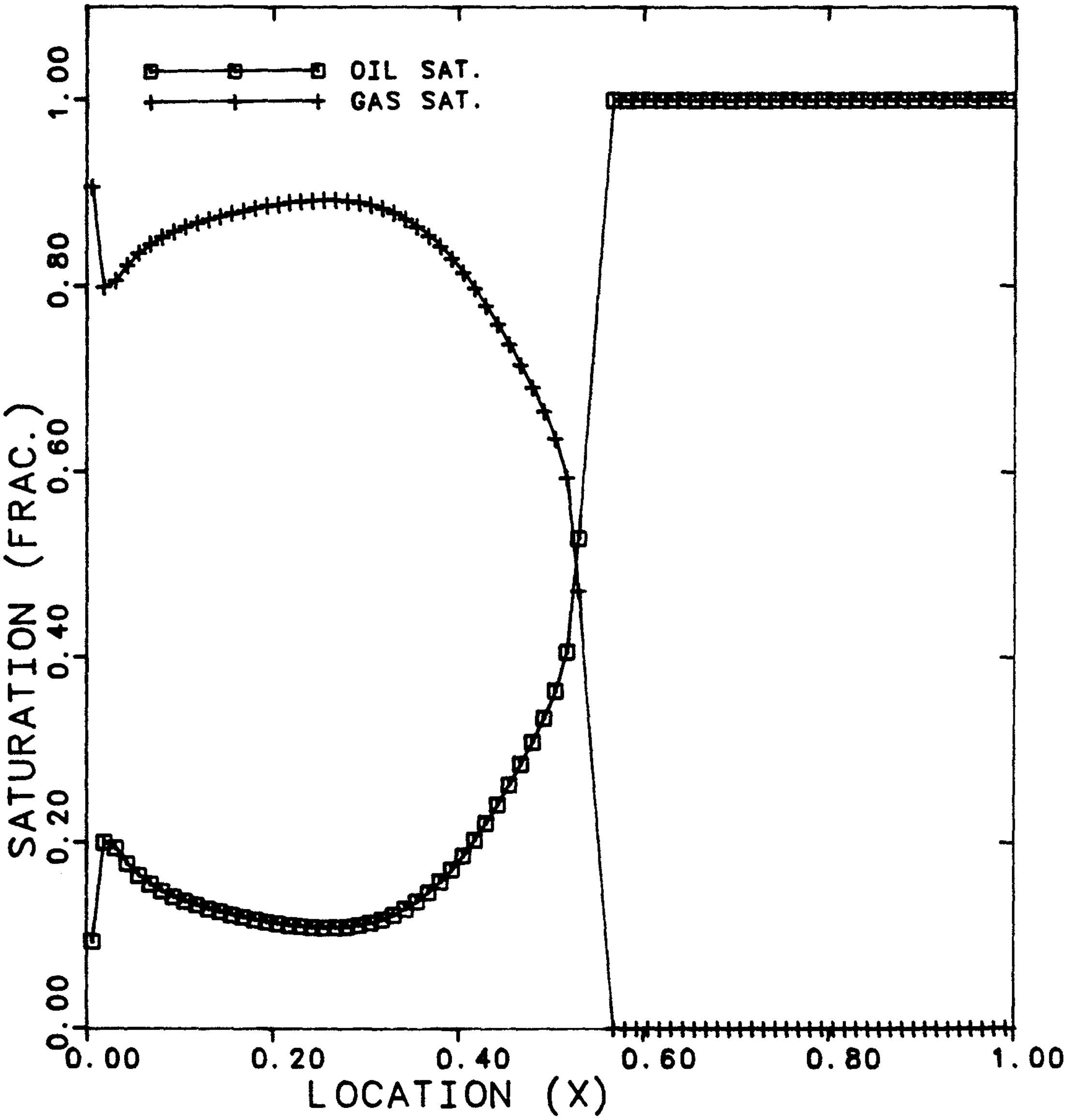

Figure 5.19 Density Profile for Maljamar Separator Oil at 0.514 Pore Volumes CO2 Injected (3 components)

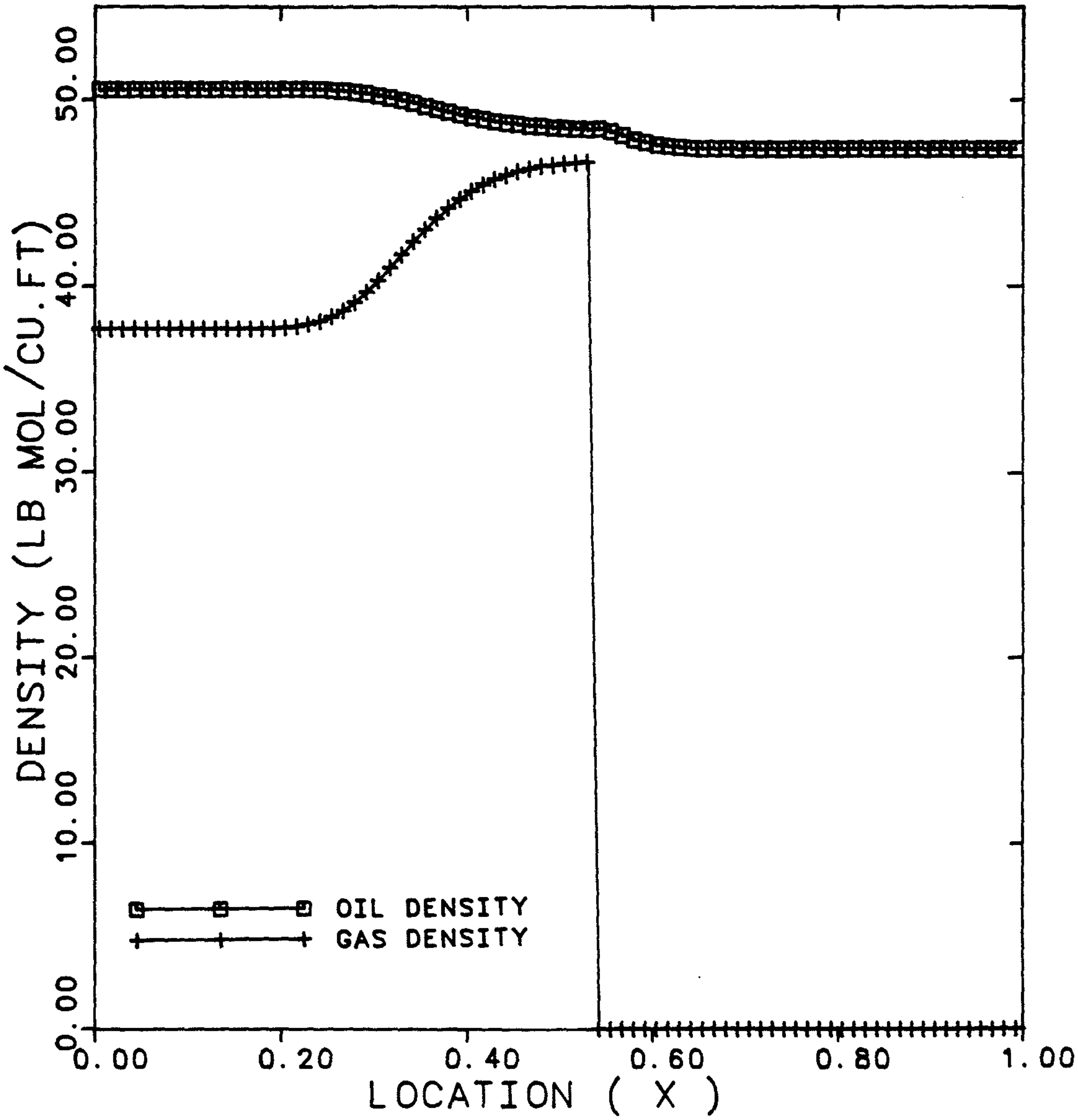

Figure 5.20 Overall Composition Profile for Maljamar Separator Oil at 0.514 Pore Volumes CO2 Injected (3 components)

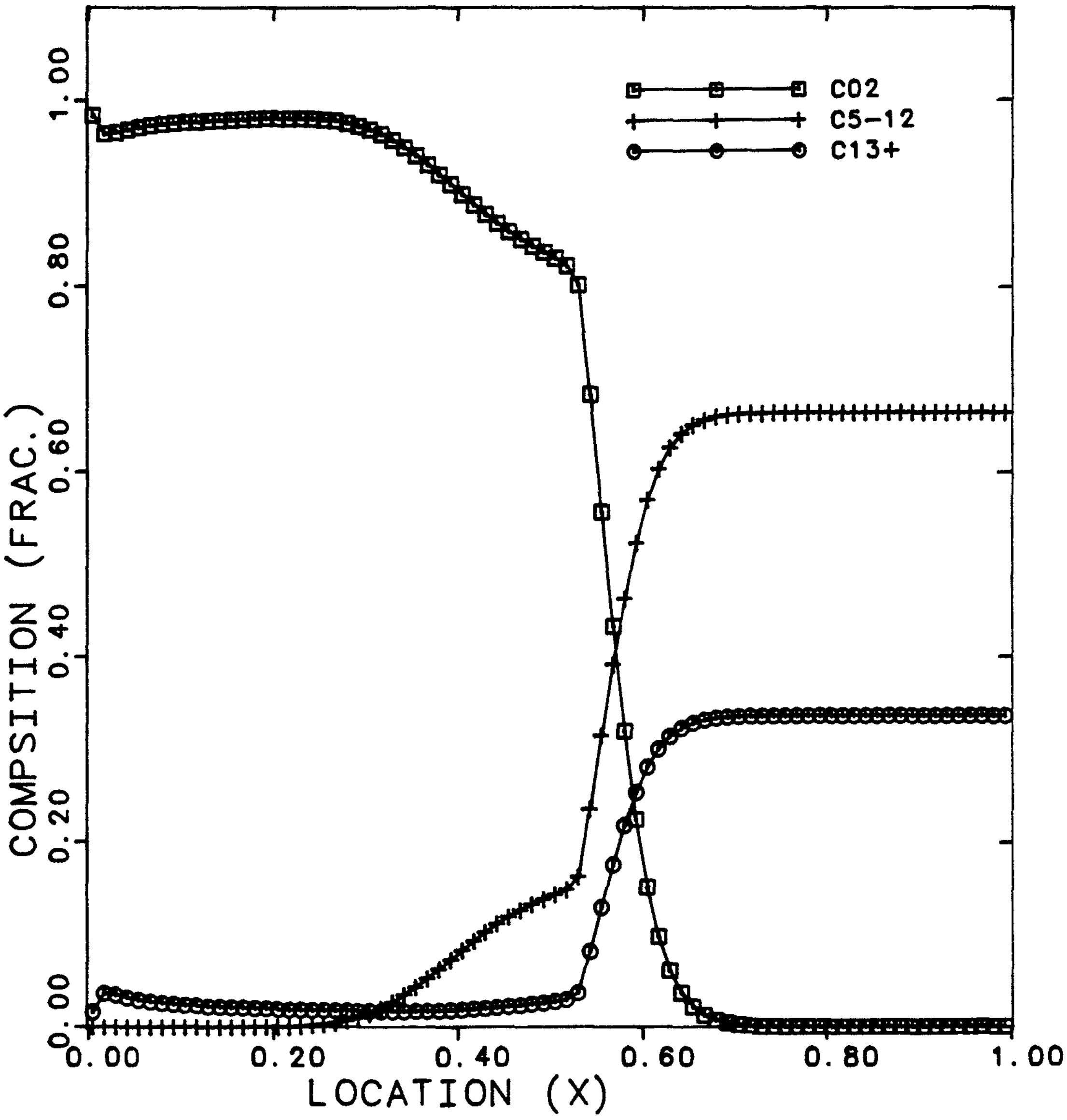

Figure 5.21 Oleic Phase Concentration Profile for Maljamar Separator Oil at 0.514 Pore Volumes CO2 Injected (3 components)

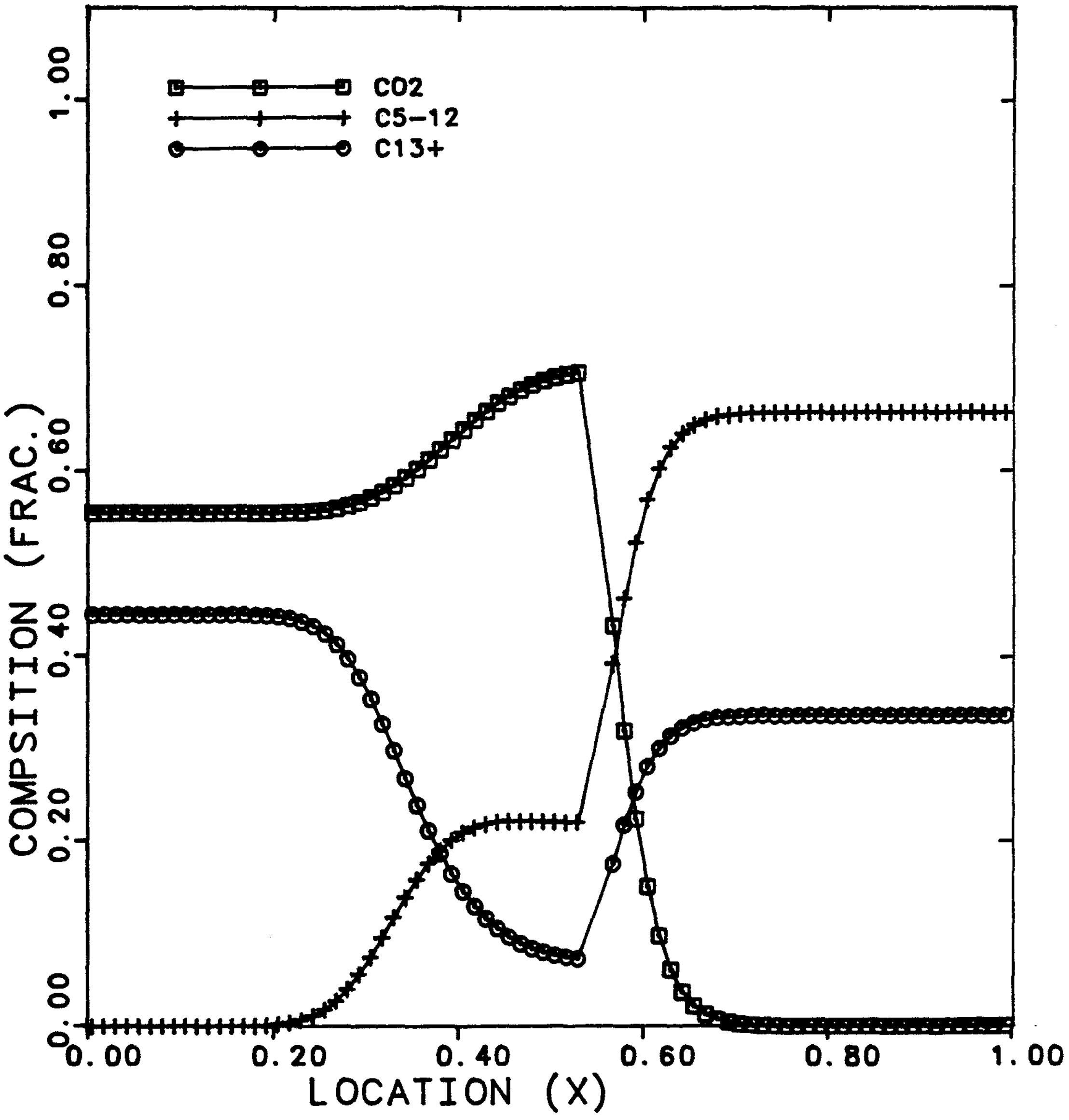

Figure 5.22 Composite-Diagram for Profiles at 0.514 Pore Volumes CO2 Injected

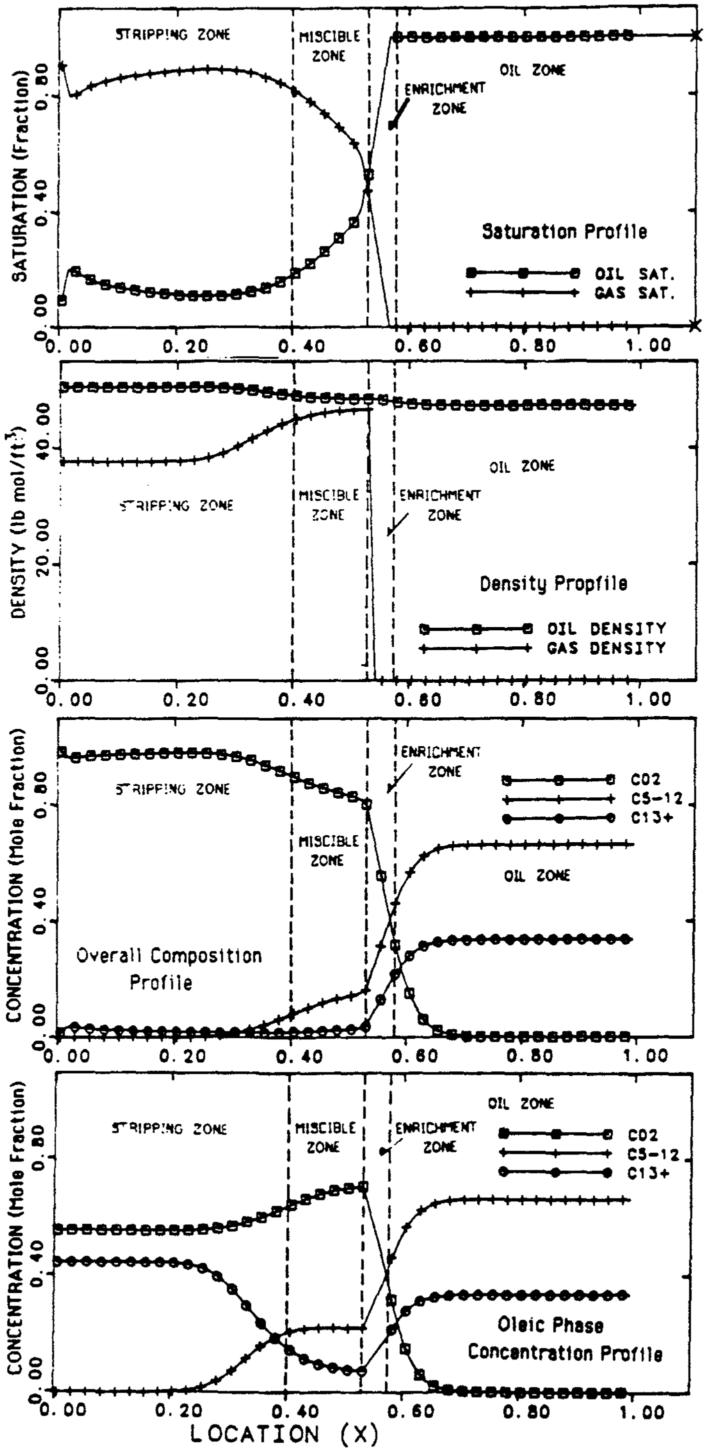

Figure 5.23 Saturation Profile for Maljamar Separator Oil at 0.8081 Pore Volumes CO2 Injected (7 components)

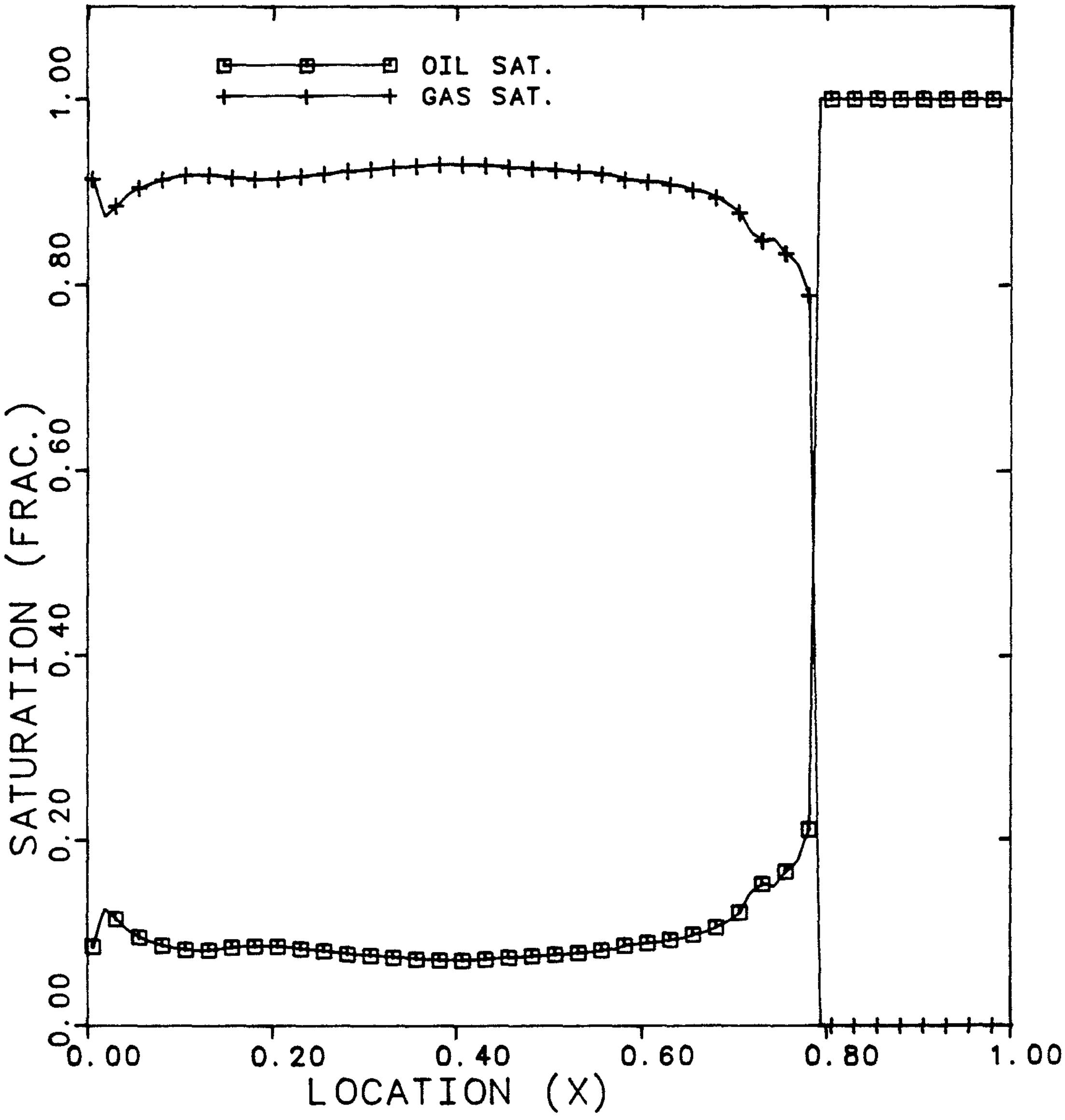

Figure 5.24 Oleic Phase Concentration Profile for Maljamar Separator Oil at 0.8081 Pore Volumes CO2 Injected (7 components)

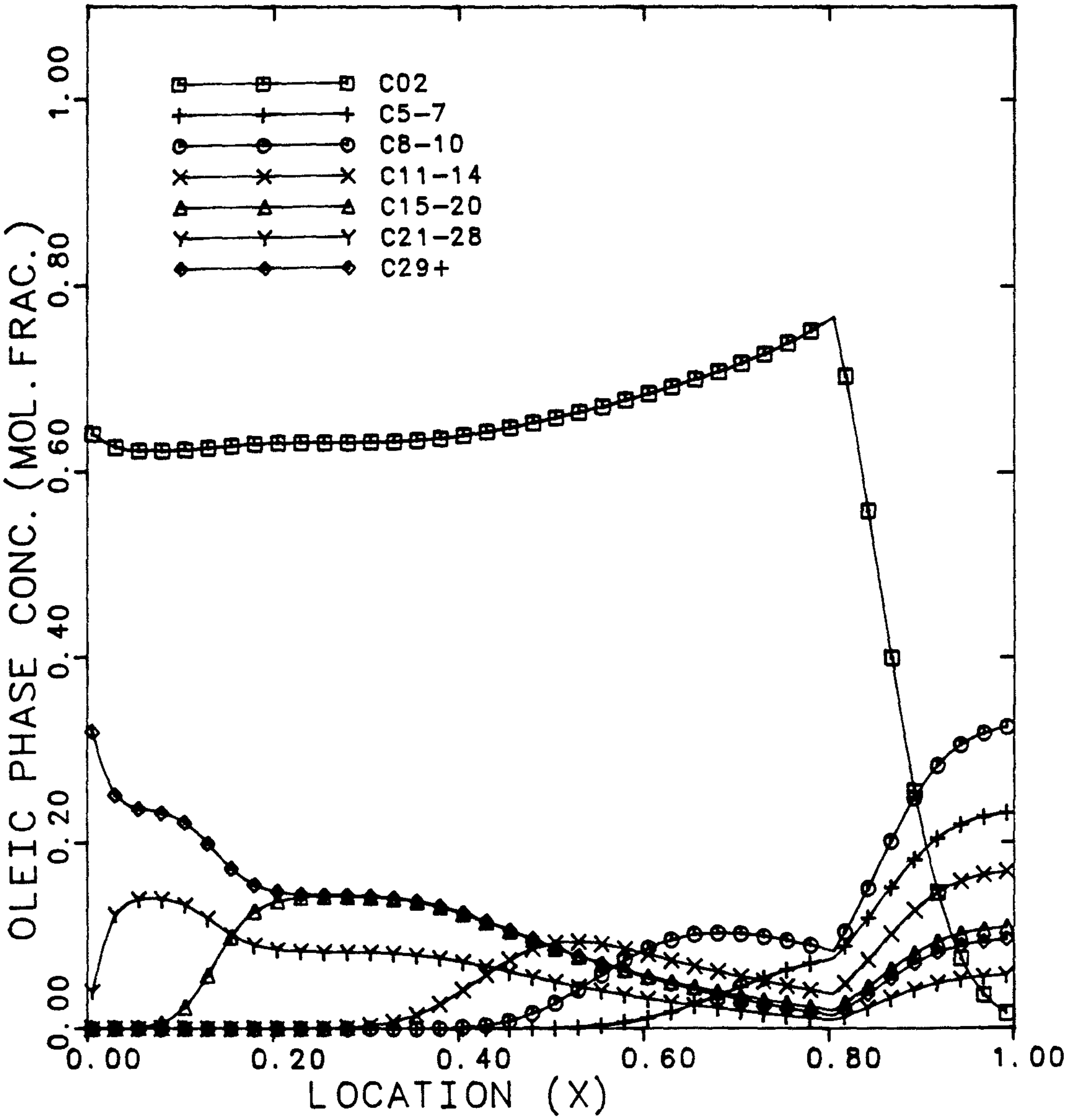

Figure 5.25 Gas Phase Concentration Profile for Maljamar Separator Oil at 0.8081 Pore Volumes CO2 Injected (7 components)

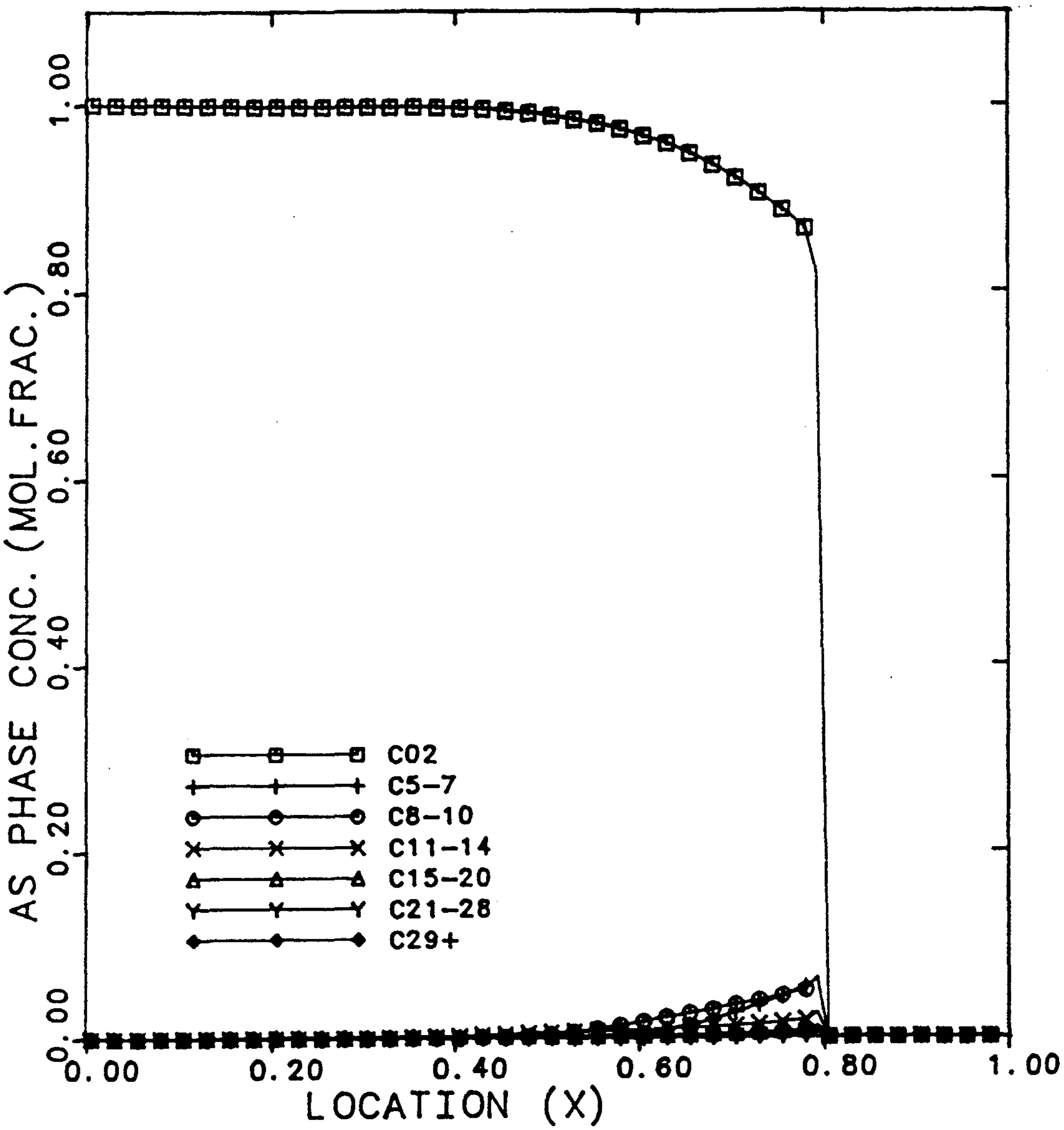

Figure 5.26 Overall Composition Profile for Maljamar Separator Oil at 0.8081 Pore Volumes CO2 Injected (7 components)

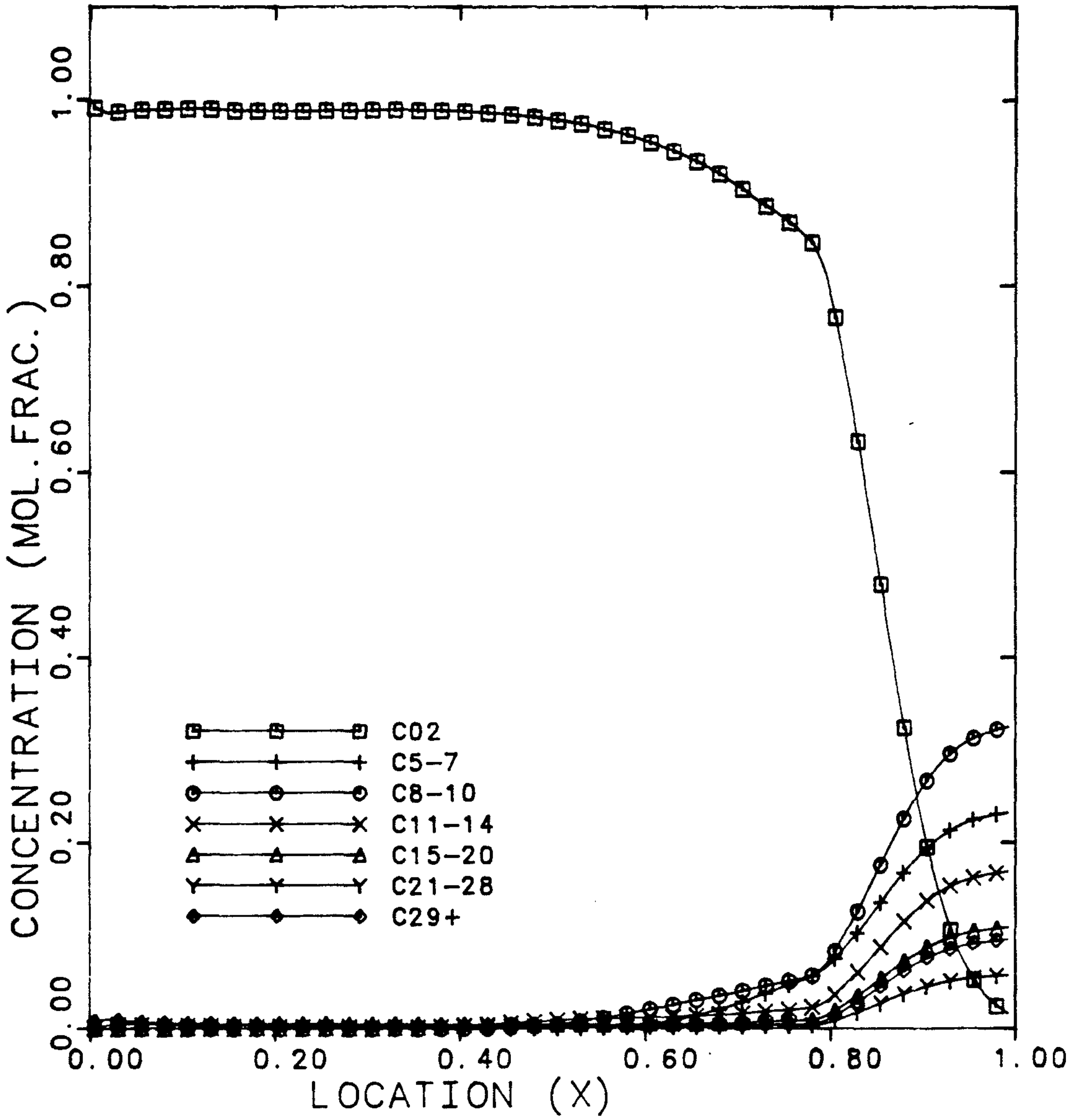

Figure 5.27 Density Profile for Maljamar Separator Oil at 0.8081 Pore Volumes CO2 Injected (7 components)

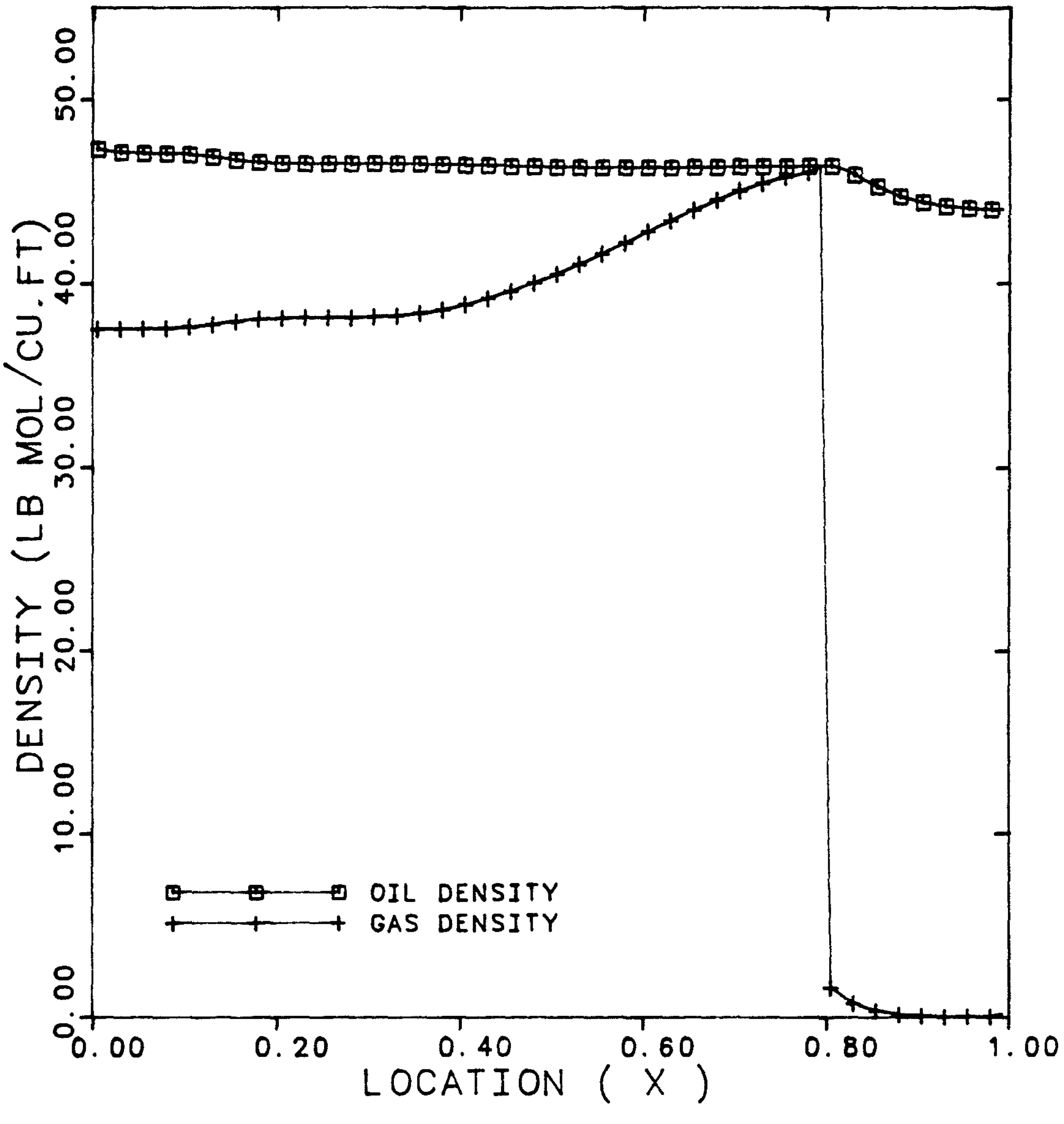

Figure 5.28 Density Profiles at Different Times (0.17, 0.34, 0.51, 0.68, & 0.85 Pore Volumes CO2 Injected) (7 components)

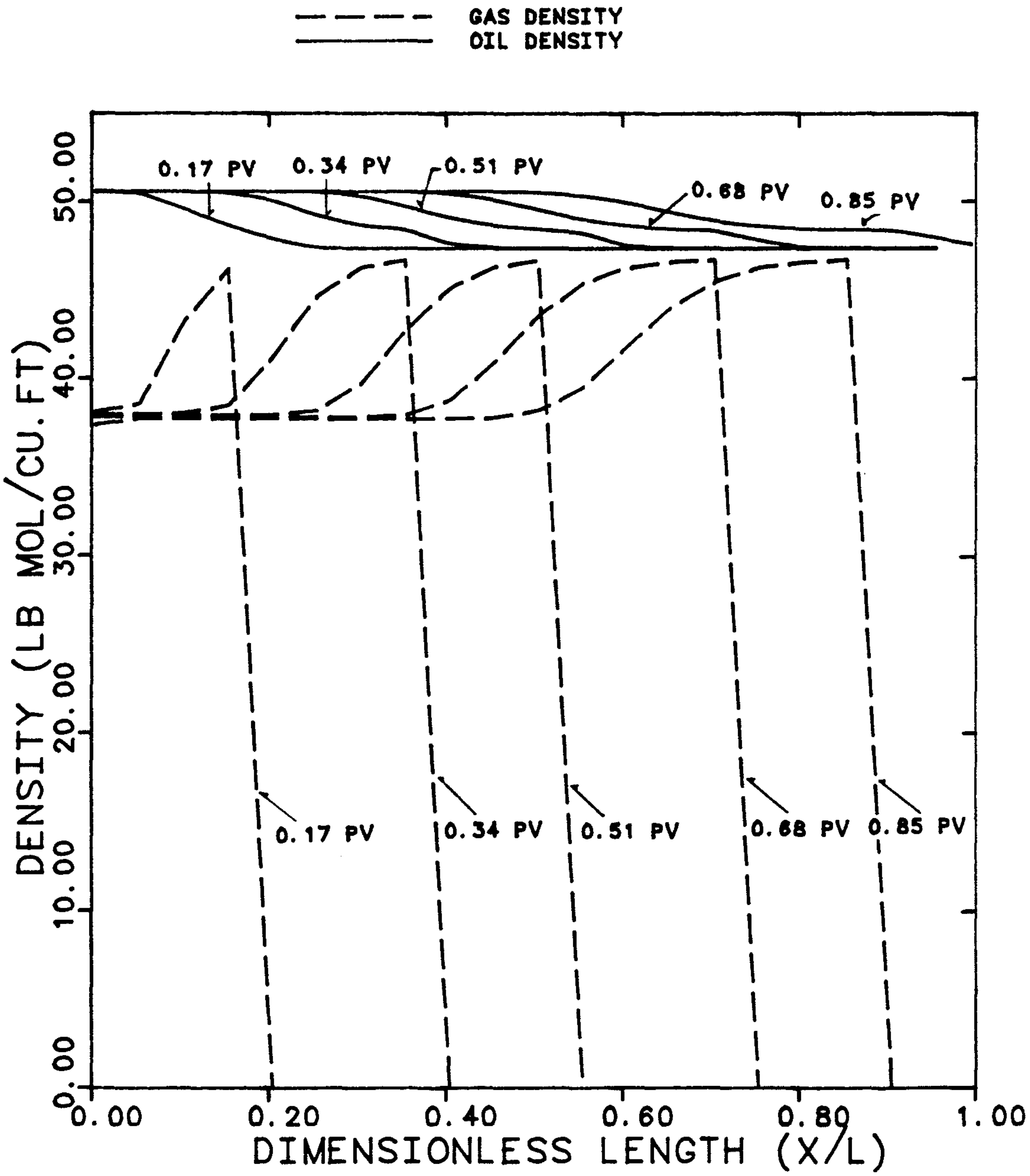

Figure 5.29 Recovery Curve for Maljamar Separator Oil at 800 psia

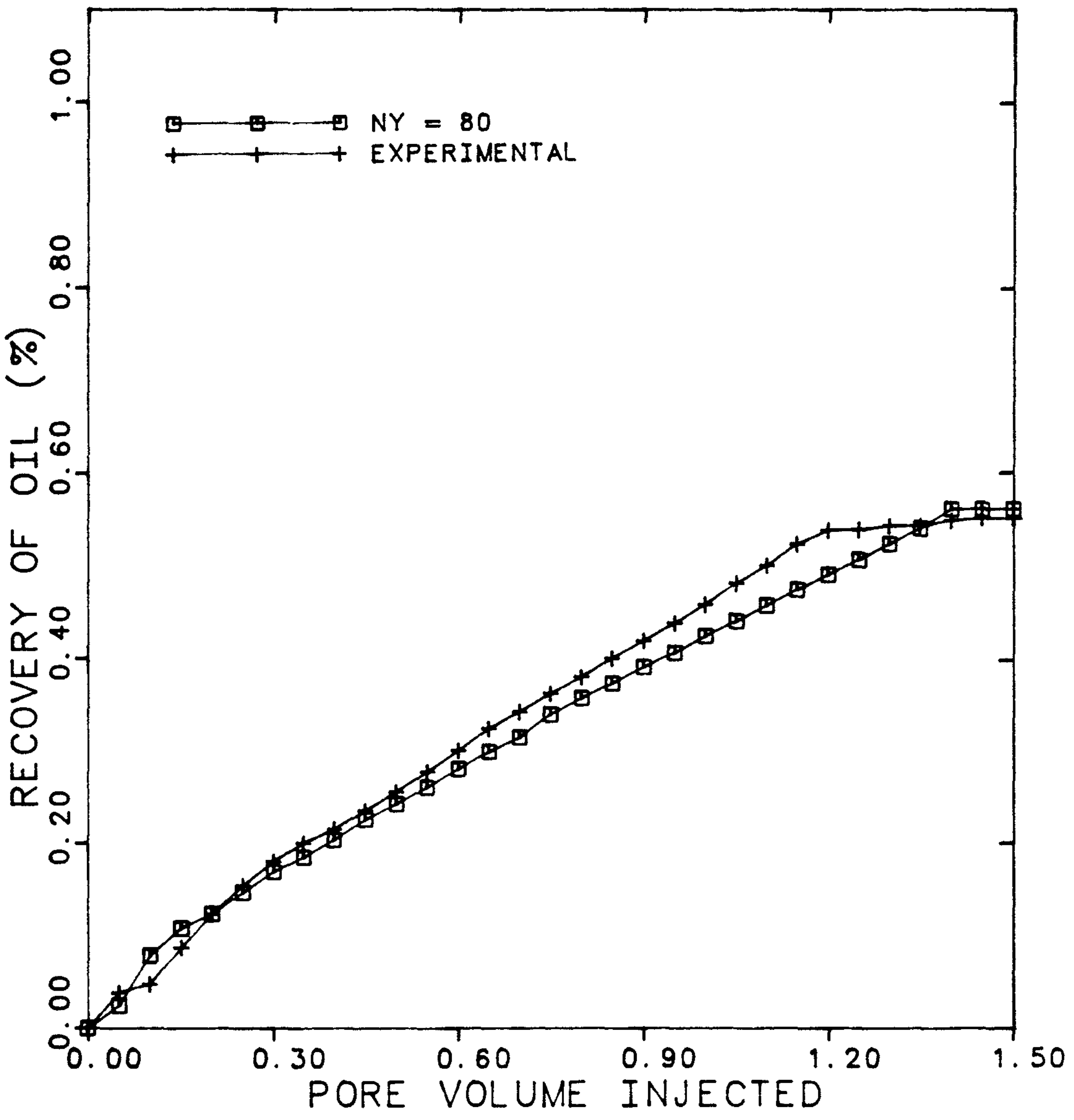

Figure 5.30 Oil Saturation Profiles for Maljamar Separator Oil at Different Times (0.34, 0.68, 0.86, 1.20, & 1.38 Pore Volumes CO2 Injected) (7 components and 800 psia)

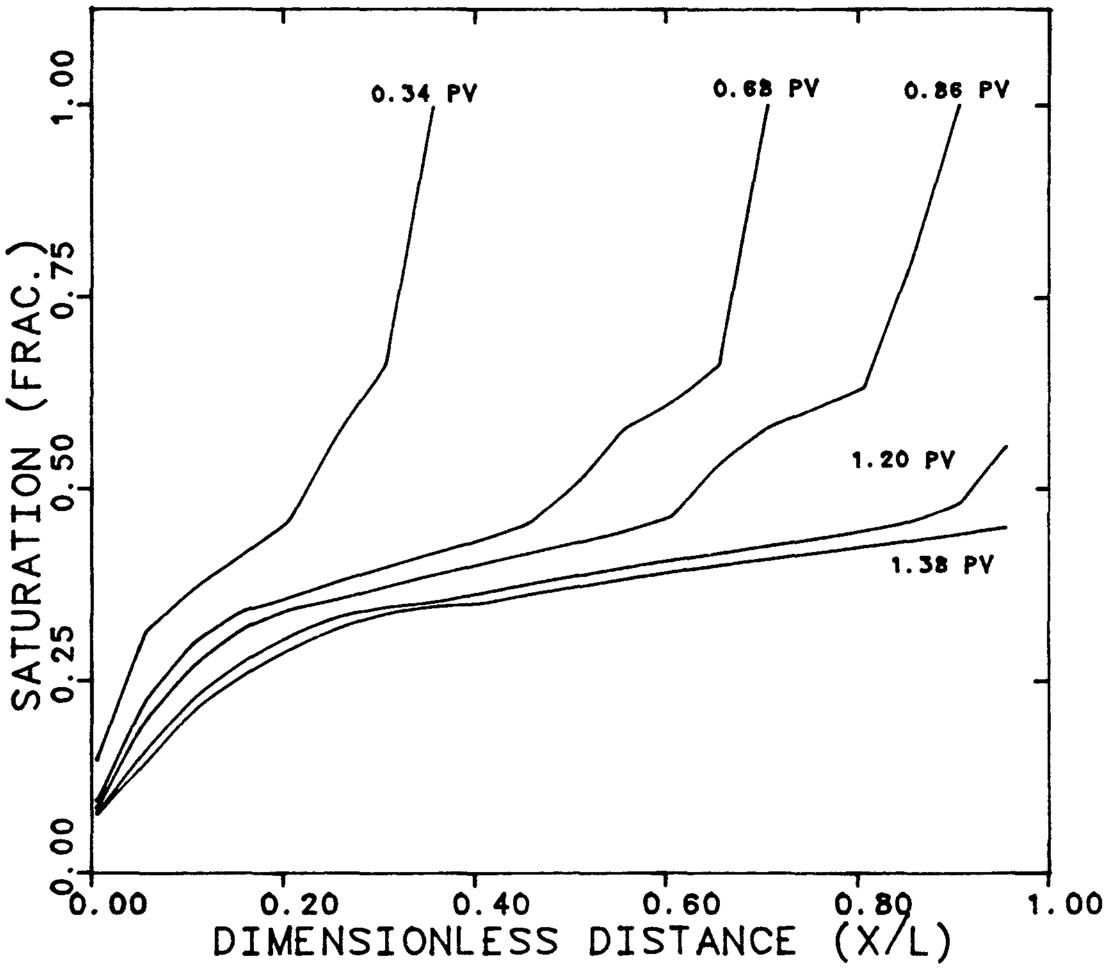

Figure 5.31 Density Profiles for Maljamar Separator Oil at 0.68 Pore Volume CO2 Injected (7 components and 800 psia)

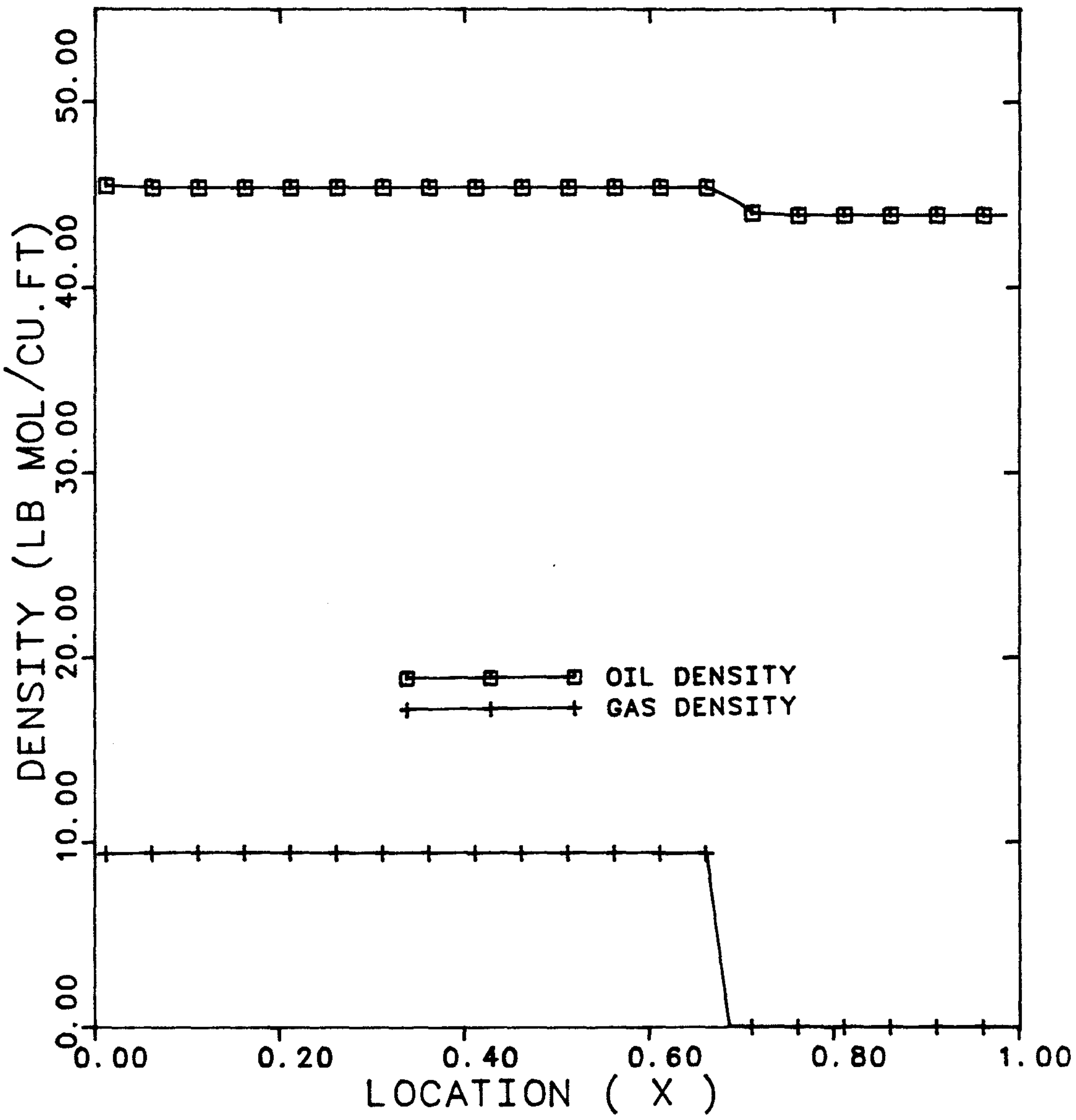

Figure 5.32 Oil Saturation Profiles for Maljamar Separator Oil at Different Times (0.17, 0.34, 0.51, 0.68, & 0.85 Pore Volumes CO2 Injected)
(7 components and 1200 psia)

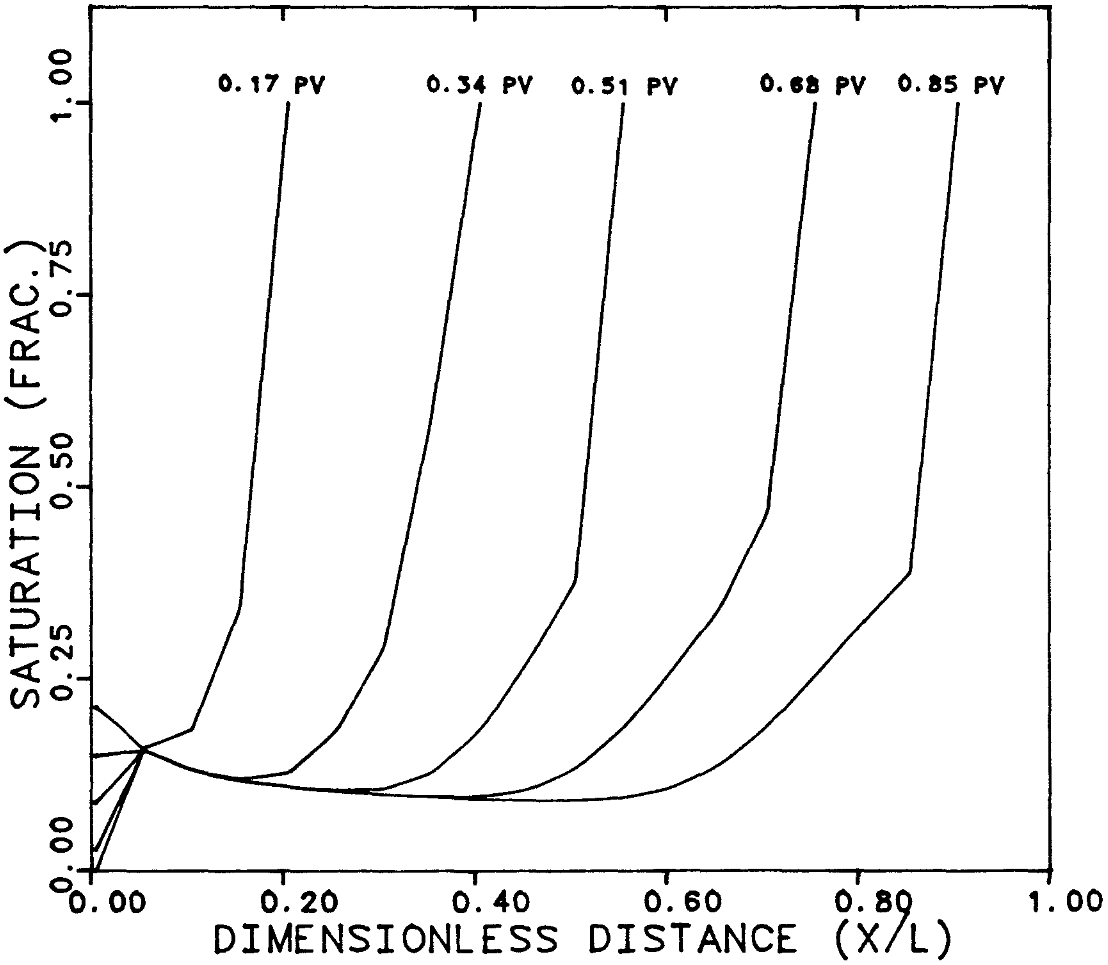

Chapter 6 Simulation of Typical West Texas Reservoir Recombine Fluid Case

6.1 Input Data Review

In the previous chapter, slim-tube displacements were simulated. For slim-tube displacements, fluid flow is stable and dispersion is very low, so oil displacement should be mainly dependent upon phase behavior.

Core tests have two advantages over slim-tubes, even though it is recognized that dispersion and instabilities may affect their performance. Core tests can be more representative of the reservoir process and they provide an opportunity to collect effluent samples from which compositions, densities and viscosities can be determined.

Kremesec and Sebastian [K2] conducted CO_2 displacements of three different reservoir oils from long Berea cores with the pressures always above the slim tube minimum miscibility pressure. They used a fully compositional simulator and the Redlich-Kwong equation of state (RK EOS) to simulate the detailed performance of the displacement.

A fairly good agreement between experimental oil recovery and GOR results and simulations were obtained and also good qualitative simulation of the phase behavior of the effluent and of the overall shape of the component separation of the effluent profiles were obtained. Their simulation assumed a stable one-dimensional displacement and phase behavior effects play the primary role in the displacement, and the number of grid blocks needs to be adjusted to mimic physical dispersion.

In this chapter, one of the reservoir oils which Kremsec and Sebastian used in their study was selected for simulation. A Typical oil from the San Andres formation in West Texas was named Oil-A in their study. This oil is from a reservoir with a low temperature (105°F), has a relatively high viscosity (3cp), and regions of liquid-liquid and liquid-liquid-vapor immiscibility in addition to a region of vapor-liquid immiscibility on first contact with CO_2.

The RK EOS parameter set for this oil reported by Kremesec and Sebastian is given in Table 6-1. Slightly different oil compositions were used in the phase equilibria studies and the oil displacement studies (both are shown in the table). The major differences between these oils are the bubble point and base oil GOR. Core displacement tests were carried out to define the efficiency of continuous CO_2 injection in a secondary mode of Test #1 (27% connate water saturation) and Test #2 (no connate water saturation). Core test summary is given in Table 6-2.

The displacement was done at an injection rate of 0.004 moles/day in a Berea core (16 feet long with a diameter of 2 inches). The block area used in the 1-D simulation was 0.0218 ft^2. The gas-oil relative permeability curves are shown in Fig. 6.1. The end points were shifted when connate water was present.

6.2 Phase Behavior Matching of Twelve Component Mixture

The number of components used in this study was twelve compared to twenty-one used by Kremesec and Sebastian. The procedure to determine the hydrocarbon data for this study was as follows:

1. Normal and iso-butane and pentane were combined and represented as one component.
2. Heptane plus (C_7^+) components were computed using Whitson's scheme.
3. Molecular weights, critical values (T_c, P_c, V_c) and acentric factors were taken from Table 6-1. Kay's rule was used to combine component.
4. Critical volume and molecular weight of heptane plus components were adjusted to match the original oil viscosity and density.

Table 6-3 shows this regrouping for Oil-A. The binary interaction coefficients from Kremesec and Sebastian could not be used since they used the RK-EOS whereas the PR EOS is used in this study. Kato et al.'s [K5] correlation of CO_2 binary interaction coefficients was used for obtaining the first trial values. The boiling point and acentric factor for each pseudo component are required. Table 6-4 shows these CO_2 binary interaction coefficients.

The first trial computation of the phase boundary was made using the data from Tables 6-3 and 6-4 (Fig 6.2). The calculated phase boundary increases too quickly above 1400psia. On the same Fig 6.2, the calculated phase boundary by using the RK EOS is shown. Several trials of adjusting the CO_2 binary interaction coefficients are required to get a better match of the phase behavior. The data set given in Table 6-5 gave the best result (Fig. 6.2). The CO_2 binary interaction coefficients were selected to increase with increasing molecular weight.

A better calculated oil recovery can be expected for the final trial compared to the first trial since its single phase region is larger.

Simulation of the core displacement at without connate water saturation (Test #2) was conducted for both these cases. Fig. 6.3 shows the recovery curves. For both cases, 20 grid blocks were used in the simulation. The experimental oil recovery was 85%. Additional results will be discussed later.

6.3 Simulation of Core Displacement

Effluent samples and production GOR give very important information about the reservoir displacement process. Although breakthrough time can be estimated from the change of the recovery curve, it can be more accurately estimated from the increase in the GOR. The GOR is related to the effluent composition, especially CO_2 concentration.

Production GOR matching and effluent composition profile matching are difficult because they are very sensitive to the phase behavior (that means EOS parameters). In the following section, the sensitive change of production GOR and effluent composition profiles can be seen by using several EOS parameter data sets. Table 6-6 shows four cases of EOS parameter sets, and Figs. 6.4 through 6.7 show the pressure composition diagram for these same four cases. The critical values and acentric factors are the same as shown in Table 6-3 except for CO_2. The binary interaction coefficients between hydrocarbon and hydrocarbon are set to zero in all cases.

In the Case-A, all CO_2 binary interaction coefficients were set to 0.12.

In the Case-B, the binary interaction coefficients increase with molecular weight except for the heaviest hydrocarbon component.

In the Case-C, the critical values of CO_2 were adjusted and the CO_2 binary interaction coefficients were all 0.13.

In the Case-D, the critical values of CO_2 were adjusted and the binary interaction coefficients varied.

The adjustment of the critical values of CO_2 will be discussed in the next chapter. In this section, only the results of influence by the EOS parameter are discussed. The simulations of the core displacement at 27% connate water saturation (Test #1) were performed by using the above four data sets. Figs. 6.8 through 6.11 show these simulation results.

The number of grid blocks was varied from 20 to 80 for Case-A of Fig. 6.8, and the recovery increases with increasing number of grid blocks. The simulated GOR curves show quite a different shape than the experimental results. The simulated GOR curves increase too rapidly, especially for the larger number of grid blocks.

In Case-B (Fig. 6.9), 20 grid blocks gave a fairly good match of the recovery curve, but the simulated GOR increases too rapidly starting at 0.75 pore volumes CO_2 injected, although it is better than that of Case-A. Twenty grid blocks gave a better match than 40 grid blocks.

Case-C (Fig. 6.10) shows quite different results for both oil recovery and GOR. The slope of the calculated recovery curve before breakthrough is steeper than that of the experiment, and breakthrough occurred earlier than that of the experiment. The GOR curve goes up suddenly after breakthrough and reaches a very high GOR.

Case-D (Fig. 6.11) shows the best match of these cases. Both the recovery curve and the GOR curve using 40 grid blocks show better agreement with experiment than those using 20 grid blocks.

From comparisons of these four cases, the following observations can be made:

1. Identical values of CO_2 binary interaction coefficients for all CO_2-Hydrocarbon combinations may enlarge the gap in the production GOR curve.
2. Adjustment of the CO_2 critical values affects both recovery and GOR very much.
3. The number of grid blocks which gives the best match depends on the phase behavior. In this study, the data-set of Case-D gives the best match of both the pressure-composition diagram and the core displacement where 40 grid blocks is used.

Simulation of the core displacement without connate water saturation (Test #2) was done next. Since no experimental oil recovery and GOR history of Test #2 were reported by Kremesec and Sebastian, only simulated recovery and GOR are shown in Figure 6.12. Forty grid blocks were used for each case. As discribed by Kremesec and Sebastian, about 5% smaller oil recovery can be obtained in this case than that with connate water. Effluent composition profiles are shown in

Figs. 6.13 through 6.16. In each figure, the value of calculated and experimental concentration divided by initial concentration (C/CO) for methane and heptane plus (C_7^+) and injection concentration for CO_2 are plotted. Figures 6.13 and 6.15 show the results for Case-A and Case-C, respectively. There are differences in the slope of each hydrocarbon curve and in the cross-over point of CO_2 and methane or C_7^+ between the simulation results and the experiment. Case-A shows a methane bank after CO_2 breakthrough. The C/CO value of C_7^+ increases for a while and after that keeps almost same level. GOR curve of Fig. 6.8 reflects this phenomena, that is the rate of increasing GOR is decreasing after break-through even if the flat level of GOR can be seen in the 80 grid blocks. Rapid change of CO_2 and C_7^+ in Figures 6.13 and 6.14 cause sudden change of GOR as shown in Fig. 6.8 of Case-A and Fig. 6.10 of Case-C. After rapid change of C_7^+, the composition profile of C_7^+ still decreases gradually and this causes continuous increase of GOR.

Case-B (Fig. 6.14) shows fairly good outlook, but the cross over point of CO_2 and methane or C_7^+ is about 0.15 pore volumes earlier than that of the experiment. Case-D (Fig. 6.16) shows the best match of the effluent composition profile. Both the slope of each component and the cross-over points agree better with the experiment.

Discrepancies between simulated and experimental compositions after breakthrough cause the difference between the simulated and experiment GOR.

The predicted and experimental effluent density and viscosity profiles of Test #2 are compared in Figs. 6.17 and 6.18. The experimental density and viscosity were measured under the reservoir conditions, on the other hand the effluent density and viscosity at the producer (very last block from the injector) were calculated using

Case-D data. In both figures the properties of CO_2-rich phase and CO_2-lean phase are calculated and plotted. Some Discrepancies exist in both density and viscosity of effluent profiles, but the overall trend was predicted.

From the above study the following summary and discussion can be made. Although the small discrepancies exist between the simulation of this study and the experiments, a fairly good agreement canbe obtained by tuning the EOS parameters. Oil recovery is perfectly matched and other profiles also agree with the experiments using Case-D data set. Figure 6.19 shows the comparison of the calculated GOR of Test #1 by Kremesec and Sebastian and that of Case-D. The experimental GOR also plotted on this figure. The simulated GOR curve of Kremesec and Sebastian is much closer to the experimental data than that of this study. This difference is probably caused by the difference in the number of pseudo components used (this also leads to the difference of the EOS parameters).

Kremesec and Sebastian conducted CO_2 displacements of four different reservoir oils from the Berea cores. They showed the effect of viscosity ratio on CO_2 breakthrough time and final oil saturation (Figs. 6.20 and 6.21). These figures indicate an earlier oil breakthrough time and higher final oil saturation for oil A compared to other types of oil used. The probable reason for this is the high oil A to CO_2 viscosity ratio of about 50 which may lead to viscous instability. Other physical phenomena that should be considered are physical dispersion and gravity force. Therefore, a 2-D cross-sectional simulation run is required to match the results of these experiments. This approach will be discussed in the next chapter.

Table 6-1

Redlich-Kwong Parameter Set and Oil Compositions for Oil A

Component	Molecular Weight	Critical Tc (°R)	Properties Pc (psia)	Vc (ft^3/lbmde)	Acentric Factor	Mole Fraction Phase Studies	Displacement Studies
CO_2	44.01	547.49	1073.00	1.51	0.23	0.0000	0.0110
CH_4	16.04	343.91	673.10	1.59	0.01	0.1524	0.1087
C_2H_6	30.06	550.01	709.80	2.37	0.10	0.0369	0.0366
H_2S	34.08	672.39	1306.00	1.56	0.10	0.0000	0.0010
C_3H_8	44.09	665.95	617.40	3.21	0.15	0.0466	0.0435
i-C_4	58.12	734.65	529.10	4.21	0.18	0.0000	0.0116
n-C_4	58.12	765.31	550.90	4.08	0.20	0.0389	0.0436
i-C_5	72.14	828.69	483.00	4.90	0.22	0.0149	0.0182
n-C_5	72.14	845.19	489.50	4.73	0.25	0.0180	0.0273
n-C_6	86.17	913.79	440.00	5.93	0.30	0.0237	0.0277
P1	100.20	969.67	432.00	6.56	0.34	0.0705	0.0707
P2	114.23	1021.85	391.92	7.49	0.39	0.0749	0.0752
P3	128.26	1073.64	359.92	8.43	0.43	0.0677	0.0679
P4	142.29	1117.20	333.34	9.39	0.47	0.0444	0.0446
P5	156.31	1156.46	309.92	10.35	0.51	0.0345	0.0346
P6	170.34	1190.38	287.45	11.34	0.54	0.0297	0.0298
P7	184.37	1224.54	267.78	12.30	0.57	0.0276	0.0277
P8	198.39	1253.77	250.89	13.30	0.61	0.0266	0.0267
P9	219.07	1291.94	229.90	14.80	0.66	0.0496	0.0498
P10	260.03	1360.32	188.89	17.50	0.78	0.0776	0.0778
P11	303.31	1423.60	151.00	20.00	0.90	0.0296	0.0297
P12	331.29	1460.54	135.00	22.40	0.97	0.0261	0.0263
P13	378.31	1520.23	117.00	24.60	1.10	0.0468	0.0469
P14	486.06	1642.12	97.00	33.00	1.40	0.0630	0.0632

Table 6-2

Core Test Summary

Test NO.	Oil	Temp.(F°)	Press.(psia)	Length(ft)	S_{wc}	Mode
Test #1	A	105.0	2000.0	16.0	0.27	Sec.
Test #2	A	105.0	2000.0	16.0	0.00	Sec.

Flow rate ~	1.0 ft/day
Porosity	20.0%
Core diameter	2.0 in

Table 6-3

Twelve Components description of Oil A

Component	Mole Fraction (%)	Molecular Weight	Critical Properties T_c (°R)	P_c (psia)	V_c (ft^3/lbmole)	Acentric Factor
CO_2	0.0	44.01	547.49	1073.00	1.51	0.23
CH_4	0.1524	16.04	343.91	673.10	1.59	0.01
C_2H_6	0.0369	30.06	550.01	709.80	2.37	0.10
C_3H_8	0.0466	44.09	665.95	617.40	3.21	0.15
C_4	0.0389	58.12	758.87	546.32	4.11	0.19
C_5	0.0329	72.14	838.59	486.90	4.80	0.24
C_6	0.0237	86.17	913.79	440.00	5.93	0.30
C_{7A}	0.2131	114.00	1021.00	395.00	9.95	0.39
C_{7B}	0.1362	160.50	1164.80	304.10	15.65	0.51
C_{7C}	0.0762	211.90	1278.60	236.80	19.28	0.63
C_{7D}	0.1333	283.60	1394.10	169.90	27.10	0.88
C_{7E}	0.1098	440.10	1590.20	105.50	37.00	1.20

Table 6-4

CO_2 Binary Interaction

Coefficients (by Kato et al.)

CO_2-C_1	0.109
CO_2-C_2	0.157
CO_2-C_3	0.162
CO_2-C_4	0.165
CO_2-C_5	0.168
CO_2-C_6	0.170
CO_2-C_{7A}	0.172
CO_2-C_{7B}	0.173
CO_2-C_{7C}	0.163
CO_2-C_{7D}	0.138
CO_2-C_{7E}	0.045

Table 6-5

CO_2 Binary Interaction

Coefficients (Phase matching)

CO_2-C_1	0.060
CO_2-C_2	0.081
CO_2-C_3	0.086
CO_2-C_4	0.086
CO_2-C_5	0.096
CO_2-C_6	0.096
CO_2-C_{7A}	0.102
CO_2-C_{7B}	0.108
CO_2-C_{7C}	0.108
CO_2-C_{7D}	0.112
CO_2-C_{7E}	0.106

Table 6-6

Critical Properties and CO_2 Binary Interaction

Coefficients of Four Cases

	Case-A	Case-B	Case-C	Case-D
Pc of CO_2	1073.0	1073.0	1216.0	1144.0
Tc of CO_2	547.5	547.5	574.98	533.0
Binary Interaction Coefficient				
CO_2-C_1	0.12	0.06	0.13	0.04
CO_2-C_2	0.12	0.081	0.13	0.04
CO_2-C_3	0.12	0.086	0.13	0.04
CO_2-C_4	0.12	0.086	0.13	0.08
CO_2-C_5	0.12	0.096	0.13	0.08
CO_2-C_6	0.12	0.096	0.13	0.08
CO_2-C_{7A}	0.12	0.102	0.13	0.10
CO_2-C_{7B}	0.12	0.108	0.13	0.10
CO_2-C_{7C}	0.12	0.108	0.13	0.10
CO_2-C_{7D}	0.12	0.112	0.13	0.10
CO_2-C_{7E}	0.12	0.106	0.13	0.12

Note: Critical values and acentric factors except for CO_2 are same as those shown in Table 6-3.

Binary interaction coefficients except those of hydrocarbon CO_2 interaction coefficients are set to zero.

Fig 6.1 Gas/Oil Relative Permeability Curves

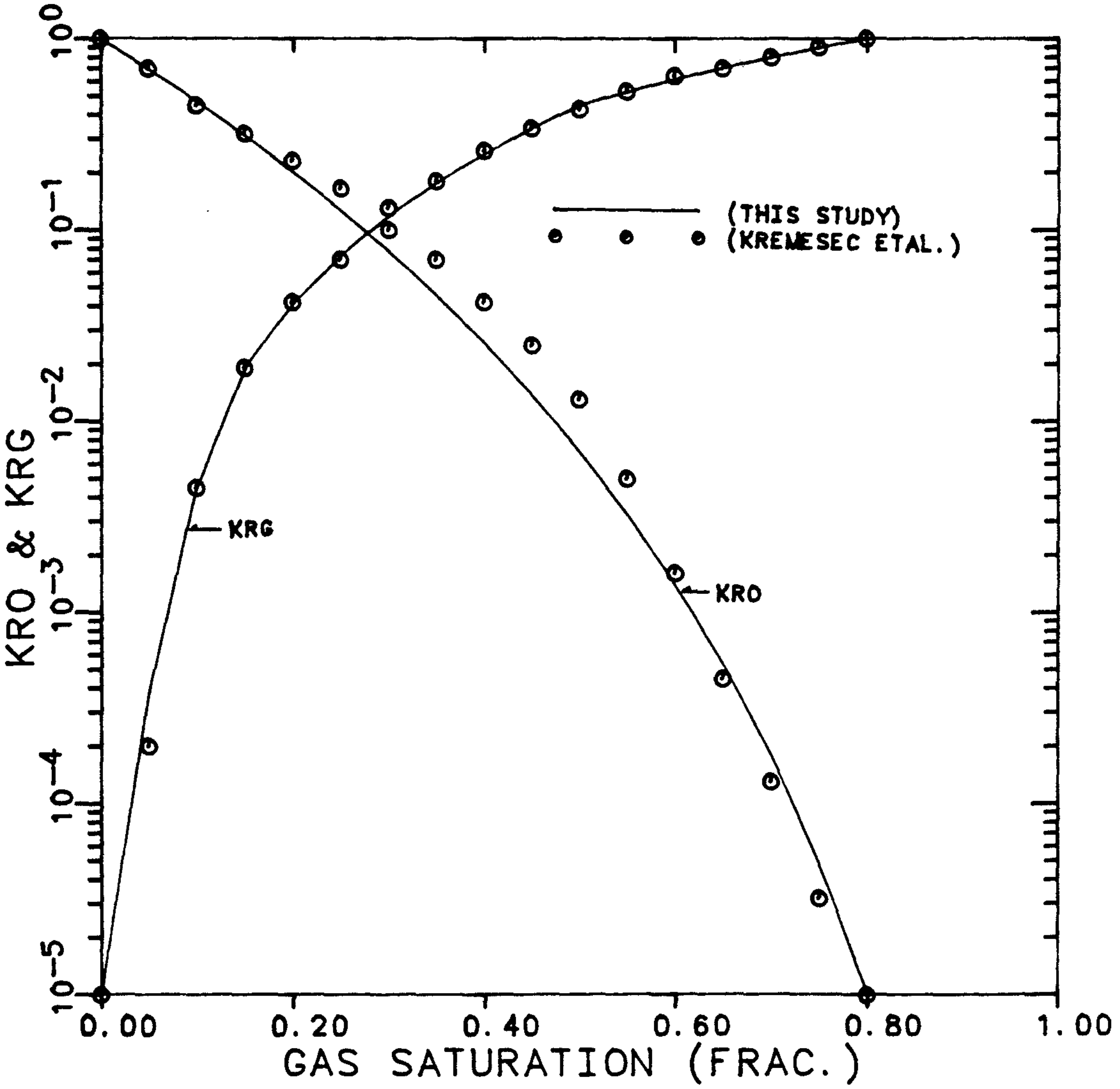

Figure 6.2 Comparison of Calculated and Experimental Phase Behavior for Oil-A and CO2 Mixtures at 105 °F

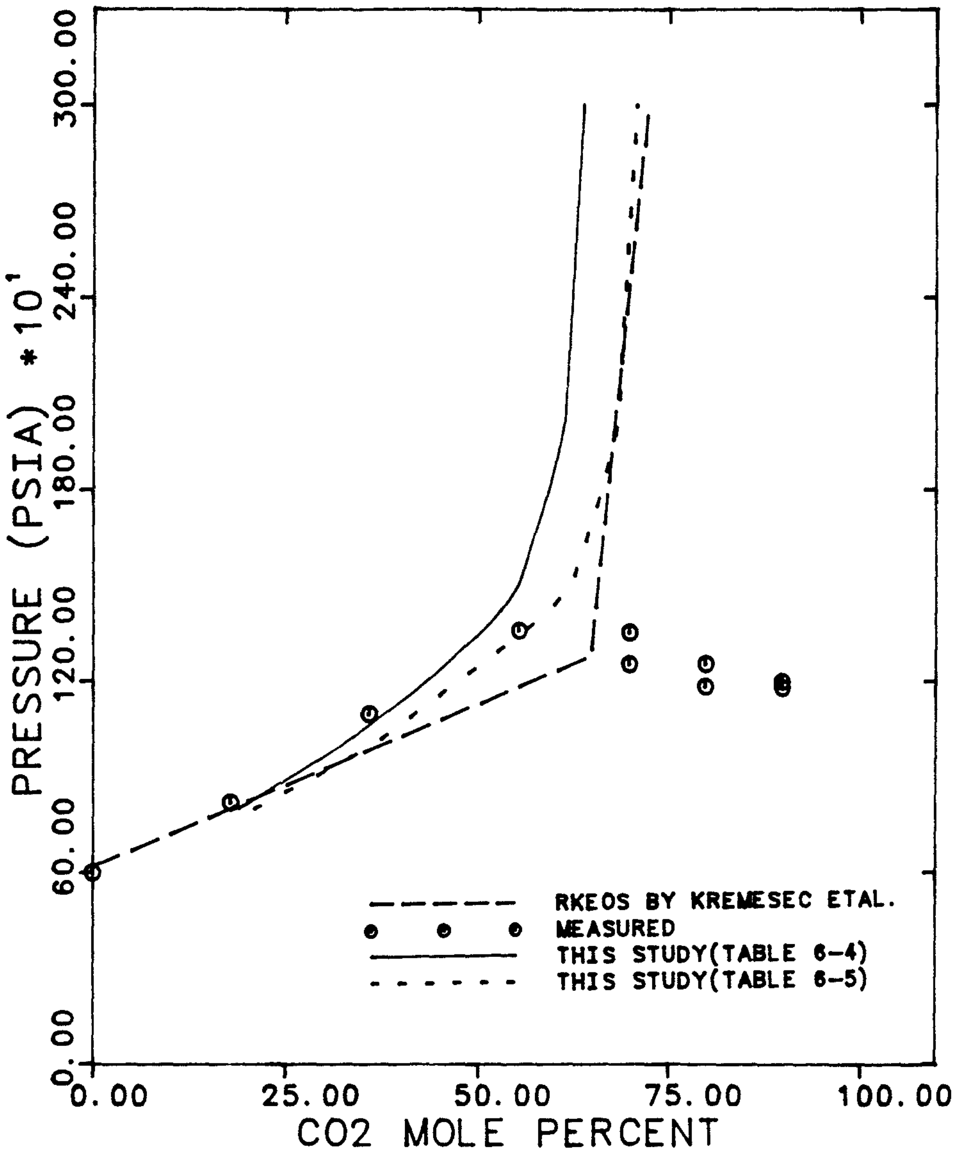

Figure 6.3 Composition of Calculated Oil Recoveries of Test #2 using 2 Different Data-sets of Binary - Interaction Coefficients

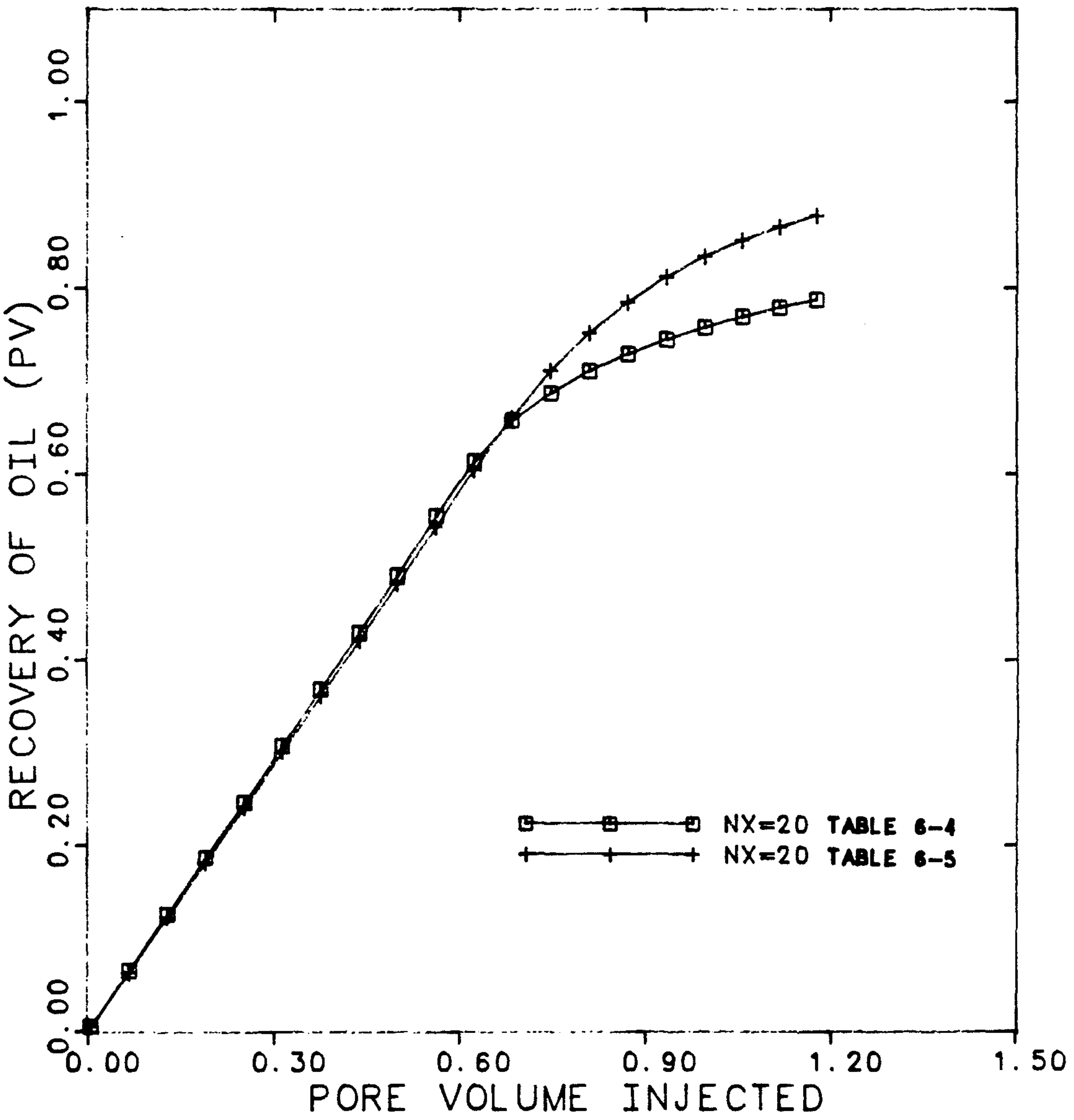

Figure 6.4 Comparison of Calculated and Experimental Phase Behavior using Data-set of Case A at 105 °F

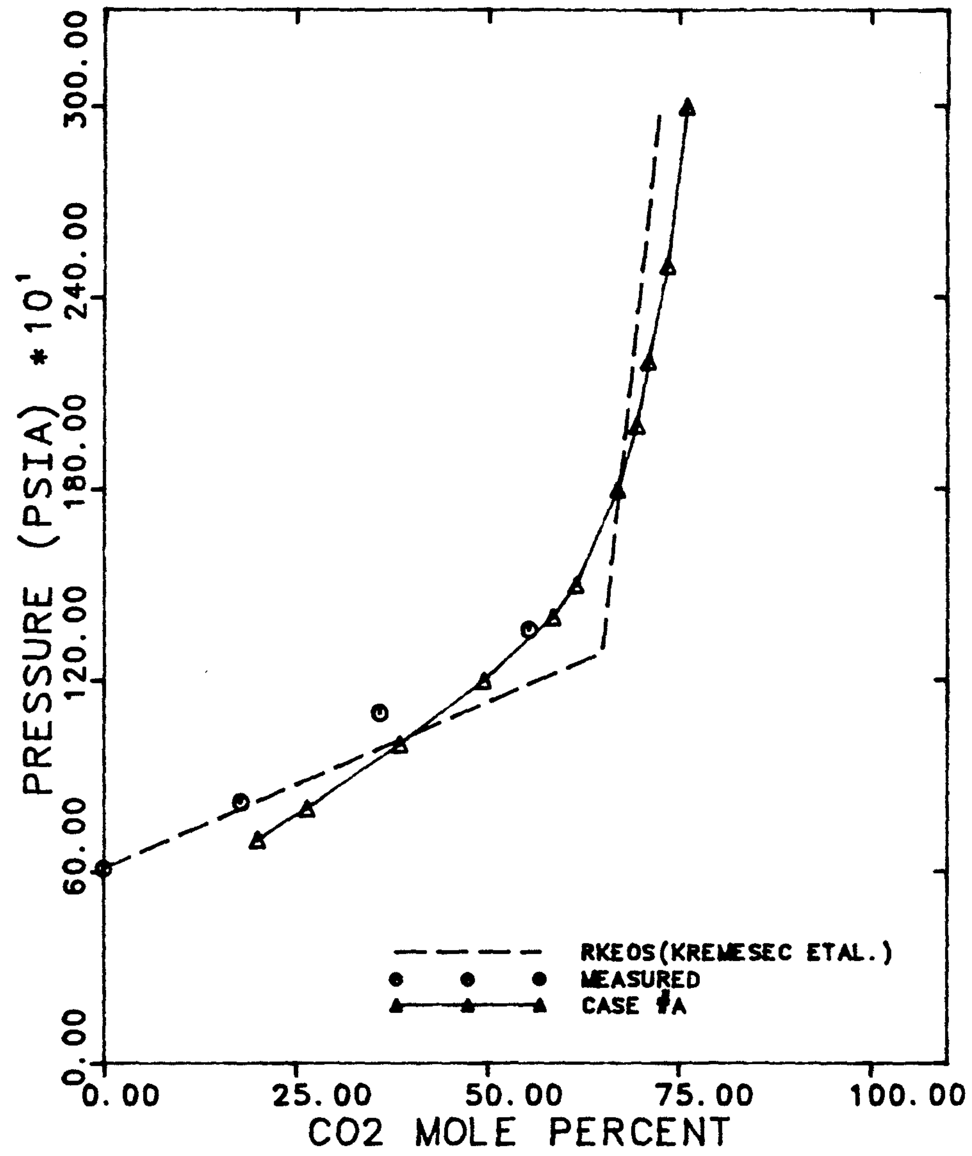

Figure 6.5 Comparison of Calculated and Experimental Phase Behavior using Data-set of Case B at 105 °F

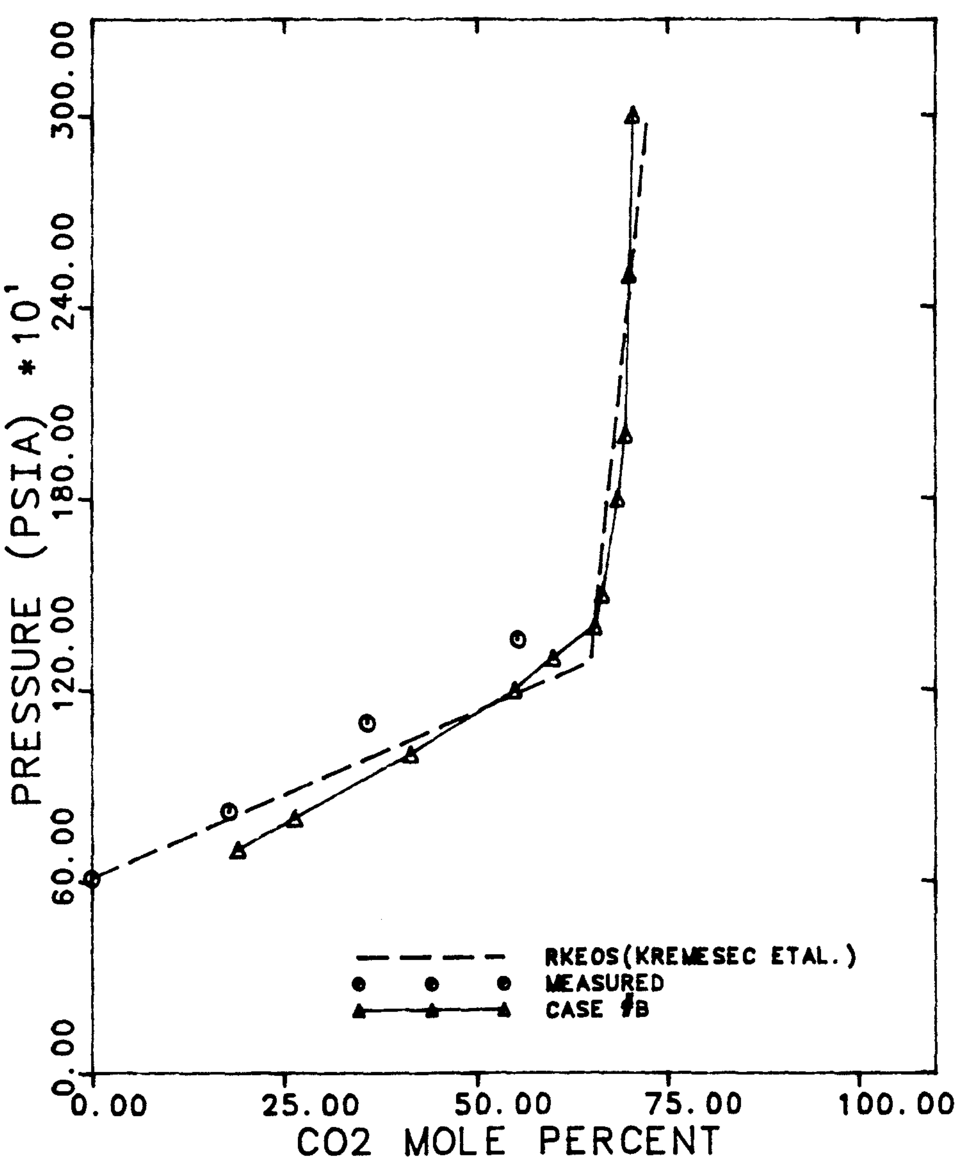

Figure 6.6 Comparison of Calculated and Experimental Phase Behavior using Data-set of Case C at 105 ° F

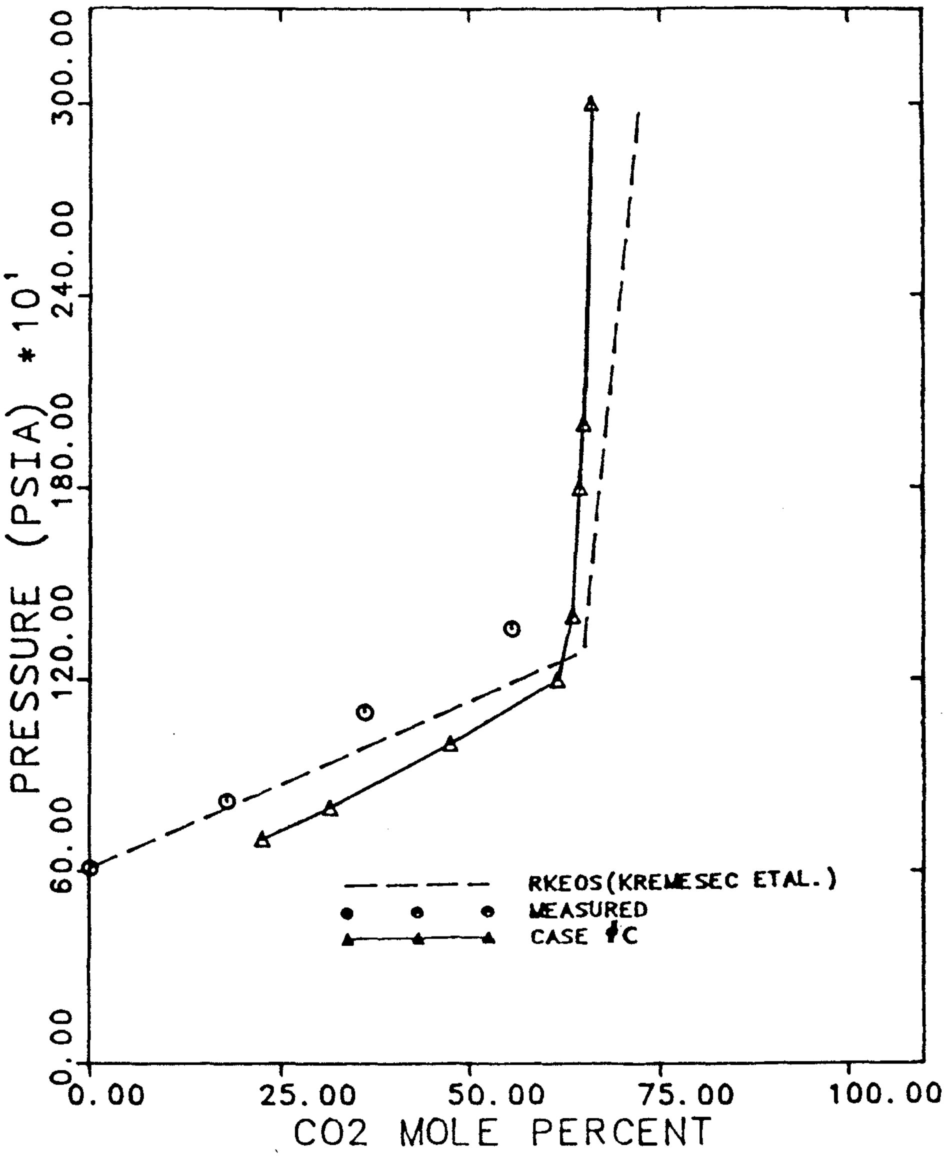

Figure 6.7 Comparison of Calculated and Experimental Phase Behavior using Data-set of Case D at 105 °F

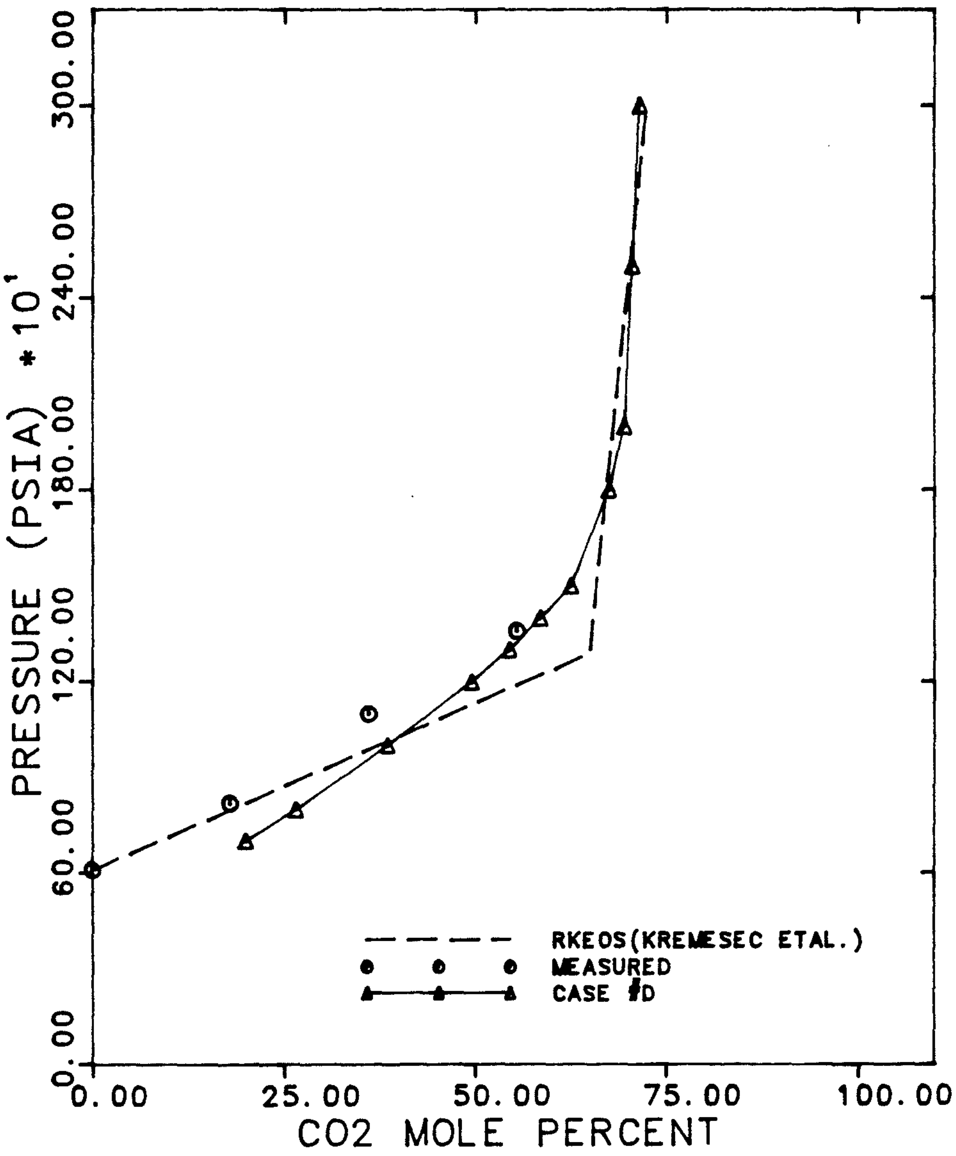

Figure 6.8 Comparison of Case A Simulated Oil recovery and GOR with Core Flood Displacement Test #1

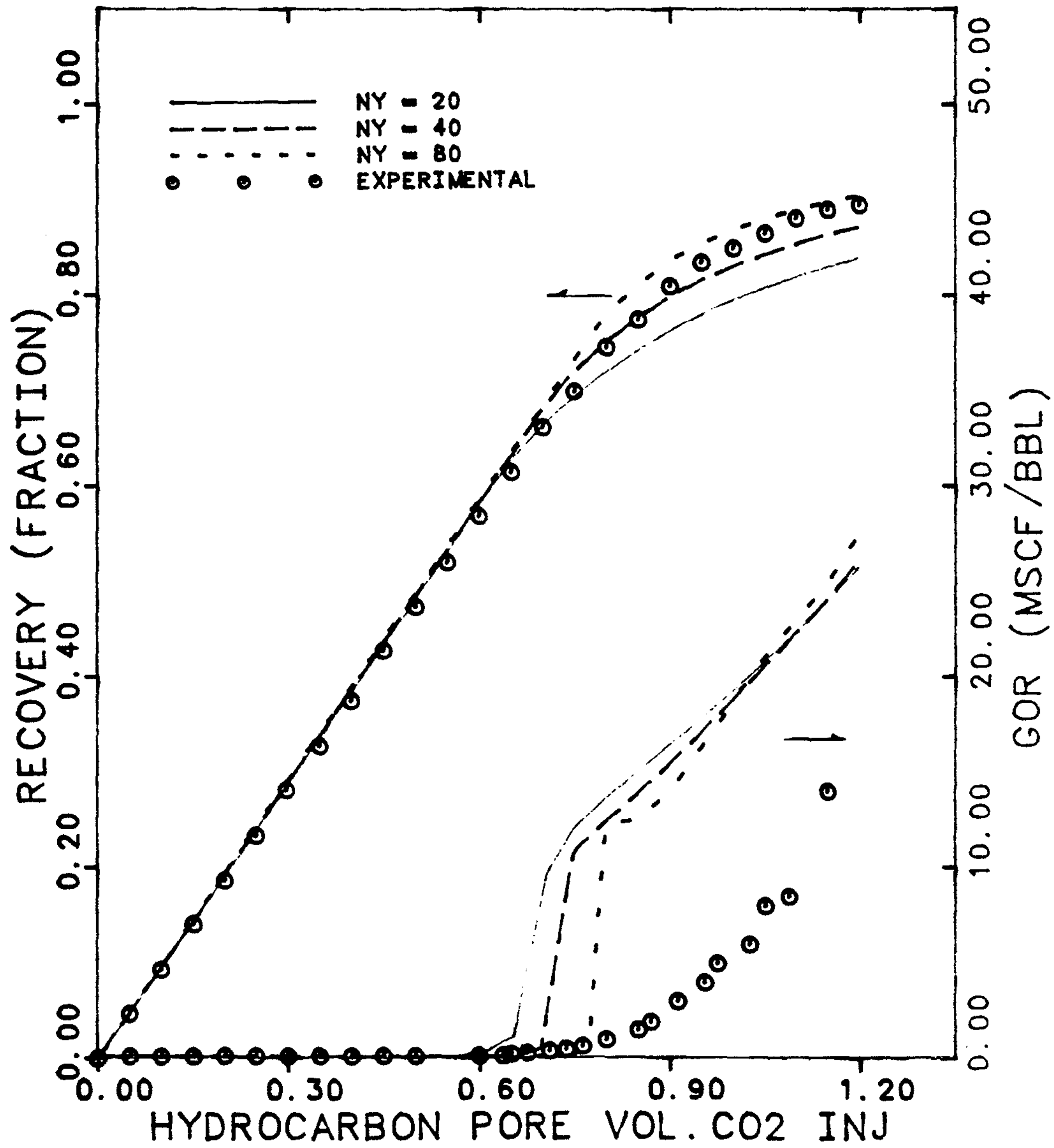

Figure 6.9 Comparison of Case B Simulated Oil recovery and GOR with Core Flood Displacement Test #1

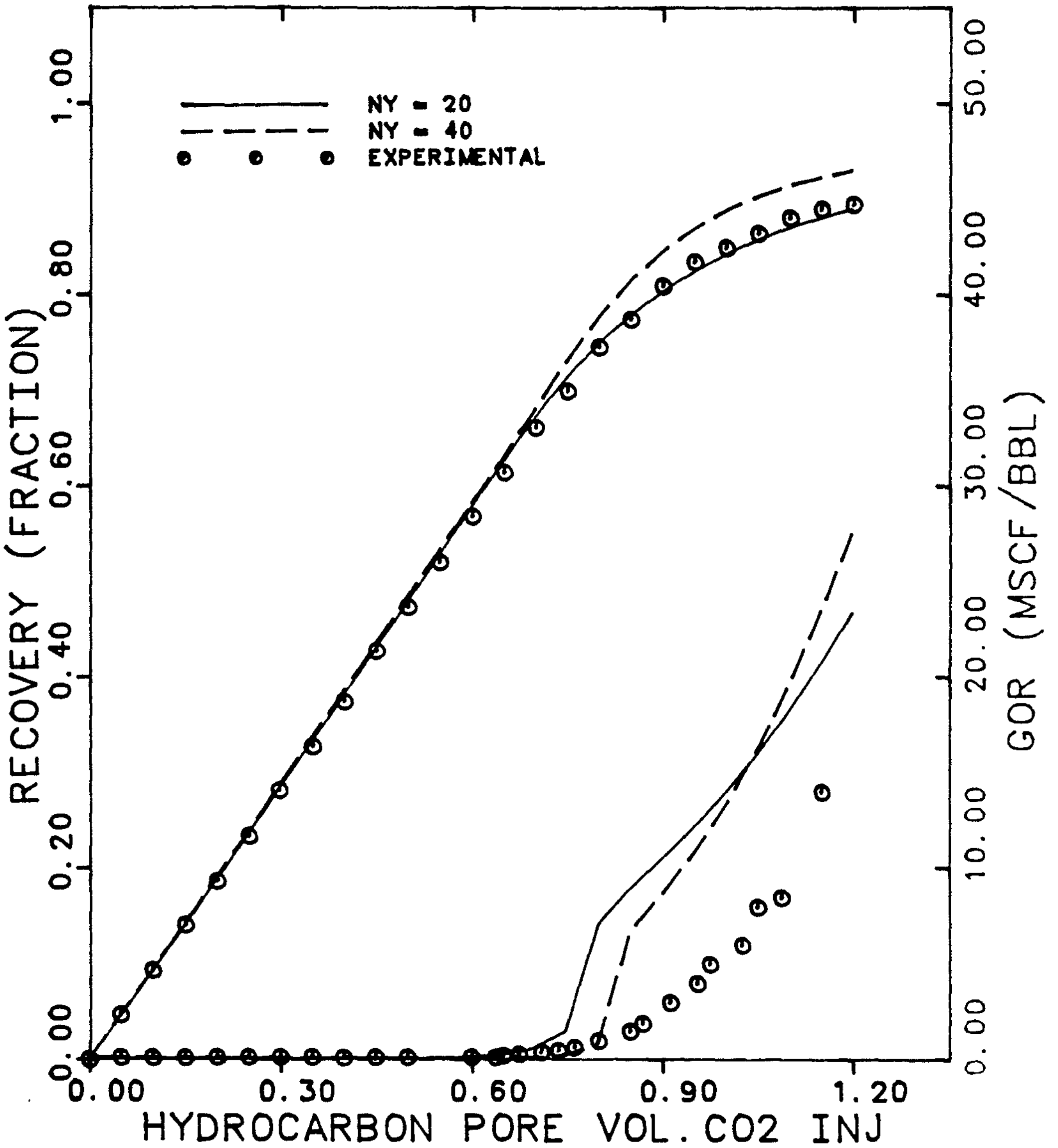

Figure 6.10 Comparison of Case C Simulated Oil recovery and GOR with Core Flood Displacement Test #1

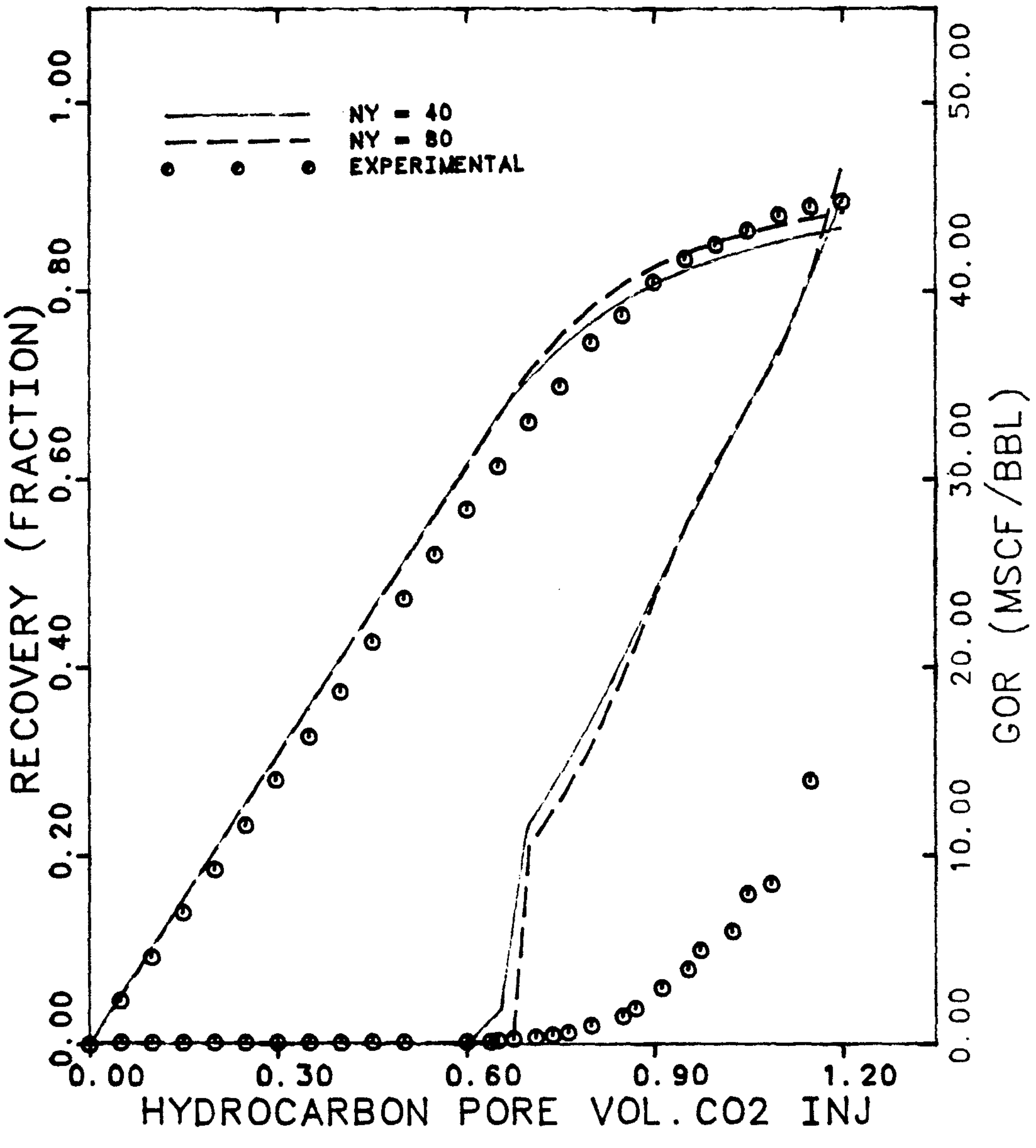

Figure 6.11 Comparison of Case D Simulated Oil recovery and GOR with Core Flood Displacement Test #1

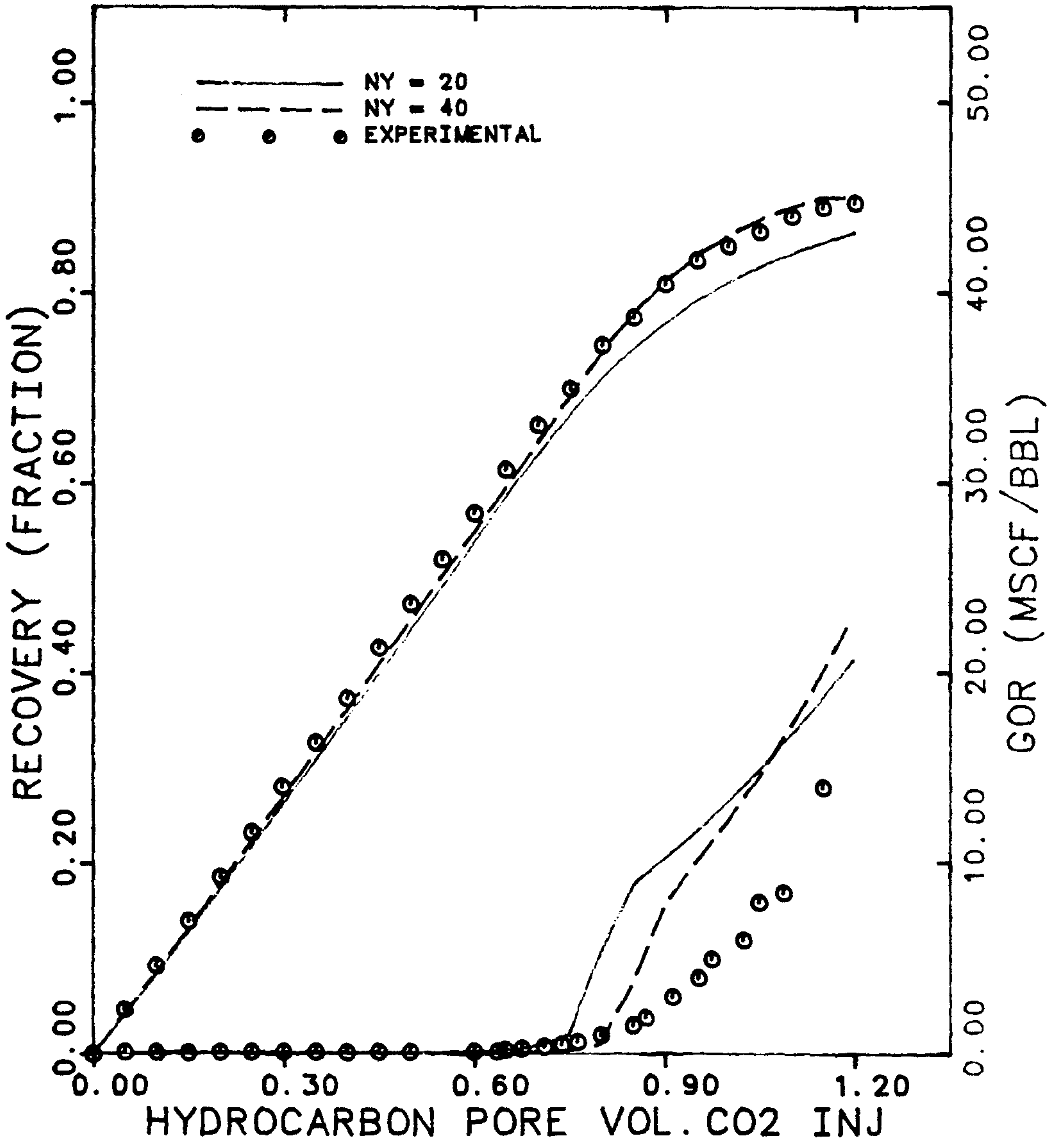

Figure 6.12 Comparison of Calculated Oil Recovery and GOR of Test #2 for different cases

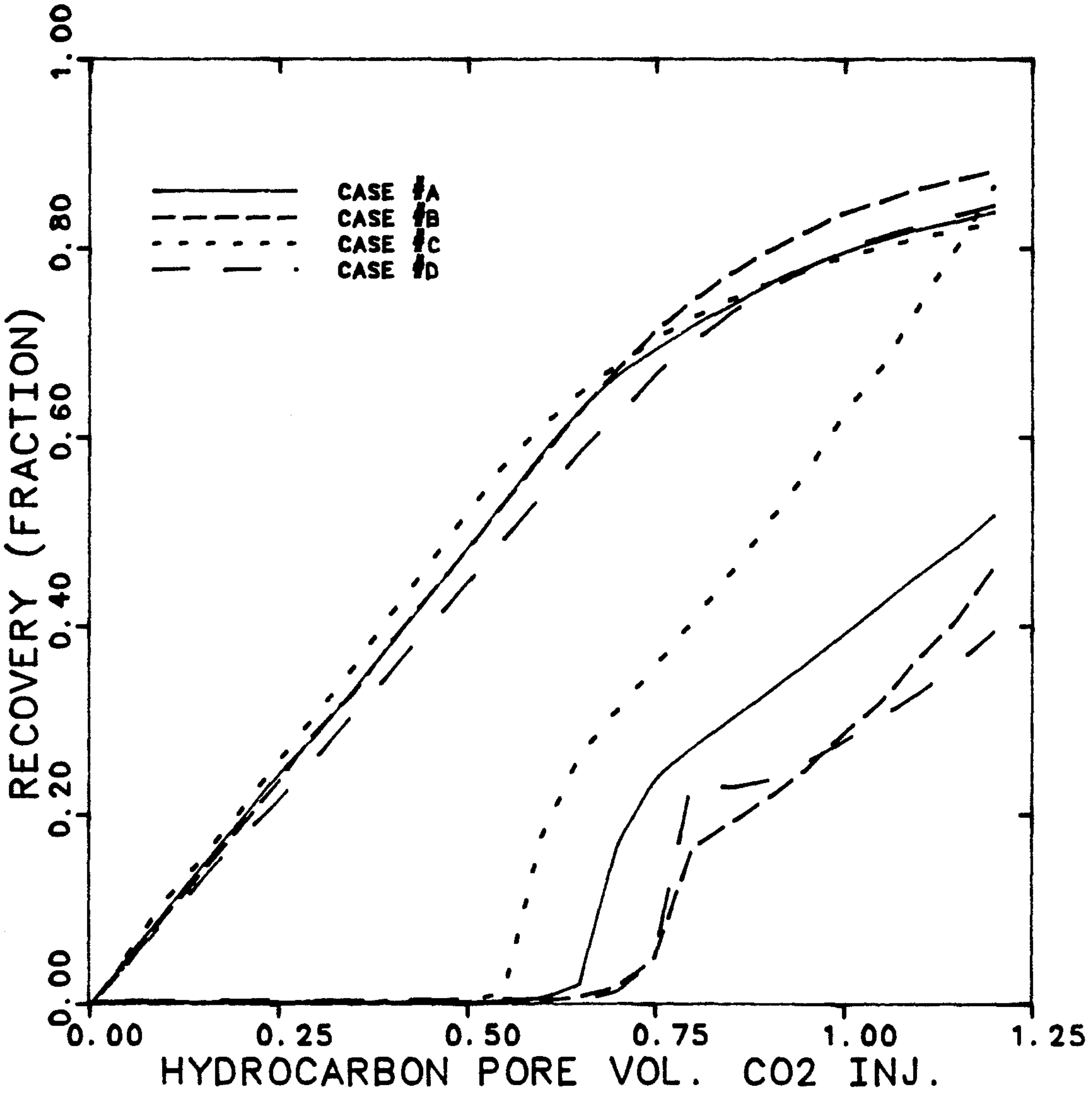

Figure 6.13 Comparison of Effluent compositional Profiles of Oil A , Test #2, Case A

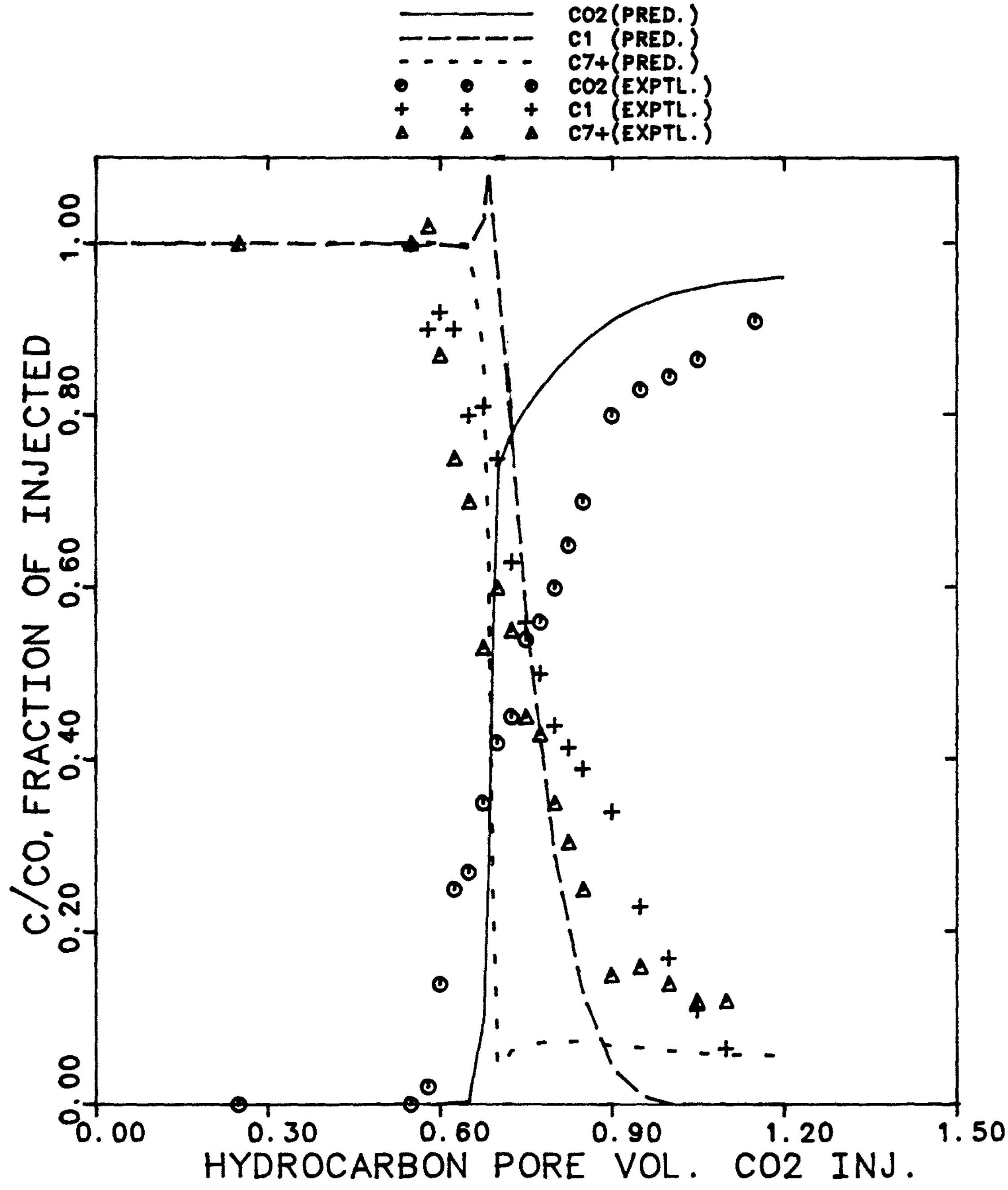

Figure 6.14 Comparison of Effluent compositional Profiles of Oil A , Test #2, Case B

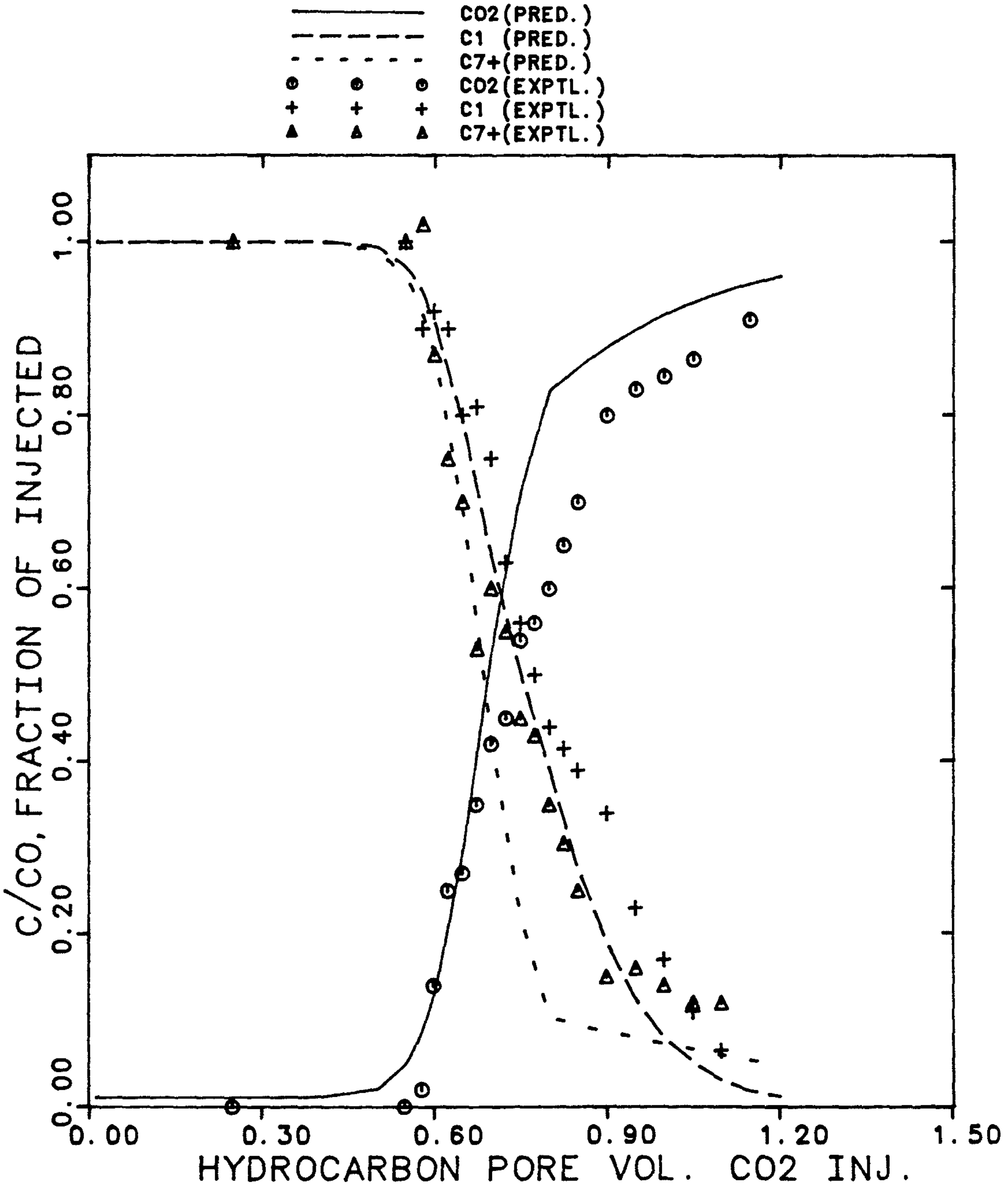

Figure 6.15 Comparison of Effluent compositional Profiles of Oil A, Test #2, Case C

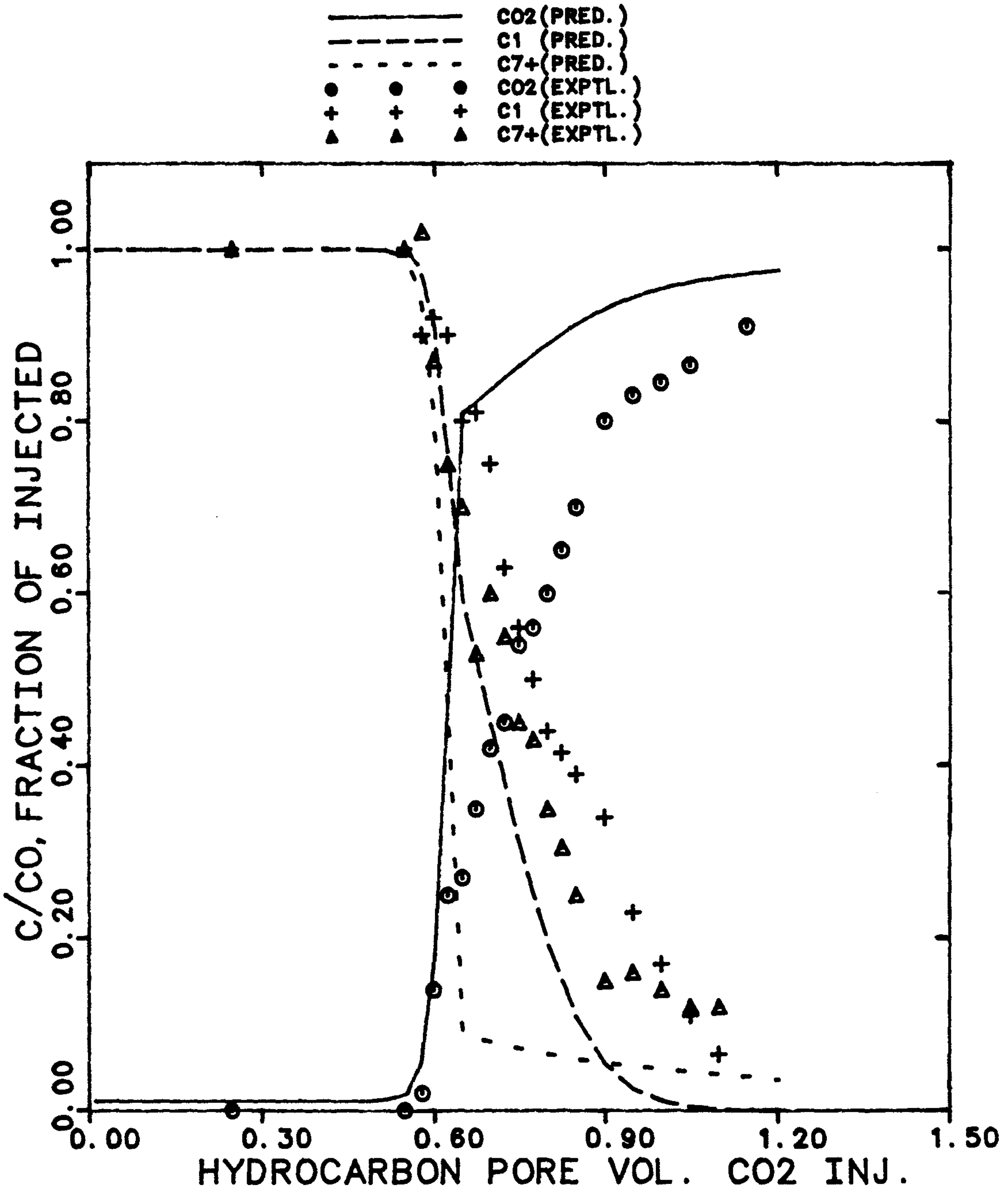

Figure 6.16 Comparison of Effluent compositional Profiles of Oil A , Test #2, Case D

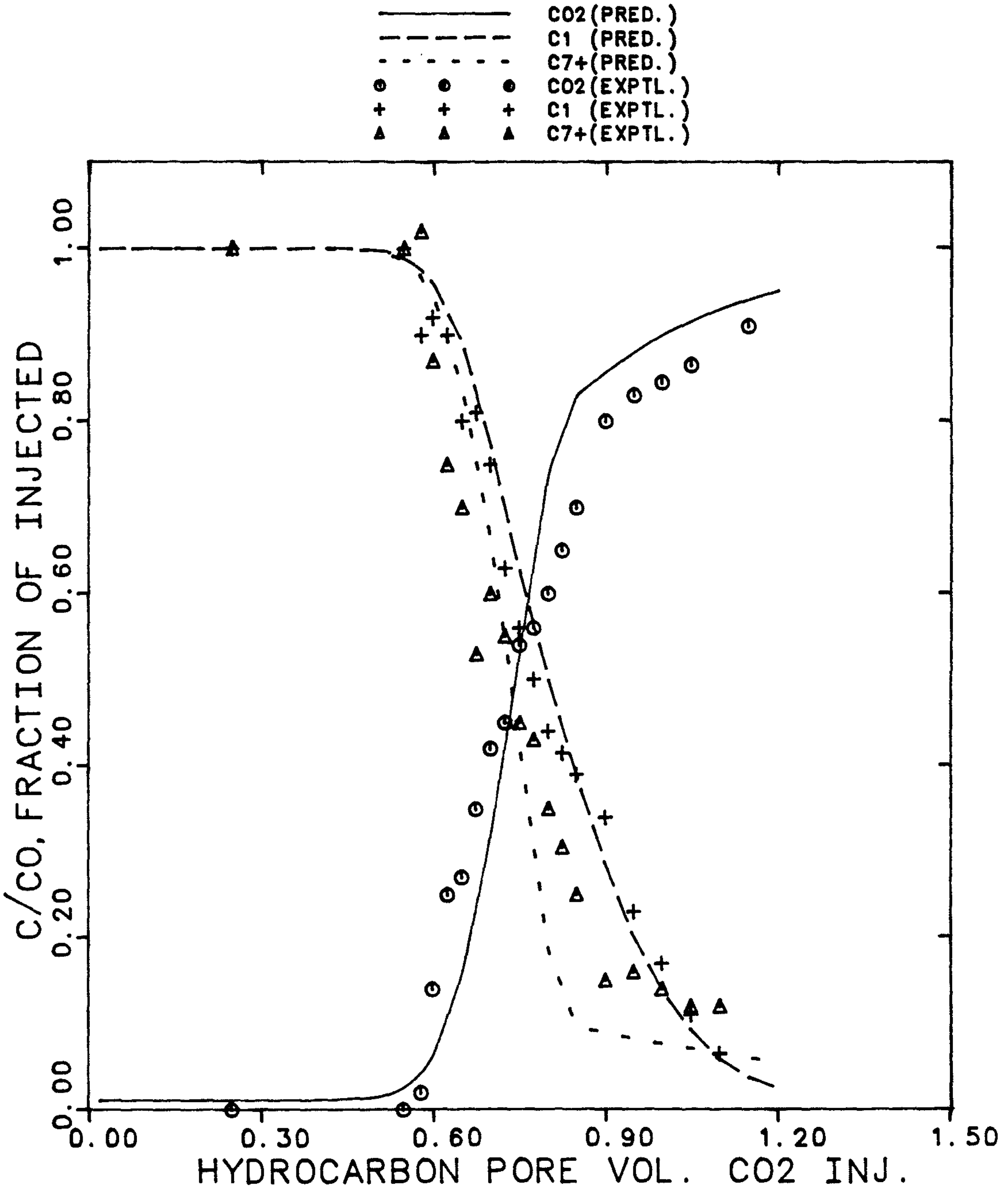

Figure 6.17 Comparison of Calculated and Measured Density Profile of Test #2

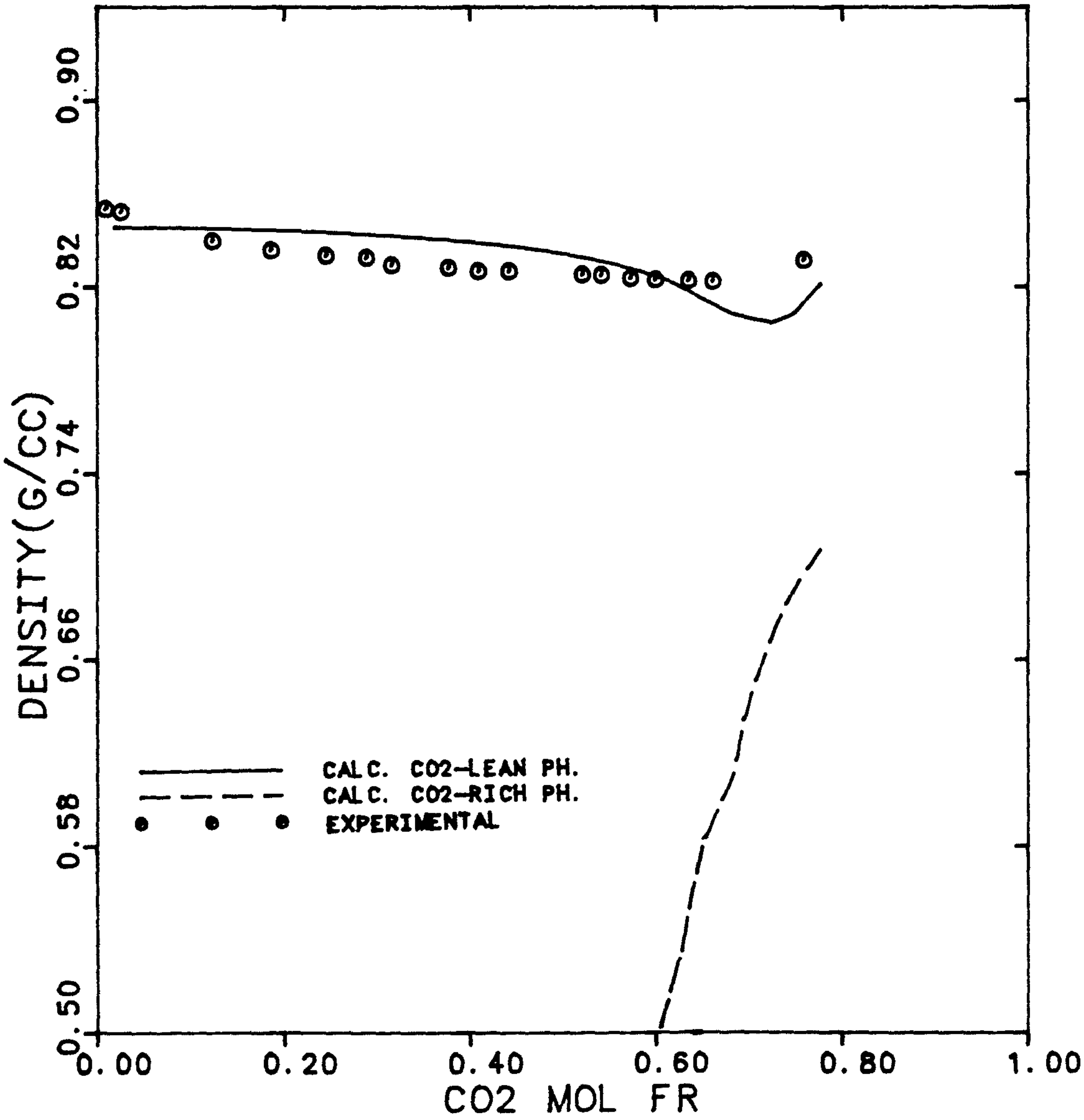

Figure 6.18 Comparison of Calculated and Measured Viscosity Profile of Test #2

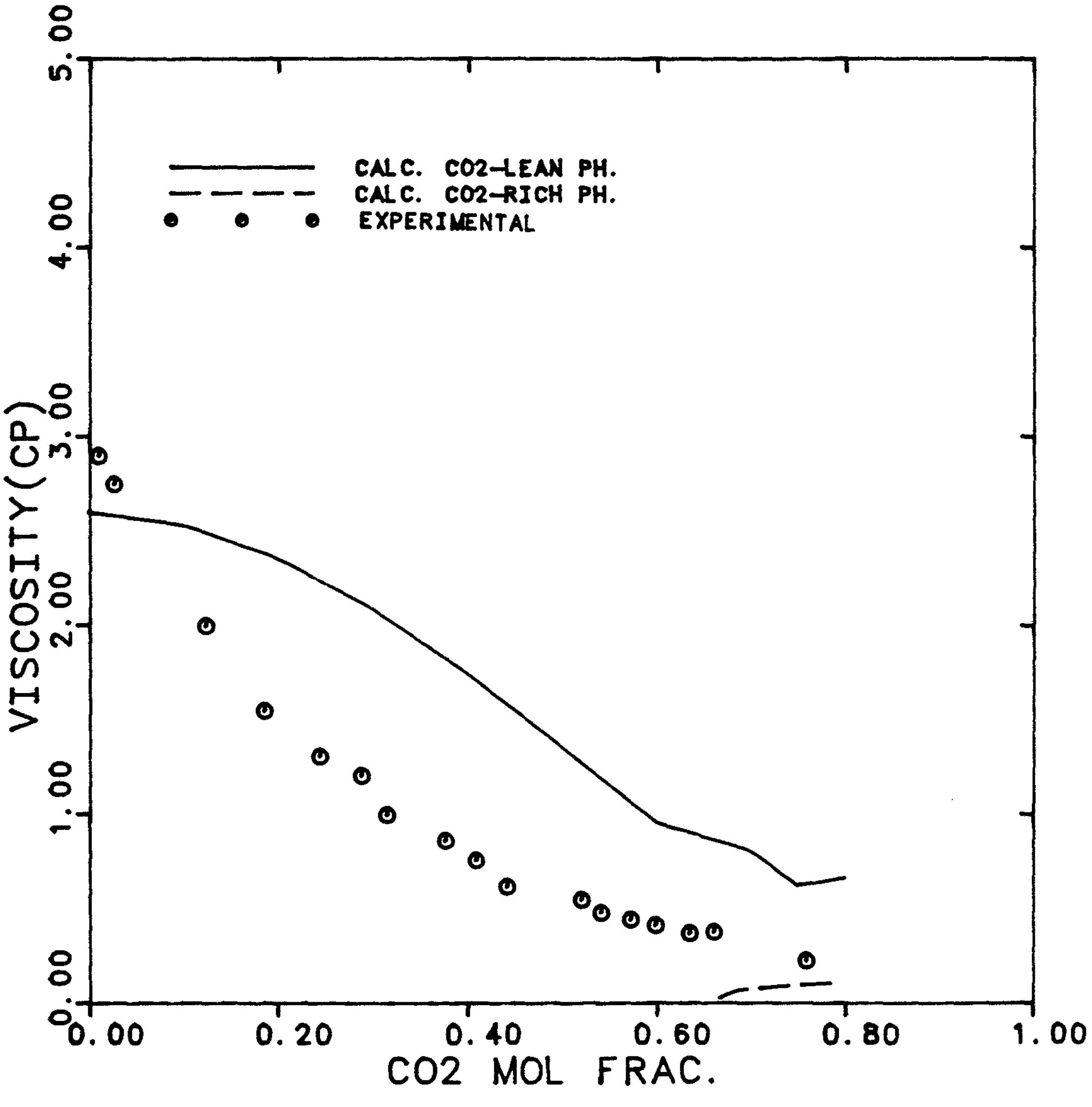

Figure 6.19 Comparison of Calculated GOR of Test #1 by Kremesec and Sebastian and this study

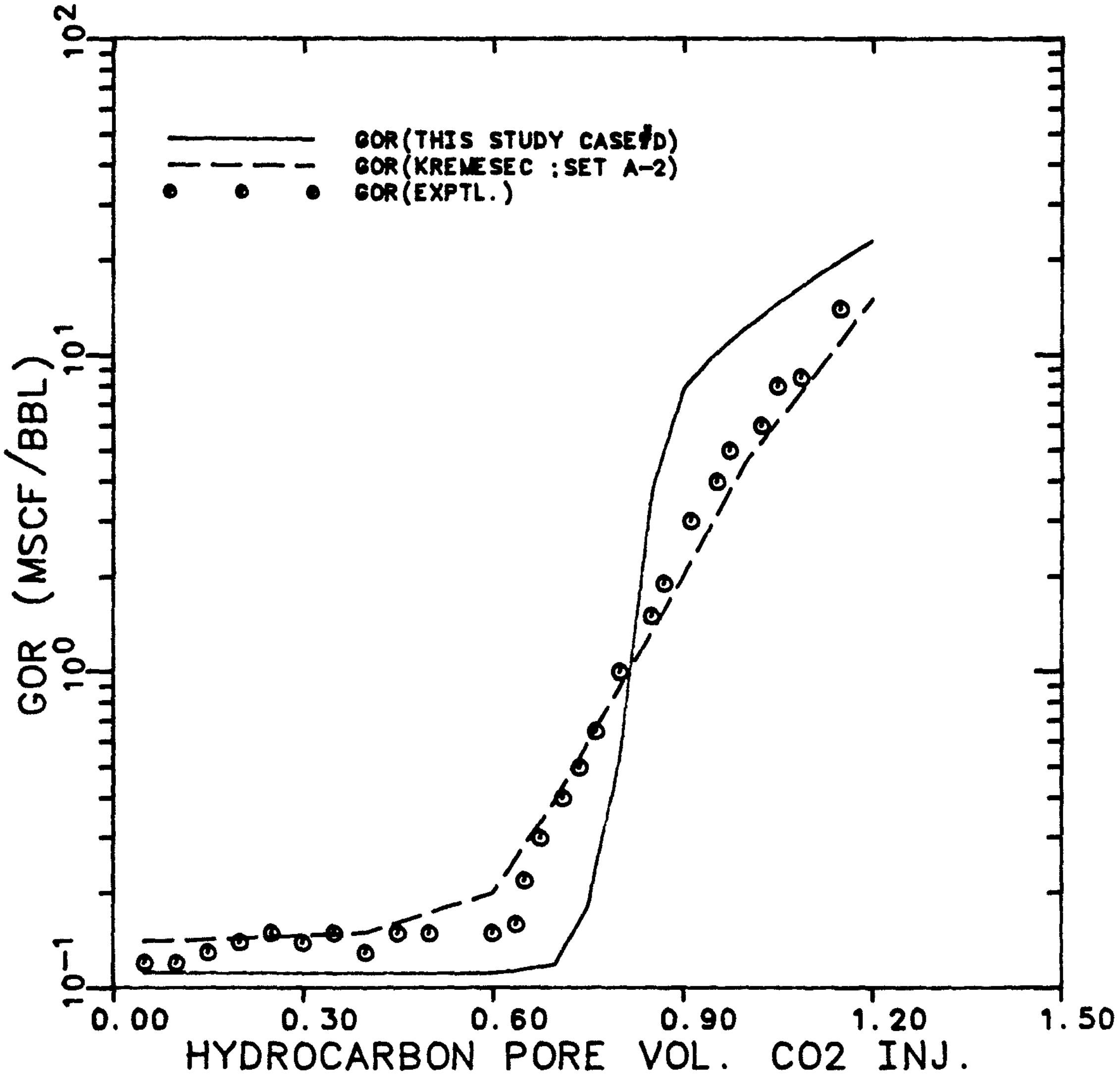

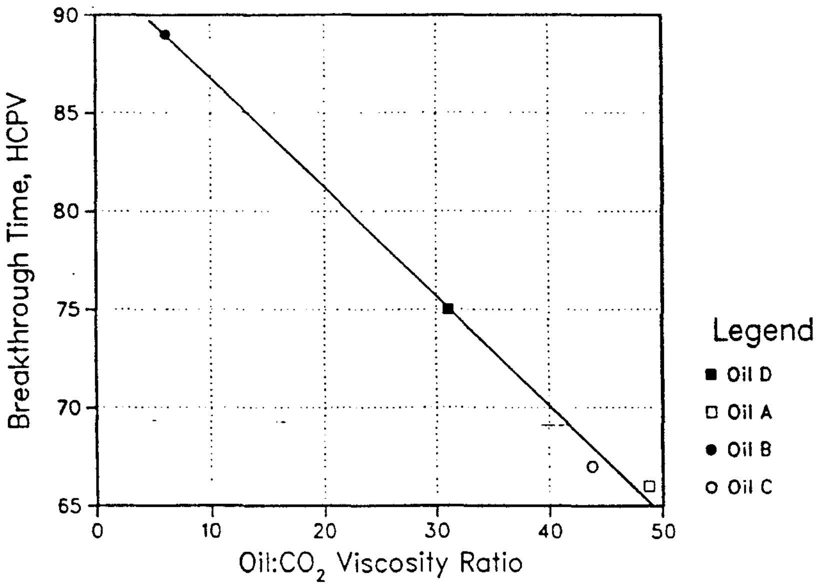

Figure 6.20 CO2 Breakthrough time vs. Oil :CO2 Viscosity Ratio for Secondary Displacements with Connate Water (Ref.K1)

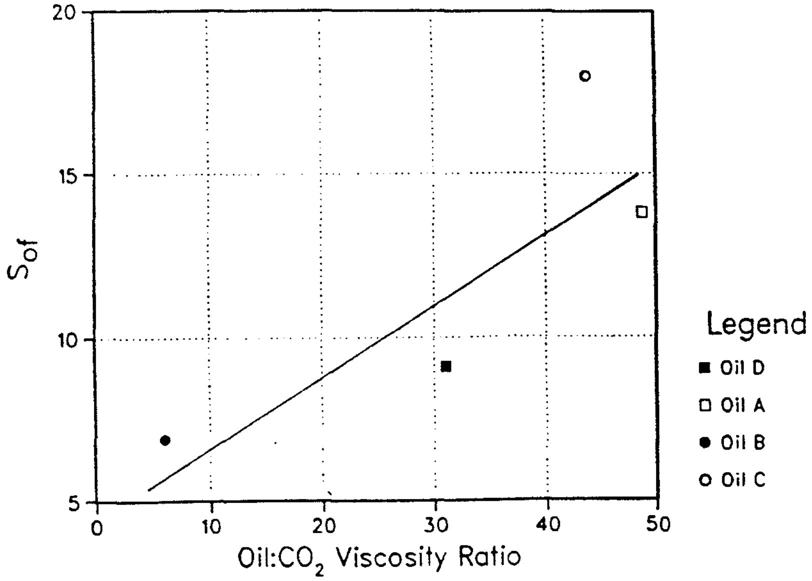

Figure 6.21 Final Oil Saturation vs. Oil :CO2 Viscosity Ratio for Secondary Displacements with Connate Water (Ref.K1)

Chapter 7 Simulation of Amarume Stock Tank Oil Case

Phase behavior calculations and compositional simulations with an equation of state require the use of pseudo-components to represent the crude oil and gas mixture. Because of the large number of components which form the heavy fractions, it is necessary to group them into pseudo-components. Furthermore, to minimize simulation costs, it is also advantageous to combine some of the light fractions.

The general procedure for the Amarume case which was used to determine the pseudo-components can be described as below:

1. Weight fractions of each SCN group are determined up to C_{35}^{+} or more by gas chromatography.
2. Molar distribution is calculated by using molecular weight corresponding to each SCN group which was published by Katz and Firoozabadi [K4], or corresponding to each SCN group by using the molecular weight of the normal alkane.
3. Critical properties in each SCN are obtained using the correlations of Katz-Firoozabadi [K4], Riazi-Daubert [R1], Kesler-Lee [K3], and Whitson [W2].
4. Lumping into pseudo-components using either the scheme of Li et al. [L1] or Whitson [W1].
5. Determining the critical properties of pseudo-components using Kay's mixing rule.

6. Determining the binary interaction coefficients between the pseudo-components and carbon dioxide [K4,K5,L4,W1].

This procedure is used to give an initial estimate only. The binary interaction coefficients and critical parameters are adjusted if needed to give a better match of the phase behavior and the slim-tube experiment.

7.1 Input Data Review

An important step prior to the displacement test predictions by compositional simulation is to adjust EOS parameters for matching laboratory phase behavior test data. EOS constants Ω_a, Ω_b and the binary interaction coefficients between CO_2 and hydrocarbons are the most sensitive parameters. Inoue et al. [I1, I2] conducted an excellent series of laboratory experiments and simulations to evaluate CO_2 flood displacement performance. The stock tank oil from Amarume field in Japan was used for their study. The typical properties of this oil are given in Table 7.1. A hydrocarbon analysis was performed using a gas chromatograph (Table 7.2).

Conventional phase behavior experiments were performed and results of the phase behavior experiments are illustrated as the observed pressure-composition diagram of the Amarume STO - CO_2 mixtures (Fig. 7.1). There is a three phase region [L_1 - L_2 - V] at about 1500 psia and above 75% mole percent CO_2 . Above this three phase region there is a liquid-liquid (CO_2 rich and CO_2 lean) phase region . Slim-tube tests were performed at several pressures (1855 psia, 1625 psia, 1480 psia, 1285 psia, and 1125 psia). The slim-tube was first cleaned with normal hexane, dried with nitrogen, evacuated and saturated with test oil. The temperature and outlet pressure were brought to the desired level, and then CO_2 was injected continuously until the test was terminated. Characteristic data of the slim-tube test are described in the simulation part of this chapter. A core displacement test using Amarume STO was also conducted. This test was carried out at reservoir temperature and a pressure above the MMP. Core data are also described below.

Figures 7.2 and 7.3 are the oil recovery curves of the slim-tube test and the core displacement test respectively.

7.2 Sensitivity Study for EOS Parameter

Whitson [W2] showed that the adjustment of EOS constants a and b (or Ω_a and Ω_b) is essentially the same as the adjustment of the critical properties of each component.

For the Peng-Robinson EOS:

$$a = \Omega_a \frac{R^2 T_c^{\,2}}{P_c} \left[1+m\left(1-T_r^{1/2}\right)\right]^2 \tag{7.1.a}$$

$$b = \Omega_b \frac{Rc}{Pc} \tag{7.1.b}$$

$$m = k_0 + k_1\ \omega + k_2\ \omega^2 \tag{7.1.c}$$

where $\Omega_a = 0.45724$

$\Omega_b = 0.07780$

$k_0 = 0.37464$

$k_1 = 1.54226$

$k_2 = -0.26992$

If the adjusted constants are defined as

$\Omega_a^* = \alpha\,\Omega_a$

$\Omega_b^* = \beta\,\Omega_b$

where α and β are correction factors, equivalent results may then be obtained using the following equations instead of adjusting Ω_a and Ω_b

$$T_c^* = \frac{\alpha}{\beta} T_c \qquad (7.2.a)$$

$$P_c^* = \frac{\alpha}{\beta^2} P_c \qquad (7.2.b)$$

$$\omega^* = \frac{-k_1 + \sqrt{k_1^2 - 4k_2(k_0 - m^*)}}{2k_2} \qquad (7.2.c)$$

$$m^* = m \frac{1 - \sqrt{T/T_c}}{1 - \sqrt{T/T_c^*}} \qquad (7.2.d)$$

Eqs. (7.2.a) through (7.2.d) illustrate that adjustments of a and b can be directly translated to adjustments of T_c, P_c and ω. If $\alpha/\beta = 1$, only P_c is adjusted. If $\alpha/\beta^2 = 1$, only T_c and ω are adjusted. All other combinations of α and β correspond to an adjustment of all three critical properties.

Amarume stock tank oil was used to investigate the influence of the following EOS parameters on both phase behavior and slim tube test calculations,

1. Binary interaction coefficients between CO_2 and the hydrocarbons
2. Critical temperatures and acentric factors of CO_2 and the heaviest pseudo component (The adjustment of Ω_a and Ω_b is such that α/β^2 is kept constant for constant P_c)
3. Critical pressures of CO_2 and the heaviest pseudo component (The adjustment of Ω_a and Ω_b is such that α/β is kept constant for constant T_c)
4. Ω_a and Ω_b (or α and β) of CO_2 and the heaviest pseudo component

Fig. 7.4 summarizes this sensitivity study.

7.2.1 Simulation of Slim Tube Test for the Base Case

Inoue et al. [I1,I2] used the splitting scheme presented by Li et al. [L1], and the pseudo-component properties used are shown in Table 7-3. These properties were used as the initial values in this study.

Binary interaction coefficients between CO_2 and the pseudo components are all set to the identical values of 0.12 and all others are zero. Computed and measured phase behavior are compared on the pressure-composition diagram of Fig. 7.5. This case is defined as the base case of this study (Case #2).

The characteristic data for this slim-tube are shown in Table 7-4. The gas-oil relative permeabilities for unconsolidated sands presented by Naar et al. [N3] were used without modification (Fig. 5.11). The sensitivity of oil recovery to grid block size was first examined by dividing the total length into 20, 40, 80, 160, and 200 grid blocks and these results are shown in Fig. 7.6. The input data used in this study are the same as that of Case #2 except that the CO_2 binary interaction coefficients were all 0.1 and the pressure was 1855 psia. The complete input to UTCOMP for the base case are given in Appendix (HC.DAT of Example #4). Very little change in numerical precision occurs for more than 80 grid blocks, so 80 grid blocks appears to be enough for this case.

7.2.2 Effect of Binary Interaction Coefficient

The influence of CO_2 binary interaction coefficient was investigated using the following cases,

$$\delta_{CO_2\text{-}HC} = 0.11 \text{ for Case \#1}$$

$$\delta_{CO_2\text{-}HC} = 0.12 \text{ for Case \#3}$$

where hydrocarbon/hydrocarbon binary interaction coefficients were all zero, and the same hydrocarbon data-set as Case #2 was used otherwise.

Fig. 7.7 shows the pressure-composition diagram for these cases (Case #1, 2, 3 and experimental). The single phase region shrinks with increasing CO_2 binary interaction coefficient.

Fig. 7.8 shows the oil recovery at 1.2 pore volumes of CO_2 injected as a function of pressure. According to the experimental results of Inoue et al. [I1,I2], the minimum miscibility pressure (MMP) of Amarume STO was about 1500 psia, which is shown on this figure as the bending point of the experimental curve. The bending point of this curve can be seen clearly, while the calculated results do not show such a point. This was the reason why other parameters were varied as discussed below.

7.2.3 Effect of Critical Properties of CO_2

7.2.3.1 Critical Temperature and Acentric Factor of CO_2

The influence of critical temperature and acentric factor of CO_2 on the phase behavior and slim-tube displacement test is given in this section. As shown in Eqs. (7.2.a) through (7.2.d), α/β^2 is kept constant for constant P_c.

The α/β values are 1.05 for Case #4 and 1.01 for Case #5. In these cases, acentric factor (ω) is also adjusted because T_c is adjusted. The binary interaction coefficient between CO_2 and the hydrocarbons is set to 0.12. Other critical properties of this oil are the same as those of Case #2.

Fig. 7.9 shows the pressure-composition diagram for these cases (Case #2, 4, 5 and experimental). This figure shows that the phase boundary (saturation pressure) is shifted downward with increasing value of α/β (this also means that the single phase region expands with increasing α/β). These differences are greatest below 1500 psia. The oil recovery as a function of pressure is given in Fig. 7.10. The increased oil recovery of Case #4 was anticipated because it has a larger single phase region than Case #2 or Case #3. As expected, the recovery differences between Case #4 and #2 or #5 become larger below 1500 psia. Case #4 also shows a sharper break in the recovery curve, so increasing α/β improves the character of the curve in this respect.

7.2.3.2 Effect of critical Pressure of CO_2

The adjustment of critical pressure of CO_2 was performed using Eq. (7.2.b), where α/β is kept constant. The value of α/β^2 is set to 1.05 for Case #6 and 0.9 for Case #7. Other critical properties are the same as those of Case #2. The calculated pressure-composition diagram and recovery-pressure correlation are shown in Figures 7-11 and 7-12. There is not too much difference between these cases with this magnitude of adjustment. Fig. 7.11 shows that below 1500 psia, the single phase region expands with a decrease in α/β^2, while the reverse results occur above 1500 psia.

Around 1800 psia, the phase boundary curves of these three cases cross. The recovery increases as α/β^2 decreases and decreases slightly above 1600 psia (Fig. 7.12).

Thus, the adjustment of critical pressure (α/β^2) of CO_2 shows the expected trend exists between the pressure-composition diagram and the recovery curves.

7.2.3.3 Effect of α and β of CO_2

The influence of α of CO_2 was investigated in the following cases, $\alpha = 1.05$ for Case #8 and $\alpha = 0.9$ for case #9. β is kept constant and other critical properties and binary interaction coefficients are the same as those of Case #2 (T_c, P_c and ω were adjusted). Figures 7.13 and 7.14 show the pressure-composition diagram and the recovery curves. Large effects on phase behavior and slim-tube displacements can be seen from these figures.

The single phase region expands (Fig. 7.13) with an increase in α and large differences in the recoveries can be seen between Case #8 and #9 (Fig. 7.14). The influence of β for CO_2 was investigated for $\beta = 0.94$ (Case #10) and $\beta = 1.053$ (Case #11). Binary interaction coefficients and other critical properties are the same as Case #2 (that is, only the T_c, P_c, and ω for CO_2 were adjusted). Figures 7.15 and 7.16 show these results. Fig. 7.15 shows that the single phase region expands with a decrease in β and there is a sharper bend or change in slope of the phase boundary curve.

Fig. 7.16 reflects the tendency of the phase behavior very well, that is to say, recoveries increase with a decrease of value β and there is a greater change in the slope of the oil recovery curve (Case #10). The effect of β is contrary to that of α.

7.2.4 The Effect of the Critical Parameters of the Heaviest Pseudo-Component

The influence of Ω_a and Ω_b of the heaviest pseudo-component (C_{21+}) of this oil was investigated by using adjustments similar to those mentioned above for CO_2.

The pressure-composition diagrams are calculated for the four cases which are described in Table 7-5. In Case A, the influence of the critical temperature and acentric factor of the heaviest pseudo component is investigated by increasing α/β 5 percent over the base Case #2.

In each case the binary interaction coefficients and other critical properties are the same as that of Case #2. Figures 7.17 through 7.20 show these results. The influence of T_c and ω is very small and opposite to that of T_c for CO_2 (Fig. 7.17). That is, an increase in T_c for C_{21}^+ results in a decrease in the size of the single phase region. The influences of P_c for C_{21}^+ is extremely small . The influence of both α and β for C_{21}^+ is small and opposite to those for CO_2 (Figs. 7.19 and 7.20).

7.2.5 Observations of Effect of EOS Parameter

From section 7.2.1 through 7.2.4, the following observations can be seen,

1. The influence of CO_2 binary interaction coefficient:

A decrease in CO_2-hydrocarbon binary interaction coefficients expands the single phase region and increases the liquid fractions (decreases the quality) in the pressure-composition diagram, and therefore, oil recoveries increase with a decrease of these coefficients.

2. The influence of critical temperature (T_c) and acentric factor (ω):

   An increase in T_c of CO_2 (ω of CO_2 also increases with an increase of T_c of CO_2) shows expansion of the single-phase region and an increase in liquid fraction, and therefore, oil recoveries increase. A sharper bending can be seen in the recovery curve when T_c of CO_2 increases. An increase in T_c of the heaviest pseudo-component causes a decrease in the single-phase region,but the effect is very small.

3. The influence of the critical pressure (P_c):

   An increase in P_c of CO_2 results in a decrease in the single phase region and a decrease in the liquid fraction, and therefore oil recoveries decrease.

4. The influence of α:

   An increase in $\alpha(CO_2)$ results in an expansion of the single phase region and an increase in the liquid fraction, and therefore, oil recoveries increase.

5. The influence of β:

   Changes in β of CO_2 has the reverse effect on the phase behavior and oil recovery of α of CO_2. A sharper bending can be seen in the recovery and pressure diagram curves with an increase of β of CO_2.

6. The effects of the EOS parameters of the heaviest pseudo-component are opposite to those of CO_2, and they are relatively smaller than those of CO_2.

7.3 History Matching of the Slim Tube Displacement

7.3.1 Seven Hydrocarbon Pseudo-Components

In the previous section, a sensitivity study of the EOS parameters on the phase behavior and slim-tube displacement was performed and various effects of these parameters were obtained. By using these characteristics of the parameter, the best fitting data set can be determined for Amarume STO case. The experimental pressure-composition diagram of Amarume STO shows distinctive characteristics. Above 1400 psia, the two phase boundary (saturation pressure) increases almost vertically. The two phase region above 1400 psia is a liquid-liquid (CO_2 rich and CO_2 lean) phase region. Below this pressure, the two phase region is a liquid-liquid phase region. For pressures close to 1400 psia, there is a three phase region (L_1 + L_2 + V) between these liquid-liquid and liquid-vapor regions. In the phase behavior matching process, it is important to describe these characteristics accurately. An increase of T_c for CO_2 or a decrease of β for CO_2 makes its bend in both the pressure-composition diagram and the recovery curve sharper. Adjustment of binary interaction coefficients between the CO_2 and the hydrocarbons produces a parallel shift in both the pressure-composition diagram and the recovery curve. Therefore, a combination of these adjustments was investigated next.

As described in the previous section, Case #10 ($\beta = 0.94$) shows a clear bending point on both diagrams, but the oil recovery is much higher than the experimental results. Lower oil recovery can be obtained when the CO_2 binary interaction coefficient increases, because the size of the single phase region is reduced. Cases #10A and #10B were performed to check this. Binary interaction coefficients between CO_2 and the hydrocarbons were 0.14 for Case #10A and 0.15 for Case #10B. Results are given in Figures 7.21 and 7.22. The best of these results appears to be for $\delta = 0.15$ (Case #10B).

7.3.2 Six Hydrocarbon Pseudo Components

All the basic parameters used in the previous section are given by Inoue et al. [I1,I2], in which the splitting method of Li et al. [L1] was used for grouping the hydrocarbon components and the Katz and Firoozabadi correlation was used for determining the critical properties.

Hence, the new data set was obtained by using Whitson's splitting scheme for grouping and several correlations which are described in Chapter 5 and listed below;

1. Katz and Firoozabadi's correlation of carbon number (CN), specific gravity and the boiling point
2. for molecular weight; Katz-Firoozabadi correlation
3. for critical pressure, temperature, and volume; Riazi-Daubert correlations
4. for acentric factor; Kesler-Lee correlation

Table 7-6 shows the calculated results of each carbon number (CN) component by these correlations. Table 7-7 shows the pseudo-components and their properties using Whitson's scheme and the data of Table 7-6. Fig. 7.23 shows the recovery curves for base case #2, the experiment and for this 6 pseudo component case with a CO_2 binary interaction coefficient of 0.12 (Case #12). To obtain the pressure-composition diagram (Fig. 7.24) and the recovery curve (Fig. 7.25), the CO_2-EOS parameters were adjusted as follows:

$P_c = 1216.21$ psia $\qquad T_c = 574.98$ °R

$\omega = 0.225$ $\qquad \delta_{CO_2\text{-}HC} = 0.15$

This result is similar to that of Case #10B with 7 hydrocarbon pseudo-components.

7.3.3 Production GOR of slim-tube test

As described in the previous chapter, the producing GOR is very sensitive to the phase behavior (EOS parameters), especially the CO_2 critical parameters. In this section, the following cases are tested to investigate the GOR sensitivity to EOS parameters:

Case #2, #5 and #10 are used for this study with the following adjustments:

Case #5A, a CO_2 binary interaction coefficient of 0.125 was used.

Case #10C, a CO_2 binary interaction coefficient of 0.15 was used.

The pressure-composition and oil recovery curves for the above cases are shown in Figures 7.26 and 7.27, respectively. The results of Case #2 and Case #5A are very similar. Below 1200 psia, the phase boundaries of all three cases are almost identical.

Comparisons of calculated and experimental GOR results are shown in Figures 7.28 through 7.30. Cases #2 and #5A are very similar and agree with the experimental GOR better than Case #10C does.

These three data-sets were next used for comparisons with experimental core-floods.

7.4 Core Floods

The experimental coreflood results of Inoue et al. [I1,I2] are used in this section. CO_2 was injected continuously into the core which is at a connate water saturation of 35% (a secondary displacement). Amarume stock tank oil described in the previous section was used for the oil. Berea sandstone with the physical properties shown in Table 7-8 was used. Displacement test was carried out at reservoir temperature of 126.5°F and a pressure of 1840 psia which is above the MMP of this oil, and a frontal velocity of 2 ft/day.

The recovery curve for this test and that of the slim tube test at the same temperature and pressure are compared in Fig. 7.31. The recovery curve for the slim-tube displacement test shows that CO_2 breakthrough occurred at 0.9 hydrocarbon pore volumes of CO_2 injected and the high oil recovery, corresponding to 95% of the original oil in place, and the shape of the recovery curve are all characteristic of a miscible displacement in a homogeneous porous medium. On the other hand, the recovery curve for the core displacement test is not as steep and the oil recovery is much lower than that of the slim tube displacement test. The coreflood displacement was much less efficient than the slim-tube displacement. The most likely reason for this is viscous fingering since the mobility ratio is highly adverse and the diameter of the core is large enough to allow fingers to propagate.

7.4.1 One Dimensional Simulation Run for Core Displacement

One-dimensional simulation run was performed using the following input data. Three hydrocarbon data-sets which are described in section 7.3.3 were used in this study. For gas/oil relative permeability curves, the data of consolidated sand by Naar et al. [N3] were adopted (Fig. 7.32). The end points were shifted by the connate water saturation. The block area used in the simulation was 0.02182 ft^2 and 0.00781 ft^3/day of CO_2 was injected under reservoir conditions.

Fig. 7.33 shows the simulated oil recovery and GOR using Case #2 input. The GOR agrees relatively well with the experimental results, while a large discrepancy exists between the simulated and actual recovery. Final recovery reaches 94% of OOIP at 1.5 HCPV CO_2 injected.

Recovery increases with the number of grid blocks. Since little change occurred for more than 40 grid blocks, this number was used in the following simulation studies.

Fig. 7.34 shows the results for Case #5A input. Similar results to Case #2 can be seen, that is, relatively good GOR match, but high simulated oil recovery. The results for Case #10C are given in Fig. 7-35. The oil recovery match improved, but the GOR match is much worse. The GOR goes up suddenly after CO_2 breakthrough and reaches a plateau. The value of this plateau is twice as large as for Case #2 or #5A. The effluent compositional profiles were also calculated for Case #10C (Fig. 7-36).

Every component curve changes suddenly after breakthrough, and the slopes of the profiles are almost perpendicular. Because of the similar computed results for Case #2 and #5A in both the slim-tube test and the core displacement test, Case #2 was selected for further study. Case #10C was also selected for comparison. The previous one-dimensional simulations correspond to a stable displacement with only numerical dispersion (no physical dispersion).

Takeda [T3] modified the Young and Stephenson formulation [Y3] to model physical dispersion. In this model, the dispersion terms are treated explicitly, which means evaluated at the previous time step and added to the residual vector. In the following section, this model was used to study physical dispersion. The two point upstream weighted mole fractions option as originally proposed by Nghiem et al. [N1] ("Composition 2-point") was used for this study.

Fig. 7.37 shows the results of simulated recovery and GOR for Case #2 with 40 grid blocks. Here, the three values of longitudinal physical dispersivity were 0.0, 0.1 and 0.5 feet . The recovery decreases with increasing dispersivity, and the GOR increased and breakthrough occurred earlier with increasing dispersivity.

Fig. 7.38 shows the results for Case #10C. Similar results to Case #2 can be seen in the recovery curves, but a large discrepancy still exists in the GOR curves. In this study, physical dispersion of 0.5 ft gives a relatively good match of the recovery curve in both cases, but this value is about 50 times larger than the value typical of actual physical dispersion in Berea rock. In a convection-diffusion equation, the total dispersion coefficient in dimensionless form is

$$\alpha_D^T = \alpha_D^N + \alpha_D^P$$

where α_D^T : Total dispersion coefficient

α_D^P : Physical dispersion coefficient

α_D^N : Numerical dispersion coefficient

The magnitude of α_D^N for finite differences approximation using a backward difference for the first-order space derivative is

$$\alpha_D^N = (\Delta x_D - \Delta t_D) / 2 \quad \text{(explicit)}$$

Assuming small time truncation error,

$$(\Delta x_D - \Delta t_D) / 2 \cong \Delta x_D / 2 = 1/2\, N_x$$

Where N_x is the number of grid blocks.

For this case,

$$\alpha_D^N = 1/80 = 0.0125$$

$$\alpha_D^P = 0.5/6 \cong 0.0833$$

so $$\alpha_D^T = \alpha_D^N + \alpha_D^P \cong 0.0958$$

So, the effective longitudinal dispersion of this case is,

$$(\alpha_l)_{eff} = 0.0958 \times 6 = 0.5748 \text{ (ft)} = 17.5 \text{ (cm)}$$

Considering typical values of α_l for Berea sandstone, this value is much too large.

This result implies that other physical phenomena are causing the lower recovery (in this case fingering and gravity tongueing). Next 2-D simulations were done to investigate the effects of gravity on this CO_2 coreflood.

7.4.2 Two Dimensional Cross-Sectional Simulations

The effect of gravitational forces on the oil recovery for this core flood displacement was investigated in this section.

Figs. 7.39 and 7.40 show the calculated densities for an 85 mol% CO_2 plus 15 mol% Amarume STO mixture using Cases #2 and #10C input. The coreflood displacement was conducted at 1840 psia (pointed out by arrow). Around this pressure, the differences in liquid and vapor densities are very small in both cases studied, and density-inversion can be seen. In Case #2, the liquid density is higher than the vapor density, while in Case #10C the liquid density is a little lower than the vapor density at 1840 psia.

Several 2-D cross-sectional simulation runs were conducted and run conditions are given in Table 7-9. In the Runs #22B, 24B and 28B, Case #10C EOS parameters were used. Fig. 7.41 shows the 2-D oil saturation contours for Run #24B at different HCPV of CO_2 injected. A 20 x 4 grid was used in this case. In this figure (and all of the following contour maps), CO_2 was injected at the left side and produced at the right side. Because of the small difference between phase densities, there was little variation in the vertical direction, although as seen from the lowest map in this figure, a small gravity tongue did form under the displaced oil because the CO_2 rich phase was more dense in this case.

Case #2 parameters were used for Runs #22A, 24A and 28A. Oil saturation contour maps for Run #24A (20 x 4 grid) are given in Fig. 7.42. The lighter CO_2 phase overrides the oleic phase in this run.

Fig. 7.43 shows the cross-sectional contour map for Run #28A (20 x 8 grid). From the comparison between this figure and Fig. 7.42 of Run #24A (20 x 4), earlier breakthrough can be seen in the final panel of Fig. 7.43. Oil recovery decreases with an increase in the number of vertical grid blocks. Fig. 7.43 clearly shows a gravity tongue overriding the oil.

In Fig. 7.44, the recovery curves and production GOR curve for Runs #42A, #44A, and #48A are given. The 40 x 8 grid block run gives a very good history match of both the experimental recovery and GOR curves. From GOR curve results, the earlier breakthrough and the later GOR build-up occurred with an increasing number of grid block in the z-direction. Oscillation can be seen in the GOR curve for the 40 x 8 Run.

The simulated compositional histories (20 x 8 Run) are given in Fig. 7.45 . The slope of each component (CO_2, $C_{3\text{-}6}$, and C_{7+}) becomes much smaller than for the 1-D Run shown in Fig. 7.36.

A 2-D cross sectional run with physical dispersion was made in Run #24X with a 20 x 4 grid and Case #2 EOS parameters. The longitudinal dispersivity was 0.1 ft, and the transverse dispersivity was 0.01 ft. Fig. 7.46 shows the recovery and GOR curves compared to the experimental results and the simulation without dispersion (Run #24A). Run #24X (with dispersion) shows a slightly higher recovery than Run #24A (without dispersion). In 1-D, larger dispersion gave a smaller oil recovery. This result may be due to transverse dispersion. Fig. 7.47

shows the oil saturation contour map. There was little vertical effect in this run. On the other hand, a gravity tongue overriding the oil can be seen in the Run #24A (Fig. 7.42). The GOR curve of Fig. 7.46 shows almost the same shape as the 1-D result.

These results show the transverse dispersion prevented early breakthrough of CO_2, and effectively recovered oil from the lower grid block layers. A simulation run which had only longitudinal dispersivity (α_l = 0.1 ft) and zero transverse dispersivity was performed and the result was very similar to that of Run #24A . Oil recovery and GOR are affected more by transverse dispersion than by longitudinal dispersion.

Finally, low vertical permeability was simulated. In all the simulations so far, a homogeneous and isotropic core was assumed ($K_y = K_z$). In Run #44Y has a K_y/K_z ratio of 10.0, a 40 X 4 grid, and Case #2 EOS parameters were used. Fig. 7.48 shows the oil recovery and GOR curves. A good history match was obtained. Fig. 7.49 shows the oil saturation contour map. A gravity tongue can be seen.

In the simulations discussed above, capillary pressure was neglected, that is, P_{cwo} and P_{cgo} were zero. In the following, the effect of capillary pressure was investigated. The core displacement was carried out at connate water saturation, so P_{cwo} was zero. The capillary pressure between gas and oil, P_{cgo}, should be a function of oil saturation, S_o. The following equation was assumed,

$$P_{cgo} = a\,\sigma\,S_o^{-1.5}$$

where a is some constant value and σ is the interfacial tension between gas and oil.

In the UTCOMP simulator, interfacial tension is calculated using the MacLeod - Sugden correlation [R3] which relates the surface tension to the liquid and vapor densities.

$$\sigma_{jk}^{1/4} = 0.016018 \sum_{i=1}^{Nc} [P_i] (\xi_j x_{ij} - \xi_k x_{ik})$$

where σ_{jk} is the intefacial tension between phases j and k in dyne / cm, molar densities are in lb-moles / ft3 , and $[P_i]$ is the parachor of component i.

Fig 7.50 shows example capillary pressure curves, where σ = 1.0, 5.0, 10.0, and 20.0 dyne / cm and a was 0.02. Figures 7.51 and 7.52 show the simulation results for a 2-D cross-sectional simulation using a = 0.02 (Run #24Z). With capillary pressure [Fig. 7.52], no gravity tongue exists, and therefore the oil recovery increases compared to Run #24A (Fig. 7.42). Since σ was only about 1.0 dyne/cm in this Run, this was actually a very low capillary pressure, yet it almost completely stabilized the displacement vertically. Higher values of capillary pressure should be simulated, but convergence problems prevented this at this time.

Table 7-1

Typical Properties of Amarume Stock Tank Oil

Reservoir Temp.: 126.5 °F

Average M.W.: 174.0

Density (*): 0.9238 g/cm^3

Viscosity (*): 2.1 cp

M.W. C_{11}^+: 275

Density of C_{11}^+: 48.0 lb/ft^3

(*) 14.7 psia and reservoir temperature

Table 7-2 Composition of Amarume Stock Tank Oil

Carbon Number	Stock Tank Oil (Mole%)
CO_2	0.05
3	0.075
4	3.39
5	6.70
6	6.88
7	15.56
8	14.90
9	7.49
10	5.21
11	4.776
12	4.056
13	3.529
14	3.254
15	2.791
16	2.365
17	1.893
18	1.501
19	1.437
20	1.369
21	1.223
22	1.092
23	0.975
24	0.892
25	0.815
26	0.726
27	0.665
28	0.574
29	0.527
30	0.513
31	0.469
32	0.429
33	0.380
34	0.336
35	0.320
36	0.293
37	0.268
38	0.255
39	0.243
40+	1.106

Table 7-3 Critical Properties by Inoue et al.(Ref.[I1,I2])

Critical Data

Compo nent	Compo- sition	Press. (psia)	Temp. (^{o} R)	Volume (ft^3/lb-mole)	Molecular Weight	Acentric Factor	Parachor
CO_2	0.05	1073.000	547.500	1.5050	44.010	0.2300	49.000
C_{3-6}	17.72	476.290	848.870	5.0620	73.730	0.2576	60.000
C_7	15.56	453.000	985.000	6.0370	96.000	0.2800	100.000
C_8	14.90	430.840	1040.250	8.7930	102.160	0.2991	300.000
C_{9-10}	12.70	376.360	1107.120	10.9610	122.660	0.3557	350.000
C_{11-14}	15.68	262.520	1220.000	15.2140	163.500	0.4614	500.000
C_{15-20}	11.40	205.980	1365.000	20.6240	227.770	0.6185	600.000
C_{21+}	11.99	147.430	1580.000	30.7760	420.240	0.9171	700.000

Binary Interaction Coefficents

	CO_2	C_{3-6}	C_7	C_8	C_{9-10}	C_{11-14}	C_{15-20}	C_{21+}
CO_2	0.0000							
C_{3-6}	0.1200	0.0000						
C_7	0.1200	0.0000	0.0000					
C_8	0.1200	0.0000	0.0000	0.0000				
C_{9-10}	0.1200	0.0000	0.0000	0.0000	0.0000			
C_{11-14}	0.1200	0.0000	0.0000	0.0000	0.0000	0.0000		
C_{15-20}	0.1200	0.0000	0.0000	0.0000	0.0000	0.0000	0.0000	
C_{21+}	0.1200	0.0000	0.0000	0.0000	0.0000	000000	0.0000	0.0000

Table 7-4

Characteristics of Slim Tube

Length	40 ft
Internal Diameter	0.171 inch
Geometry	Spiral Coil
Packing Material	100 Mesh Ottawa Sand
Air Permeability	11.6 Darcies
Porosity	47.0%

Table 7-5

Critical Properties of the Heaviest Pseudo-component

Case #	T_c (°R)	P_c (psia)	Acentric Factor	alpha (α)	beta (β)	α/β	β^2
A	1580.0	154.08	0.9415	1.1025	1.05	1.050	1.000
B	1738.0	147.43	0.9171	0.9100	0.91	1.000	1.100
C	1501.0	140.06	0.8919	0.9500	1.00	0.950	0.950
D	1788.6	156.72	0.9482	1.0000	0.94	1.063	1.132

Table 7-6 Physical Properties by Correlations

Carbon Number	Boiling Point (°R)	Spec. Gravity	Molecular Weight	Critical Temp. (°R)	Critical Pressure (psia)	Critical Volume (ft^3/lb-mole)	Acentric Factor
6	607.0	.6900	85.91	922.8	483.65	5.49	.2416
7	658.0	.7270	95.76	986.1	453.05	6.02	.2728
8	702.0	.7490	106.29	1035.4	418.00	6.66	.3067
9	748.0	.7680	119.24	1084.5	382.54	7.46	.3455
10	791.0	.7820	133.09	1128.1	350.54	8.35	.3855
11	829.0	.7930	146.67	1165.5	324.86	9.23	.4229
12	867.0	.8040	161.48	1202.6	302.39	10.18	.4610
13	901.0	.8150	175.74	1236.2	285.51	11.09	.4945
14	936.0	.8260	191.38	1270.3	269.68	12.09	.5300
15	971.0	.8360	207.96	1303.7	254.75	13.15	.5675
16	1002.0	.8430	223.41	1332.0	241.52	14.17	.6038
17	1032.0	.8510	239.03	1359.9	230.59	15.18	.6382
18	1055.0	.8560	251.43	1380.6	222.13	16.00	.6667
19	1077.0	.8610	263.63	1400.4	214.66	16.80	.6943
20	1101.0	.8660	277.31	1421.6	206.75	17.70	.7257
21	1124.0	.8710	290.78	1442.0	199.75	18.59	.7562
22	1146.0	.8760	303.97	1461.6	193.55	19.46	.7856
23	1167.0	.8810	316.84	1480.3	188.05	20.30	.8139
24	1187.0	.8850	329.35	1497.6	182.72	21.13	.8428
25	1207.0	.8880	342.10	1514.3	177.18	22.00	.8744
26	1226.0	.8920	354.42	1530.7	172.68	22.82	.9373
27	1244.0	.8960	366.28	1546.4	168.70	23.60	.9594
28	1262.0	.8990	378.31	1561.4	164.46	24.42	.9827
29	1277.0	.9020	388.48	1574.2	161.27	25.09	1.0013
30	1294.0	.9050	400.14	1588.4	157.62	25.88	1.0227
31	1310.0	.9090	411.26	1602.4	154.78	26.60	1.0412
32	1326.0	.9120	422.50	1615.8	138.28	27.36	1.0608
33	1341.0	.9150	433.15	1628.5	134.26	28.07	1.0788
34	1355.0	.9170	443.19	1639.7	130.17	28.76	1.0965
35	1368.0	.9200	452.59	1650.9	127.21	29.38	1.1114
36	1382.0	.9220	462.81	1662.1	123.43	30.08	1.1289
37	1394.0	.9250	471.64	1672.6	121.03	30.65	1.1422
38	1407.0	.9270	481.27	1683.0	117.84	31.31	1.1581
39	1419.0	.9290	490.23	1692.8	115.08	31.92	1.1725
40	1432.0	.9310	500.00	1703.2	112.11	32.59	1.1882
41	1442.0	.9330	507.57	1711.5	110.13	33.09	1.1996
42	1453.0	.9340	515.94	1719.9	107.43	33.68	1.2138
43	1464.0	.9360	524.35	1728.8	105.30	34.25	1.2265
44	1477.0	.9380	534.36	1739.2	102.69	34.94	1.2419
45	1487.0	.9400	542.11	1747.4	100.95	35.46	1.2531

Table 7-7 Physical Properties of Six Pseudo-components (Case #12)

Critical Data

Component	Press. (psia)	Temp. (° R)	Volume ft^3/lb-mole	Molecular Weight	Acentric Factor	Parachor
CO_2	1216.210	547.980	1.5100	44.010	0.2250	49.000
$C_{3\text{-}4}$	544.640	750.700	5.3550	55.480	0.1840	60.000
$C_{5\text{-}7}$	467.060	945.100	6.5610	87.970	0.2580	90.000
$C_{8\text{-}11}$	378.030	1090.800	9.8730	120.710	0.3540	100.000
$C_{12\text{-}16}$	272.240	1265.800	16.2910	187.980	0.5280	300.000
$C_{17\text{-}26}$	201.730	1440.200	26.4840	286.400	0.7590	350.000
C_{27+}	136.060	1636.800	38.2100	436.140	0.0920	500.000

Binary Interaction Coefficents

	CO_2	$C_{3\text{-}4}$	$C_{5\text{-}7}$	$C_{8\text{-}11}$	$C_{12\text{-}16}$	$C_{17\text{-}26}$	C_{27+}
CO_2	0.0000						
$C_{3\text{-}4}$	0.1400	0.0000					
$C_{5\text{-}7}$	0.1400	0.0000	0.0000				
$C_{8\text{-}11}$	0.1400	0.0000	0.0000	0.0000			
$C_{12\text{-}16}$	0.1400	0.0000	0.0000	0.0000	0.0000		
$C_{17\text{-}26}$	0.1400	0.0000	0.0000	0.0000	0.0000	0.0000	
C_{27+}	0.1400	0.0000	0.0000	0.0000	0.0000	0.0000	0.0000

Table 7-8

Physical Properties of Berea Sandstone Core

Length : 6 ft
Diameter : 2 inch
Pore volume : 700.0 cc
Porosity : 17.2%
Permeability (air) : 146 md
Connate water saturation : 35%
Temperature : 126.5 °F
Pressure : 1840 psia

Table 7-9

2-D Cross-Sectional Simulation Runs

Run #	Dimension	Physical Dispersion	K_y/K_z (md/md)	EOS Case	Cap. Press.	Oil Rec. % at 1.5 HCPV
22B	20 X 2	NO	146/146	#10	W/O	89.42
24B	20 X 4	NO	146/146	#10	W/O	87.72
28B	20 X 8	NO	146/146	#10	W/O	82.25
22A	20 X 2	NO	146/146	#2	W/O	89.20
24A	20 X 4	NO	146/146	#2	W/O	86.80
28A	20 X 8	NO	146/146	#2	W/O	86.02
42A	40 X 2	NO	146/146	#2	W/O	88.98
44A	40 X 4	NO	146/146	#2	W/O	86.98
48A	40 X 8	NO	146/146	#2	W/O	82.16
24X	20 X 4	$\alpha_l = 0.10$ $\alpha_t = 0.01$	146/146	#2	W/O	88.78
24Y	20 X 4	$\alpha_l = 0.10$ $\alpha t = 0.00$	146/146	#2	W/O	87.43
44Y	40 X 4	NO	146/14.6	#2	W/O	81.50
24Z	20 X 4	NO	146/146	#2	W/	92.10

Note: Other reservoir data are same as previous case

Oil Recovery at 1.5 HCPV CO_2 injected

Figure 7.1 Pressure-Composition Diagram for Amarume S.T.O. and CO2 Mixtures at 126.5 °F

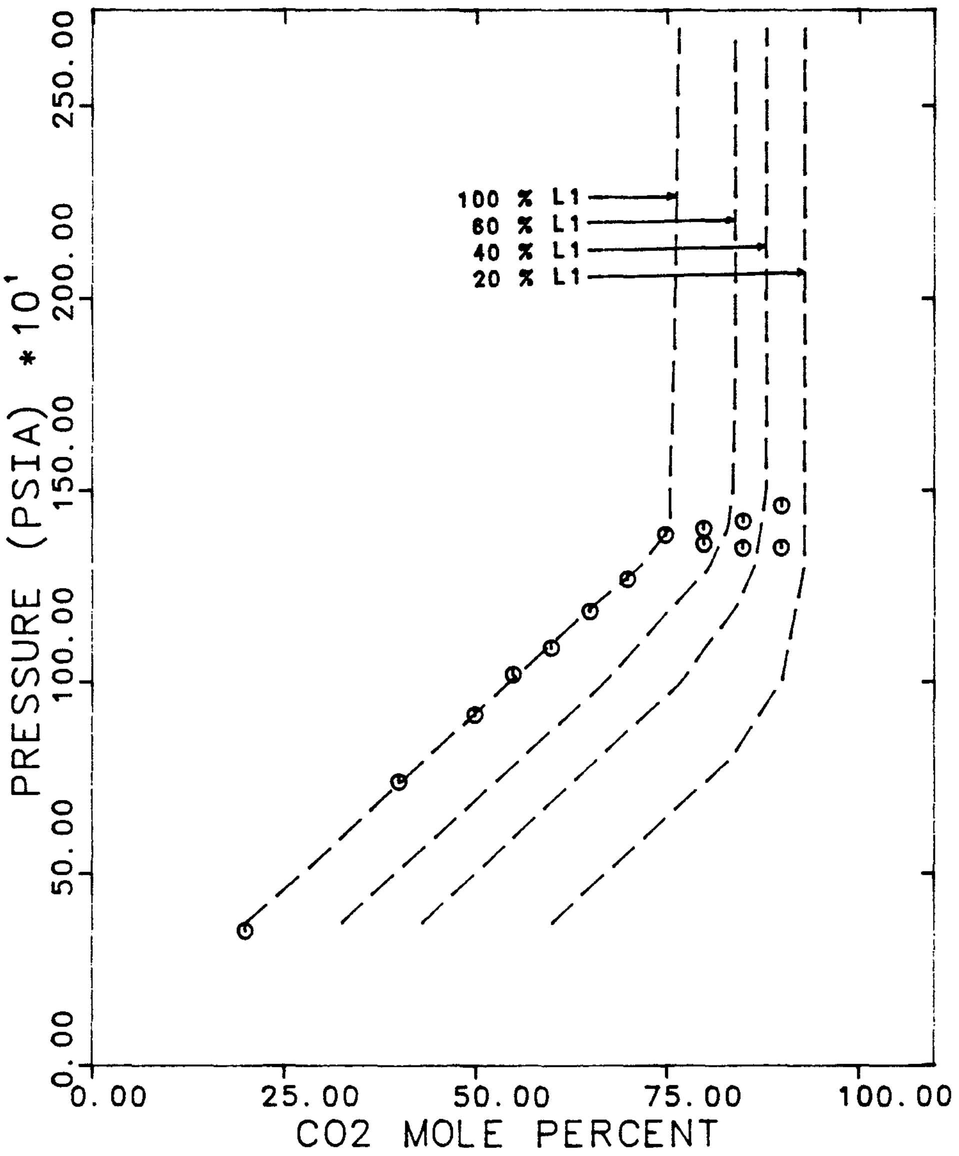

Figure 7.2 Experimental Results of Slim-tube Displacement Tests

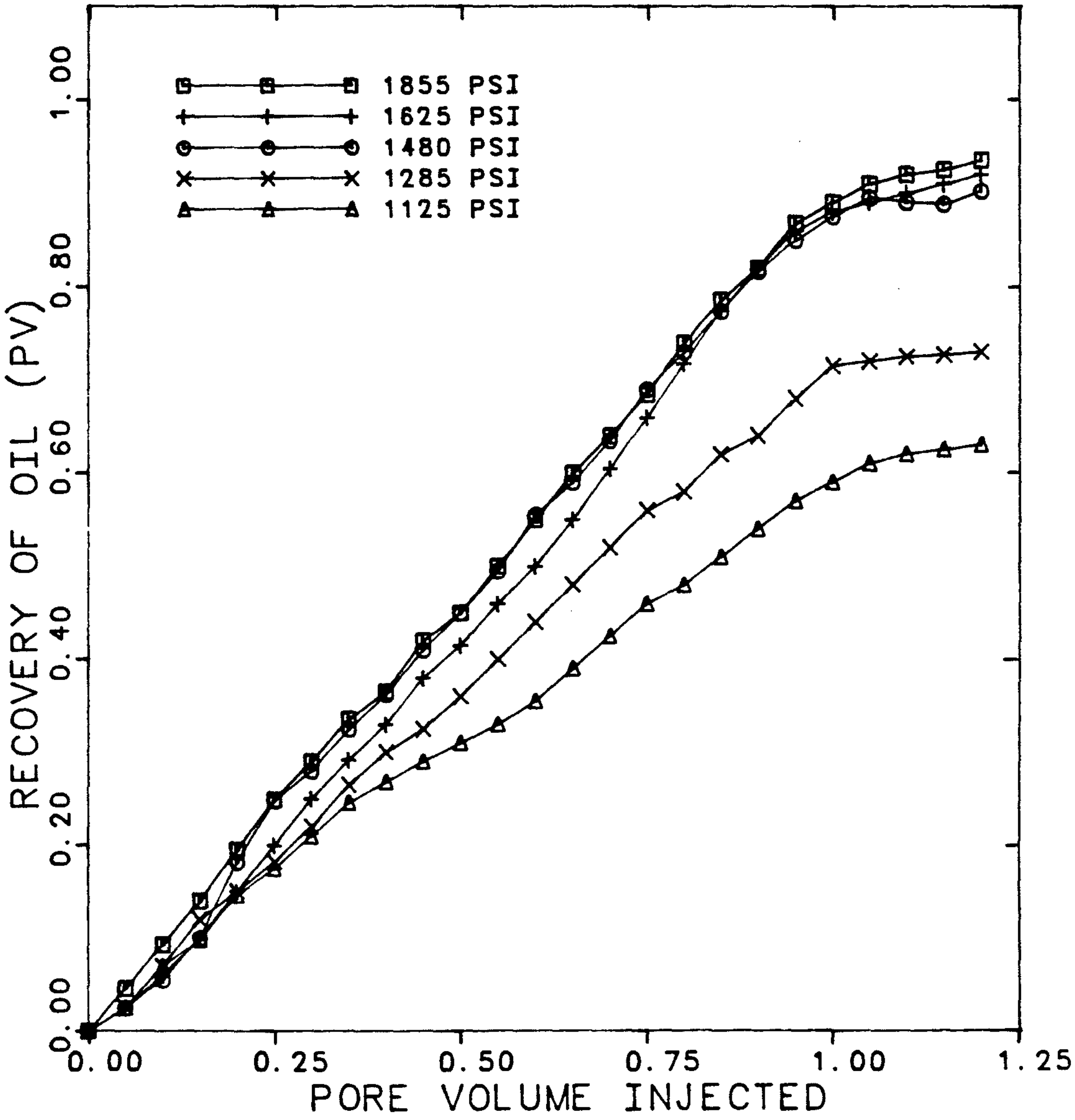

Figure 7.3 Experimental Results of Coreflood Displacement Test

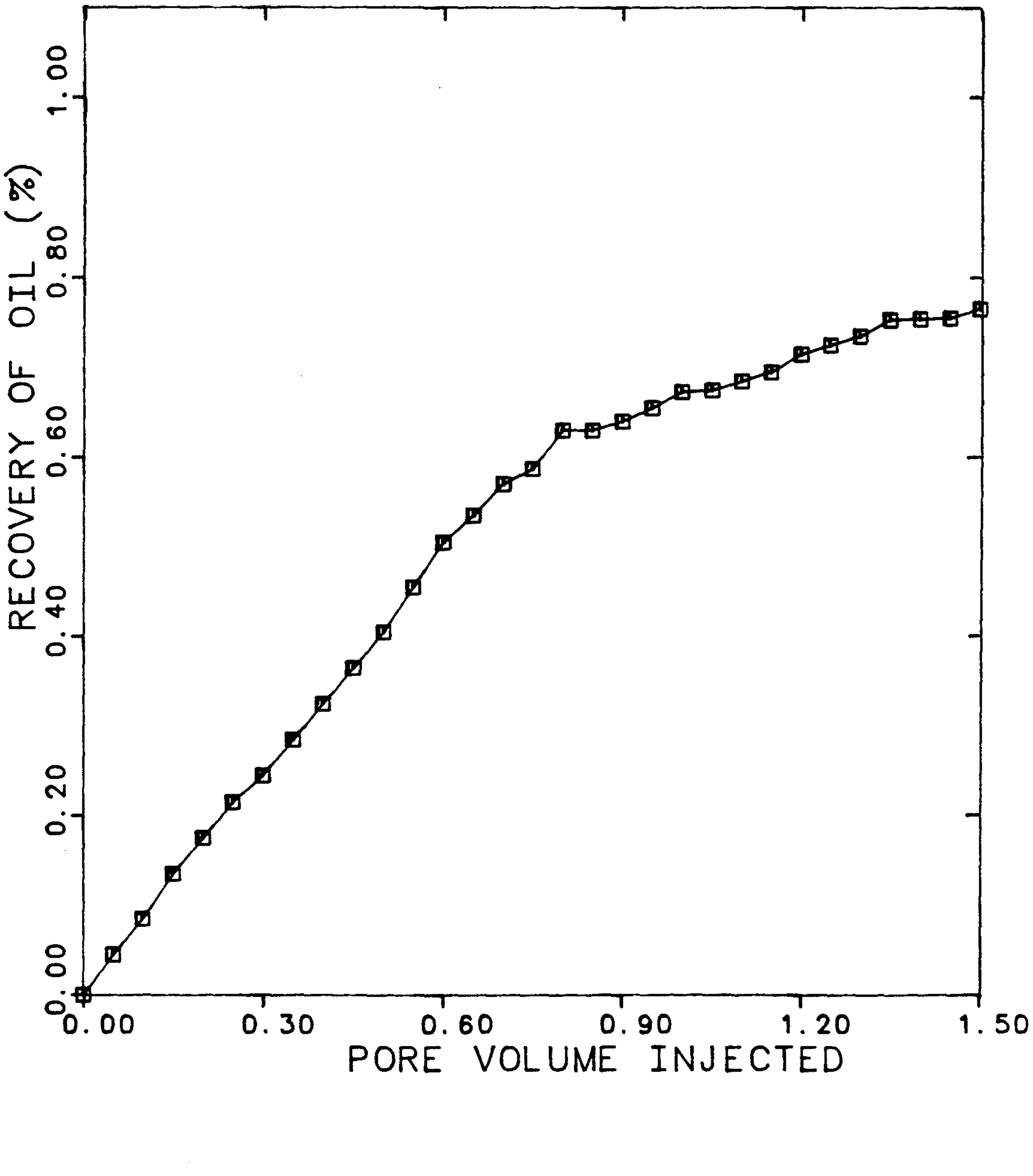

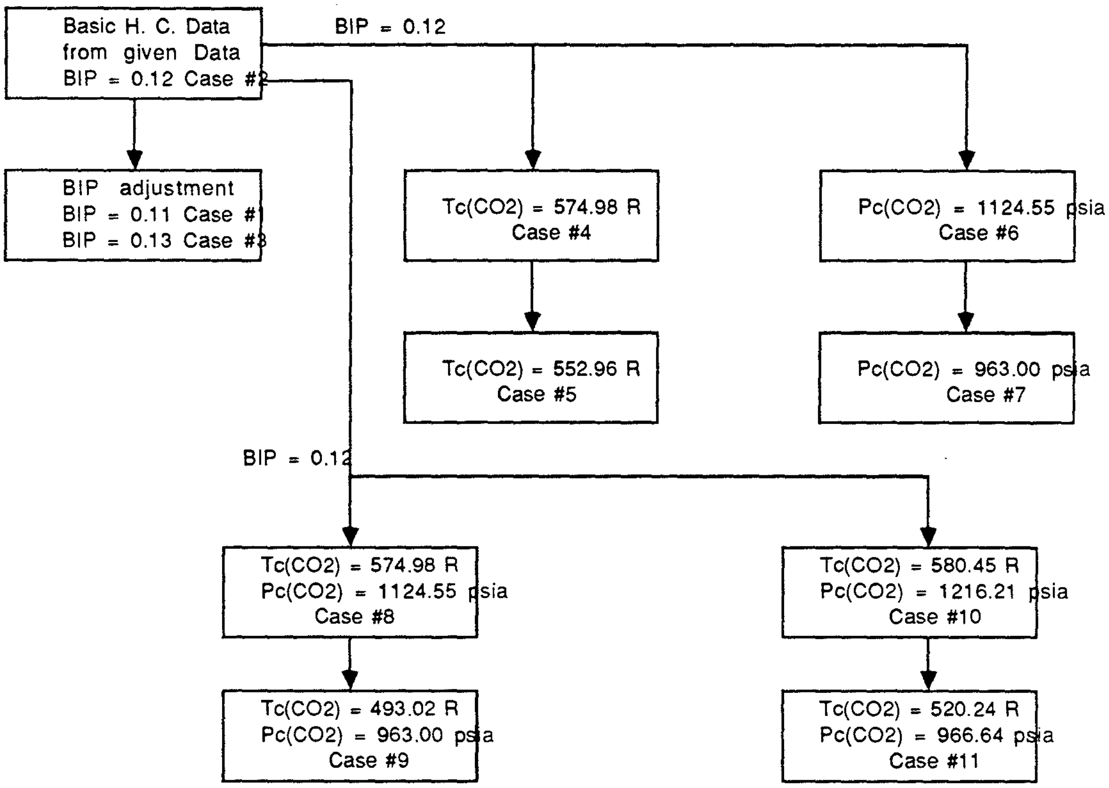

Figure 7.4 Sensitivity Study Cases of the EOS Parameter effects on Phase Behavior and Slim-tube Test

Figure 7.5 Comparison of Calculated and Experimental Phase Behavior using Case #2 EOS Parameters

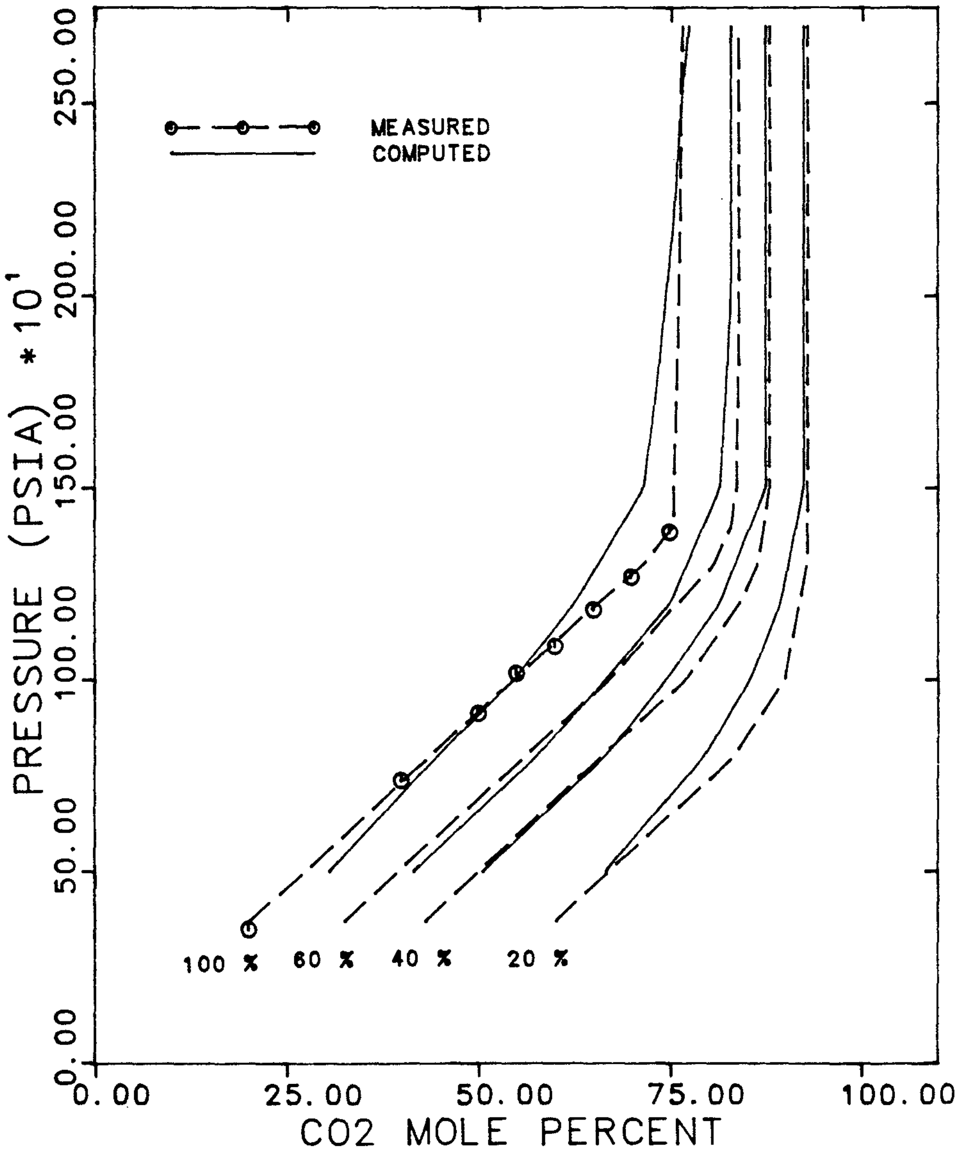

Figure 7.6 Comparison of Calculated Recoveries at 1855 psia

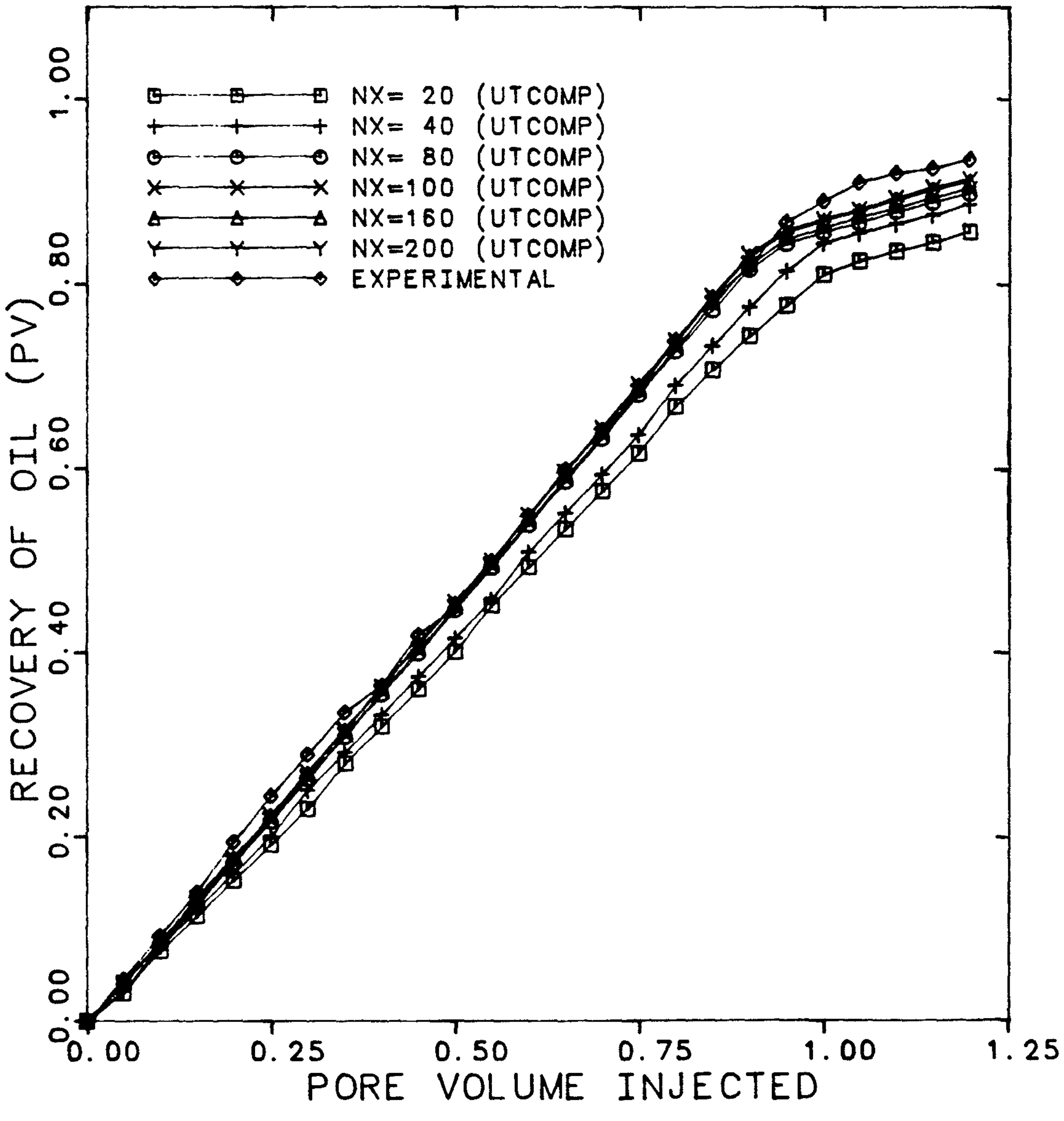

Figure 7.7 Comparison of Calculated Phase Behavior using Different sets of Binary Interaction Coefficients (Cases #1,2,&3)

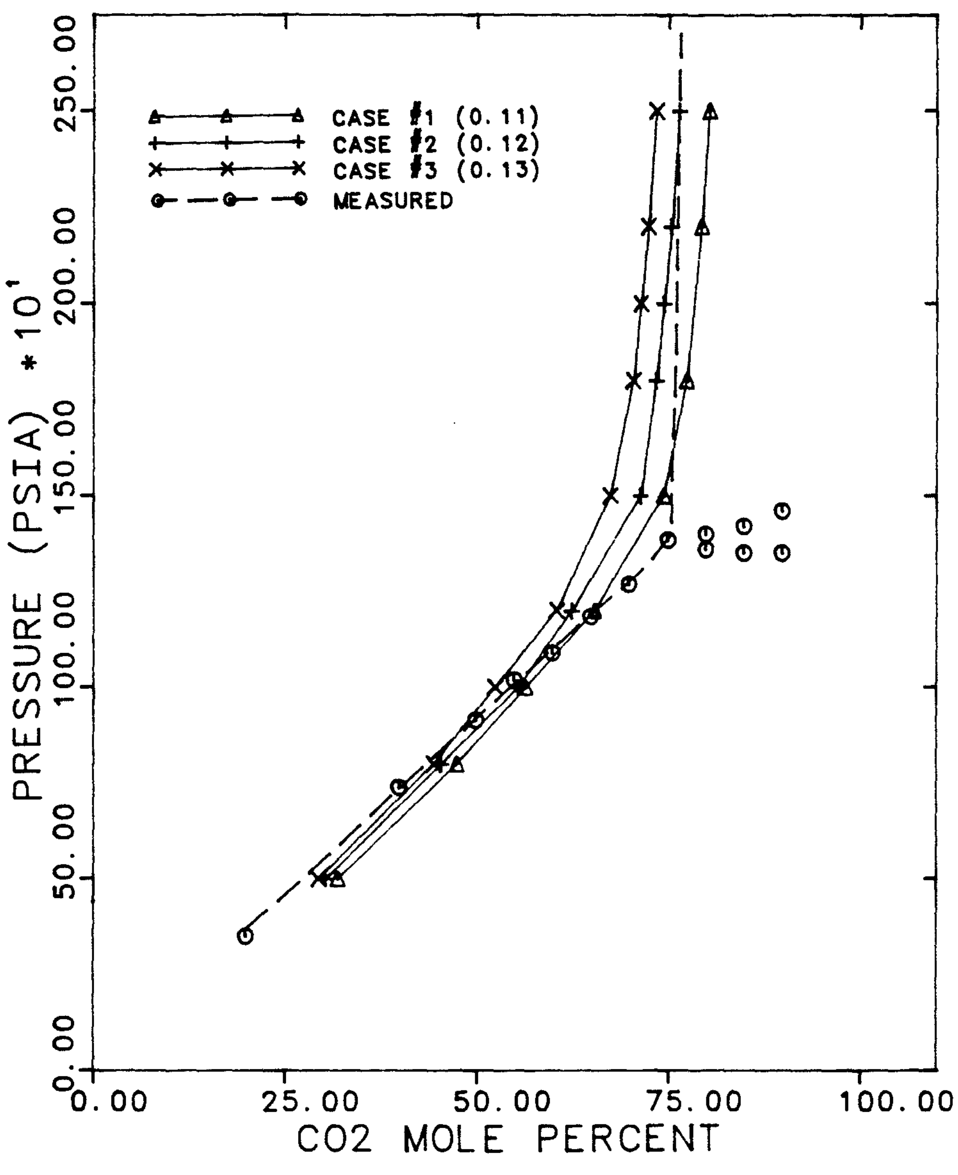

Figure 7.8 Comparison of Calculated and Experimental Recovery Curves using Different sets of Binary Interaction Coefficient (Cases # 1,2,&3)

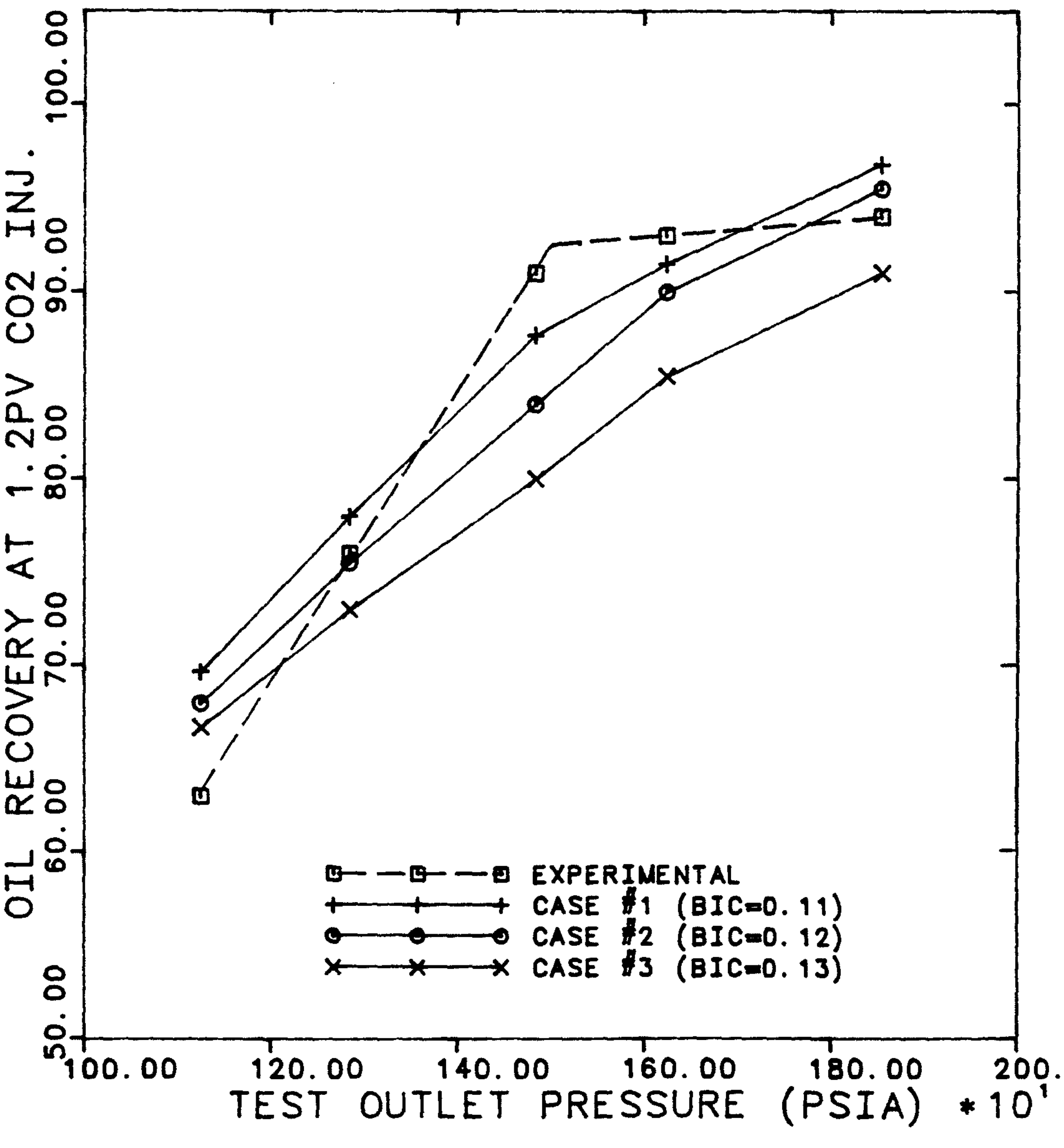

Figure 7.9 Comparison of Calculated Phase Behavior for Cases #2,4,&5

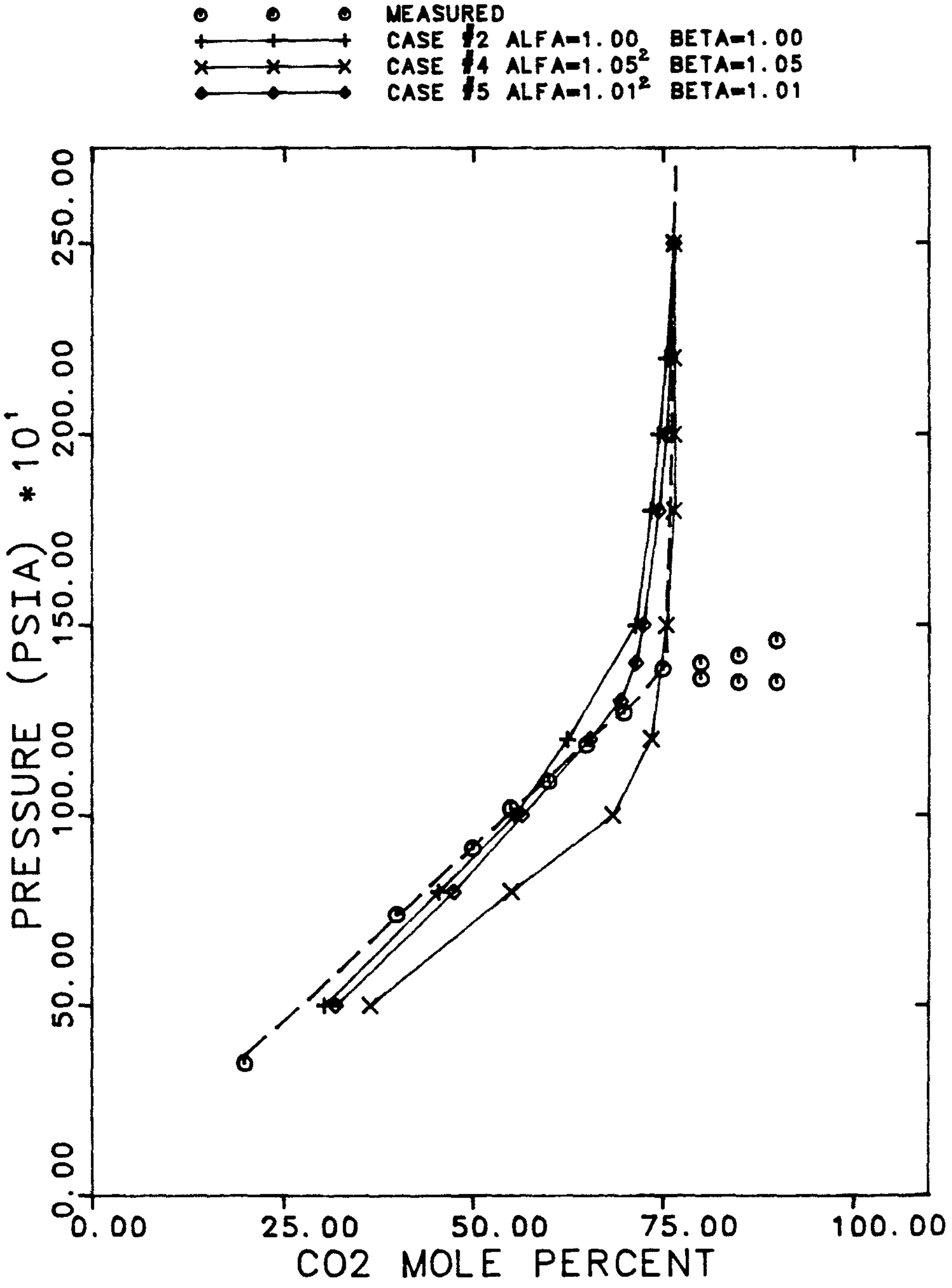

Figure 7.10 Comparison of Calculated and Experimental Recovery Curves for Cases # 2,4,&5

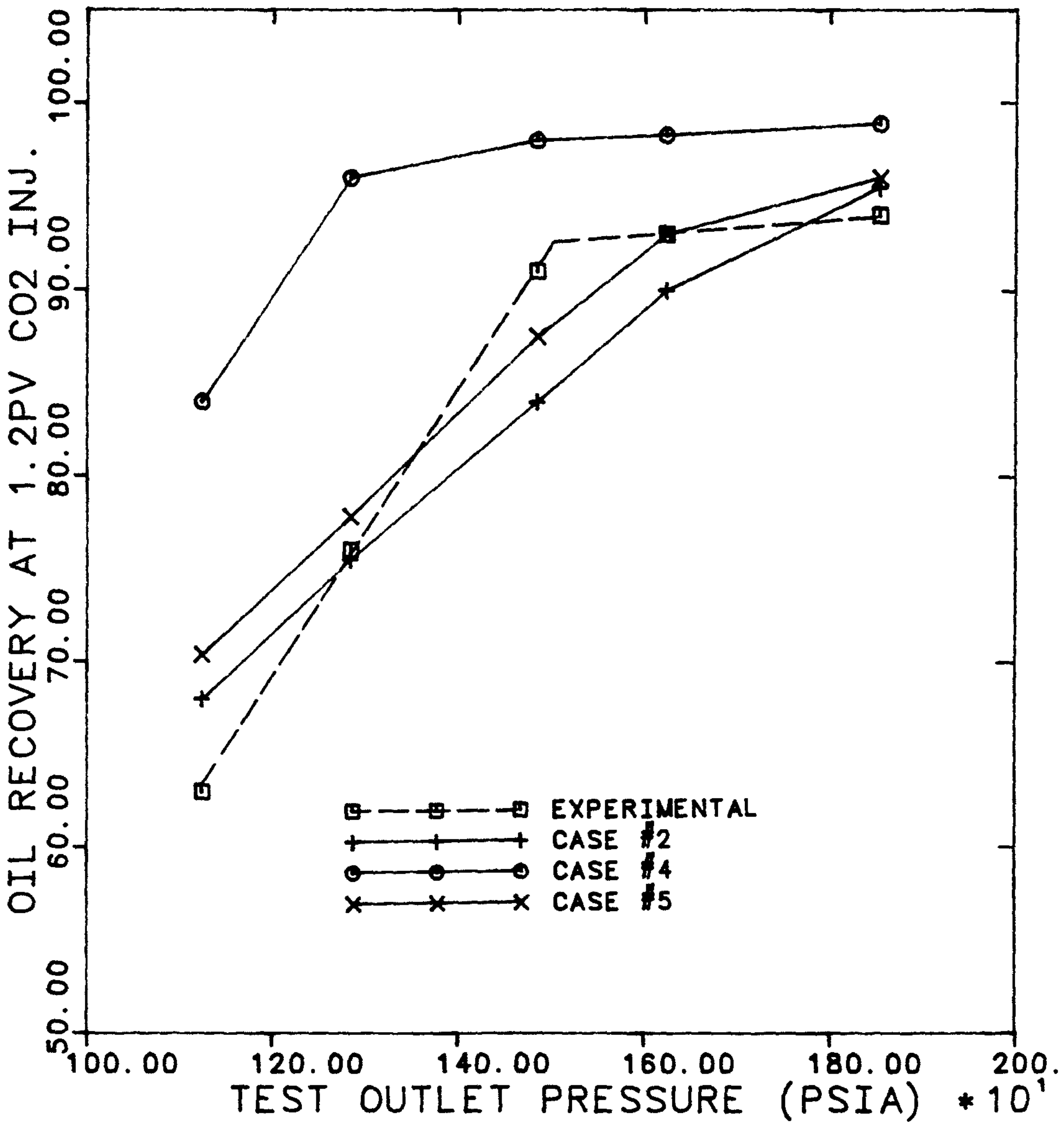

Figure 7.11 Comparison of Calculated Phase Behavior for Cases #2,6,&7

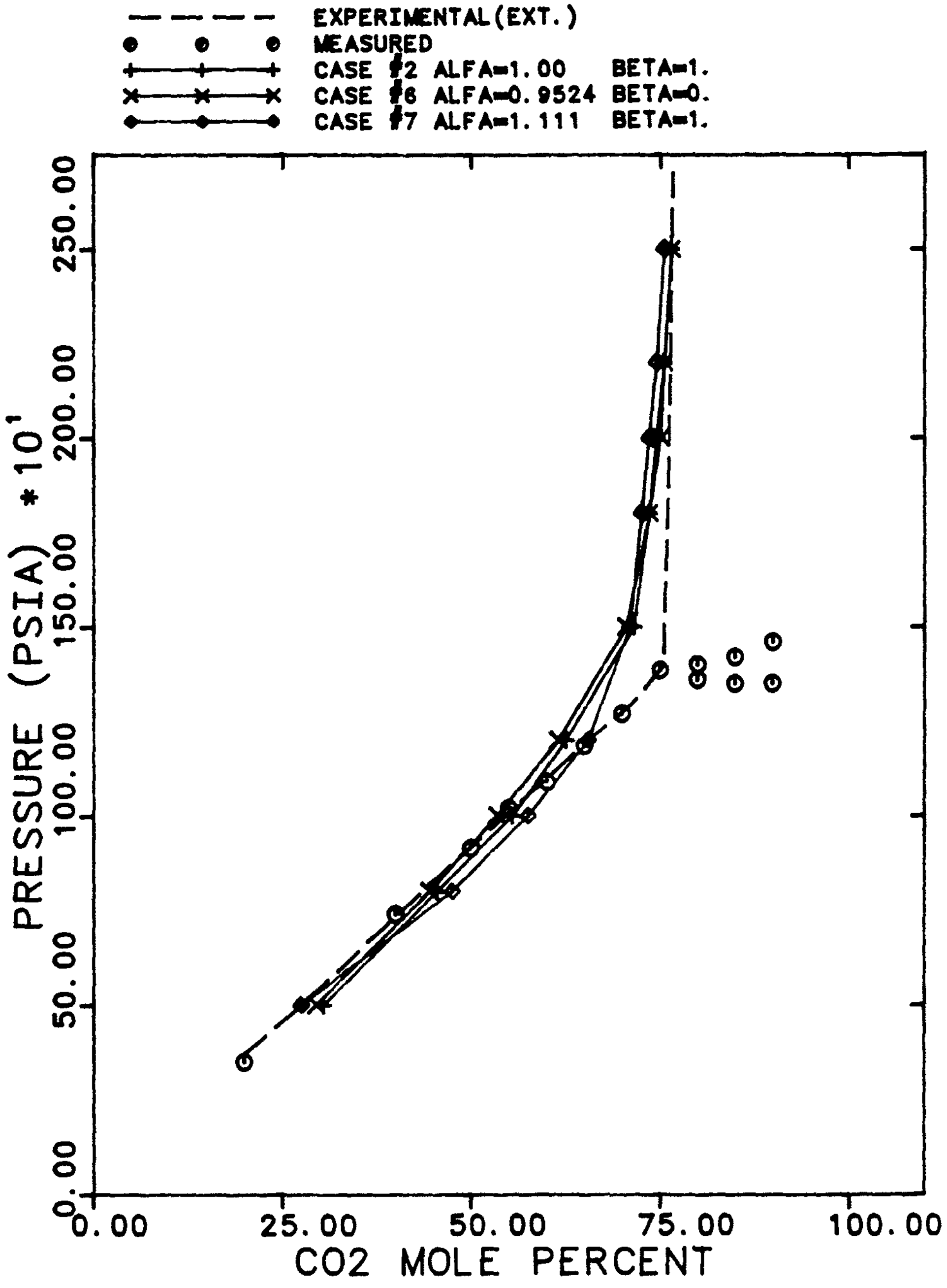

Figure 7.12 Comparison of Calculated and Experimental Recovery Curves for Cases # 2,6,&7

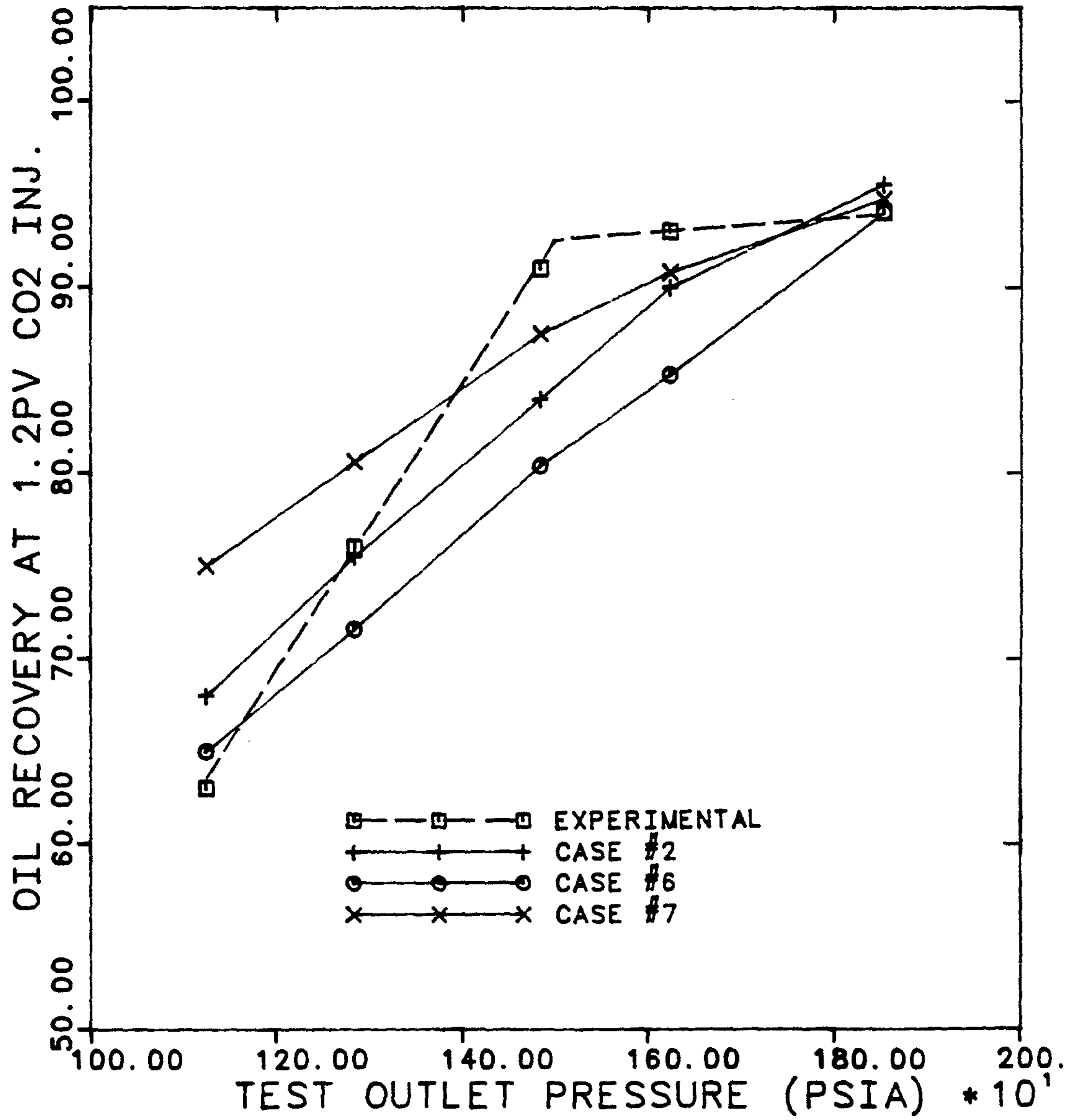

Figure 7.13 Comparison of Calculated Phase Behavior for Cases #2,8,&9

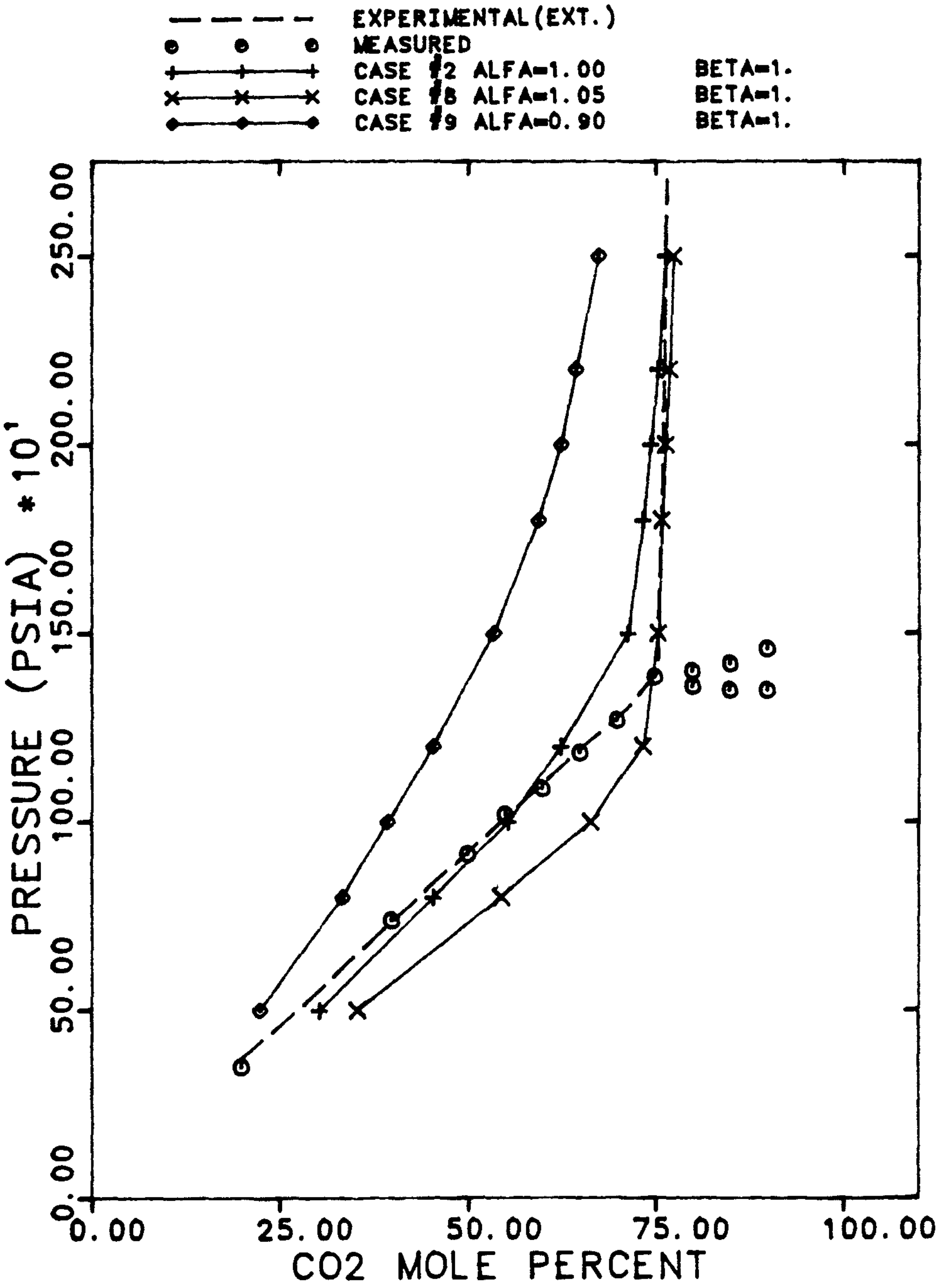

Figure 7.14 Comparison of Calculated and Experimental Recovery Curves for Cases # 2,8,&9

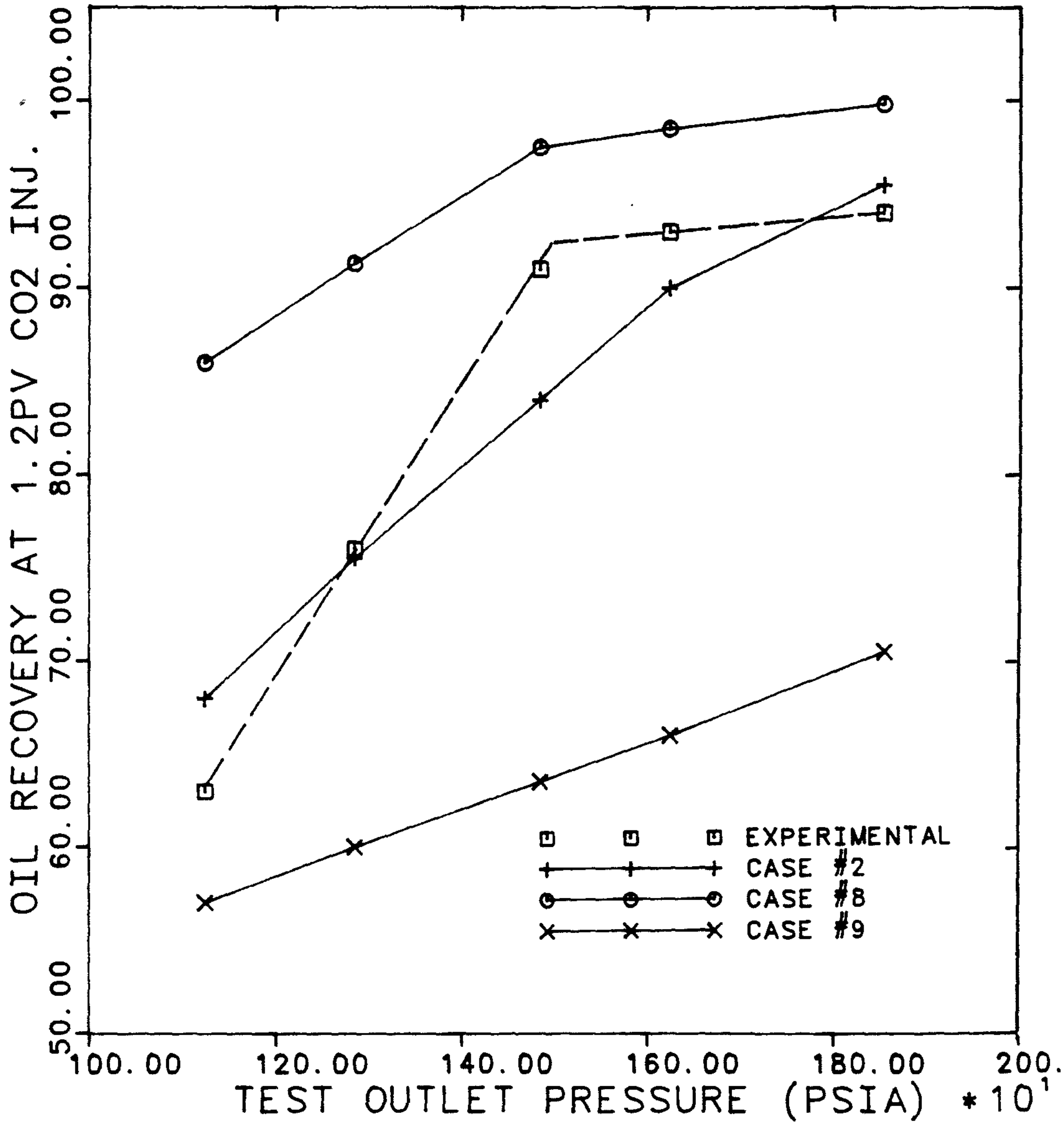

Figure 7.15 Comparison of Calculated Phase Behavior for Cases #2,10,&11

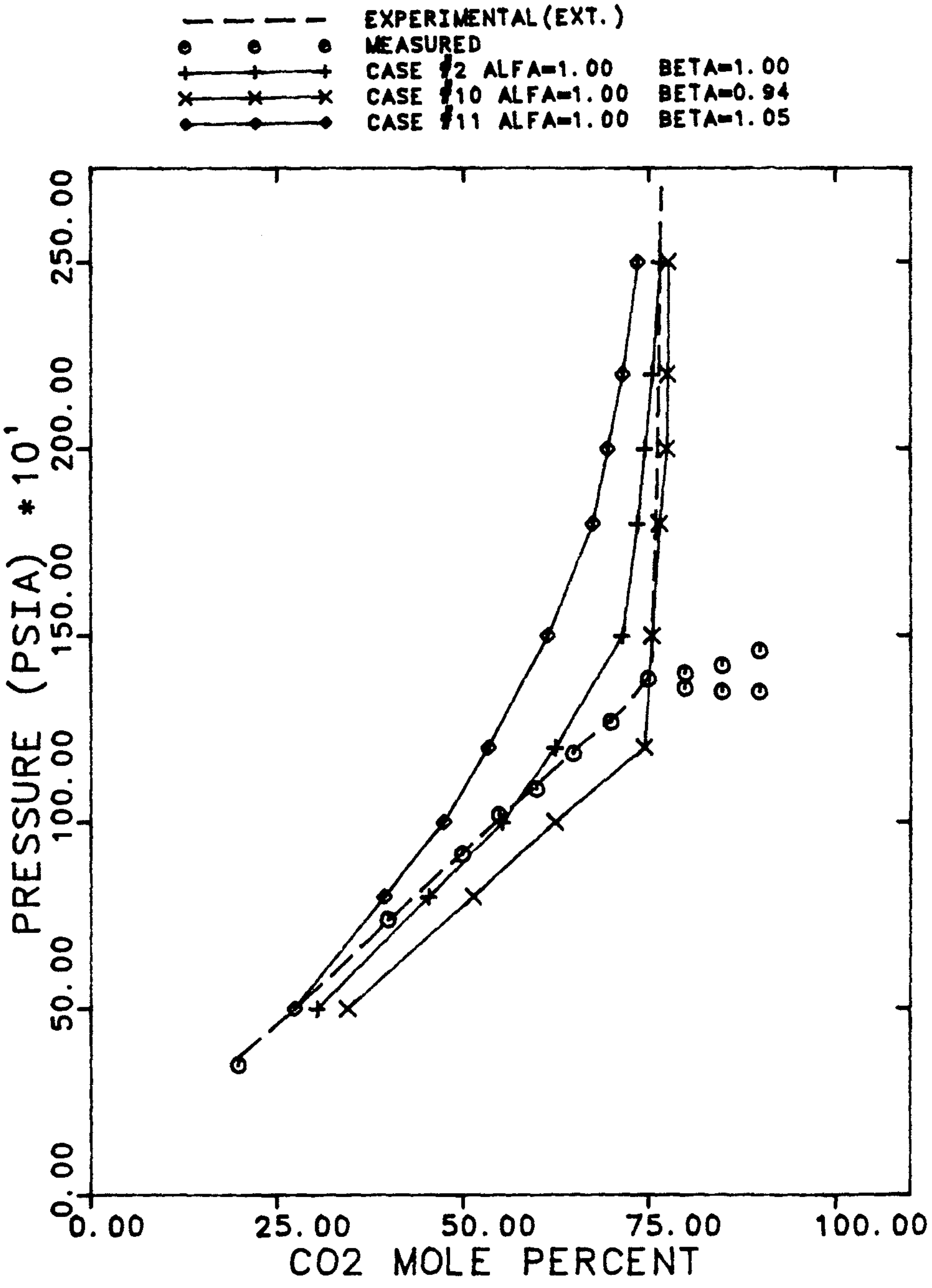

Figure 7.16 Comparison of Calculated and Experimental Recovery Curves for Cases # 2,10,&11

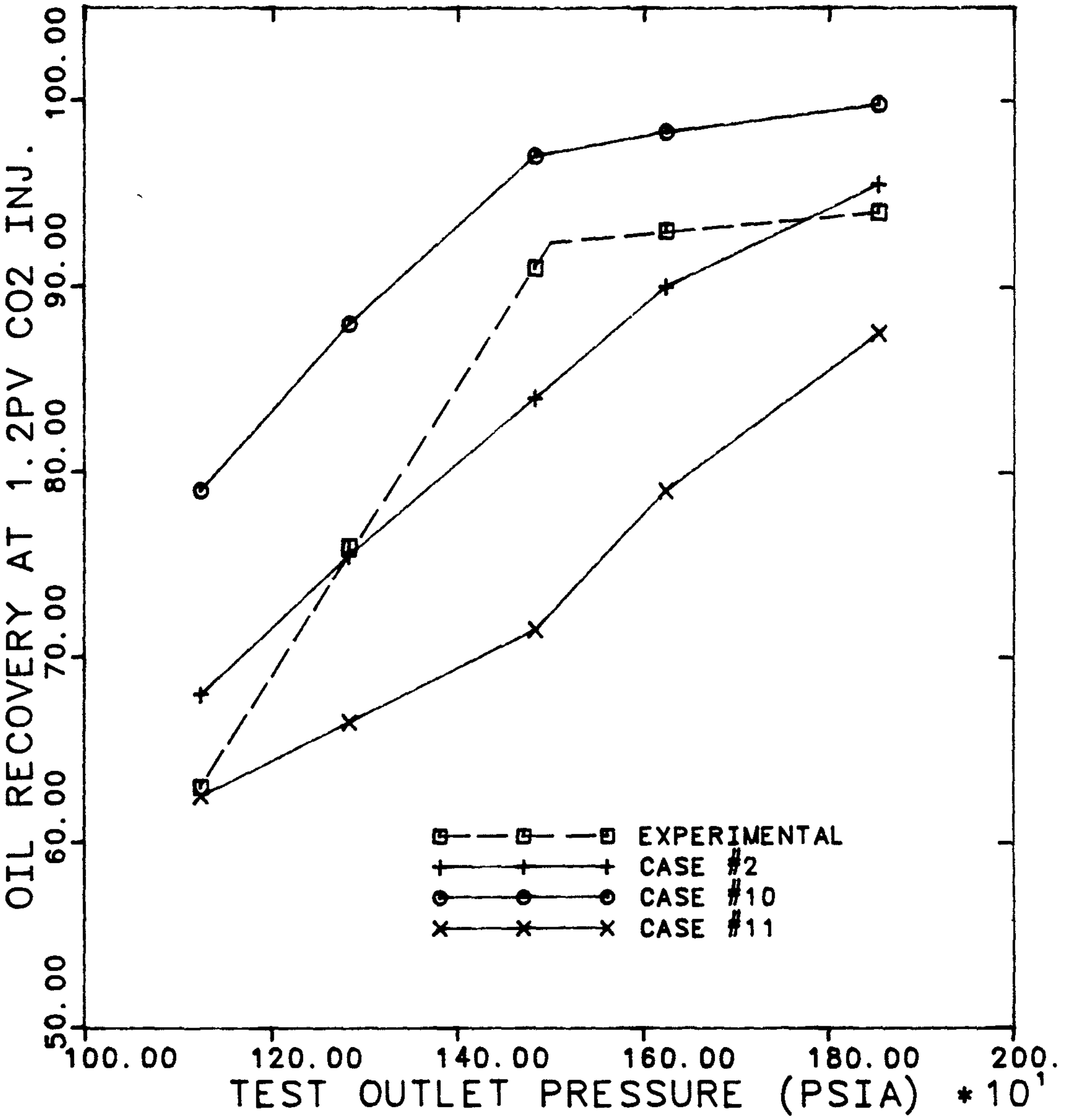

Figure 7.17 Comparison of Calculated and Experimental Phase Behavior using Case #A EOS parameters

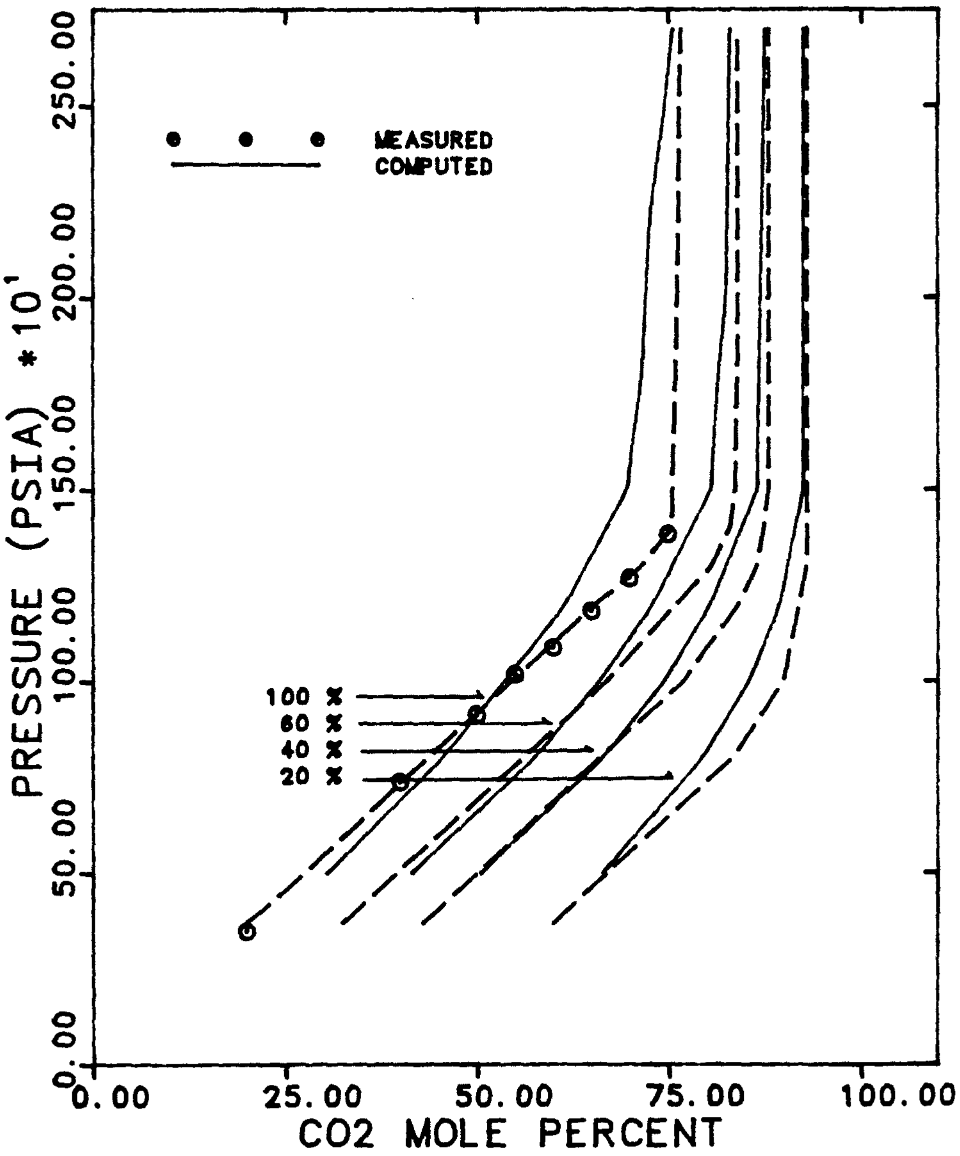

Figure 7.18 Comparison of Calculated and Experimental Phase Behavior using Case #B EOS parameter

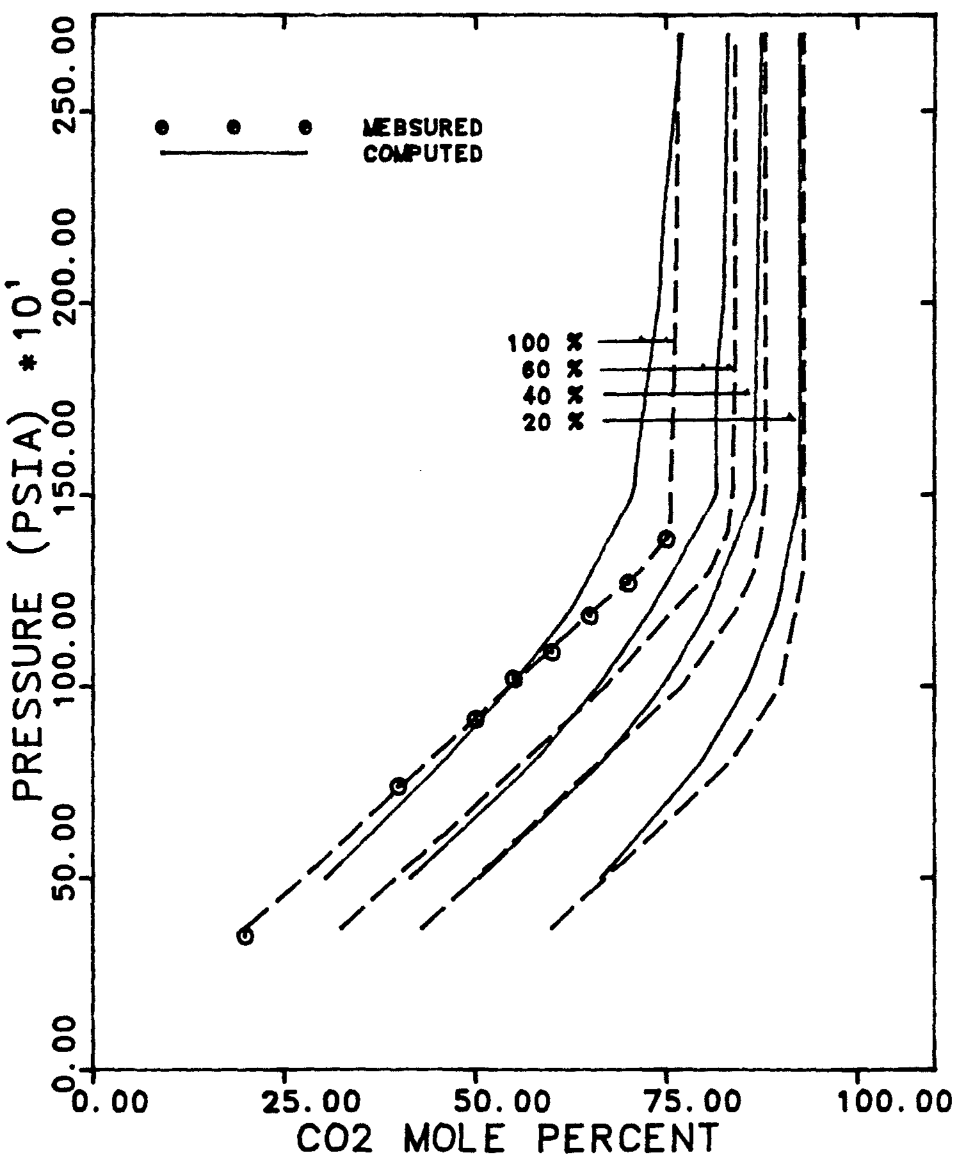

Figure 7.19 Comparison of Calculated and Experimental Phase Behavior using Case #C EOS parameter

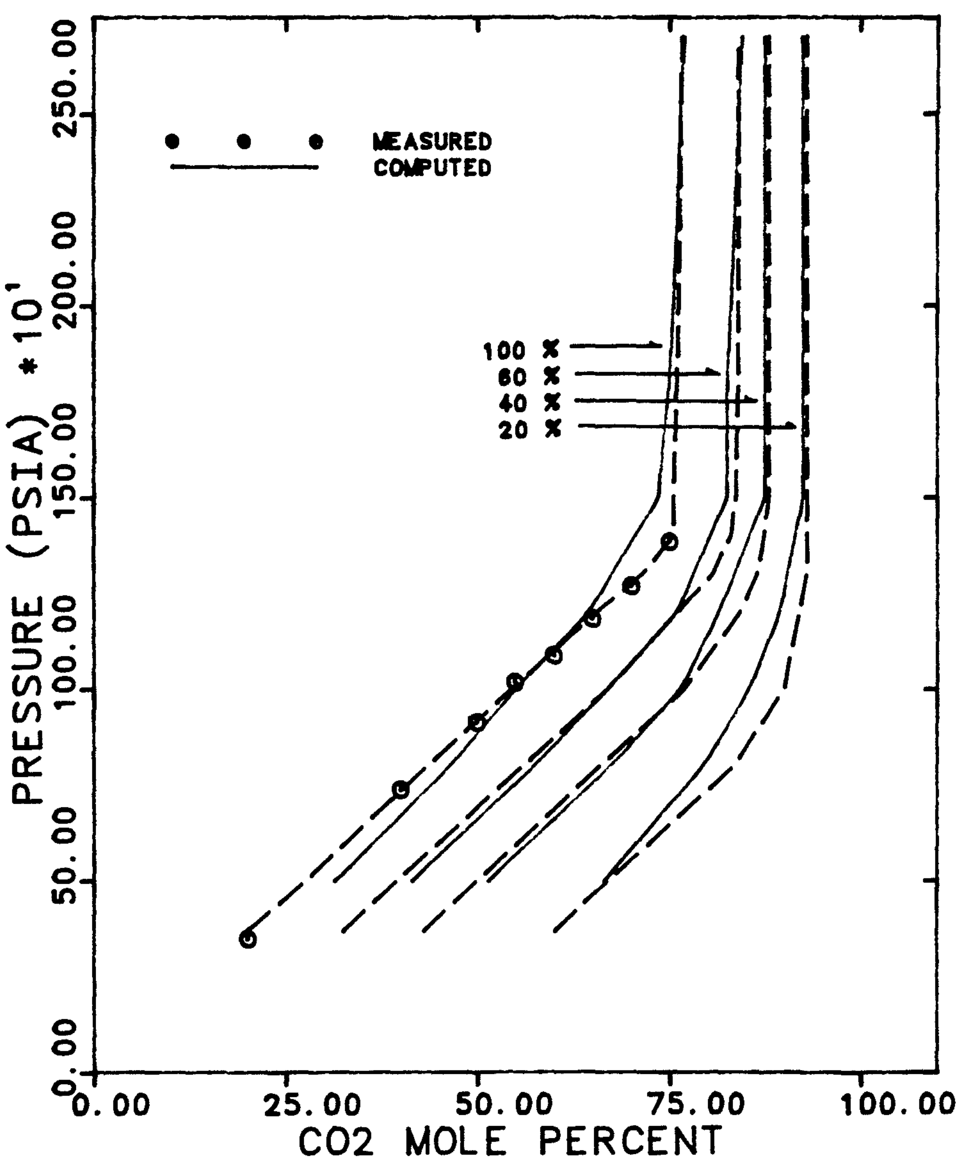

Figure 7.20 Comparison of Calculated and Experimental Phase Behavior using Case #D EOS parameter

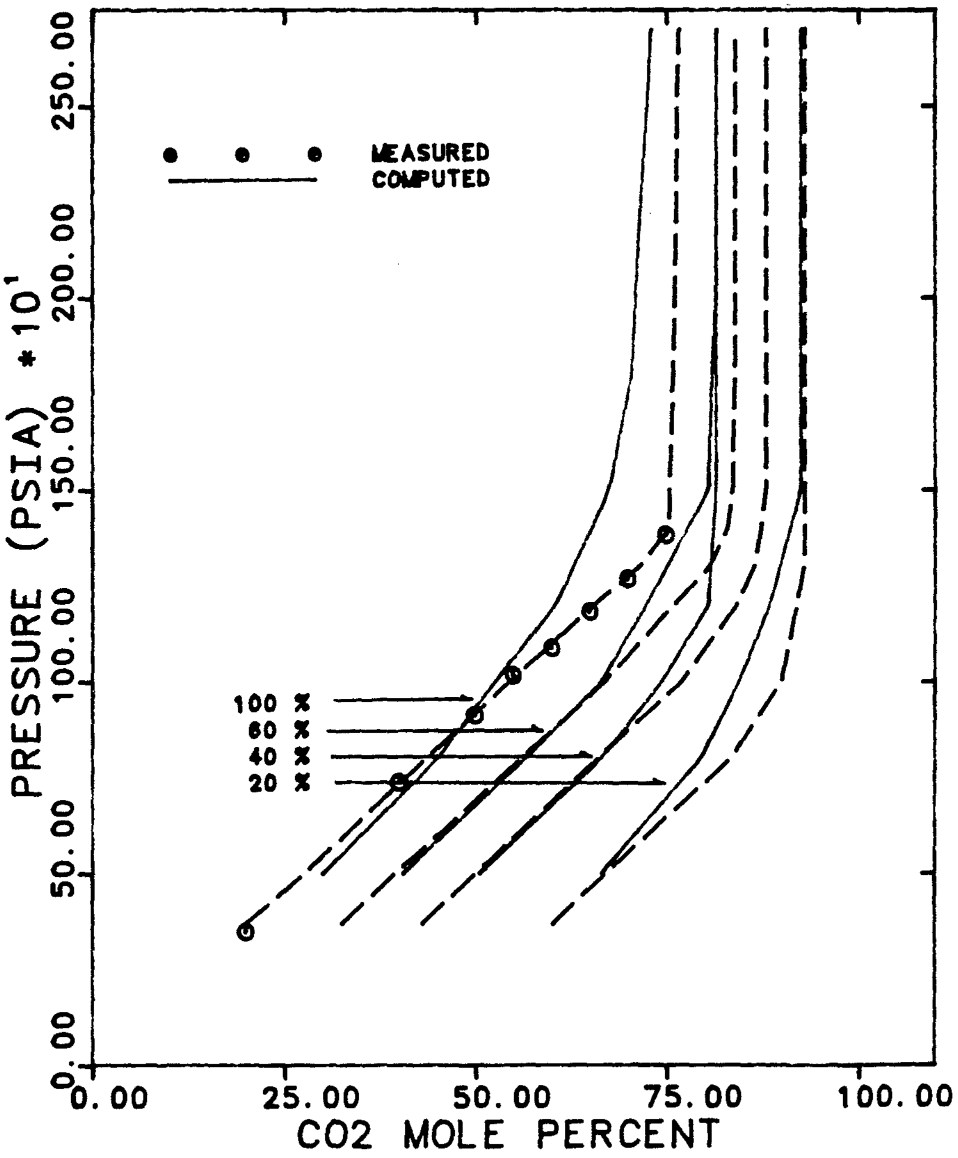

Figure 7.21 Comparison of Calculated Phase Behavior using Different sets of Binary Interaction Coefficients (Cases #10,10A,&10B)

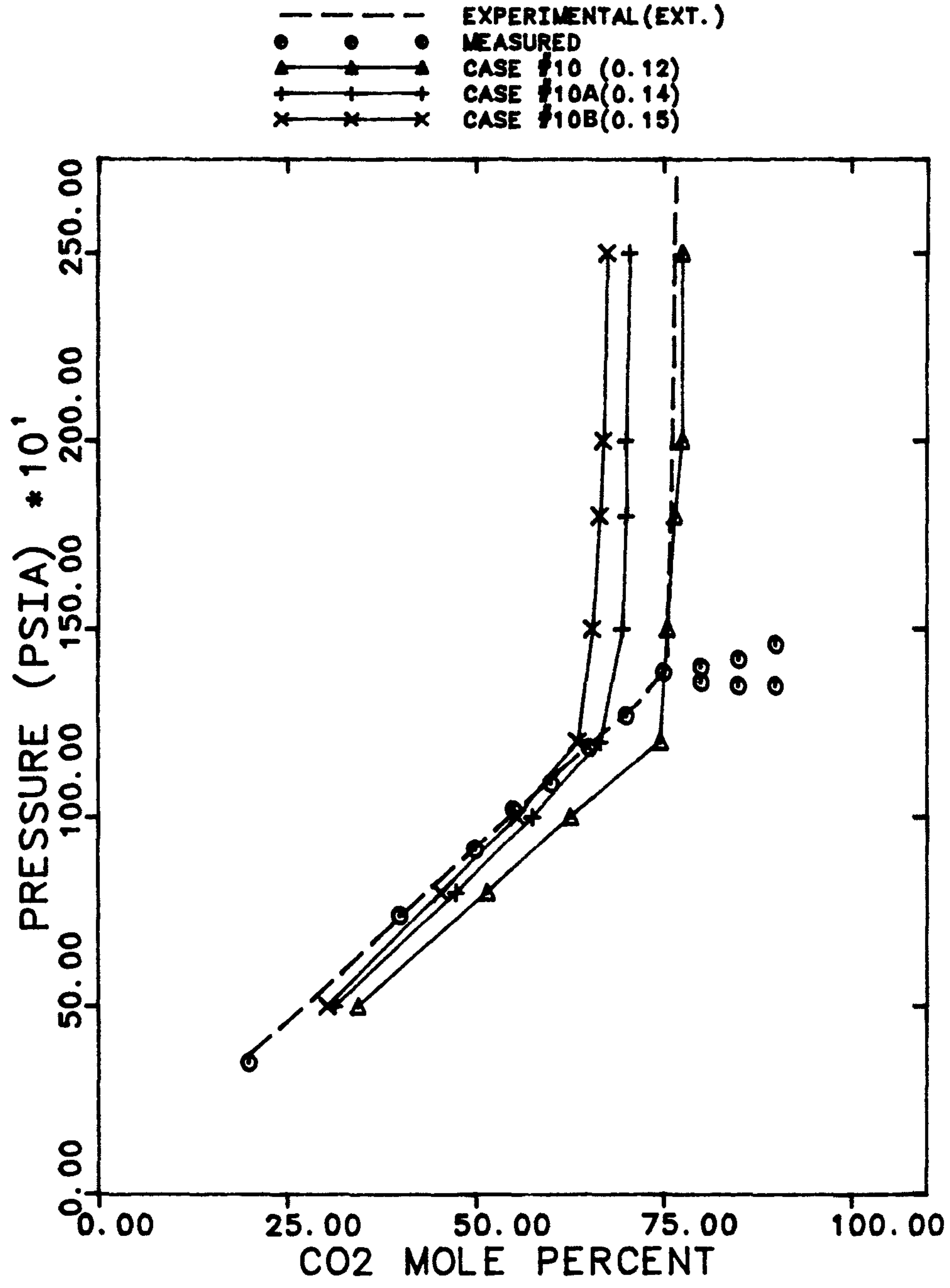

Figure 7.22 Comparison of Calculated and Experimental Recovery Curves for Cases # 2,10A,&10B

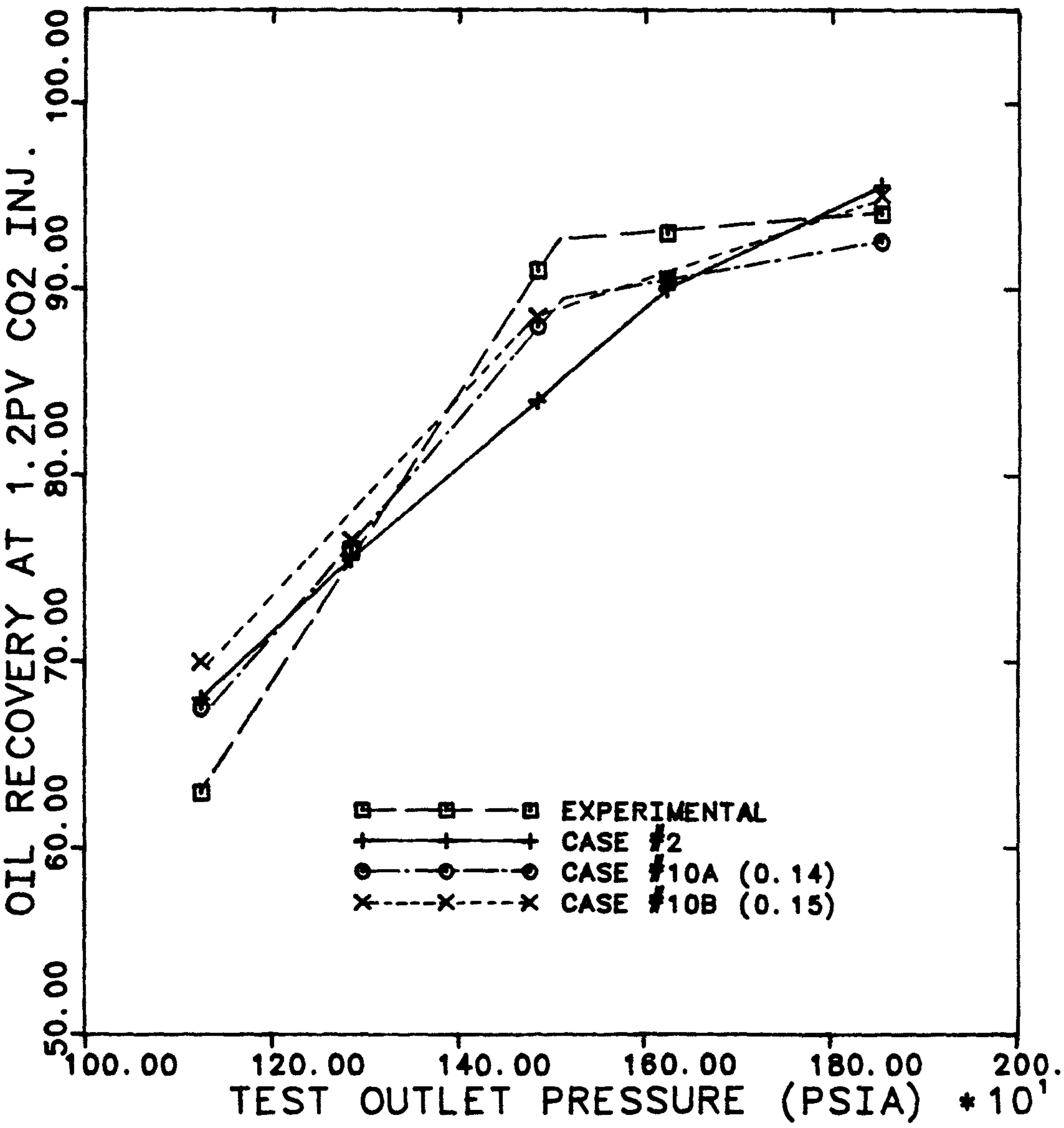

Figure 7.23 Comparison of Calculated and Experimental Recovery Curves for Case # 2 and the Case of 6 components with $\delta_{ij} = 0.12$

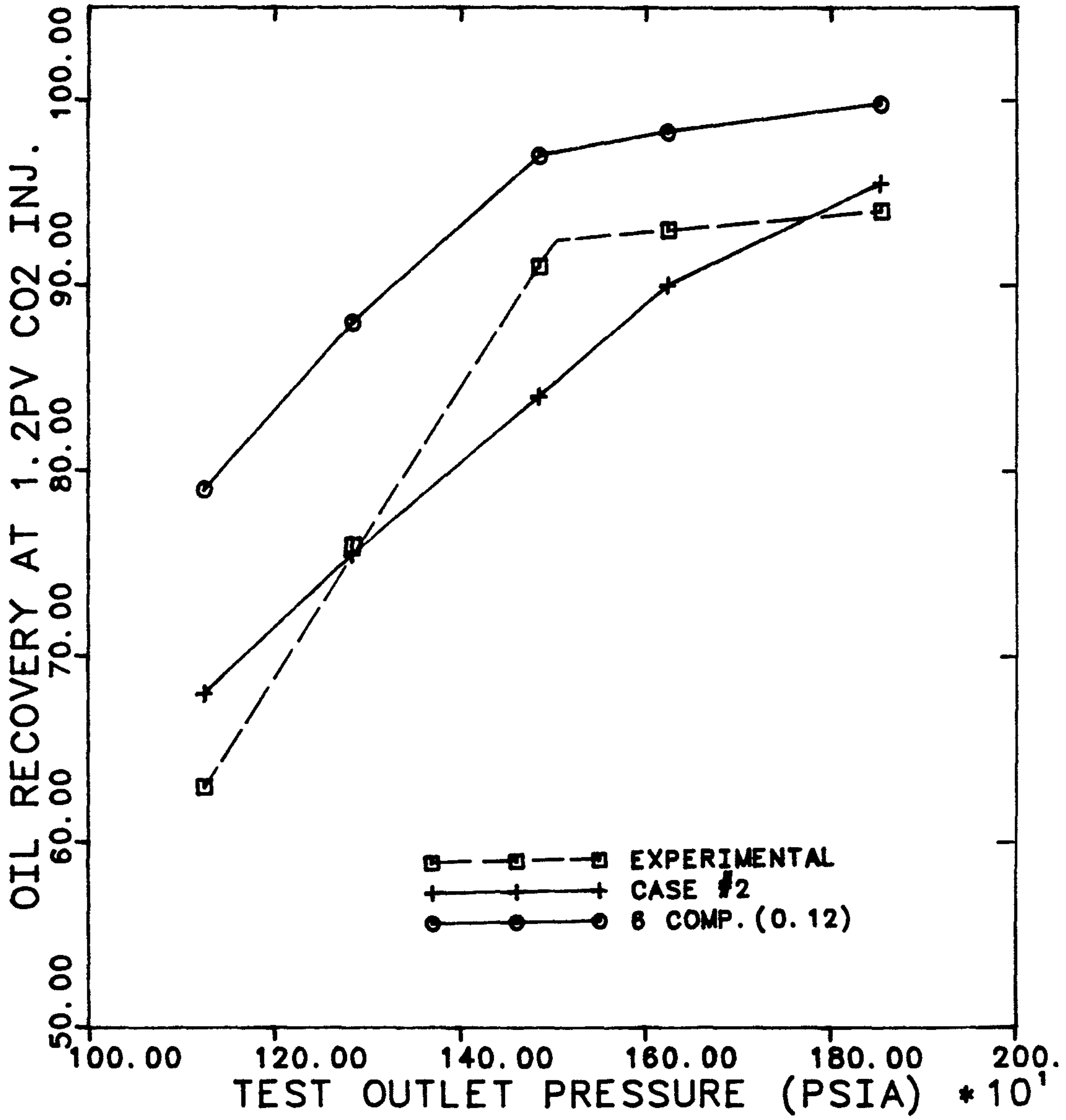

Figure 7.24 Comparison of Calculated Phase Behavior using 6 components ($\delta_{ij} = 0.15$)

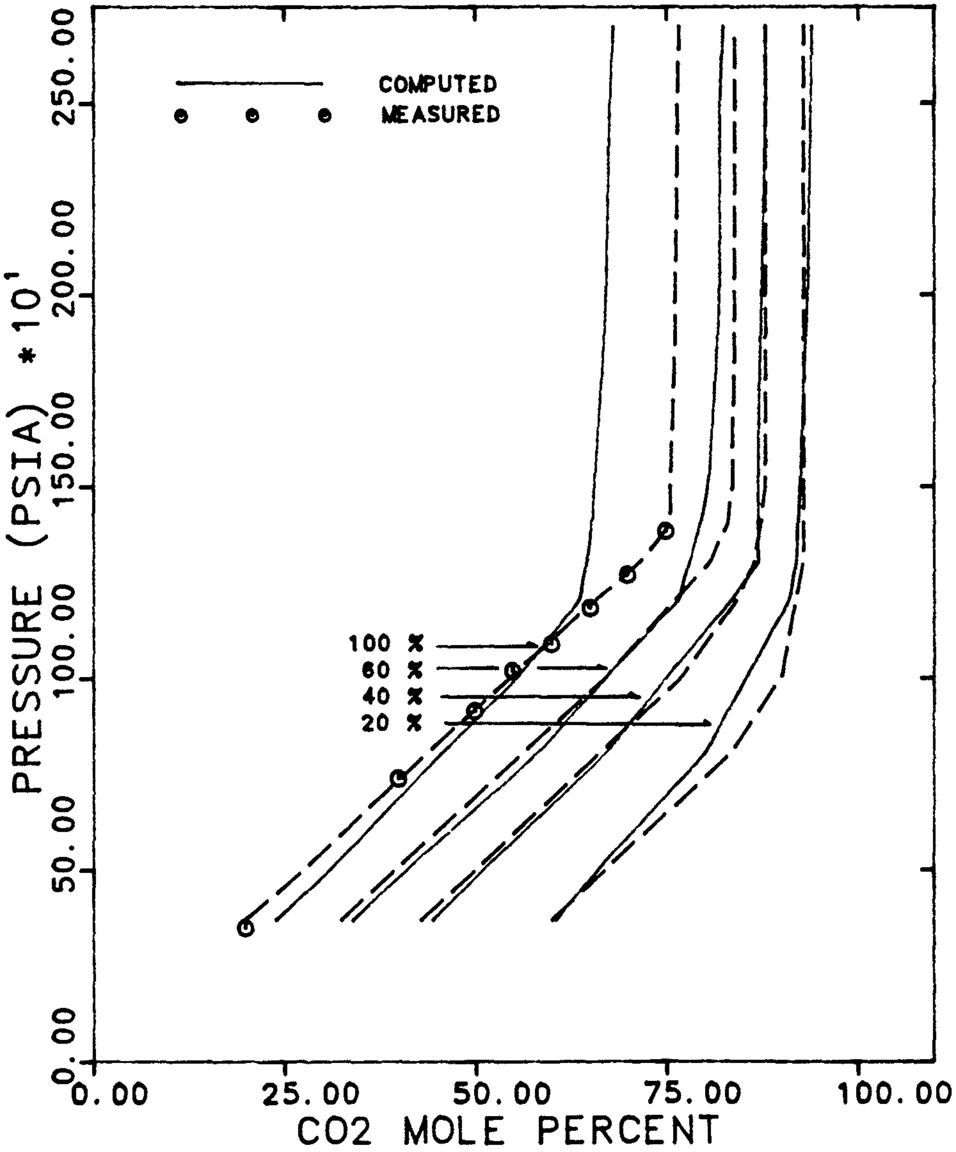

Figure 7.25 Comparison of Calculated and Experimental Recovery Curves using 6 components ($\delta_{ij} = 0.15$)

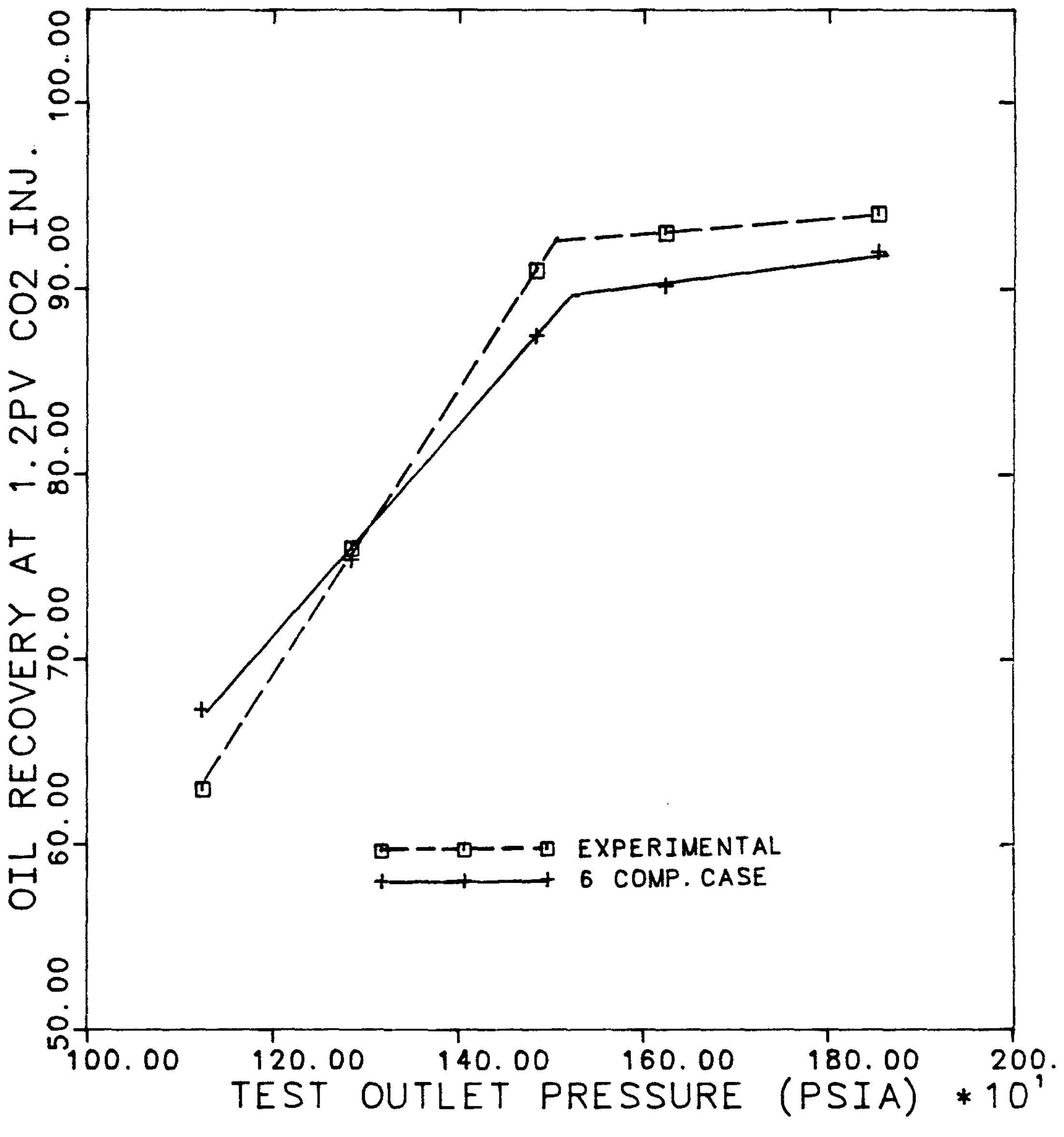

Figure 7.26 Comparison of Calculated Phase Behavior for Cases #2,5A,&10C

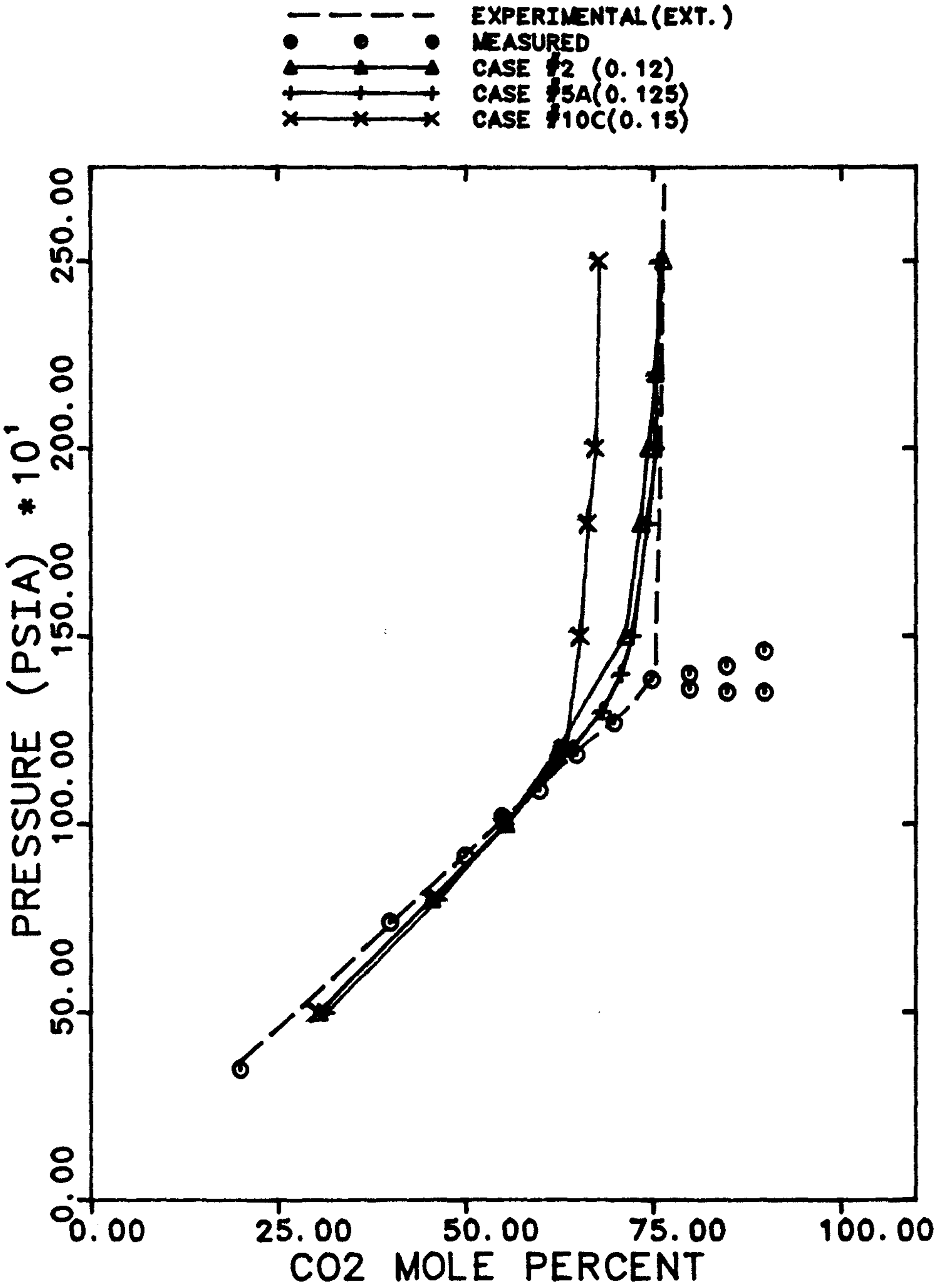

Figure 7.27 Comparison of Calculated and Experimental Recovery Curves for Cases # 2,5A,&10C

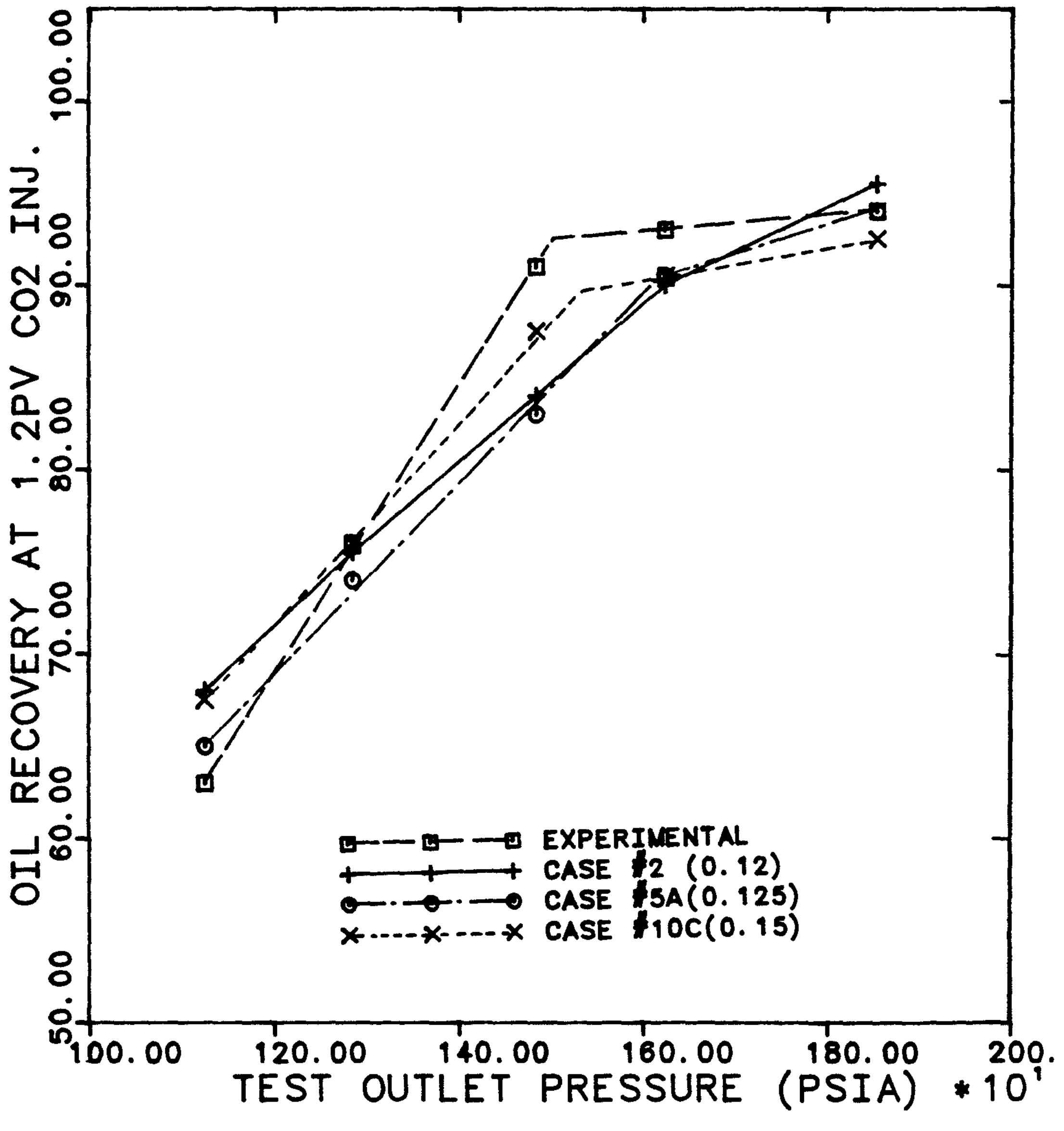

Fig. 7.28 Comparison of Calculated adn Experimental Slim-tube.
Test GOR for Case #2 at 1125, 1480, & 1855 psia

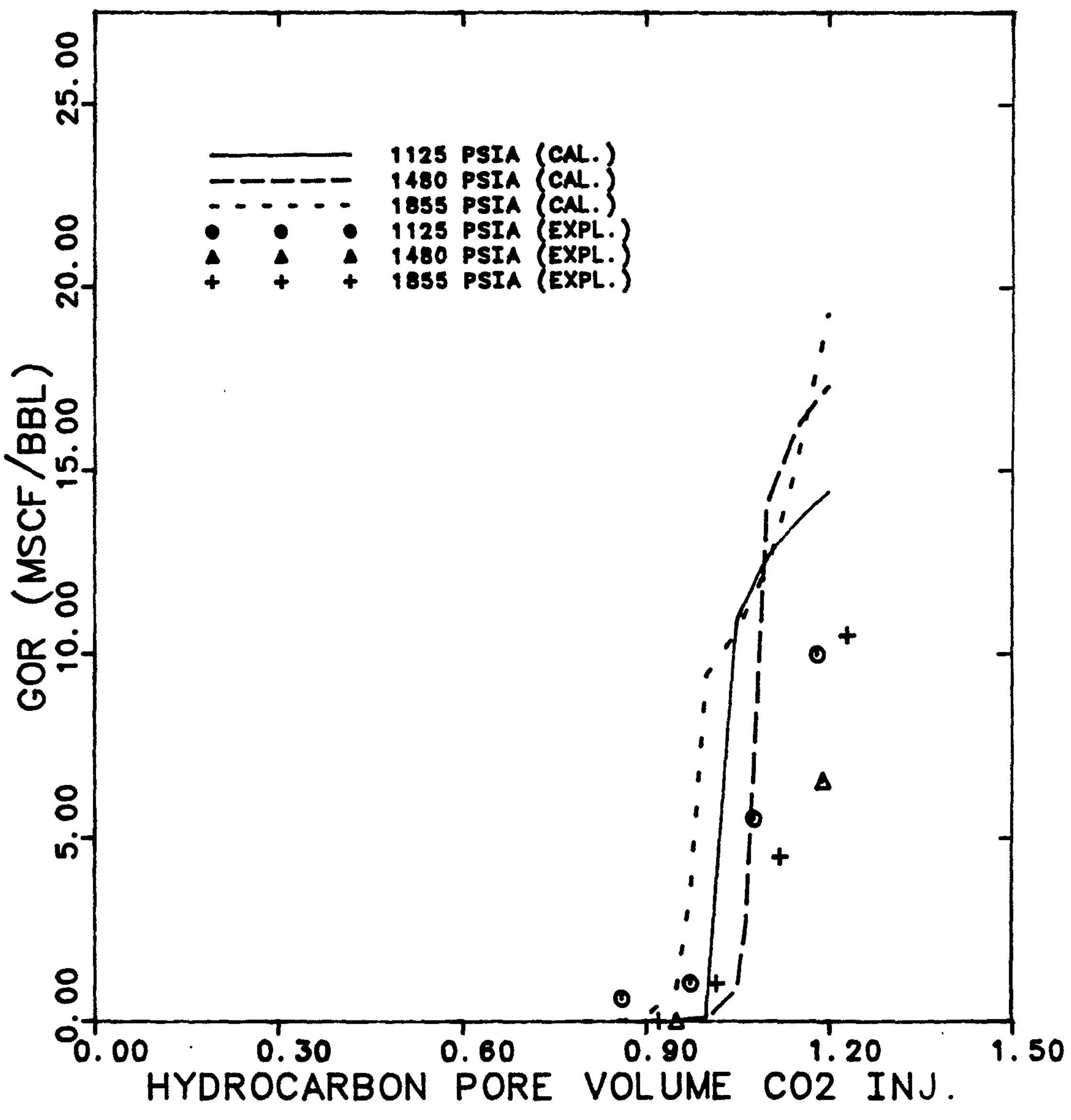

Figure 7.29 Comparison of Calculated and Experimental Slim-tube Test GOR for Case #5A at 1125,1480,&1855 psia

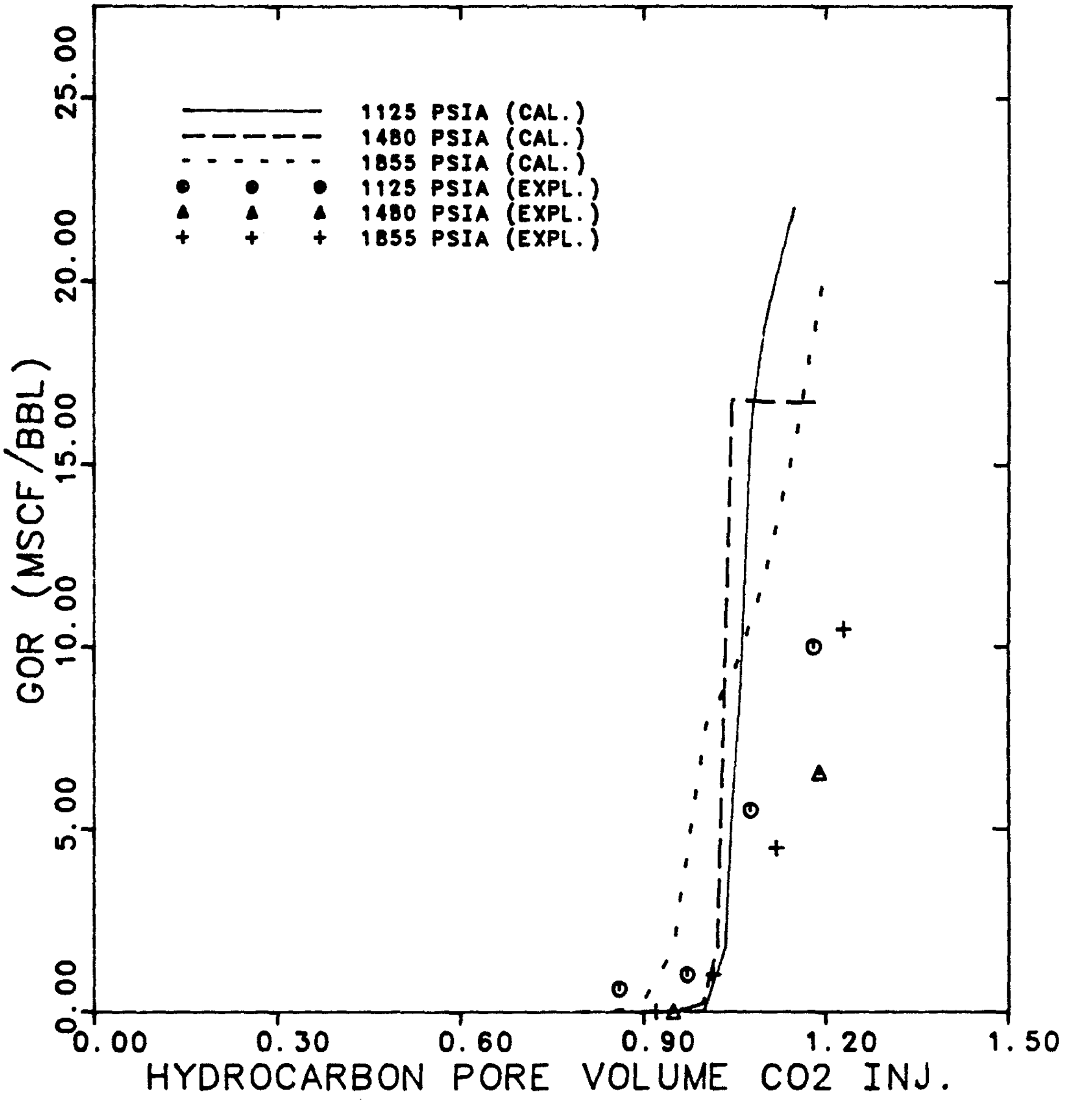

Figure 7.30 Comparison of Calculated and Experimental Slim-tube Test GOR for Case #10C at 1125,1480,&1855 psia

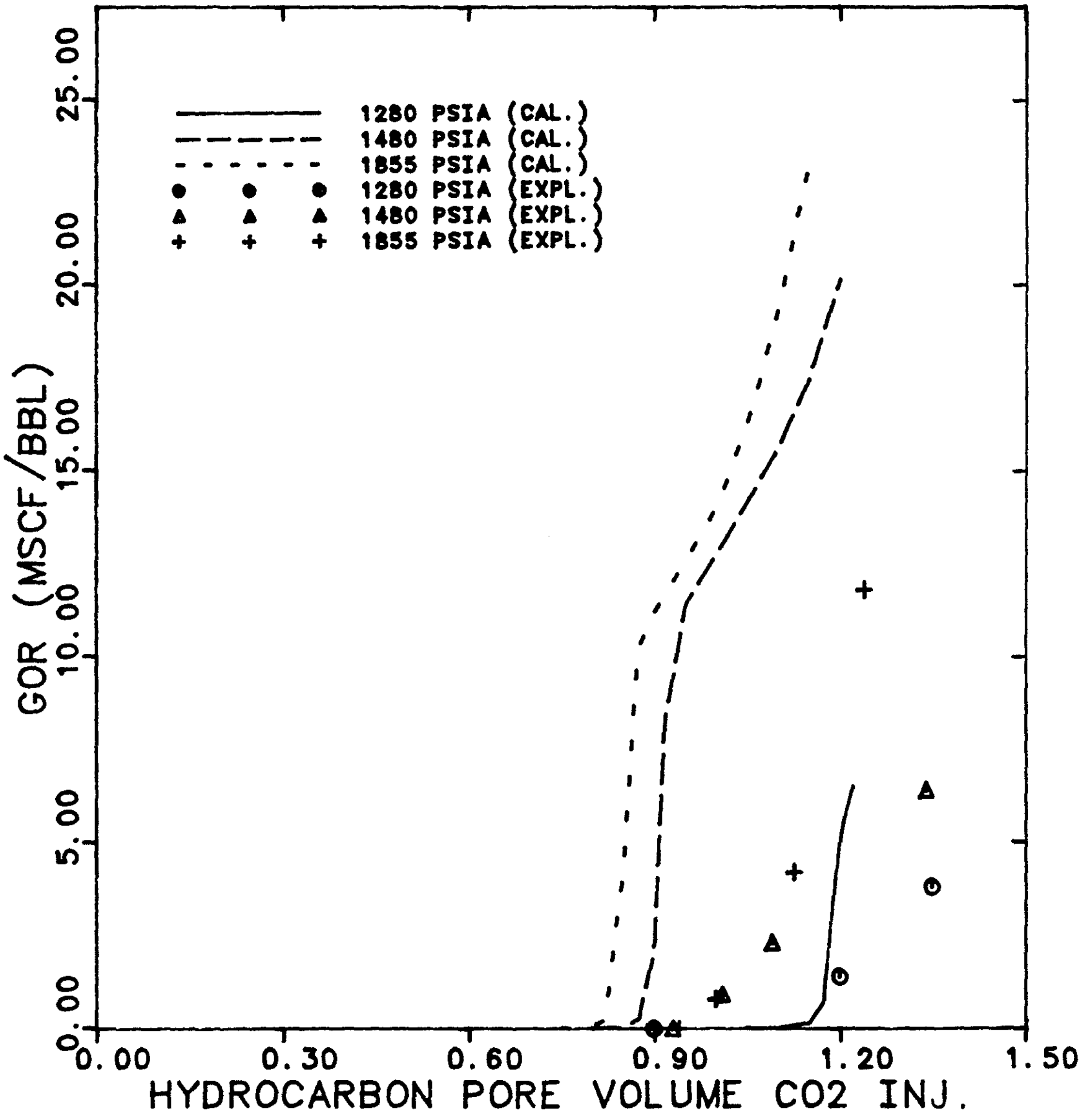

Figure 7.31 Experimental Results of the Displacement Tests

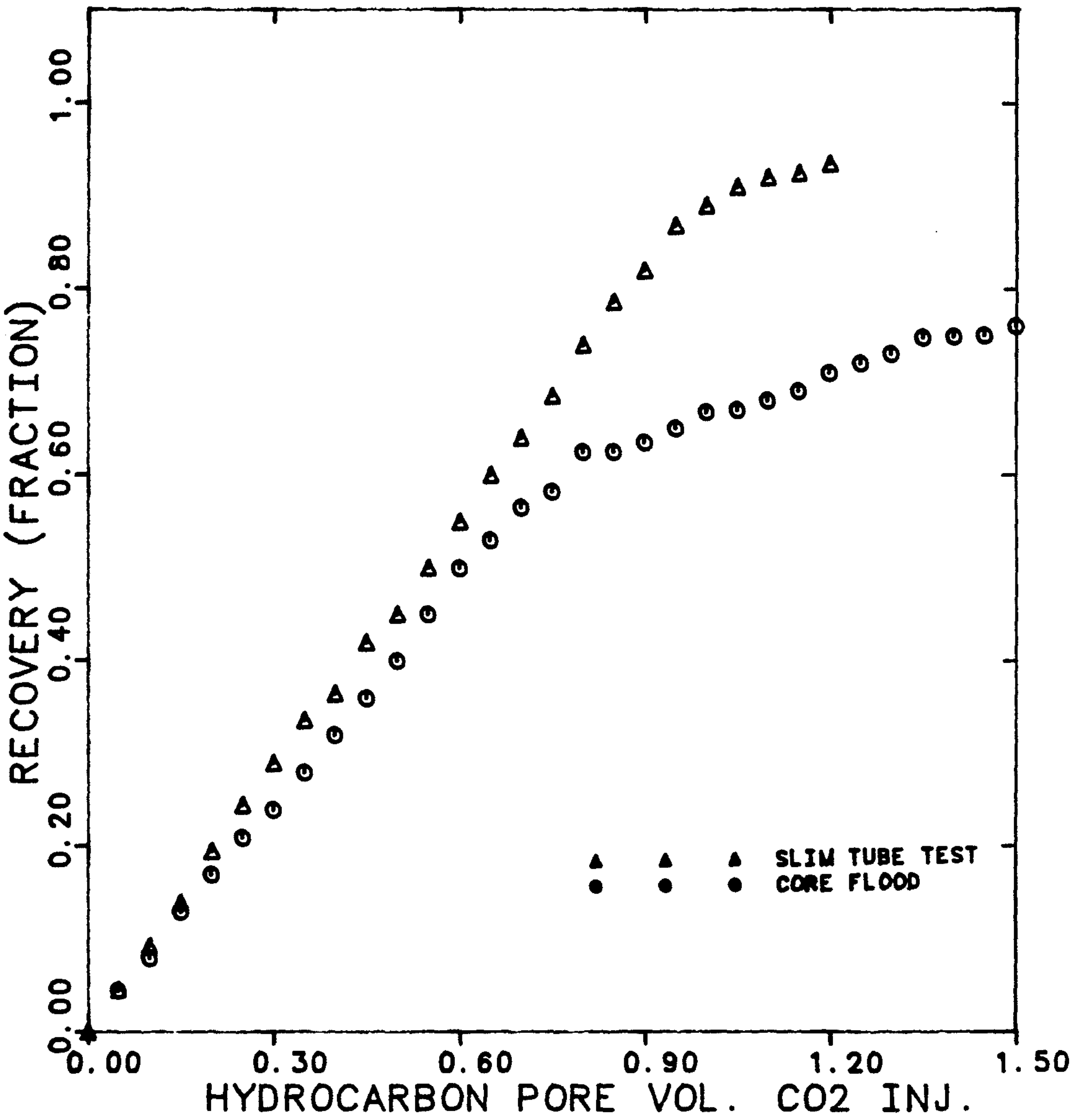

Fig. 7.32 Gas/Oil Relative Permeability Curves of Naar et al. [N3]
used for the Amarume Coreflood Displacement

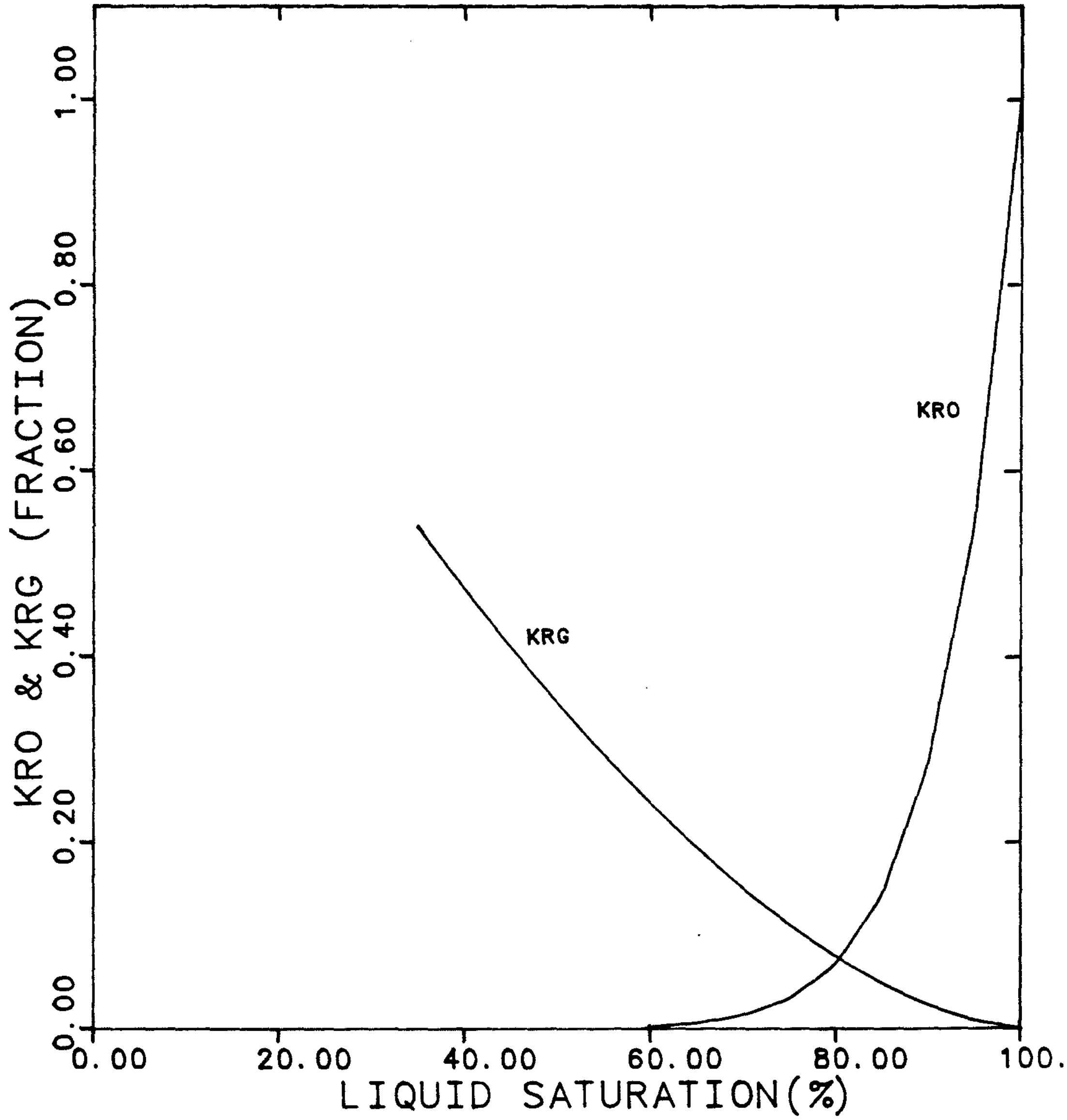

Figure 7.33 Comparison of Calculated and Experimental Coreflood Displacement Recovery and GOR of using Amarume S.T.O. (Case #2 ,1-D)

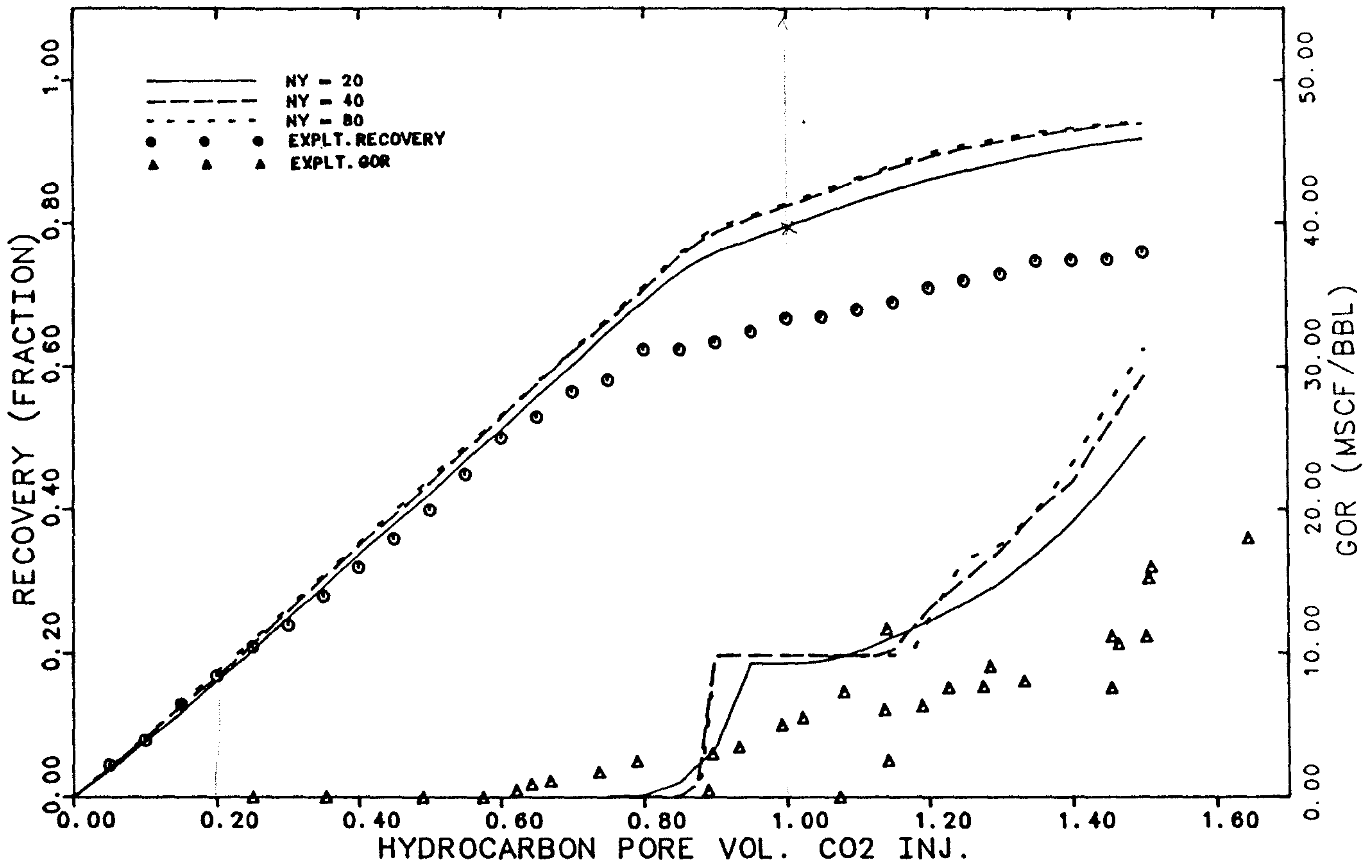

Figure 7.34 Comparison of Calculated and Experimental Coreflood Displacement Recovery and GOR using Amarume S.T.O. (Case #5A ,1-D)

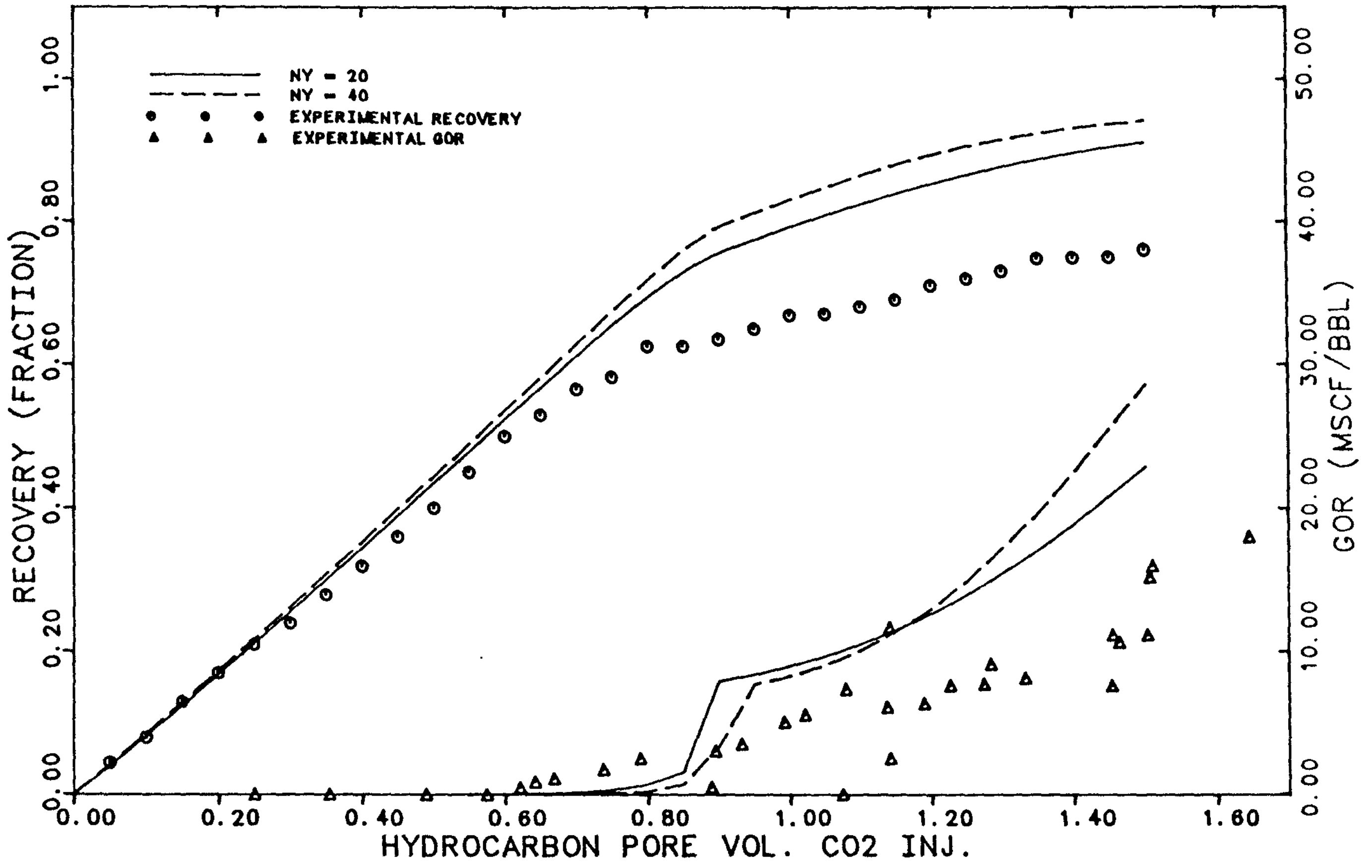

Figure 7.35 Comparison of Calculated and Experimental Recovery and GOR . curves using Amarume S.T.O. (Case #10C ,1-D)

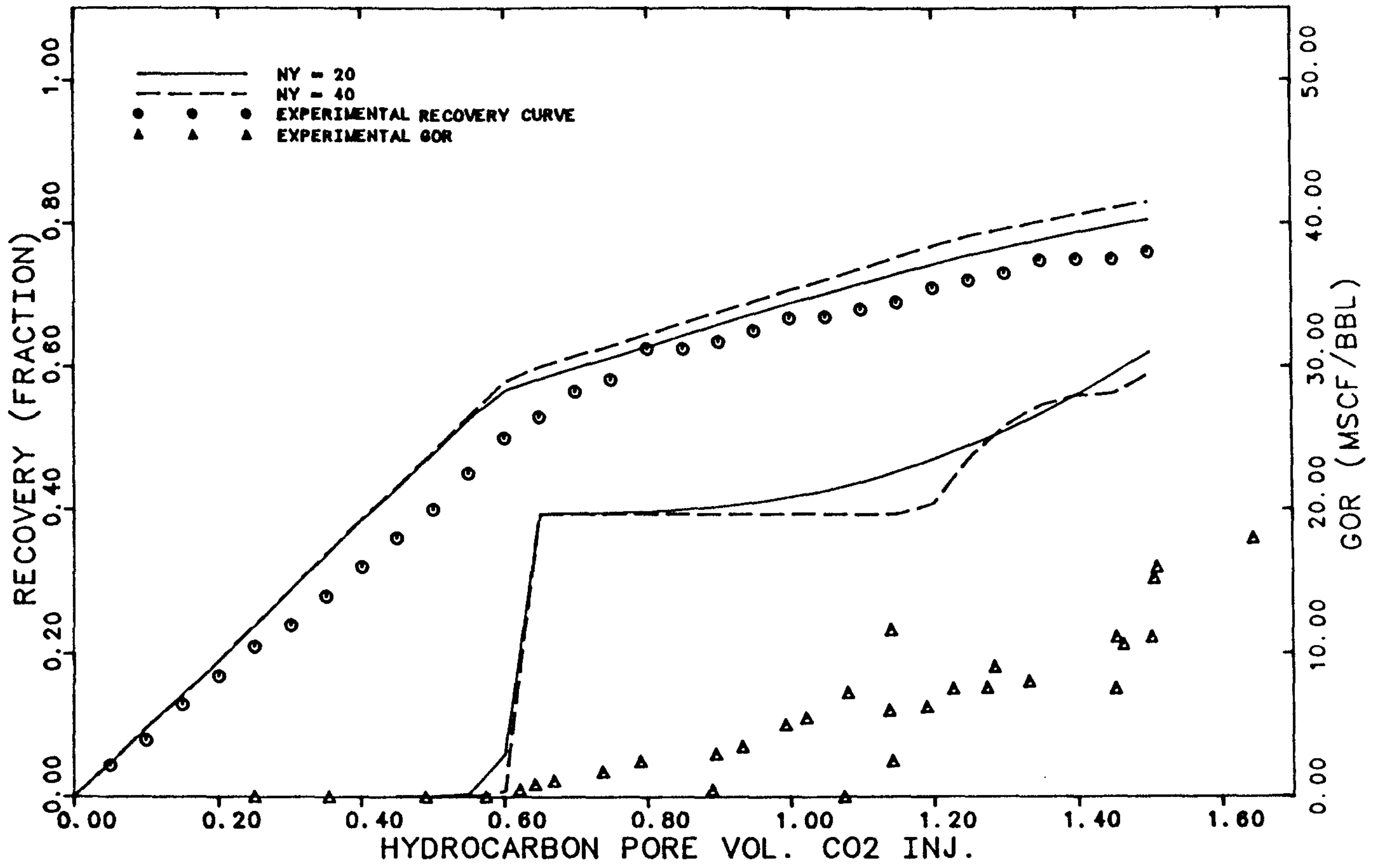

Figure 7.36 Calculated Effluent Composition Profile for the Amarume S.T.O. (Case #10C)

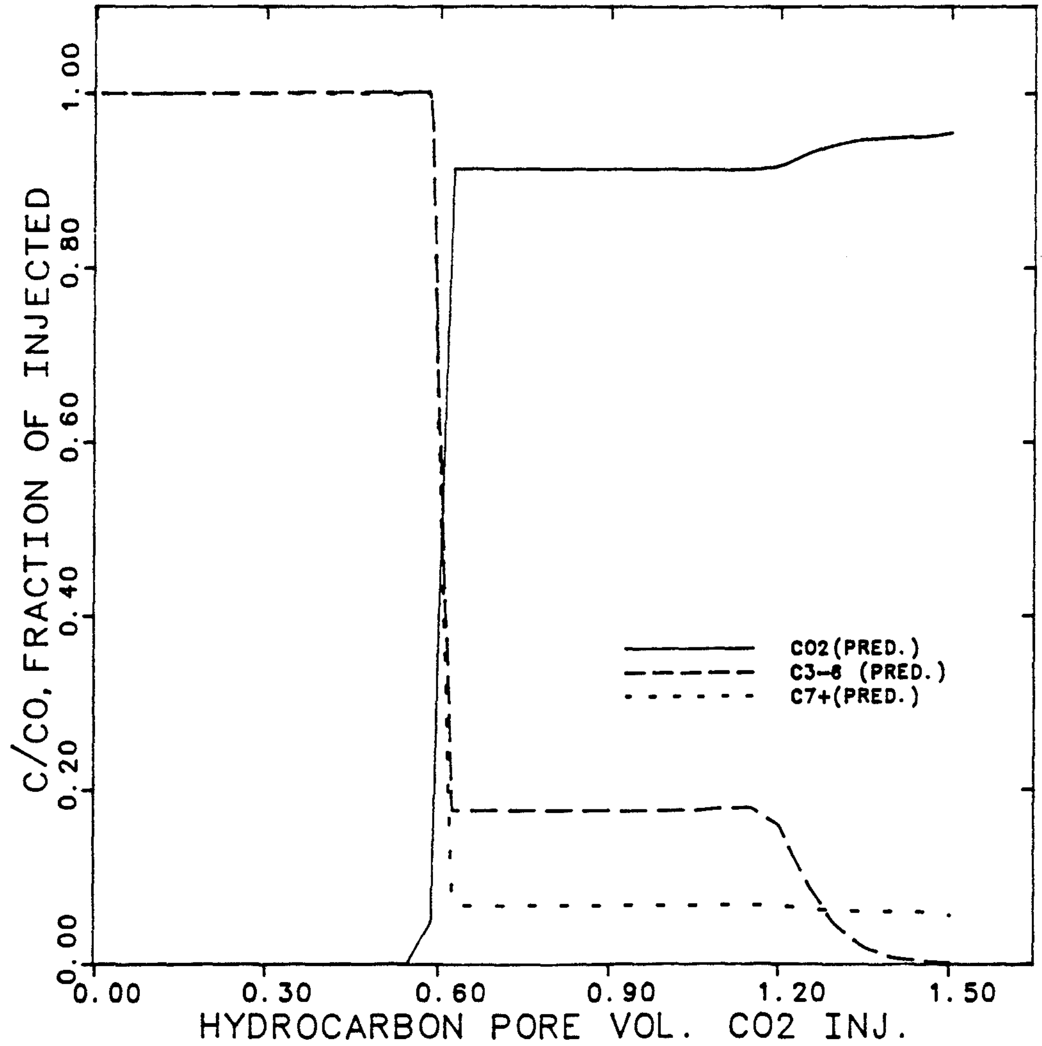

Figure 7.37 Comparison of Calculated and Experimental..Coreflood Displacement Recovery and GOR curves using Amarume S.T.O. with Longitudinal Dispersivity (Case #2 , 1-D)

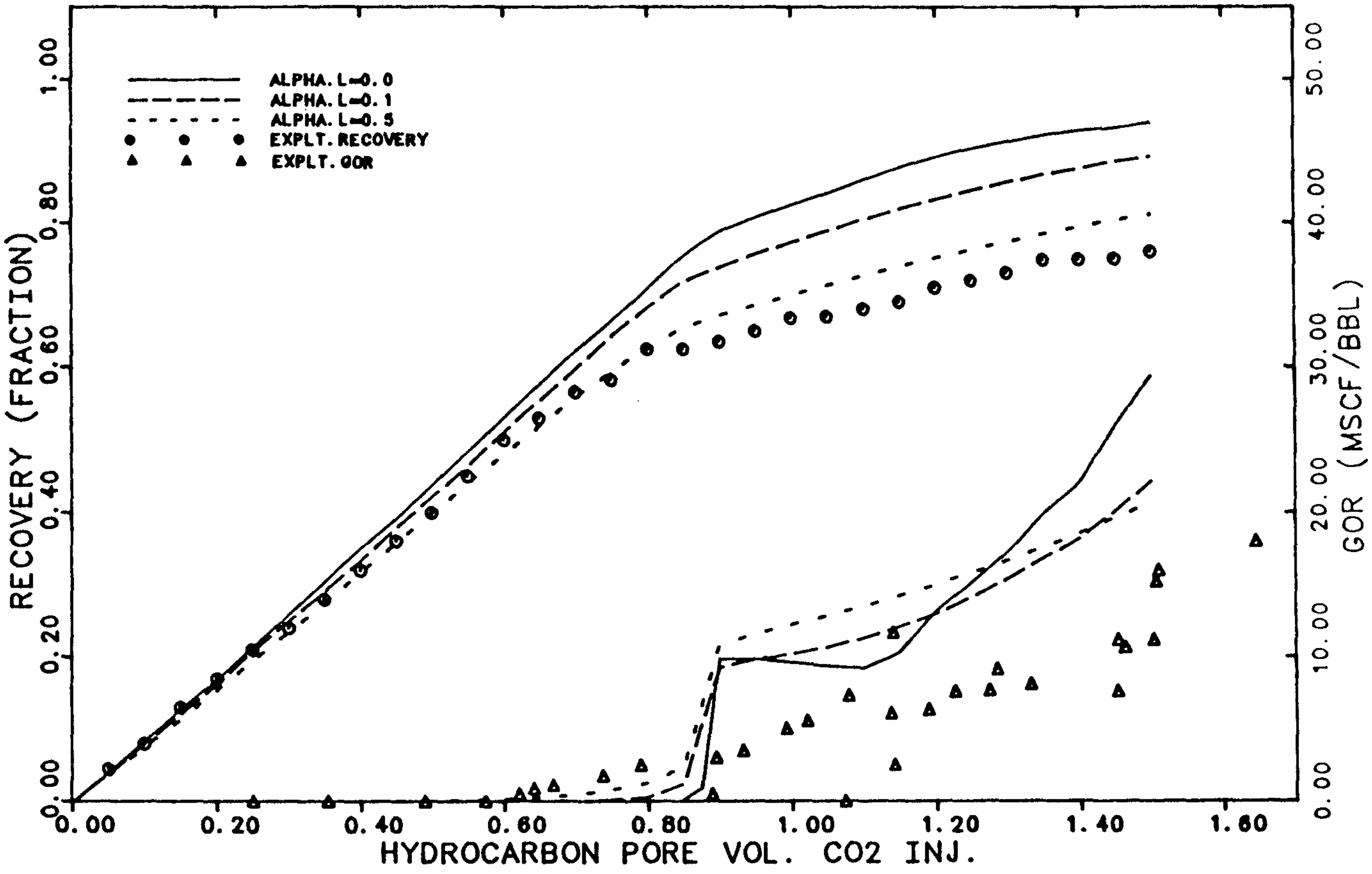

Figure 7.38 Comparison of Calculated and Experimental Coreflood Displacement Recovery and GOR curves using Amarume S.T.O. with Longtudinal Dispersivity (Case #10C , 1-D)

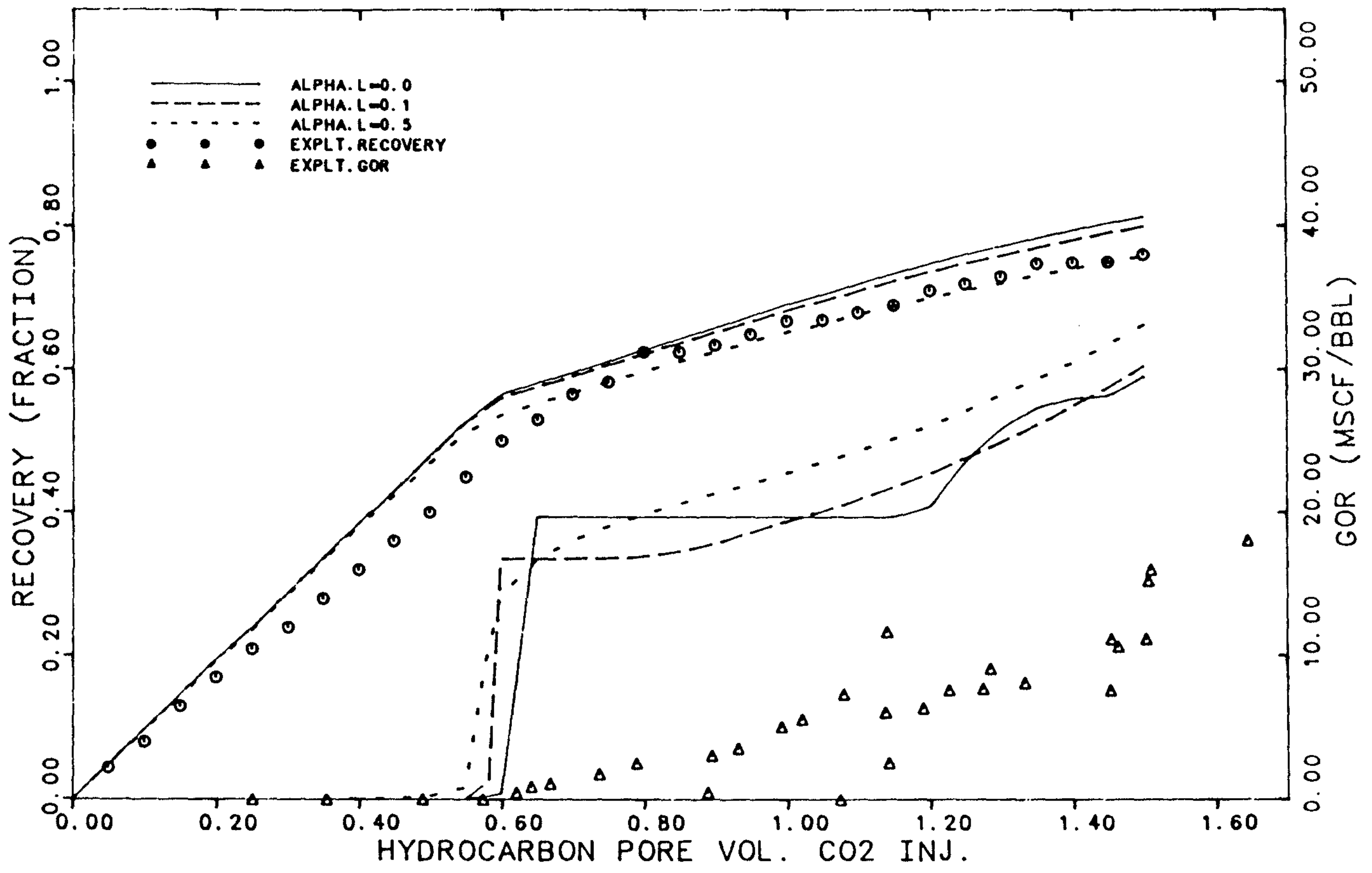

Figure 7.39 Calculated Densities for the mixture of 85 mol % CO2 and 15 mol % Amarume S.T.O. (Case # 2)

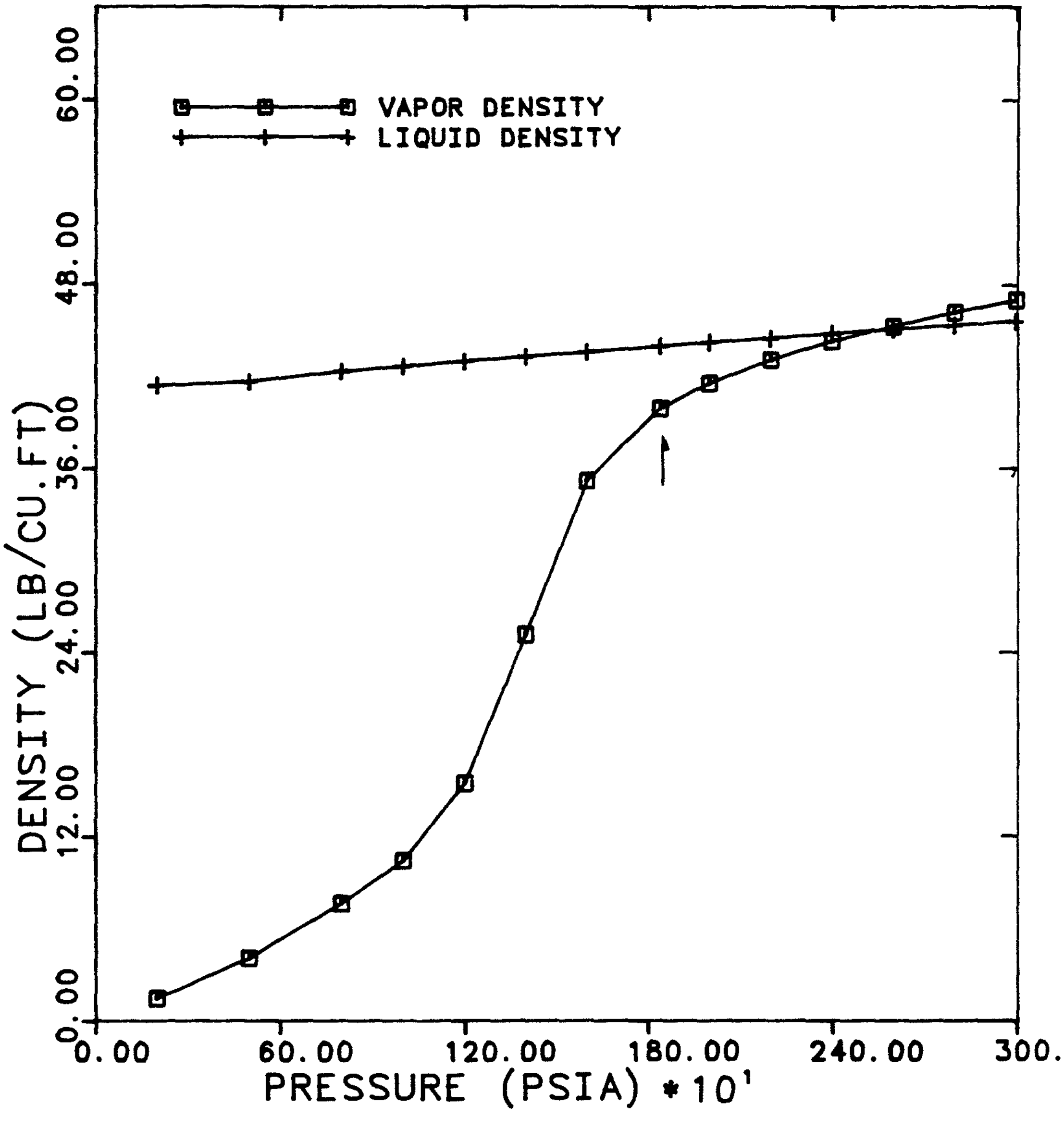

Figure 7.40 Calculated Densities for the mixture of 85 mol % CO2 and 15 mol % Amarume S.T.O. (Case # 10C)

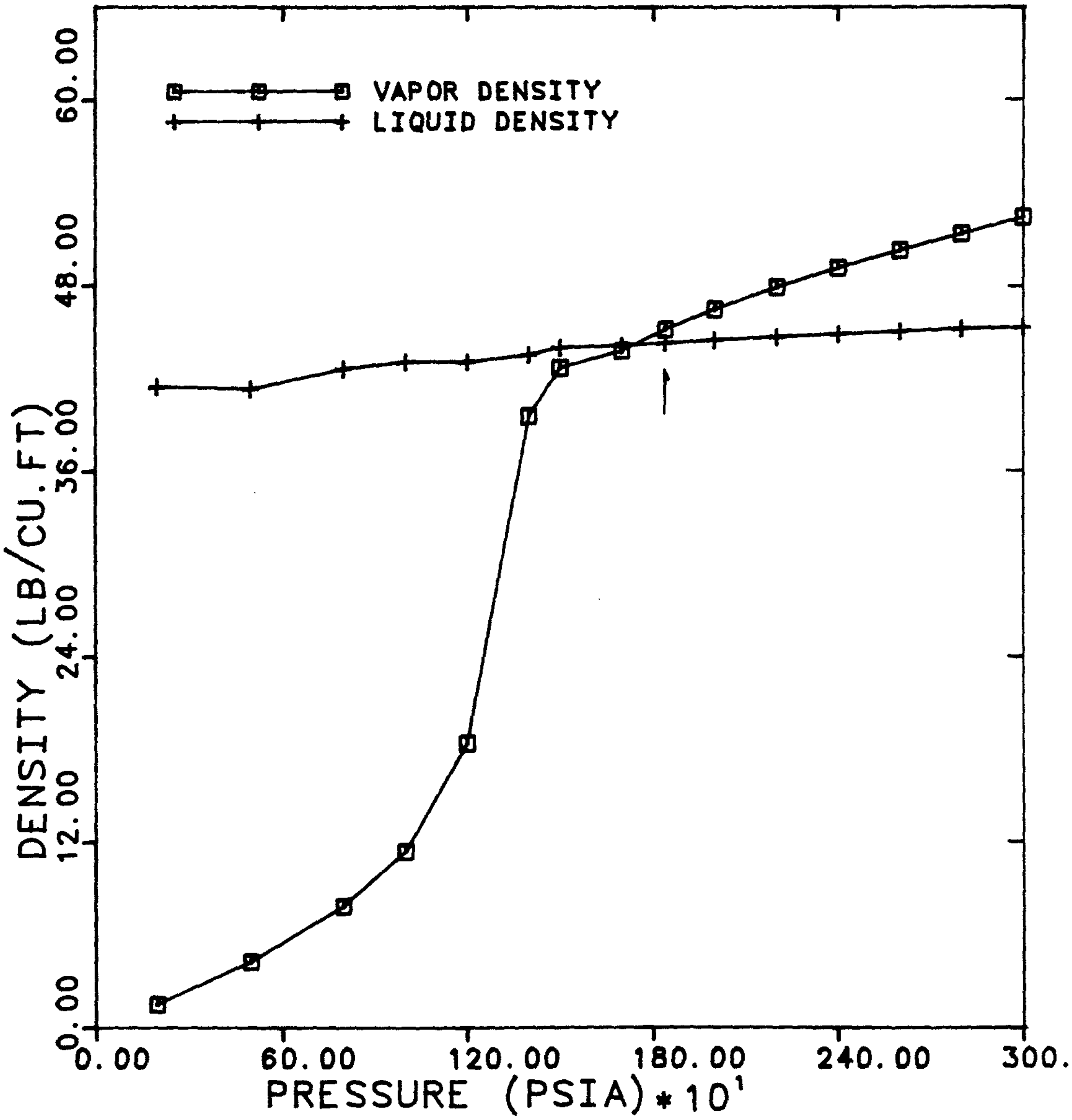

Figure 7.41 Oil Saturation Contours for 2 - D Cross-sectional Run (20 x 4) at 0.265, 0.53, & 1.06 PV CO2 injected (Run #24B)

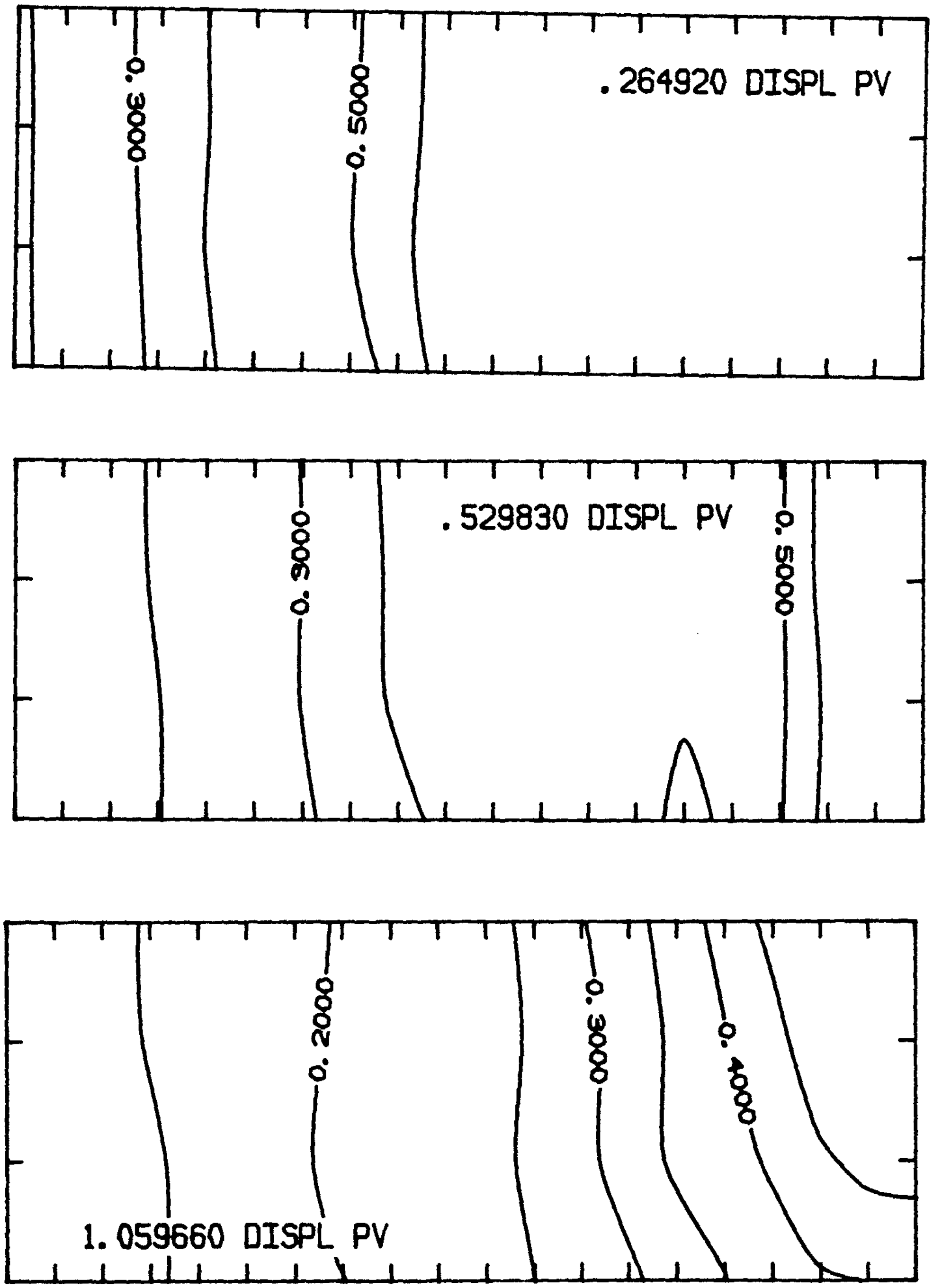

Figure 7.42 Oil Saturation Contours for 2 - D Cross-sectional Run (20 x 4) at 0.265, 0.53, & 1.06 PV CO2 injected (Run #24A)

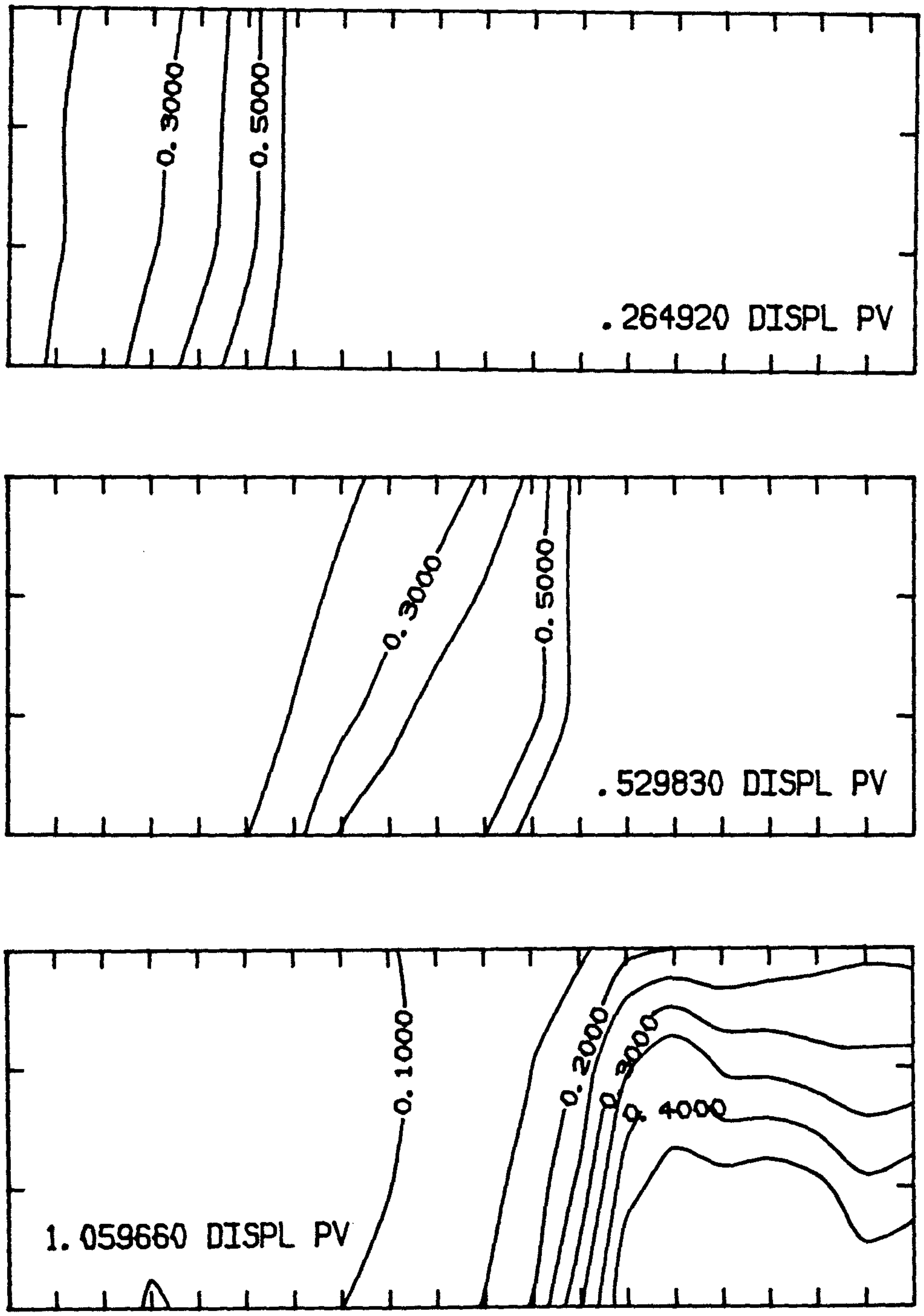

Figure 7.43 Oil Saturation Contours for 2 - D Cross-sectional Run (20 x 4) at 0.265, 0.53, & 1.06 PV CO2 injected (Run #28A)

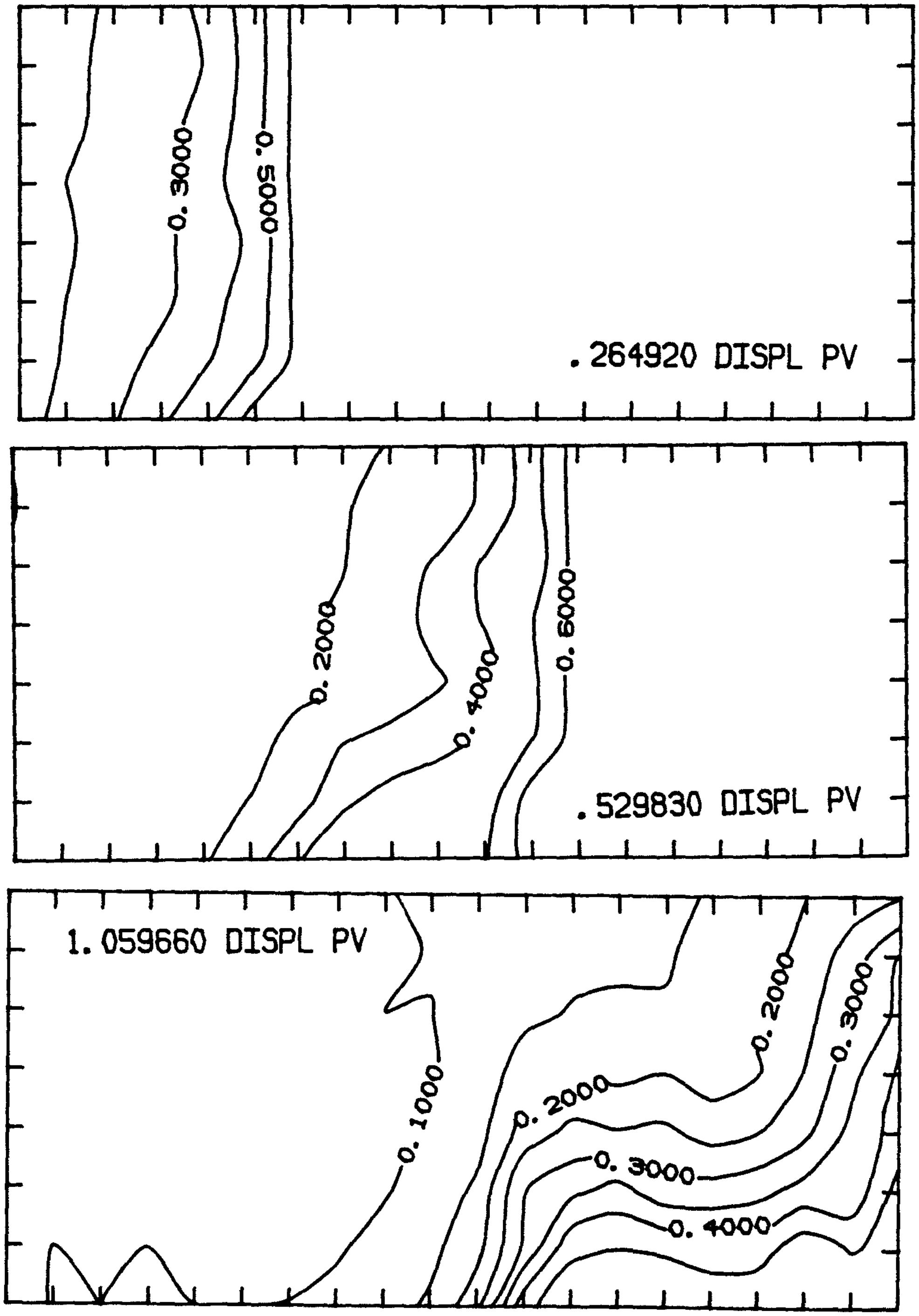

Figure 7.44 Comparison of Calculated and Experimental Coreflood Displacement Recovery and GOR. curves using Different Number of Vertical Grid Blocks (Runs #42A,44A,&48A)

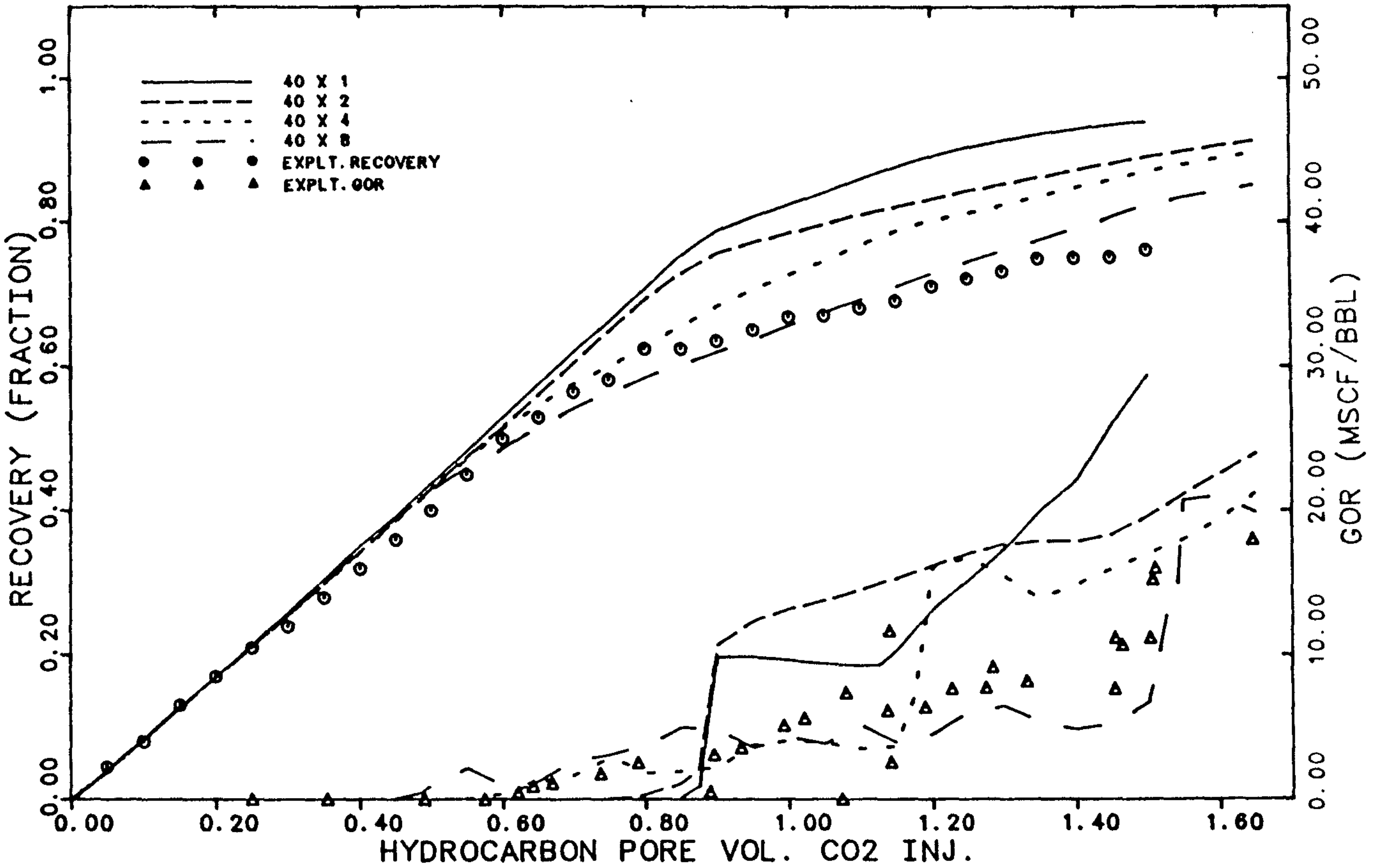

Figure 7.45 Calculated Effluent Composition Profile for the Amarume S.T.O. (Run #28A))

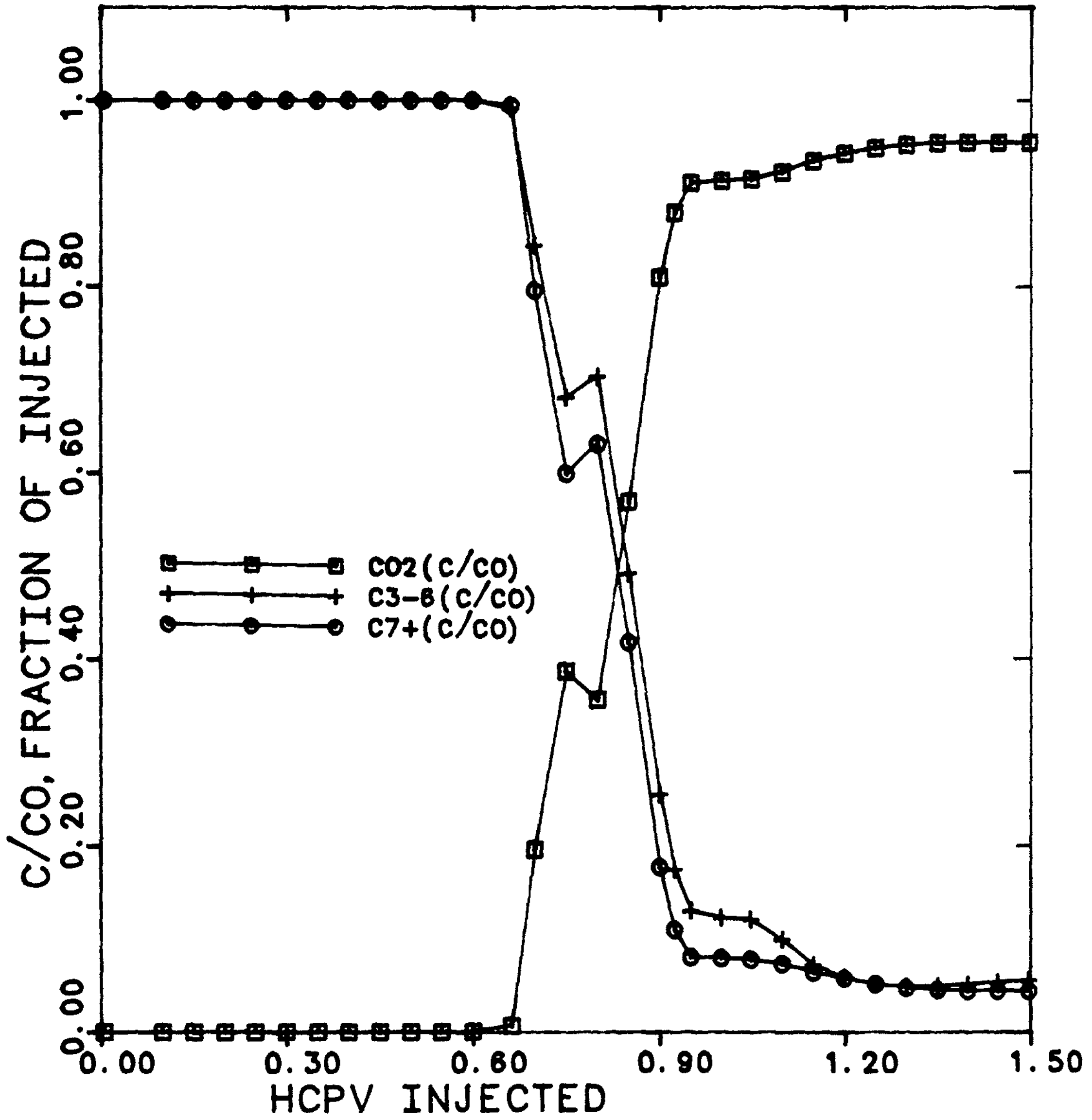

Figure 7.46 Comparison of Calculated and Experimental Coreflood Displacement Recovery and GOR curves using Amarume S.T.O. with and without Dispersion (Run #24X))

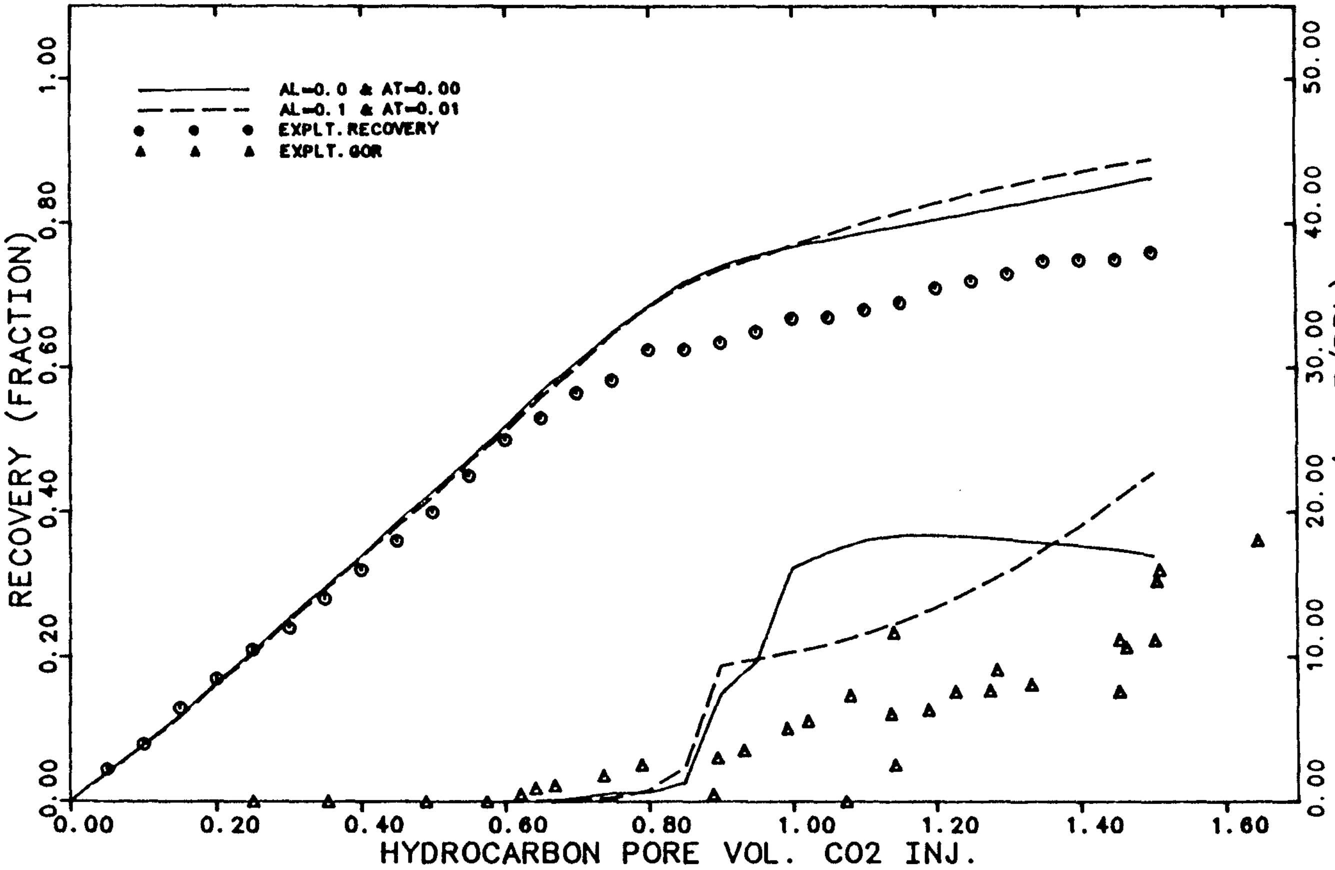

Figure 7.47 Oil Saturation Contours for 2 - D Cross-sectional Run (20 x 4) at 0.265, & 1.06 PV CO2 injected (Run #24X)

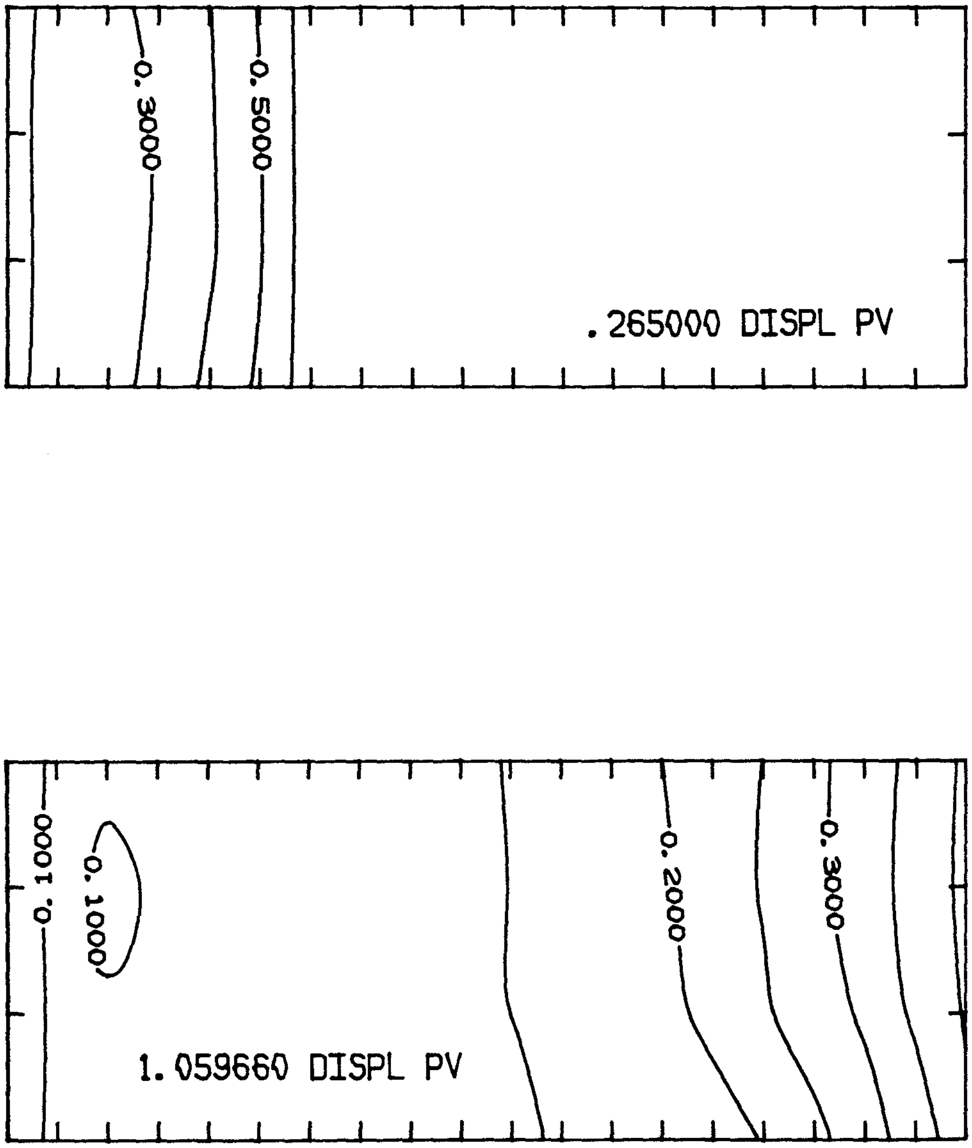

Figure 7.48 Comparison of Calculated and Experimental Coreflood Displacement Recovery and GOR curves using Amarume S.T.O. with Low vertical permeability (Run #44Y)

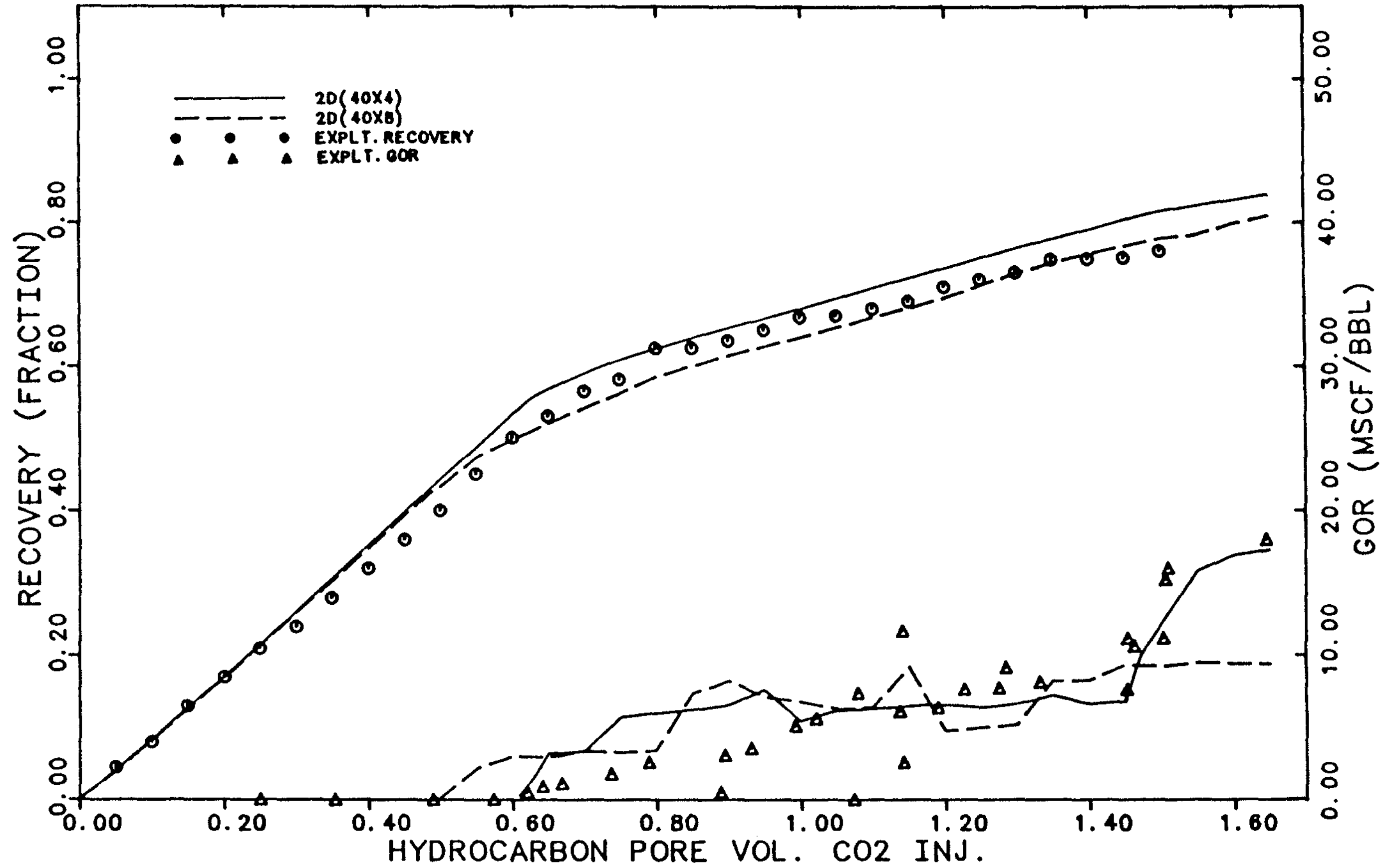

Figure 7.49 Oil Saturation Contours for 2 - D Cross-sectional Run (40 x 4) at 0.265, 0.53, & 1.06 PV CO2 injected (Run #44Y)

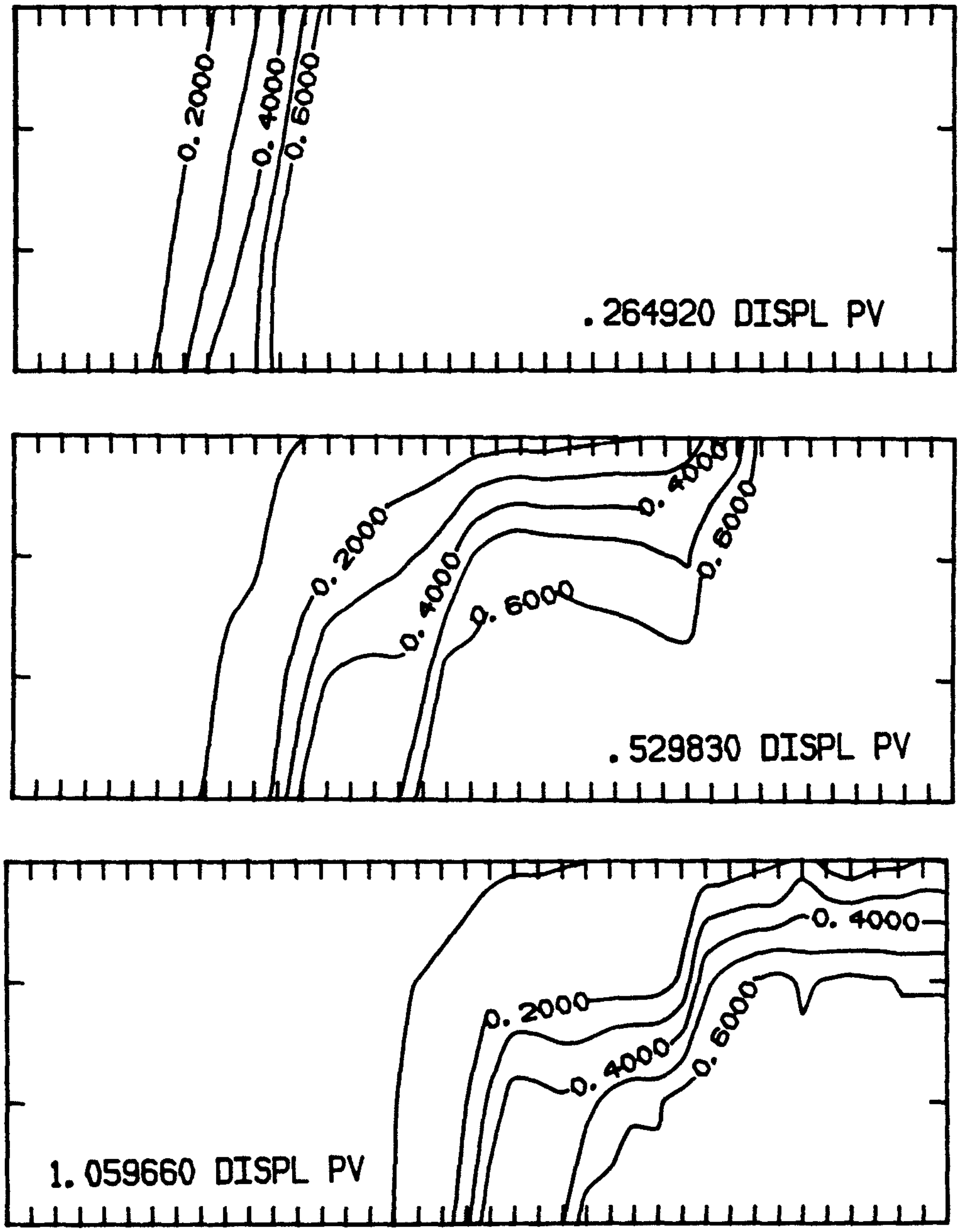

Figure 7.50 Capillary Pressure Functions in Amarume Coreflood Simulation

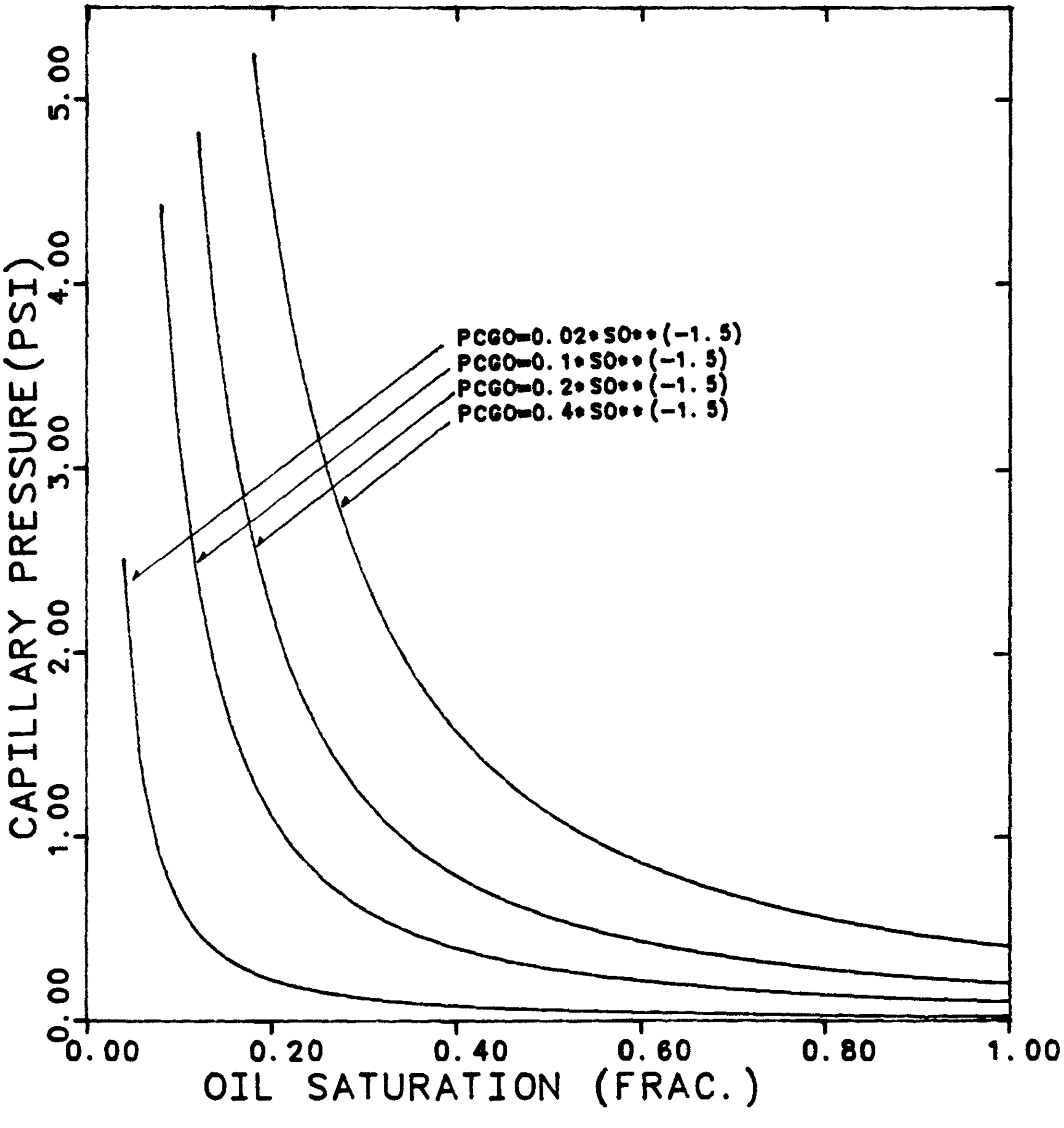

Figure 7.51 Comparison of Calculated and Experimental Coreflood Displacement Recovery and GOR. curves using Amarume S.T.O. with Capillary Pressures (Run #24Z)

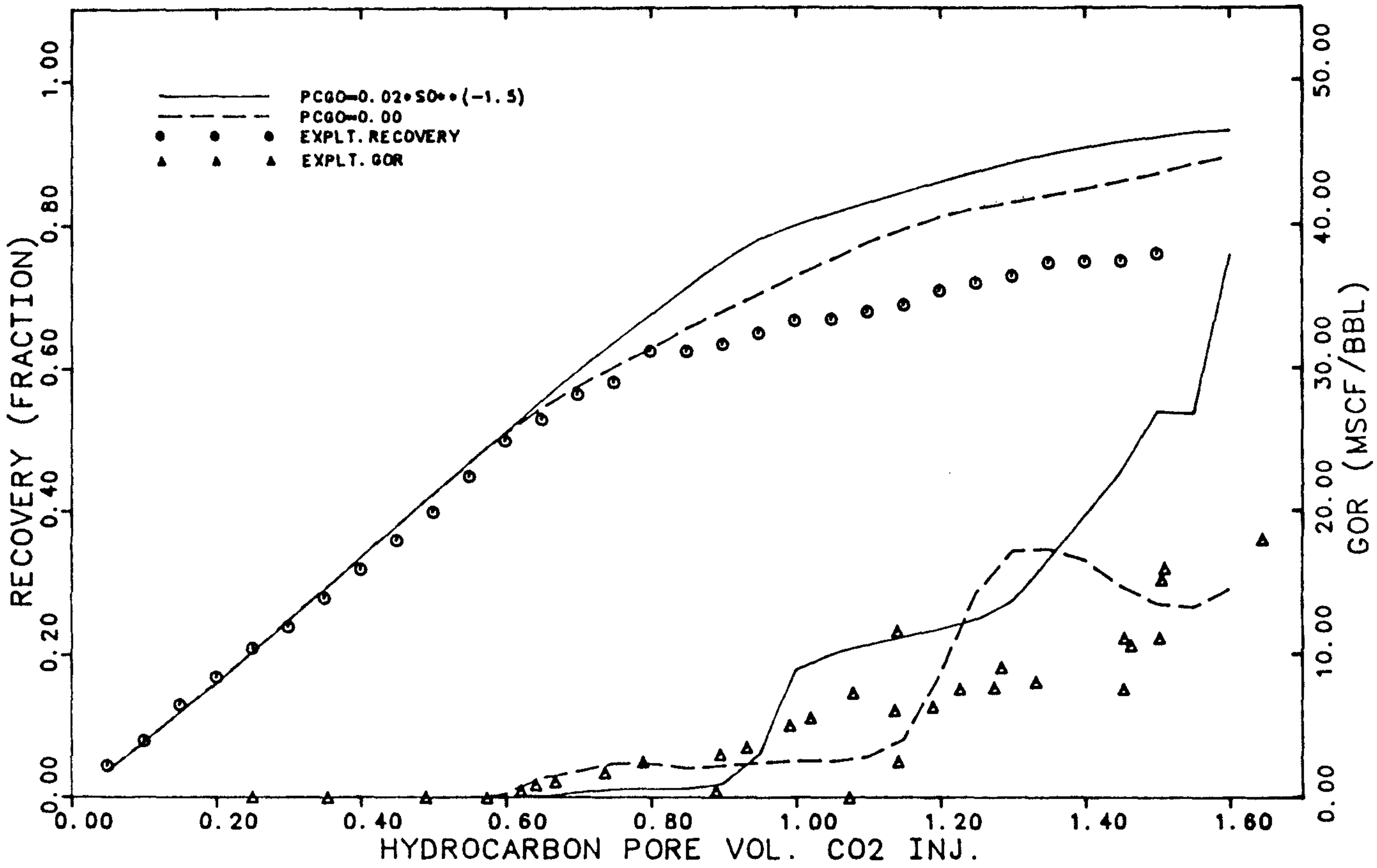

Figure 7.52 Oil Saturation Contours for 2 - D Cross-sectional Run (20 x 4) at 0.265, 0.53, & 1.06 PV CO2 injected with Capillary Pressures (Run #24Z)

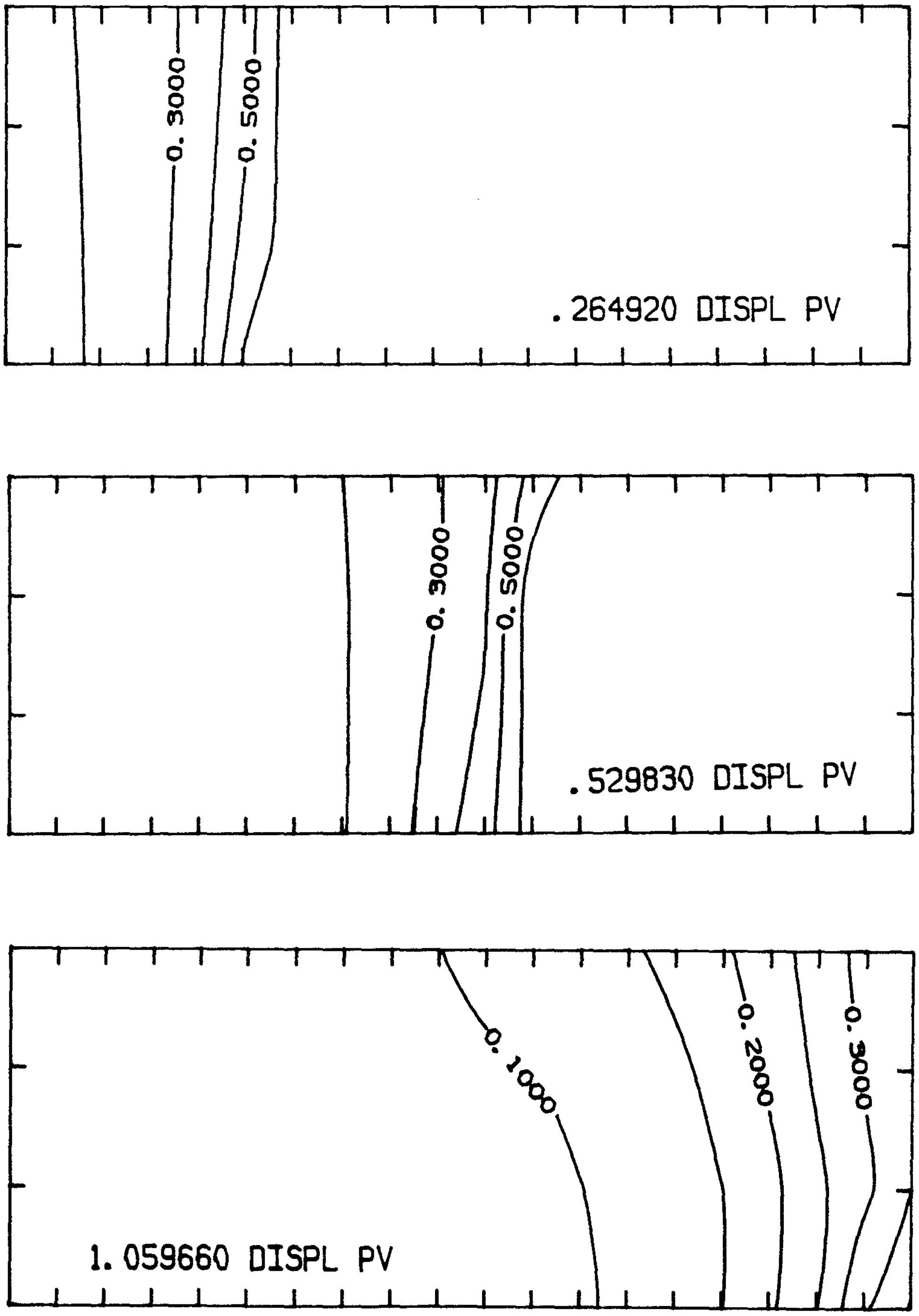

CHAPTER 8 Summary, Conclusions and Recommendations

8.1 Summary and Conclusions

The following conclusions can be obtained from this study.

1. A good agreement between experimental and simulated recoveries was obtained in the slim-tube displacement of three pure components (Chapter 4), after getting a good phase behavior match. The binary interaction coefficients had a large effect on the phase behavior and the slim-tube oil recovery matches.

2. Both three and seven pseudo-components were used in the case of Maljamar separator oil (Chapter 5). Pseudo-ternary diagrams and pressure-composition diagrams were used for the phase behavior matching. Better agreement between experimental and simulated recoveries was obtained using seven pseudo-components, since a better agreement between the calculated and experimental pressure-composition diagram was obtained. This means that an adequate prediction of the slim-tube displacement can be obtained after a good phase behavior match has been achieved.

3. By using the UTCOMP simulator, useful insight into the displacement mechanism was achieved for the Maljamar separator oil case both below and near the Minimum Miscibility Pressure (MMP).
4. The displacement of an oil from the San Andreas formation in West Texas by CO_2 in a Berea core was simulated (Chapter 6). The pressure-composition diagrams for oil and CO_2 mixtures were used for phase behavior matching. The simulated oil recovery, producing GOR and concentration histories were compared with the experimental results. The GOR and the concentrations of CO_2 and heavy hydrocarbon are related and both are important in the matching process.

5. The phase behavior, slim tube experiment and coreflood experiment were all matched for CO_2 and Amarume stock tank oil. A sensitivity study of EOS parameters showed that the critical parameters of CO_2 had the most effect on the phase behavior. Matching the slim tube experiment was helpful in understanding the coreflood since fingering had a large effect on the coreflood and this complicates its simulation compared to the slim tube.

6. Dispersion, gravity, and capillary pressure were taken into account in the simulation of Amarume STO with a sensitivity study. In the 1-D case, the oil recovery decreases with increasing longitudinal dispersivity. The results of the 2-D cross-sectional simulation shows that transverse dispersion prevented early breakthrough of CO_2, and effectively recovered oil from the lower layer.

Therefore, the oil recovery increases with increasing transverse dispersion. The 2-D simulated oil recovery was greater with capillary pressure than without due to the stabilization of the displacement i.e. a decrease in gravity tonguing. Decreasing the vertical permeability in the 2-D simulation decreased the oil recovery because of less crossflow.

8.2 Recommendations

The following recommendations for further research are made:

1. The regression method to tune the EOS parameters for the PVT phase match should be tried for this type of study.

2. An automatic time step size selector should be incorporated as has been done in the latest version of the UTCOMP [C3].

3. Because of the small size of the three phase region, the restriction to a two phase flash calculation as used in this study was assumed to be reasonable. However, as pointed out by Nghiem and Li [N2], this approach does not consider the interaction of L-L and L-V regions on the flow behavior in the transition zone. This phenomenon is still not well understood; therefore the current model can predict accurately only displacements where this phenomenon is negligible. The importance of a second liquid phase should be investigated. The latest version of UTCOMP will implement the three hydrocarbon flash calculation with four phase relative permeability [P4].

4. Viscous fingering should be taken into account for actual application in the field.

5. Trapped hydrocarbon fraction and the solubility of CO_2 in water should be modeled.

Nomenclature

a_i = temperature dependent parameter in Peng-Robinson equation of state for component i (FL^3).

b_i = constant in Peng-Robinson equation of state for component i (L^3).

a', b', c' = acentric factor dependent parameter in Kato et al.´s correlation.

c_i = water compressibility factor (L^2/F).

c_f = formation compressibility factor (L^2/F).

D_{ij} = effective molecular diffusion coefficient of component i in phase j (L^2/t).

f_{ij} = component fugacity for component i of phase j, i = l, ...nc, j = 2, ...np (F/L^2).

$f_{w,\, inj}$ = fractional flow of water at injection.

I = multiple carbon number index (=1,2, ...N_g).

K = absolute permeability (L^2).

K_x = absolute permeability in x-direction (L^2).

K_y = absolute permeability in y-direction (L^2).

K_{ij} = dispersion tensor for component i in phase j (L^2/t).

Kw = Watson characterization factor.

k_{rj} = relative permeability to phase j (dimension less).

M_N = molecular weight of last single carbon number (or multiple carbon number) in a C_n^+ fraction

M_n = molecular weight of first SCN in a C_n^t fraction.

Mwi = molecular weight of component i.

N = last SCN (or MCN) in a C_n^+ fraction.

Ng = number of MCN groups.

N_i = number of moles of component i.

N_t = total number of moles of all components.

Nx = number of grid blocks in x-direction.

n = first SCN in a C_n^+ fraction.

N_c = number of non aqueous components.

Np = number of phases.

n_f = constant exponent for family of binaries in Lawal's correlation.

P = gas phase pressure (F/L^2).

$[P_i]$ = parachor of component i

q_i = rate of component i (moles/t).

q_t = total rate (moles/t).

R = universal gas constant (FL/T).

r_o = equivalent radius for radial form of well model (L).

r_w = wellbore radius (L).

S_j = saturation of phase j; j=1,2, ... np (fraction).

T = temperature (T).

T_b = normal boiling point (T).

T_{ci} = critical temperature of component i (T).

T_{ri} = reduced temperature for component i = T/T_{ci} (dimensionless).

u_j = superficial velocity of phase j (L/t)

V_b = grid block bulk volume (L^3)

V_{ci} = critical volume of component i.

V_p = grid block pore volume (L^3).

V_t = total fluid volume (L^3).

v = molar volume (L^3/mole).

x_{ij} = mole fraction of component i in place of j.

Z = compressibility factor (dimensionless).

$z_{nc,inj}$ = injection overall mole fraction of hydrocarbon phase.

α = correction factor for EOS constant a_i.

α_{lj} = longitudinal dispersivity in phase j (L).

α_{tj} = transverse dispersivity in phase j (L).

$\alpha_D{}^T$ = dimensionless total dispersion coefficient.

$\alpha_D{}^P$ = dimensionless physical dispersion coefficient.

$\alpha_D{}^N$ = dimensionless numerical dispersion coefficient.

β = correction factor for EOS constant b_i.

γ_j = specific weight of phase j (F/L^3).

δ_{ij} = binary inceraction coefficient between component i and j (dimensionless).

θ = reduced normal boiling point ($=T/T_b$).

θ_p = constant for family of binaries in Lawal's correlation.

λ_{rj} = relative mobility of phase j ($L^2F^{-1}T^{-1}$).

ρ_j = mass density of phase j (mass of j/L^3).

ω_i = Pitzer acentric factor for component i (dimensionless).

ω_{ij} = mass fraction of component i in phase j (mass of i in j/mass of j).

ξ_j = molar density of phase j (molar /L^3).

ϕ = porosity (fraction).
ϕ^o = porosity at reference pressure (fraction).
ϕ_i = fugacity coefficient of component i (dimensionless).
Φ_j = flow potential of phase j (F/L$^{2)}$.
∇ = gradient operator (1/L).
Δt = time step (t).
Δx, ΔZ = grid block length (L).
ΔX_d = dimensionless length.
Ω_a, Ω_b = constant of equation of state.

Superscripts

n = time level
p = reference state

Subscripts

I = list of component indices i, i=1, ...nc, nc +1
i = component index
j = phase index
k = block index
x = x-direction
y = y-direction

Appendix

Input Data-set for UTCOMP

The UTCOMP simulater requires three input data-sets , those are HC.DAT , RS.DAT , and OP.DAT . The following lists are the example data-sets which were used in this study.

Example #1	HC.DAT and RS.DAT for the slim-tube test simulation using three pure components (Case #9 ; Chapter 4)
Example #2(a)	HC.DAT and RS.DAT for the slim-tube test simulation using Maljamar separator oil (3 pseudo-components by Method #1; Chapter 5)
Example #2(b)	HC.DAT and RS.DAT for the slim-tube test simulation using Maljamar separator oil (7 pseudo-components by Method #1; Chapter 5)
Example #3	HC.DAT and RS.DAT for the core flood test simulation using West Texas reservoir oil (12 pseudo-components by Case #A; Chapter 6)
Example #4	HC.DAT , RS.DAT and OP.DAT for the coreflood test simulation using Amarume S.T.O.(8 pseudo-components Case #2; Chapter 7)

HC.DAT for Example #1

```
*NUMBER OF COMPONENTS
    3
*COMPONENT NAMES(1X,2A4)
  CH4
  C3H8
  C10H22
*Pc(psi)     Tc(R)     Vc(cu ft)     M.W.       OMEGA     PARACHOR
    667.80     343.40     1.5492      16.00      0.0104      49.0
    616.40     666.00     3.1090      44.10      0.1524      60.0
    334.29    1112.10    10.7455     142.276     0.4885     100.0
*BINARY INTERACTION COEFFICIENTS
 0.00
 0.076  0.0
 0.000  0.040    0.0
*NUMBER OF PHASES EXPECTED
 3
*LTCOMP       ZLTCMP
 1             0.65
*MAXITF     KFLAG     DKTOL1     DKTOL2    MAXITV    TOLV
  8000          1     1.0E-16    1.0E-08    8000    1.0E-09
*METHOD     ACSS   MAXITN     EPSR     EPSV     EPSL     EPSU
    -1        6.0     10       0.6     1.E-2    1.E-4    1.E-2
```

RS.DAT for Example #1

```
*HEADER(): case name
 1-D (Y) 3-COMPONENT,(KOSSACK & HAGEN SLIM-TUBE) MISCIBLE FLOODING.
*MCONFG(O OR 1): flag for grid block configurattion
 0
*NX      NY      NZ: number of grid blocks in x, y, and z
 1       40      1
*NW: number of wells
 2
*RW(): wellbore ratius (ft)
 0.333   0.333
*LXW          LYW          LZWF          LZWL: well locations
 1            1             1             1
 1            40            1             1
*MDX(O OR 1): flag for grid block size in x-direction
 0
*DX: constant grid block size in x-direction (ft)
 0.017
*MDY(O OR 1): flag for grid block size in y-direction
 0
*DY: constant grid block size in y-direction (ft)
 1.396
*MDZ(O OR 1): flag for grid block size in z-direction
 0
*DZ: constant grid block size in z-direction (ft)
 0.017
*MD(O OR 1): flag for formation depth
 0
*D(1): depth (ft) of the most upper layer, for horizontal reservoirs
 0.0
*MPOR(O OR 1): flag for formation porosity
 0
*PORSTD(1): homogeneous porosity (fraction) at standard condition
 0.39
*MPERMX(O OR 1): flag for permeability in x-direction
 0
*PERMX(1): homogeneous permeability (md) in x-direction
 73300.0
*MPERMY(O OR 1): flag for permeability in y-direction
 0
*PERMY(1): homogeneous permeability (md) in y-direction
 73300.0
*MPERMZ(O OR 1): flag for permeability in z-direction
 0
*PERMZ(1): homogeneous permeability (md) in z-direction
 73300.0
*CF      PF: formation compressibility (1/psi) and reference pressure (psi)
 4.0E-6  14.7
*OOIP
 0.6357E-2
*CW      PW    DENMWS: water compr. (1/psi), ref. pres (psi) and mol. density
 3.0E-6  14.7  3.467
*MW      VISCW: water molecular weight (lbm/lbm-mole) and viscosity (cp)
 18.0    0.5
*TEMPF: formature temperature (f)
 100.0
*TFSTD   PSTD: standard temperature (f) and standard pressure (psi)
 60.0    14.7
*IUPSTW (1 OR 2): number of points in composition upstream weighting
 1
*ISTART(1 OR 2)     ISTORE(O OR 1): flags for reading and storing data
```

```
 1                   1
*ISINGL(0 OR 1): flag for flash calculations
 1
*T: initial time (days)
 0.0
*MP (0 OR 1): flag for initial pressure
 0
*P(1): constant initial pressure (psia)
 3118.
*MSAT(0 OR 1): flag for initial water saturation
 0
*SAT(1,1): constant initial water saturation (fraction)
 0.0
*MOMFR(0 OR 1): flag for initial overall composition
 0
*OMFR(1,K): constant initial composition (mole fraction)
 1.E-4    1.E-4    0.9998
*TM(days)   DT(days)    NWELLS   GORLIM(scf/stb)    WORLIM(stb/stb) <<<---
 0.15       0.0005           2        1.0E+10            10.
*LW   IQTYPE: well no. and well type
 1     1
*QTML(moles/d) WFRACT(fraction) NCOMP ISWITCH(0=N,1=Y) PBH(psi) DPVML(moles/pv)
 0.407E-1        0.0              2      0         3118.0    0.4446E-2
*KC   Z1  composition no. and composition (fraction)
 1   0.85
 2   0.15
*LW   IQTYPE: well no. and well type
 2     -2
*PBH(LW,LZ): constant bottom hole pressure (psi)
 3118.0
*TM(days)   DT(days)    NWELLS   GORLIM(scf/stb)    WORLIM(stb/stb) <<<---
 -1.0           -1.0    -1       0                   0.
```

HC.DAT for Example #2(a)

```
*NUMBER OF COMPONENTS
    3
*COMPONENT NAMES(1X,2A4)
  CO2
  C5-12
  C13+
*Pc(psi)      Tc(R)      Vc(cu ft)      M.W.       OMEGA      PARACHOR
   1071.0      548.0       1.20         44.0       0.2230        49.0
    366.7     1031.9       6.85        118.5       0.34353      351.5
    189.4     1423.5      20.843        331.1       0.86845      800.0
*BINARY INTERACTION COEFFICIENTS
 0.00
 0.090  0.0
 0.140  0.000  0.0
*NUMBER OF PHASES EXPECTED
 3
*LTCOMP        ZLTCMP
 1              0.5
*MAXITF     KFLAG      DKTOL1      DKTOL2     MAXITV     TOLV
  2000          1      1.0E-15     1.0E-12     2000     1.0E-10
*METHOD     ACSS    MAXITN      EPSR       EPSV       EPSL       EPSU
    -1        6.0      10         0.6       1.E-2      1.E-4      1.E-2
```

RS.DAT for Example #2(a)

```
*HEADER(): case name
 1-D (Y) 3-COMPONENT,(MALJAMAR STO) IMMISCIBLE FLOODING.
*MCONFG(0 OR 1): flag for grid block configurattion
 0
*NX      NY      NZ: number of grid blocks in x, y, and z
 1       80      1
*NW: number of wells
 2
*RW(): wellbore ratius (ft)
 0.333   0.333
*LXW          LYW          LZWF         LZWL: well locations
 1            1            1            1
 1           80            1            1
*MDX(0 OR 1): flag for grid block size in x-direction
 0
*DX: constant grid block size in x-direction (ft)
 0.018463
*MDY(0 OR 1): flag for grid block size in y-direction
 0
*DY: constant grid block size in y-direction (ft)
 0.5
*MDZ(0 OR 1): flag for grid block size in z-direction
 0
*DZ: constant grid block size in z-direction (ft)
 0.018463
*MD(0 OR 1): flag for formation depth
 0
*D(1): depth (ft) of the most upper layer, for horizontal reservoirs
 0.0
*MPOR(0 OR 1): flag for formation porosity
 0
*PORSTD(1): homogeneous porosity (fraction) at standard condition
 0.3812
*MPERMX(0 OR 1): flag for permeability in x-direction
 0
*PERMX(1): homogeneous permeability (md) in x-direction
 5800.0
*MPERMY(0 OR 1): flag for permeability in y-direction
 0
*PERMY(1): homogeneous permeability (md) in y-direction
 5800.0
*MPERMZ(0 OR 1): flag for permeability in z-direction
 0
*PERMZ(1): homogeneous permeability (md) in z-direction
 5800.0
*CF      PF: formation compressibility (1/psi) and reference pressure (psi)
 4.0E-6  14.7
*OOIP
 0.5214101611E-2
*CW      PW    DENMWS: water compr. (1/psi), ref. pres (psi) and mol. density
 3.0E-6  14.7  3.467
*MW      VISCW: water molecular weight (lbm/lbm-mole) and viscosity (cp)
 18.0    0.5
*TEMPF: formature temperature (f)
 90.0
*TFSTD   PSTD: standard temperature (f) and standard pressure (psi)
 60.0    14.7
*IUPSTW (1 OR 2): number of points in composition upstream weighting
 1
*ISTART(1 OR 2)    ISTORE(0 OR 1): flags for reading and storing data
```

```
 1                   1
*ISINGL(0 OR 1): flag for flash calculations
 1
*T: initial time (days)
 0.0
*MP (0 OR 1): flag for initial pressure
 0
*P(1): constant initial pressure (psia)
 800.0
*MSAT(0 OR 1): flag for initial water saturation
 0
*SAT(1,1): constant initial water saturation (fraction)
 0.0
*MOMFR(0 OR 1): flag for initial overall composition
 0
*OMFR(1,K): constant initial composition (mole fraction)
 1.0E-8  0.66399999  0.336
*TM(days)    DT(days)    NWELLS    GORLIM(scf/stb)    WORLIM(stb/stb) <<<---
 0.62        0.001          2        8000000.            10.
*LW    IQTYPE: well no. and well type
 1     1
*QTML(moles/d) WFRACT(fraction) NCOMP ISWITCH(0=N,1=Y) PBH(psi) DPVML(moles/pv)
 0.21091E-2        0.0              1      0                800.    0.1078144E-2
*KC    Z1: composition no. and composition (fraction)
 1    1.00
*LW    IQTYPE: well no. and well type
 2     -2
*PBH(LW,LZ): constant bottom hole pressure (psi)
 800.0
*TM(days)    DT(days)    NWELLS    GORLIM(scf/stb)    WORLIM(stb/stb) <<<---
 -1.0           -1.0     -1        0                   0.
```

HC.DAT for Example #2(b)

```
*NUMBER OF COMPONENTS
    7
*COMPONENT NAMES(1X,2A4)
  CO2
  C5-7
  C8-10
  C11-14
  C15-20
  C21-28
  C29+
*Pc(psi)      Tc(R)      Vc(cu ft)      M.W.        OMEGA      PARACHOR
   1071.0      548.0        1.20         44.0        0.2230        49.0
    432.8      930.0        6.142        89.93       0.2651        70.0
    344.6     1062.0        7.771       125.71       0.3644       100.0
    269.8     1203.5       12.474       174.43       0.4987       120.0
    214.8     1342.4       18.657       240.33       0.6606       250.0
    173.5     1462.8       27.257       336.06       0.8771       300.0
    123.7     1646.8       48.353       536.68       1.2789       800.0
*BINARY INTERACTION COEFFICIENTS
 0.00
 0.120  0.0
 0.120  0.0     0.0
 0.120  0.0     0.0     0.0
 0.120  0.0     0.0     0.0      0.0
 0.120  0.0     0.0     0.0      0.0      0.0
 0.120  0.0     0.0     0.0      0.0      0.0      0.0
*NUMBER OF PHASES EXPECTED
 3
*LTCOMP        ZLTCMP
 1              0.95
*MAXITF      KFLAG      DKTOL1      DKTOL2    MAXITV     TOLV
  8000          1      1.0E-15     1.0E-12    8000     1.0E-10
*METHOD      ACSS   MAXITN      EPSR       EPSV      EPSL       EPSU
    -1        6.0    10          0.6       1.E-2     1.E-4      1.E-2
```

RS.DAT for Example #2(b)

```
*HEADER(): CASE NAME
 1-D (Y) 7-COMPONENT,(MALJAMAR STO) MISCIBLE FLOODING.
*MCONFG(0 OR 1): FLAG FOR GRID BLOCK CONFIGURATTION
 0
*NX      NY      NZ: NUMBER OF GRID BLOCKS IN X, Y, AND Z
 1       40      1
*NW: NUMBER OF WELLS
 2
*RW(): WELLBORE RATIUS (FT)
 0.333   0.333
*LXW          LYW         LZWF         LZWL: WELL LOCATIONS
 1            1           1            1
 1           40           1            1
*MDX(0 OR 1): FLAG FOR GRID BLOCK SIZE IN X-DIRECTION
 0
*DX: CONSTANT GRID BLOCK SIZE IN X-DIRECTION (FT)
 0.018463
*MDY(0 OR 1): FLAG FOR GRID BLOCK SIZE IN Y-DIRECTION
 0
*DY: CONSTANT GRID BLOCK SIZE IN Y-DIRECTION (FT)
 0.25
*MDZ(0 OR 1): FLAG FOR GRID BLOCK SIZE IN Z-DIRECTION
 0
*DZ: CONSTANT GRID BLOCK SIZE IN Z-DIRECTION (FT)
 0.018463
*MD(0 OR 1): FLAG FOR FORMATION DEPTH
 0
*D(1): DEPTH (FT) OF THE MOST UPPER LAYER, FOR HORIZONTAL RESERVOIRS
 0.0
*MPOR(0 OR 1): FLAG FOR FORMATION POROSITY
 0
*PORSTD(1): HOMOGENEOUS POROSITY (FRACTION) AT STANDARD CONDITION
 0.3812
*MPERMX(0 OR 1): FLAG FOR PERMEABILITY IN X-DIRECTION
 0
*PERMX(1): HOMOGENEOUS PERMEABILITY (MD) IN X-DIRECTION
 5800.0
*MPERMY(0 OR 1): FLAG FOR PERMEABILITY IN Y-DIRECTION
 0
*PERMY(1): HOMOGENEOUS PERMEABILITY (MD) IN Y-DIRECTION
 5800.0
*MPERMZ(0 OR 1): FLAG FOR PERMEABILITY IN Z-DIRECTION
 0
*PERMZ(1): HOMOGENEOUS PERMEABILITY (MD) IN Z-DIRECTION
 5800.0
*CF      PF: FORMATION COMPRESSIBILITY (1/PSI) AND REFERENCE PRESSURE (PSI)
 4.0E-6  14.7
*ODIP
 5.202E-3
*CW      PW    DENMWS: WATER COMPR. (1/PSI), REF. PRES (PSI) AND MOL. DENSITY
 3.0E-6  14.7  3.467
*MW      VISCW: WATER MOLECULAR WEIGHT (LBM/LBM-MOLE) AND VISCOSITY (CP)
 18.0    0.5
*TEMPF: FORMATURE TEMPERATURE (F)
 90.0
*TFSTD   PSTD: STANDARD TEMPERATURE (F) AND STANDARD PRESSURE (PSI)
 60.0    14.7
*IUPSTW (1 OR 2): NUMBER OF POINTS IN COMPOSITION UPSTREAM WEIGHTING
 1
*ISTART(1 OR 2)    ISTORE(0 OR 1): FLAGS FOR READING AND STORING DATA
```

```
 1                  1
*ISINGL(0 OR 1): FLAG FOR FLASH CALCULATIONS
 1
*T: INITIAL TIME (DAYS)
 0.0
*MP (0 OR 1): FLAG FOR INITIAL PRESSURE
 0
*P(1): CONSTANT INITIAL PRESSURE (PSIA)
 800.0
*MSAT(0 OR 1): FLAG FOR INITIAL WATER SATURATION
 0
*SAT(1,1): CONSTANT INITIAL WATER SATURATION (FRACTION)
 0.0
*MOMFR(0 OR 1): FLAG FOR INITIAL OVERALL COMPOSITION
 0
*OMFR(1,K): CONSTANT INITIAL COMPOSITION (MOLE FRACTION)
 1.0E-8  0.2354  0.32949999  0.1713  0.1099  0.0574  0.0965
*TM(DAYS)   DT(DAYS)   NWELLS   GORLIM(SCF/STB)   WORLIM(STB/STB) <<<---
 0.36       0.001        2        8000000.           10.
*LW   IQTYPE: WELL NO. AND WELL TYPE
 1    1
*QTML(MOLES/D) WFRACT(FRACTION) NCOMP ISWITCH(0=N,1=Y) PBH(PSI) DPVML(MOLES/PV)
 0.41980306E-2        0.0           1     0            800.     0.10782738E-2
*KC   Z1: COMPOSITION NO. AND COMPOSITION (FRACTION)
 1   1.00
*LW   IQTYPE: WELL NO. AND WELL TYPE
 2    -2
*PBH(LW,LZ): CONSTANT BOTTOM HOLE PRESSURE (PSI)
 800.0
*TM(DAYS)   DT(DAYS)   NWELLS   GORLIM(SCF/STB)   WORLIM(STB/STB) <<<---
 -1.0          -1.0    -1       0                  0.
```

HC.DAT for Example #3

```
*NUMBER OF COMPONENTS
    12
*COMPONENT NAMES(1X,2A4)
  CO2
  CH4
  C2H5
  C3H7
  C4
  C5
  C6
  C7A
  C7B
  C7C
  C7D
  C7E
*Pc(psi)     Tc(R)     Vc(cu ft)     M.W.        OMEGA     PARACHOR
   1073.00     547.50     1.51       44.0       0.230       49.0
    673.1      343.91     1.59       16.04      0.01        50.0
    709.8      550.00     2.37       30.06      0.100       80.0
    617.4      665.95     3.21       44.09      0.150      140.0
    546.32     758.87     4.11       58.12      0.190      170.0
    486.90     838.59     4.80       72.14      0.240      200.0
    440.00     913.79     5.93       86.17      0.300      250.0
    395.00    1021.00     9.95      114.00      0.390      300.0
    304.10    1164.80    15.65      160.50      0.510      350.0
    236.80    1278.60    19.28      211.90      0.630      370.0
    169.90    1394.10    27.10      283.60      0.880      400.0
    105.50    1590.20    37.00      700.10      1.200      100.0
*BINARY INTERACTION COEFFICIENTS
 0.00
 0.120  0.0
 0.120  0.000  0.0
 0.120  0.0    0.0  0.0
 0.120  0.0    0.0  0.0  0.0
 0.120  0.0    0.0  0.0  0.0  0.0
 0.120  0.0    0.0  0.0  0.0  0.0  0.0
 0.120  0.0    0.0  0.0  0.0  0.0  0.0  0.0
 0.120  0.000  0.0  0.0  0.0  0.0  0.0  0.0  0.0
 0.120  0.000  0.0  0.0  0.0  0.0  0.0  0.0  0.0  0.0
 0.120  0.000  0.0  0.0  0.0  0.0  0.0  0.0  0.0  0.0  0.0
 0.120  0.000  0.0  0.0  0.0  0.0  0.0  0.0  0.0  0.0  0.0  0.0
*NUMBER OF PHASES EXPECTED
 3
*LTCOMP       ZLTCMP
 1            0.9
*MAXITF     KFLAG     DKTOL1     DKTOL2     MAXITV    TOLV
  2000          1     1.0E-10    1.0E-10     2000    1.0E-7
*METHOD     ACSS   MAXITN     EPSR     EPSV     EPSL     EPSU
    -1        6.0     10        0.6      1.E-2    1.E-4    1.E-2
```

RS.DAT for Example #3

```
*HEADER(): case name
 1-D (Y) 12-COMPONENT,(SPE14306 OIL-A) MISCIBLE FLOODING.
*MCONFG(0 OR 1): flag for grid block configurattion
 0
*NX     NY     NZ: number of grid blocks in x, y, and z
 1      20     1
*NW: number of wells
 2
*RW(): wellbore ratius (ft)
 0.333   0.333
*LXW        LYW        LZWF        LZWL: well locations
 1           1          1           1
 1          20          1           1
*MDX(0 OR 1): flag for grid block size in x-direction
 0
*DX: constant grid block size in x-direction (ft)
 0.14771
*MDY(0 OR 1): flag for grid block size in y-direction
 0
*DY: constant grid block size in y-direction (ft)
 0.8
*MDZ(0 OR 1): flag for grid block size in z-direction
 0
*DZ: constant grid block size in z-direction (ft)
 0.14771
*MD(0 OR 1): flag for formation depth
 0
*D(1): depth (ft) of the most upper layer, for horizontal reservoirs
 0.0
*MPOR(0 OR 1): flag for formation porosity
 0
*PORSTD(1): homogeneous porosity (fraction) at standard condition
 0.2
*MPERMX(0 OR 1): flag for permeability in x-direction
 0
*PERMX(1): homogeneous permeability (md) in x-direction
 500.0
*MPERMY(0 OR 1): flag for permeability in y-direction
 0
*PERMY(1): homogeneous permeability (md) in y-direction
 500.0
*MPERMZ(0 OR 1): flag for permeability in z-direction
 0
*PERMZ(1): homogeneous permeability (md) in z-direction
 500.0
*CF     PF: formation compressibility (1/psi) and reference pressure (psi)
 4.0E-6  14.7
*DOIP
 0.5137216068E-1
*CW     PW    DENMWS: water compr. (1/psi), ref. pres (psi) and mol. density
 3.0E-6  14.7  3.467
*MW     VISCW: water molecular weight (lbm/lbm-mole) and viscosity (cp)
 18.0    0.5
*TEMPF: formature temperature (f)
 105.0
*TFSTD  PSTD: standard temperature (f) and standard pressure (psi)
 60.0    14.7
*IUPSTW (1 OR 2): number of points in composition upstream weighting
 1
*ISTART(1 OR 2)    ISTORE(0 OR 1): flags for reading and storing data
```

```
 1                  1
*ISINGL(0 OR 1): flag for flash calculations
 1
*T: initial time (days)
 0.0
*MP (0 OR 1): flag for initial pressure
 0
*P(1): constant initial pressure (psia)
 2000.0
*MSAT(0 OR 1): flag for initial water saturation
 0
*SAT(1,1): constant initial water saturation (fraction)
 0.27
*MOMFR(0 OR 1): flag for initial overall composition
 0
*OMFR(1,K): constant initial composition (mole fraction)
 1.E-8 .1524 .0369 .0466 .0389 .0329 .0237 .2131 .1362 .0762 .1333 .1098
*TM(days)   DT(days)   NWELLS   GORLIM(scf/stb)   WORLIM(stb/stb) <<<---
 15.0      0.050        2         1.0E+10           10.
*LW   IQTYPE: well no. and well type
 1    1
*QTML(moles/d) WFRACT(fraction) NCOMP ISWITCH(0=N,1=Y) PBH(psi) DPVML(moles/pv)
 0.441278364E-2     0.0              1     0          2000.    0.5194643222E-1
*KC   Z1: composition no. and composition (fraction)
 1   1.000
*LW   IQTYPE: well no. and well type
 2     -2
*PBH(LW,LZ): constant bottom hole pressure (psi)
 2000.0
*TM(days)   DT(days)   NWELLS   GORLIM(scf/stb)   WORLIM(stb/stb) <<<---
 -1.0          -1.0    -1        0                  0.
```

HC.DAT for Example #4

```
*NUMBER OF COMPONENTS
    8
*COMPONENT NAMES(1X,2A4)
  CO2
  C3-6
  C7
  C8
  C9-10
  C11-14
  C15-20
  C21+
*Pc(psi)      Tc(R)      Vc(cu ft)      M.W.        OMEGA      PARACHOR
   1071.00     547.50      1.505        44.01      0.23000       49.0
    476.29     848.87      5.062        73.73      0.25765       60.0
    453.00     985.00      6.037        96.00      0.28000      100.0
    430.84    1040.25      8.793       102.16      0.29909      300.0
    376.36    1107.12     10.961       122.66      0.35570      350.0
    262.52    1220.00     15.214       163.50      0.46142      500.0
    205.98    1365.00     20.624       227.77      0.61854      600.0
    147.43    1580.00     30.776       420.24      0.91713      700.0
*BINARY INTERACTION COEFFICIENTS
 0.00
 0.12  0.0
 0.12  0.0     0.0
 0.12  0.0     0.0  0.0
 0.12  0.0     0.0  0.0  0.0
 0.12  0.0     0.0  0.0  0.0  0.0
 0.12  0.0     0.0  0.0  0.0  0.0  0.0
 0.12  0.0     0.0  0.0  0.0  0.0  0.0  0.0
*NUMBER OF PHASES EXPECTED
 3
*LTCOMP        ZLTCMP
 1               0.95
*MAXITF      KFLAG      DKTOL1      DKTOL2     MAXITV     TOLV
  8000           1     1.0E-16     1.0E-08     8000     1.0E-09
*METHOD      ACSS   MAXITN      EPSR      EPSV      EPSL      EPSU
    -1        6.0     10         0.6      1.E-2     1.E-4     1.E-2
```

RS.DAT for Example #4

```
*HEADER(): case name
 2-D CROSS SECT.(Y) 8-COMP.,(JNOC AMARUME STD CORE) MISCIBLE FLOODING.
*MCONFG(0 OR 1): flag for grid block configurattion
 0
*NX     NY 40  NZ: number of grid blocks in x, y, and z
 1      20     4
*NW: number of wells
 2
*RW(): wellbore ratius (ft)
 0.333   0.333
*LXW        LYW         LZWF        LZWL: well locations
 1           1           1           4
 1          40           1           4
*MDX(0 OR 1): flag for grid block size in x-direction
 0
*DX: constant grid block size in x-direction (ft)
 0.1477
*MDY(0 OR 1): flag for grid block size in y-direction
 0
*DY: constant grid block size in y-direction (ft)
 0.15
*MDZ(0 OR 1): flag for grid block size in z-direction
 0
*DZ: constant grid block size in z-direction (ft)
 0.036925
*MD(0 OR 1): flag for formation depth
 0
*D(1): depth (ft) of the most upper layer, for horizontal reservoirs
 0.0
*MPOR(0 OR 1): flag for formation porosity
 0
*PORSTD(1): homogeneous porosity (fraction) at standard condition
 0.172
*MPERMX(0 OR 1): flag for permeability in x-direction
 0
*PERMX(1): homogeneous permeability (md) in x-direction
 146.0
*MPERMY(0 OR 1): flag for permeability in y-direction
 0
*PERMY(1): homogeneous permeability (md) in y-direction
 146.0
*MPERMZ(0 OR 1): flag for permeability in z-direction
 0
*PERMZ(1): homogeneous permeability (md) in z-direction
 146.0
*CF      PF: formation compressibility (1/psi) and reference pressure (psi)
 4.0E-6  14.7
*DDIP:
 0.147279551E-1
*CW      PW    DENMWS: water compr. (1/psi), ref. pres (psi) and mol. density
 3.0E-6  14.7  3.467
*MW      VISCW: water molecular weight (lbm/lbm-mole) and viscosity (cp)
 18.0    0.5
*TEMPF: format~~ure~~ion temperature (f)
 126.5
*TFSTD   PSTD: standard temperature (f) and standard pressure (psi)
 60.0    14.7
*IUPSTW (1 OR 2): number of points in composition upstream weighting
 2
*ISTART(1 OR 2)    ISTORE(0 OR 1): flags for reading and storing data
```

```
 1                   1
*ISINGL(0 OR 1): flag for flash calculations
 1
*T: initial time (days)
 0.0
*MP (0 OR 1): flag for initial pressure
 0
*P(1): constant initial pressure (psia)
 1840.0
*MSAT(0 OR 1): flag for initial water saturation
 0
*SAT(1,1): constant initial water saturation (fraction)
 0.35
*MOMFR(0 OR 1): flag for initial overall composition
 0
*OMFR(1,K): constant initial composition (mole fraction)
 0.0005   .1772   0.1556   0.149   0.127   0.1568   0.1140   0.1199
*TM(days)   DT(days)   NWELLS   GORLIM(scf/stb)   WORLIM(stb/stb) <<<---
 3.2        0.005         2        1.0E+10           10.
*LW   IQTYPE: well no. and well type
 1    1
*QTML(moles/d) WFRACT(fraction) NCOMP ISWITCH(0=N,1=Y) PBH(psi) DPVML(moles/pv)
 0.5946701E-2      0.0             1      0          1840.0    0.112237783E-1
*KC   Z1  composition no. and composition (fraction)
 1   1.0
*LW   IQTYPE: well no. and well type
 2    -2
*PBH(LW,LZ): constant bottom hole pressure (psi)
 1840.0
```

OP.DAT for Example #4

```
*NPR: number of time step in printing into file <<TABLE.DAT>>
 3
*TPR() : time  (days)
 0.5
*MPRP() (0 OR 1): flag for pressure printing
 1
*MPMBAL() (0 OR 1): flag for overall composition printing
 1
*MPRSAT(,) (0 OR 1): flag for saturation contour
 0   1   0
*MPROMFR(,) (0 OR 1): flag for overall composition contour
 0   0   0   0   0   0   0   0   0   0   0   0
*MPRPMFR(,1,) (0 or 1): flag for phase 1 composition contour
 0   0   0   0   0   0   0   0   0   0   0   0
*MPRPMFR(,2,) (0 or 1): flag for phase 2 composition contour
 0   0   0   0   0   0   0   0   0   0   0   0
*MPRPMFR(,3,) (0 or 1): flag for phase 3 composition contour
 0   0   0   0   0   0   0   0   0   0   0   0
*MRATES(,) (0 OR 1): flag for well rates printing
 1   1
*TPR() : time  (days)
 1.0
*MPRP() (0 OR 1): flag for pressure printing
 1
*MPMBAL() (0 OR 1): flag for overall composition printing
 1
*MPRSAT(,) (0 OR 1): flag for saturation contour
 0   1   0
*MPROMFR(,) (0 OR 1): flag for overall composition contour
 0   0   0   0   0   0   0   0   0   0   0   0
*MPRPMFR(,1,) (0 or 1): flag for phase 1 composition contour
 0   0   0   0   0   0   0   0   0   0   0   0
*MPRPMFR(,2,) (0 or 1): flag for phase 2 composition contour
 0   0   0   0   0   0   0   0   0   0   0   0
*MPRPMFR(,3,) (0 or 1): flag for phase 3 composition contour
 0   0   0   0   0   0   0   0   0   0   0   0
*MRATES(,) (0 OR 1): flag for well rates printing
 1   1
*TPR() : time  (days)
 2.0
*MPRP() (0 OR 1): flag for pressure printing
 1
*MPMBAL() (0 OR 1): flag for overall composition printing
 1
*MPRSAT(,) (0 OR 1): flag for saturation contour
 0   1   0
*MPROMFR(,) (0 OR 1): flag for overall composition contour
 0   0   0   0   0   0   0   0   0   0   0   0
*MPRPMFR(,1,) (0 or 1): flag for phase 1 composition contour
 0   0   0   0   0   0   0   0   0   0   0   0
*MPRPMFR(,2,) (0 or 1): flag for phase 2 composition contour
 0   0   0   0   0   0   0   0   0   0   0   0
*MPRPMFR(,3,) (0 or 1): flag for phase 3 composition contour
 0   0   0   0   0   0   0   0   0   0   0   0
*MRATES(,) (0 OR 1): flag for well rates printing
 1   1
*NPF: number of time step in printing into <<PROFILE.DAT>>
 3
*TPF(): time (days)
 0.50
```

```
*MPFP() (0 OR 1): flag for pressure profile
 1
*MPFSAT() (0 OR 1): flag for saturation profile
 1
*MPFOMFR() (0 OR 1): flag for overall composition profile
 1
*MPFPMFR(,) (0 OR 1): flag for phase composition profile
 0    1    1
*MPFMOLE() (0 OR 1): flag for phase molar density profile
 0
*MPFMASS() (0 OR 1): flag for phase mass density profile
 1
*MPFIFT() (0 OR 1): flag for interfacial tensiion
 0
*TPF(): time (days)
 1.0
*MPFP() (0 OR 1): flag for pressure profile
 1
*MPFSAT() (0 OR 1): flag for saturation profile
 1
*MPFOMFR() (0 OR 1): flag for overall composition profile
 1
*MPFPMFR(,) (0 OR 1): flag for phase composition profile
 0    1    1
*MPFMOLE() (0 OR 1): flag for phase molar density profile
 0
*MPFMASS() (0 OR 1): flag for phase mass density profile
 1
*MPFIFT() (0 OR 1): flag for interfacial tensiion
 0
*TPF(): time (days)
 2.0
*MPFP() (0 OR 1): flag for pressure profile
 1
*MPFSAT() (0 OR 1): flag for saturation profile
 1
*MPFOMFR() (0 OR 1): flag for overall composition profile
 1
*MPFPMFR(,) (0 OR 1): flag for phase composition profile
 0    1    1
*MPFMOLE() (0 OR 1): flag for phase molar density profile
 0
*MPFMASS() (0 OR 1): flag for phase mass density profile
 1
*MPFIFT() (0 OR 1): flag for interfacial tensiion
 0
*NCT: number of time step in printing into <<CONTOUR.DAT>>
 3
*TCT(): time (days)
 0.50
*MCTP() (0 OR 1): flag for pressure contour
 1
*MCTSAT(,) (0 OR 1): flag for saturation contour
 0    1    0
*MCTOMFR(,) (0 OR 1): flag for overall composition contour
 0    0    0    0    0    0    0    0    0    0    0    0
*MCTPMFR(,1,) (0 or 1): flag for phase 1 composition contour
 0    0    0    0    0    0    0    0    0    0    0    0
*MCTPMFR(,2,) (0 or 1): flag for phase 2 composition contour
 0    0    0    0    0    0    0    0    0    0    0    0
```

```
*MCTPMFR(,3,) (0 or 1): flag for phase 3 composition contour
 0    0    0    0    0    0    0    0    0    0    0    0
*TCT(): time (days)
 1.0
*MCTP() (0 OR 1): flag for pressure contour
 1
*MCTSAT(,) (0 OR 1): flag for saturation contour
 0    1    0
*MCTOMFR(,) (0 OR 1): flag for overall composition contour
 0    0    0    0    0    0    0    0    0    0    0    0
*MCTPMFR(,1,) (0 or 1): flag for phase 1 composition contour
 0    0    0    0    0    0    0    0    0    0    0    0
*MCTPMFR(,2,) (0 or 1): flag for phase 2 composition contour
 0    0    0    0    0    0    0    0    0    0    0    0
*MCTPMFR(,3,) (0 or 1): flag for phase 3 composition contour
 0    0    0    0    0    0    0    0    0    0    0    0
*TCT(): time (days)
 2.00
*MCTP() (0 OR 1): flag for pressure contour
 1
*MCTSAT(,) (0 OR 1): flag for saturation contour
 0    1    0
*MCTOMFR(,) (0 OR 1): flag for overall composition contour
 0    0    0    0    0    0    0    0    0    0    0    0
*MCTPMFR(,1,) (0 or 1): flag for phase 1 composition contour
 0    0    0    0    0    0    0    0    0    0    0    0
*MCTPMFR(,2,) (0 or 1): flag for phase 2 composition contour
 0    0    0    0    0    0    0    0    0    0    0    0
*MCTPMFR(,3,) (0 or 1): flag for phase 3 composition contour
 0    0    0    0    0    0    0    0    0    0    0    0
```

References

[A1] Altson, R.B., Kokolis, G.P., and James, C.F.: "CO_2 Minimum Miscibility Pressure: Correlation for Impure CO_2 Streams and Live Oil System," paper SPE 11959 presented at the SPE 58th Annual Technical Conference and Exhibition, San Fransico, California (Oct., 1983).

[A2] Acs, G., Doleschall, S. and Farkas E.: "General Purpose Compositional Model," Soc. Pet. Eng. J. (Aug, 1985).

[B1] Benham, A.L., Dowden, W.E., and Kunzman, W.J.: "Miscible Fluid Displacement – Prediction of Miscibility," Trans. AIME Vol. 219, pp. 229-237 (1960).

[B2] Bear, J.: "Dynamics of Fluids in Porous Media," American Elsevier Publishing Co, Inc., New York (1972).

[C1] Coats, K.H.: "An Equation of State Compositional Model," Soc. Pet. Eng. J. (Oct, 1980).

[C2] Craig, F.F., Sanderlin, J.L., Moore, D.W. and Geffen, T.M.: "A Laboratory Study of Gravity Segregation in Frontal Drives," J. Pet. Tech. (Oct, 1957).

[C3] Chang, Y.B.: Ph.D. Dissertation, The University of Texas at Austin (in progress).

[C4] Coats, K.H.: "Simulation of Gas Condensate Reservoir Performance," paper SPE 10512 presented at the Sixth SPE Symposium on Reservoir Simulation, New Orleans, (Jan 31-Feb 3, 1982).

[D1] Dumoré, J.M., Hagoort, J. and Risseeuw, A.S.: "An Analytical Model for One-Dimensional, Three-Component Condensing and Vaporizing Gas Drives," Soc. Pet. Eng. J. (April, 1984).

[D2] Doss, M.P.: "Physical Constants of the Principal Hydrocarbons," Technical and Research Division of the Texas Company, 2nd edition, NY (1939).

[F1] Firoozabadi, A., Hekim, Y., and Katz, D.L.: "Reservoir Depletion Calculations for Gas Condensates Using Extended Analyses in the Peng-Robinson Equation of State," Cdn. J. Chem. Eng. (1978) 56, 610-15.

[G1] Gardner, J.W., Orr, F.W. and Patel, P.D.: "The Effect of Phase Behavior on CO_2-Flood Displacement Efficiency," J. Pet. Tech. (Nov, 1981).

[G2] Gardner, J.W., and Ypma, J.G.J.: "An Investigation of Phase Behavior - Macroscopic Bypassing Interaction in CO_2 Flooding," paper SPE/DOE10686 presented at the 3rd Joint DOE/SPE symposium on Enhanced Oil Recovery, Tulsa, (April, 1982).

[H1] Holm, L.W. and Josendal, V.A.: "Mechanisms of Oil Displacement by Carbon Dioxide," J. Pet. Tech. (Dec, 1974).

[H2] Holm, L.W. and Josendal, V.A.: "Discussion of Determination and Prediction of CO_2 Minimum Miscibility Pressures," J. Pet. Tech. (May, 1980).

[H3] Holm, L.W. and Josendal, V.A.: "Effect of Oil Composition on Miscible-Type Displacement by Carbon Dioxide," Soc. Pet. Eng. J. (Feb, 1982).

[H4] Herning, F. and Zipperer, L.: "Calculation of the Viscosity of Technical Gas Mixtures from the Viscosity of Individual Gases." Gas and Wassertach, 79, No. 49, 69 (1936).

[H5] Hoffmann, A.E., Crump, J.S. and Hocott, C.R.: "Equilibrium Constants for a Gas-Condensate System," SPE Trans. 1953, Vol. 198.

[I1] Inoue, S., Yazawa, N. and Arihara, N.: "Experimental and Simulation Studies of CO_2 Flood Performance at High Water Saturation," SPE 14305, 60th Annual Technical Conference and Exhibition, Las Vegas (1985).

[I2] Inoue, S., Mitsuishi, H., Morii, S., Nanba, T. and Yazawa, N.: "An Evaluation of Possible CO_2 Flooding in an Oil Reservoir," paper presented at the Workshop of the IEA collaborative project on the enhanced oil recovery, Vienna (Aug. 1983).

[J1] Johnson, J.P. and Pollin, J.S.: "Measurement and Correlation of CO_2 Minimum Miscibility Pressure," paper SPE/DOE 9790 presented at the SPE/DOE Second Joint Symposium on Enhanced Oil Recovery, Tulsa, Oklahoma (April, 1981).

[J2] Jossi, J.A., Stiel, L.I., and Thodos, G.: "The Viscosity of Pure Substance in the Dense Gaseous and Liquid Phases," AICHE Journal, 8, 59, (1962).

[K1] Kossack, C.A. and Hagen, S.: "The Simulation of Phase Behavior and Slim-Tube Displacements With Equations of State," SPE 14151, 60th Technical Conference and Exhibition, Las Vegas (1985).

[K2] Kremesec Jr, V.J and Sebastian, H.M.: "CO_2 Displacements of Reservoir Oils From Long Berea Cores: Laboratory and Simulation Results," SPE 14306, 60th Annual Technical Conference and Exhibition, Las Vegas (1985).

[K3] Kesler, M.G., and Lee, B.I.: "Improve Prediction of Enthalpy of Fractions," Hydrocarbon Processing, Vol. 55 (1976), pp. 153-158.

[K4] Katz, D.L., and Firoozabadi, A.: "Predicting Phase Behavior of Condensate/Crude-Oil System Using Methane Interaction Coefficients," J. Pet. Tech. (Nov. 1988).

[K5] Kato, K., Nagahama, K. and Hirata, M.: "Generalized Interaction Parameter for Systems Containing CO_2 and Normal Parattines," Fluid Phase Equilibria, 7 (1981).

[K6] Kenyon, D.E. and Behie, G.A.: "Third SPE Comparative Solution Project: Gas Cycling of Retrograde Condensate Reservoirs," paper SPE 12278 presented at the 1983 SPE Reservoir Simulation Symposium, San Fransisco, Nov. 15-18.

[L1] Li, Y.K., Nghiem, L.X. and Siu, A.: "Phase Behavior Computations for Reservoir Fluids: Effect of Pseudo-Components on Phase Diagrams and Simulation Results," J. of Can. Pet. (Nov-Dec, 1985).

[L2] Leach, M.P. and Yellig, W.F.: "Compositional Model Studies - CO_2 Oil-Displacement Mechanisms," Soc. Pet. Eng. J. (Feb, 1981).

[L3] Lohrenz, J., Bray, B.G. and Clark C.R.: "Calculating Viscositities of Reservoir Fluids From Their Compositions," J. Pet. Tech. (Oct, 1964).

[L4] Lawal, A.S.L.: "Improved Fluid Property Predictors for Reservoir Compositional Simulation," Ph.D. Dissertation, The University of Texas at Austin (1981).

[M1] Monger, T.G.: "The Impact of Oil Aromaticity on Carbon Dioxide Flooding," paper SPE/DOE 12708 presented at the SPE/DOE Fourth Symposium on Enhanced Oil Recovery, Oklahoma (April, 1984).

[M2] Metcalfe, R.S. and Yarborough, L.: "Effect of Phase Equilibria on the CO_2 Displacement Mechanism," Soc. Pet. Eng. J. (Aug, 1979).

[M3] Mehra, R.K., Heidemann, R.A., and Aziz, K.A.: "Acceleration of the Successive Substitution Method of Vapor-Liquid Equilibrium Calculations," paper presented at the 30th Canadian Chemical Engineering Conference, Edmonton (Oct, 1980).

[M4] Morii, S., Yazawa, N., Inoue, S. and Arihara, N.: "Effects of Oil Composition on CO_2-Flood Displacement Performance," paper presented at the 3rd European Meeting of Improved Oil Recovery, Roma (April, 1985).

[N1] Nghiem, L.X., Fong, D.K. and Aziz, K.: "Compositional Modeling With an Equation of State," Soc. Pet. Eng. J. (Dec, 1981).

[N2] Nghiem, L.X. and Li, Y.K.: "Effect of Phase Behavior on CO_2 Displacement Efficiency at Low Temperatures: Model Studies with an Equation of State," Soc. Pet. Eng. Res. Eng (July, 1986).

[N3] Naar, J., Wygal, R.J. and Henderson, J.H.: "Imbibition Relative Permeability in Unconsolidated Porous Media," Soc. Pet. Eng. J. (March, 1962).

[N4] Nanba, T., Kiuchi, T. and Tanakadate, T.: "Multiphase Equilibrium Calculations for CO_2 Flooding," paper presented at the 7th Workshop of the IEA Collaborative Project on EOR, Hannover (Sept, 1986).

[O1] Orr, F.M. and Silva, M.K.: "Effort of Oil Composition on Minimum Miscibility Pressure – Part 2: Correlation," SPE 14150, 60th Annual Technical Conference and Exhibition, Las Vegas (1985).

[O2] Orr, F.M., Silva, M.K., Lien, C.L. and Pelletier, M.T.: "Laboratory Experiments to Evaluate Field Prospects for CO_2 Flooding," J. Pet. Tech. (April, 1982).

[O3] Orr, F.M., Silva, M.K. and Lien, C.L.: "Equilibrium Phase Compositions of CO_2/Crude Oil Mixtures – Part 2: Comparison of Continuous Multiple-Contact and Slim-Tube Displacement Tests," Soc. Pet. Eng. J. (April, 1983).

[O4] Orr, F.M., Yu, A.D. and Lien, C.L.: "Phase Behavior of CO_2 and Crude Oil in Low-Temperature Reservoirs," Soc. Pet. Eng. J. (Aug, 1981).

[O5] Orr, F.M. and Taber, J.J.: "Displacement of Oil by Carbon Dioxide," Report DOE/ET/12082-9, Final Report for U.S. DOE, Contract No. DE-AC21-78 ET 12082 (May, 1981).

[P1] Perschke, D.R.: "Equation of State Phase Equilibria Calculations," M.S. Thesis, The University of Texas at Austin (1984).

[P2] Pope, G.A. and Sepehrnoori, K.: "Carbon Dioxide Flooding," 4th Annual Report of Center for Enhanced Oil and Gas Recovery Research, The University of Texas at Austin (March, 1987).

[P3] Pope, G.A. and Sepehrnoori, K.: "Carbon Dioxide Flooding," 5th Annual Report of Center for Enhanced Oil and Gas Recovery Research, The University of Texas at Austin (March, 1988).

[P4] Perschke, D.R.: Ph.D. Dissertation, The University of Texas at Austin (in progress).

[R1] Riazi, M.R. and Daubert, T.E.: "Simplify Property Predictions," Hydrocarbon Processing (March, 1980).

[R2] Reid, R.C., Prausnitz, J.H. and Sherwood, T.K.: "The Properties of Gases and Liquids," 3rd Edition, McGraw-Hill, New York (1977).

[R3] Reid, R.C., Prausnitz, J.M., and Sherwood, T.K.: The Properties of Gases and Liquids, Third Edition, McGraw-Hill Book Company, New York, 1977.

[S1] Sebastian, H.M., Wenger, R.S., and Renner, T.A.: "Correlation of Minimum Miscibility Pressure for Impure CO_2 Streams," paper SPE/DOE 12648 presented at the SPE/DOE Fourth Symposium of Enhanced Oil Recovery, Tulsa, Oklahoma (April, 1984).

[S2] Sigmund, P.M., Aziz, K., Lee, J.T., Nghiem, L.X., and Mehra, R.: "Laboratory CO_2 Floods and Their Computer Simulation," paper presented at the 10th World Pet. Cong., Bucharest. (Sept., 1979).

[S3] Stiel, L.I., and Thodos, G.: "The Viscosity of Nonpolar Gases at Normal Pressures," AIChE Journal, 7, 611 (1961).

[S4] "Selected Values of Properties of Hydrocarbons and Related Compounds," API Project 44, Texas A&M University, College Station (1969).

[T1] Tittin, D.L., and Yellig, W.F.: "Effects of Mobile Water Multiple Contact Miscible Gas Displacements," paper SPE/DOE paper 10687 presented at the 3rd Joint SPE/DOE Symposium on Enhanced Oil Recovery, Tulsa, (April, 1982).

[T2] Thele, K.J.: "A Comparison of Three Equation of State Compositional Simulators," M.S. Thesis, The University of Texas at Austin (1984).

[T3] Takeda, H.: "Including Dispersion in an Equation of State Compositional Simulator," M.S. Thesis, The University of Texas at Austin (1985).

[W1] Whitson, C.H.: "Characterizing Hydrocarbon Plus Fractions," Soc. Pet. Eng. J. (Aug, 1983).

[W2] Whitson, C.H.: "Effect of Physical Properties Estimation on Equation-of-State Predictions," SPE 11200, 57th Annual Fall Technical Conference and Exhibition, New Orleans (1982).

[W3] Watts, J.W.: "A Compositional Formulation of the Pressure and Saturation Equations," Soc. Pet. Eng. J. (May, 1986).

[Y1] Yellig, W.F. and Metcalfe, R.S.: "Determination and Prediction of CO_2 Minimum Miscibility Pressures," J. Pet. Tech (Jan, 1980).

[Y2] Yellig, W.F.: "Carbon Dioxide Displacement of a West Texas Reservoir Oil," SPE/DOE 9785, SPE/DOE 2nd Jonit Symposium on Enhanced Oil Recovery, Tulsa (1981).

[Y3] Young, L.C., and Stephenson, R.E.: "A Generalized Compositional Approach for Reservoir Simulation," Soc. Pet. Eng. J. (Oct, 1983).

VITA

Kiyoshi Ogino was born in Tokyo, Japan, on October 22, 1950, the son of Ichigoro and Kyoko Ogino. After completing his work at Kitazono High School, Tokyo, in 1971, he entered Kyoto University. He received his B.S. and M.S. degrees in Mineral Engineering, in 1975 and 1977 respectively from Kyoto University. In 1977, he entered Japan Petroleum Exploration Company, Ltd., and has been employed as a production engineer since then. In September, 1985, he entered the Graduate School of the University of Texas at Austin.

Permanent address:
409-3 Bessho
Urawa-shi, Saitama
Japan

This thesis was typed by Longhorn Copies